



THE UNIVERSITY

of ADELAIDE

FACULTY OF SCIENCES, ENGINEERING AND
TECHNOLOGY

SCHOOL OF PHYSICS, CHEMISTRY AND EARTH SCIENCES

DEPARTMENT OF PHYSICS

The Compton Amplitude from the Lattice
Feynman-Hellmann Method

Alec Hannaford Gunn

Supervisors:

A. Prof. Ross YOUNG

A. Prof. James ZANOTTI

Dr. Kadir Utku CAN

June 2023

Contents

Abstract	iii
Declaration	iv
Acknowledgements	v
1 Introduction	1
2 Quantum Chromodynamics	5
2.1 Formulation of QCD	6
2.2 Compton Scattering	11
3 Lattice QCD	28
3.1 Formulation of Lattice QCD	29
3.2 Lattice Parton Distributions	38
4 Lattice Feynman-Hellmann	45
4.1 Feynman-Hellmann Derivation	48
4.2 Implementation and Interpretation	61
5 The Off-Forward Compton Amplitude: Part I	67
5.1 Theoretical Parameterisation	68
5.2 Lattice Results	80
5.3 Conclusion and Outlook	90
6 The Off-Forward Compton Amplitude: Part II	91
6.1 Set-up and Parameterisation	92
6.2 Lattice Results and Phenomenology	98
6.3 Conclusion and Outlook	117
7 Polarised Forward Compton Amplitude	119
7.1 Set-up and Parameterisation	120
7.2 Lattice Results and Phenomenology	124
7.3 Conclusion and Outlook	136
8 The Compton Amplitude Subtraction Function	137
8.1 Background and Existing Results	139
8.2 Investigating Short-Distance Artefacts	143
8.3 Conclusion and Outlook	161
9 Conclusion and Outlook	163

A	Definitions and Conventions	165
B	Analyticity of the Compton Amplitude	167
C	Operator Product Expansion	173
D	More Fun with GPDs	178
E	Off-Forward OPE and Tensor Decomposition (Ch. 5)	180
	E.1 Operator Product Expansion	180
	E.2 Tensor Decomposition	184
F	Dirac Traces (Chs. 5-7)	188
G	Feynman-Hellmann Parameter Fits (Chs. 5-8)	192
H	Additional Lattice Results (Ch. 6)	195
I	Supplementary Calculations (Ch. 8)	199
	I.1 OPE of the Subtraction Function	199
	I.2 Structureless Fermion Scalar Charge	199
	Bibliography	203

Abstract

In both experiment and theory, Compton scattering provides a unique window into the internal structure of hadrons. At high energies the Compton amplitude is parameterised by parton distributions, which describe the properties of hadrons in terms of their fundamental constituents, quarks, anti-quarks and gluons—a vital bridge between the quark-gluon picture of quantum chromodynamics (QCD) and the hadronic picture that characterises experiment. Despite their importance, the Compton amplitude and parton distributions have both proven difficult to determine from first principles QCD.

In this thesis, we perform the first calculations of the unpolarised off-forward and polarised forward Compton amplitudes in lattice QCD. By extending the Feynman-Hellmann theorem to second-order, we are able to calculate these amplitudes from lattice two-point functions computed in the presence of a background field, and thereby overcome difficulties associated with direct calculations. Since we determine the Compton amplitude, we not only have the potential to determine parton distributions, but also a wealth of complementary properties such as scaling behaviour, higher-twist effects, and the subtraction function.

For the present investigation, we focus on determining the Mellin moments of these amplitudes. In both the unpolarised off-forward and polarised forward cases, we find that our leading moments agree reasonably well with both phenomenological expectations and determinations in other lattice methods. However, in attempting to constrain higher moments and reconstruct the parton distributions, we encounter a range of difficulties. We discuss key lattice systematics and identify strategies to overcome these in future work.

Following this discussion of lattice systematics, we devote the last chapter to an investigation of short-distance artefacts affecting our calculations. Focusing on the Compton amplitude subtraction function, we show that such short-distance artefacts are significant. However, we also demonstrate that these artefacts can be controlled using a range of tools including varying the discretisation and an analytic expansion, thus paving the way for much improved calculations in future work.

The ultimate aim of our method is a first principles calculation of the Compton amplitude with good control of all systematics. Such a calculation would have a far-reaching impact on our understanding of nucleon structure, in areas as varied as the proton spin puzzle, the proton-neutron mass difference, the proton radius puzzle and the strong coupling in the confined regime—not to mention the immense significance of the parton distributions themselves. This thesis takes us a step closer to that goal, extending the Feynman-Hellmann method to new kinematics and spin-dependent amplitudes, and starting the work to address key systematics.

Declaration

I certify that this work contains no material which has been accepted for the award of any other degree or diploma in my name, in any university or other tertiary institution and, to the best of my knowledge and belief, contains no material previously published or written by another person, except where due reference has been made in the text. In addition, I certify that no part of this work will, in the future, be used in a submission in my name, for any other degree or diploma in any university or other tertiary institution without the prior approval of the University of Adelaide and where applicable, any partner institution responsible for the joint award of this degree.

I give permission for the digital version of my thesis to be made available on the web, via the University's digital research repository, the Library Search and also through web search engines, unless permission has been granted by the University to restrict access for a period of time.

I acknowledge the support I have received for my research through the provision of an Australian Government Research Training Program Scholarship.

Acknowledgements

Despite taking place during a global pandemic, the last three years have been full of good times and good people.

Firstly, I want to thank my supervisors, Ross, James and Utku: the faith you've put in me as a researcher truly means a lot to me. You've given me the guidance and freedom I needed to develop, and have been incredibly generous with your time and knowledge. Ross, thank you for always having your door open (literally!) for any sort of physics chat, which were a great way for me to learn physics and test my ideas. James, for all the HPC help and for generally keeping us all on track—without you I'm sure every meeting would be five hours long and we'd never get anything done. Last but not least, Utku, I couldn't imagine anyone better to work on these problems with—I've learnt a lot from you.

Secondly, I feel very fortunate to have been part of such a great group of physics PhDs. I know that the many pub quizzes, whiteboard sessions, the trips to Cairns and Europe, among other shenanigans, kept me sane and provided me with a lot of joy through this journey. Not to mention officeball, which I have complete certainty will one day be an Olympic sport. I especially want to shout out Zenon and Curtis, a great pair of lads; Brad, Tommi, Josh and Bill, who cemented room 123's status as the cool office; Shanette, Mischa, Mel, Rose and Theo, who made the trip to Bonn a great time; and finally all the officeball fanatics—Hitarthi, Liam among others—may all your nicks come true.

I'd also like to thank Sharon and Silvana, who not only work(ed in Sharon's case) tirelessly to keep the whole CSSM afloat, but also made my trips to Cairns and Europe possible, which were highlights of my PhD experience.

Finally, I'm extremely grateful to my friends and family, without whose support I definitely could never have finished. Mum, Dad, Hannah, Ian and my niece Zoe, who was born during my PhD, as well as my friends Dan, Dal, Zanny, Georg and Alex—I'm very happy to have you all in my life.

Introduction

Protons and neutrons, collectively called nucleons, are the building blocks of every atom and account for over 99% of the mass of visible matter in our universe. Despite their ubiquity, the internal structure of nucleons is still not well understood. Our best understanding of nucleon structure is inferred from quantum chromodynamics, which describes the interactions of quarks and gluons, the constituents of nucleons and other hadrons. However, experiments only ever observe hadrons, never lone quarks and gluons—a property known as ‘confinement’. As such, high-energy experiments that are capable of tearing open a hadron and revealing its internal structure have been, and continue to be, central to our understanding of hadrons’ internal structure. The stories of QCD and such scattering experiments are intertwined, and naturally frame the work in this thesis; we give a brief history below.

The background

As early as 1932, it was understood that protons and neutrons are the basic constituents of atomic nuclei [1, 2]. These particles were believed to be bound by a mysterious strong nuclear force, with a famous early model proposed by Yukawa [3]. However, in the following decades, as particle colliders increased in energy, more and more strongly interacting particles were discovered, leading to a veritable particle ‘zoo’ by the mid-1950s.

Accompanying the zoo of new particles, many new theoretical frameworks emerged to explain them: S-matrix methods, current algebra and its sum rules, and the various classification schemes all sought to circumvent the need for quantum field theory (QFT) of the strong force altogether. A major breakthrough among the classification schemes was Gell-Mann’s ‘eightfold way’ [4], which introduced quarks, fractionally charged hadron constituents. However, it offered no explanation for how quarks were held together within the hadron, never seen by experiment.

SLAC, scaling and partons

From this conceptual quagmire, the first step towards clarity came in 1967 with the prediction of ‘Bjorken scaling’ [5]. Using insights from current algebra, Bjorken argued that, for a certain type of high-energy electron-proton scattering known as deep-inelastic scattering (DIS), the amplitude should be constant in Q^2 , the probing momentum, as long as the ratio between the energy transfer and Q^2 was fixed.

Later in 1967 the Stanford linear accelerator (SLAC) began measuring DIS experiments. At first, experimentalists expected that the DIS structure functions would fall off

with Q^2 , as form factors do [6]. Instead, they observed Bjorken's predicted behaviour [7]. Feynman explained these results with his parton model, which described hadrons as a collection of *weakly interacting* particles [8]. Following this, the parton model was applied by Callan and Gross to predict their famous relation between the DIS structure functions [9], and to predict the ratio of inclusive hadron production to muon production from e^+e^- scattering.

The formulation of QCD

This marked a turning point: before the SLAC experiments, physicists were dismissive about the reality of hadron constituents. With new evidence, the task became to discover the properties of these particles. In 1972, Fritsch and Gell-Mann stepped in, drawing on existing work on non-Abelian gauge theories, current algebra, quark models and the like, to give the first articulation of a quantum field theory of the strong force: QCD [10]. Two problems remained, however: (1) the parton model assumes quarks are weakly bound, but (2) quarks and gluons are never seen in experiment, implying they are strongly bound. This latter property is known as confinement.

Part of this mystery was resolved in 1972 by Gross and Wilczek [11] and Politzer [12], who showed independently that QCD has a property known as asymptotic freedom: as the probing momentum, Q^2 , is increased, the QCD coupling becomes weaker. For this they were awarded the 2004 Nobel prize. Confinement meanwhile was first explained heuristically using the string model. Then, in 1974 Wilson gave the first formulation of QCD on a lattice as part of an analytic argument for a confining mechanism arising from QCD dynamics [13].

By the mid-1970s, with these major issues addressed, and the predictions of three jet hadronisation, logarithmic scaling, and the observation of charmonium, QCD's status was cemented as our best theory of the strong force. However, it was still not possible to get numerical predictions for most phenomena, and even experimentally it was difficult to study hadrons' internal structure.

Developments in hadron structure

Feynman's parton model described DIS experiments in terms of parton distribution functions (PDFs), which can be interpreted as probability densities to find a quark or gluon within a given hadron, where the quark or gluon carries a certain fraction of the total hadron's momentum. To cast this intuitive picture into the language of QCD, theorists developed a formal framework called factorisation [14, 15]: at high energies, QCD cross sections 'factorise' into a high-energy part that could be perturbatively calculated, and a low-energy part, the parton distribution, which could then be determined from experiment. This allowed for more precise experimental determinations of parton distribution functions (PDFs) from experiments like DIS.

The late 1970s and 1980s also saw growing interest in measurements of spin-dependent parton distributions from deep-inelastic scattering, culminating in the famous EMC measurement of the proton's spin in 1987 [16]. Prior to these experiments, it was thought that the proton's 1/2 spin could be largely accounted for by the spins of its three valence quarks. However, the valence quarks accounted for a very small amount: 30% from more recent experiments [17–19]. This result, known today as the 'proton spin puzzle', suggests

that the internal structure of hadrons is far more complex than a naive reading of QCD implies.

For the first few decades after QCD's formulation, PDFs and form factors were our main tools to study hadron structure. However, further insight into hadronic structure was sought. Beginning in the mid-1990s, theorists explored a process known as deeply virtual Compton scattering (DVCS) [20, 21]. This led to Ji's realisation that DVCS could be used to determine missing components of angular momentum that are necessary to solve the proton spin puzzle [22]. The new parton distributions from this process, dubbed generalised parton distributions (GPDs), were also shown to also contain information about the spatial distributions of quarks and gluons [23] and forces and pressure within hadrons [24]—an unprecedented level of insight into hadron structure. However, to this day experimental studies of DVCS are limited, although this is expected to change with the construction of the electron-ion collider [25].

Numerical lattice QCD

Although QCD could be applied to interpret and even predict some experimental results, the coupling strength of QCD, α_S , is too large at low energies to apply perturbative techniques. Even at high energies, where perturbation theory is applicable, QCD amplitudes retain a low-energy contribution given by parton distributions.

Therefore, as early as 1979 Creutz and collaborators applied Wilson's lattice formulation to numerical calculations [26]. However, it was not until the '80s and '90s, with improvements in the formulation [27] and increases in computing power, that lattice QCD calculations became feasible. Today, numerical lattice methods provide a tool to calculate many otherwise inaccessible QCD observables from first-principles, including hadron masses, CKM matrix elements, and hadron structure quantities.

Given the importance of parton distributions to our understanding of the internal structure of hadrons, these quantities have long been a major focus of lattice QCD. However, as we will discuss in the following chapters, parton distributions cannot be accessed directly on the lattice. Nonetheless their leading Mellin moments were first calculated in the 1980s [28, 29], but the calculation of higher moments was found to be inhibited by lattice artefacts [30, 31]. As such, for a long time partonic calculations in lattice QCD were limited to these low moments.

Then beginning in 2015, a range of new lattice methods were put forward, aiming at a more complete reconstruction of parton distributions. The most prominent of these methods are the quasi- [32] and pseudo-distribution [33] approaches, but there are numerous others [34, 35], including the Feynman-Hellmann Compton amplitude method [36].

The Feynman-Hellmann method was first applied by the CSSM/QCDSF collaboration to calculate the unpolarised forward Compton amplitude [36–38]. Our method is fairly unique in that it calculates a discrete version of the physical amplitude from which parton distributions are measured, giving us access to properties that are phenomenologically and physically interesting. This thesis extends our method to the unpolarised off-forward and polarised forward Compton amplitudes, and begins an in-depth investigation of systematics.

Chapter outline

In Chapter 2 we give a brief outline of the properties of QCD, followed by a more in-depth look at forward Compton scattering (related to spin-dependent and -independent PDFs), and off-forward Compton scattering (related to GPDs). Then in Chapter 3 we give a very brief formal description of lattice QCD, as well as an account of the various other methods to calculate partonic information on the lattice.

We begin our results in Chapter 4 with a derivation of the Feynman-Hellmann relations for spin-dependent and off-forward Compton scattering. Such relations are extremely powerful in that they allow us to determine a four-point correlation function in terms of two-point functions computed in the presence of a perturbing background field.

In Chapter 5, we start our work on the off-forward Compton amplitude (OFCA) and GPDs. As most existing parameterisations of this amplitude use collinear light-like kinematics [22], we derive our own parameterisation that is suitable for Euclidean lattice calculations. We then apply this formalism and the Feynman-Hellmann relation to determine the Mellin moments of GPDs in a proof-of-principle calculation. The results of this chapter were published in Ref. [39].

We continue and improve on our calculation of the OFCA in Chapter 6. Our major improvement is showing the kinematics necessary to separate the helicity-conserving and -flipping parts of the amplitude. Hence we calculate these components separately and determine their Mellin moments, showing they are consistent with comparable three-point studies. We also perform a Regge-inspired model fit. Although this fit shows the limitations of the present method, it is instructive in pointing to the areas we need to address in future work.

Next, in Chapter 7 we perform a determination of the polarised forward Compton amplitude. As in the previous chapter, we separate the two spin-dependent amplitudes and calculate their moments, from which we determine the axial coupling and the higher-twist d_2 term—the latter quantity has proven difficult to determine with more direct lattice calculations. These determinations are broadly consistent with existing lattice and experimental results.

Finally, in Chapter 8 we investigate the Compton amplitude subtraction function. Previous lattice calculations using Feynman-Hellmann have found that this subtraction function violates behaviour predicted by the operator product expansion [40]. As such, we investigate short-distance lattice artefacts that could cause this behaviour. We demonstrate that such artefacts are significant and develop methods to control them, thereby paving the way for much improved accuracy and precision in our calculations.

Quantum Chromodynamics

Quantum chromodynamics (QCD) is the gauge field theory (GFT) that describes the strong interaction: the interactions of quarks and gluons that give rise to hadrons such as protons and neutrons. It is part of the Standard Model (SM) of particle physics, which describes three of the four fundamental forces of nature—the electromagnetic, weak and strong forces—in terms of GFTs. However, among the GFTs of the SM, QCD has perhaps the most non-trivial dynamics. Due in part to the strength of the force (the strong coupling is $\alpha_S \sim 1$ at standard energy scales—i.e. on the order of the low lying hadronic masses), QCD exhibits complex emergent behaviour such as confinement and asymptotic freedom. Moreover, as the strong coupling is close to unity at low energies, standard perturbation theory cannot be applied to QCD and we must use alternative methods—see Chapter 3.

One way we can understand the non-trivial behaviour of QCD is through hadronic structure: the study of how properties of hadrons emerge from the interactions of their quarks and gluons. For instance, although protons are defined by their three valence quarks, the sum of these quarks' masses is ≈ 9 MeV, whereas the total proton mass is ≈ 938 MeV. This means that the vast majority of the proton's mass, and hence the vast majority of visible matter, is generated by the strong interaction. Similarly, approximately 30% of the proton's spin can be attributed to the spin of its valence quarks [17–19], with the rest coming from internal dynamics of the proton: the orbital angular momentum of its constituents and the spins of quarks and gluons in the QCD vacuum. As almost all visible matter is composed of protons and neutrons, the dynamical behaviour of QCD is therefore central to understanding the properties of such matter.

To understand hadronic structure, one of the most important processes to study is high-energy nucleon-electron scattering. In such processes, the target nucleon is ripped apart by the incoming electron, and its internal structure revealed. More formally, we describe these high-energy scattering cross sections in terms of parton distributions, among the most important of which are the parton distribution functions (PDFs), introduced in the late 1960s by Feynman [8] and Bjorken and Paschos [41]. PDFs from spin-dependent and spin-independent deep-inelastic scattering (DIS) are probability densities that describe how the momentum and spin of hadrons are distributed among their constituents*. Then in the 1990s generalised parton distributions (GPDs) were introduced [22, 42, 43]. In addition to providing further information about the partition of hadron spin among its constituents, these GPDs also provide information about the spatial distribution of quarks and gluons within a hadron.

*Moreover, PDFs are used ubiquitously as Standard Model backgrounds in searches for Beyond Standard Model (BSM) physics.

Moreover, nucleon-electron scattering is interesting as it allows us to study the energy regimes of QCD. At low energies we are in the confined region, where quarks and gluons appear bound within hadrons, and we are limited to a description in terms of hadronic resonances. At high energies we are in the asymptotically free region of QCD, where scattering is described in terms of quark and gluon degrees of freedom, parameterised by the parton distributions. The transition between these two regions in nucleon-electron scattering can greatly help further our understanding of the non-trivial dynamics of QCD [44].

In this chapter, we start in Section 2.1 with a very brief introduction to the QCD Lagrangian, and a discussion of the dynamical properties of QCD: confinement, asymptotic freedom and factorisation. Then in Section 2.2, we give an overview of important observables in hadronic structure: elastic form factors (EFFs), structure functions and PDFs (spin-dependent and -independent), and finally off-forward Compton scattering and GPDs.

2.1 Formulation of QCD

In this section, we describe some of the formal properties of the classical QCD Lagrangian, and introduce the dynamical properties of QCD: asymptotic freedom and confinement. Quantum chromodynamics is defined by its gauge invariance—the QCD Lagrangian and all QCD observables are invariant under the SU(3) group of transformations. Importantly, this invariance is local, meaning that different spacetime points will have different gauge spaces.

An element of SU(3) as a function of a spacetime point, z , can be expressed as

$$V(z) = \exp [i\alpha^a(z)t^a], \quad (2.1)$$

where $\alpha^a(z)$ is a phase factor, and t^a are the generators of the group[†]. Note that the elements of SU(3) do not commute—a property that gives rise to the non-trivial dynamics of QCD.

The fermion (quark) fields transform like

$$\psi_i(z) \rightarrow \psi'_i(z) = [V(z)]_{ij}\psi_j(z), \quad (2.2)$$

where i, j are colour indices[‡].

To start constructing a gauge-invariant Lagrangian, we need to define a covariant derivative, D_μ , such that kinetic term $D_\mu\psi$ and ψ transform in the same way. Consider a naive derivative:

$$n^\mu\partial_\mu\psi(z) = \lim_{\epsilon \rightarrow 0} \frac{\psi(z + \epsilon n) - \psi(z)}{\epsilon}. \quad (2.3)$$

Since our quark fields are locally gauge invariant, $\psi(z + \epsilon)$ and $\psi(z)$ occupy different gauge spaces, and hence this naive derivative does not have the desired transformation.

[†]In terms of the Gell-Mann matrices, λ^a , we can write $t^a = \frac{\lambda^a}{2}$ for the fundamental representation of SU(3).

[‡]There are two types of colour indices used here: (1) indices of the 3×3 SU(3) matrices in the fundamental representation: i, j . Second, the indices that label the individual generators t^a for SU(3): a, b, c .

Therefore, to define a covariant derivative, we need an operator, $U(z_1, z_2)$, such that $U(z + \varepsilon n, z)\psi(z)$ transforms like $\psi(z + \varepsilon n)$. This operator is the Wilson line, defined as

$$U(z_1, z_2) \equiv \mathcal{P} \exp \left\{ ig \int_{z_2}^{z_1} dz^\mu t^a A_\mu^a(z) \right\}, \quad (2.4)$$

where \mathcal{P} denotes path-ordering, t^a are again the generators, and g is the strong coupling constant. The Wilson line satisfies the transformation law

$$U(z_1, z_2) \rightarrow V(z_1)U(z_1, z_2)V(z_2)^{-1}. \quad (2.5)$$

Therefore, as desired, the derivative of quark fields transforms like

$$n_\mu D_{ij}^\mu \psi_j(z) = \lim_{\varepsilon \rightarrow 0} \frac{\psi(z + \varepsilon n) - U(z + \varepsilon n, z)\psi(z)}{\varepsilon} \rightarrow [V(z)]_{ij} n_\mu D_{jk}^\mu \psi_k(z). \quad (2.6)$$

For an infinitesimal path,

$$U(z + \varepsilon n, z) = \mathbb{I} + i\varepsilon n^\mu g A_\mu^a(z) t^a, \quad (2.7)$$

and hence, by comparison with Eq. 2.3, we write the covariant derivative as

$$D^\mu = \partial^\mu - ig A_a^\mu t^a, \quad (2.8)$$

where we interpret A_μ^a as the gauge boson fields—the gluon fields. Since there are eight SU(3) generators, there are eight types of gluon.

It is also useful to define the field strength tensor, $F_{\mu\nu}^a$:

$$[D_\mu, D_\nu] = -ig F_{\mu\nu}^a t^a, \quad (2.9)$$

which can be used to construct gauge invariant quantities.

The Classical Lagrangian

Our QCD Lagrangian then must satisfy: (1) local gauge invariance, and (2) renormalisability (it has mass dimension four: $[\mathcal{L}] = 4$). We also neglect the CP-violating ‘QCD theta term’, $\epsilon_{\mu\nu\rho\sigma} F^{a\mu\nu} F^{a\rho\sigma}$, which is known from experiment to have an extremely small coefficient[§] [46].

One can then enumerate all possible structures that satisfy these conditions [47] to construct the Lagrangian:

$$\mathcal{L} = \sum_f \bar{\psi}_f^i (\not{D}^{ij} - \delta^{ij} m_f) \psi_f^j - \frac{1}{4} F^{a\mu\nu} F_{\mu\nu}^a. \quad (2.10)$$

Note that f is the flavour index that runs over the species of quarks: $f = u, d, s, c, b, t$.

For the quantised QCD Lagrangian density, we must include ghost terms that arise from the gauge-fixing condition, and counter-terms from renormalisation. For the purposes of our simple description of QCD, we omit such terms.

[§]The search for a mechanism to explain this coefficient’s small size is known as the ‘strong CP problem’ [45], and is a major puzzle in physics but not relevant to the present thesis.

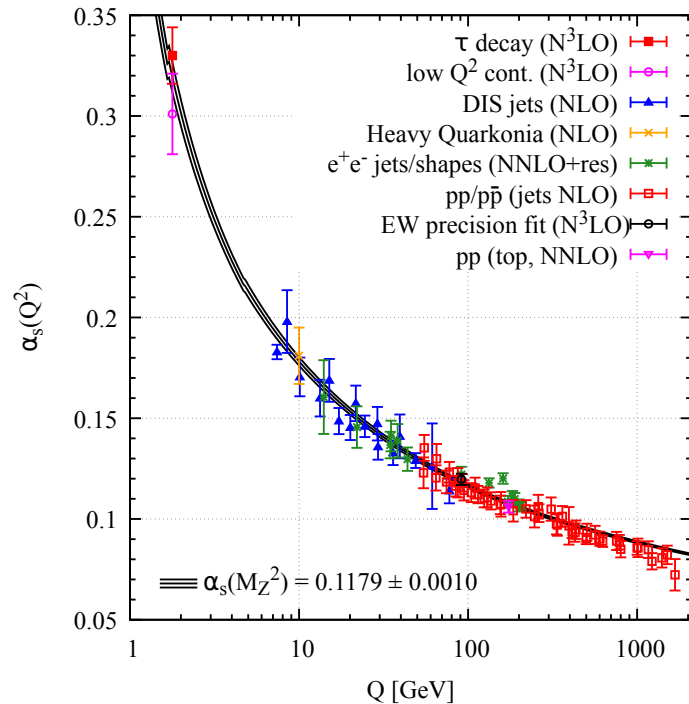


Figure 2.1: The strong coupling measured across a range of momentum scales, using different processes—figure from Particle Data Group [48].

Since the elements of $SU(3)$ do not commute, there are interaction terms in the Lagrangian that are cubic and quartic in the A_μ^a fields: $A_\mu^b A_\nu^c \partial^\mu A^{a\nu}$ and $A^{b\mu} A^{c\nu} A_\mu^a A_\nu^d$, respectively. Physically, these terms can be interpreted as self-interactions of the gluons, which gives rise to non-trivial properties of QCD.

2.1.1 Asymptotic freedom and confinement

Due to the nature of gluon self-interaction, QCD is divided into two domains: the long-distance/low-energy domain, where the strength of QCD interactions is strong. In this region, quarks and gluons are completely confined within colour neutral hadrons, such as baryons (e.g. protons and neutrons) and mesons (e.g. pions). On the other hand, in the short-distance/high-energy domain, QCD interactions become weaker, which is referred to as “asymptotic freedom”.

The strength of QCD interactions are described in terms of the strong coupling:

$$\alpha_S \equiv g^2/4\pi, \quad (2.11)$$

where g is the QCD coupling constant, introduced in Eq. (2.4). For a momentum scale Q such that $Q \gg \Lambda_{\text{QCD}}$ with Λ_{QCD} being the QCD scale, we can calculate the coupling to one-loop order in perturbation theory:

$$\alpha_S(Q) \propto \frac{1}{\log(Q/\Lambda_{\text{QCD}})}. \quad (2.12)$$

Note that $\Lambda_{\text{QCD}} \approx 0.2$ GeV is on the order of low-lying hadronic masses.

The property of asymptotic freedom follows from Eq. (2.12): for $Q \gg \Lambda_{\text{QCD}}$, the coupling is small and hence the interactions are weak. See Fig. 2.1 for the experimental determination of $\alpha_S(Q)$. By contrast, for low-energies, $Q \lesssim \Lambda_{\text{QCD}}$, we are in the confined regime, where quarks and gluons are completely bound and for which $\alpha_S \gtrsim 1$. Note that the property of confinement does not follow from Eq. (2.12), which is only valid for high energies. As yet, no first principles proof of confinement exists [49].

2.1.2 Factorisation

As discussed above, for $Q \gg \Lambda_{\text{QCD}}$, the strong coupling is small enough to permit perturbation theory: $\alpha_S < 1$. Consequently, for high-energy QCD processes, we can apply perturbation theory. However, even for such processes, most QCD cross sections cannot be calculated from perturbation theory alone. Instead, QCD cross sections ‘factorise’ into short-distance/high-energy contributions, which are calculable in perturbation theory, and long-distance/low-energy contributions which are not**.

The most basic form of a factorisation relation for a high energy quantity, F , is

$$F(Q^2) = \underbrace{\mathcal{C}(\alpha_S(Q))}_{\text{short-distance}} \otimes \underbrace{q}_{\text{long-distance}} + \underbrace{\mathcal{O}\left(\frac{\Lambda_{\text{QCD}}^2}{Q^2}, \frac{m_N^2}{Q^2}\right)}_{\substack{\text{power-suppressed corrections} \\ \text{(higher-twist and target mass corrections)}}, \quad (2.13)$$

where \otimes represents a convolution or a simple multiplication, depending on what F is. The scale is $Q \gg \Lambda_{\text{QCD}}$, which is often referred to as the hard scale, and q is low-energy/long-distance contribution such as a parton distribution. In this thesis, we neglect the renormalisation scale dependence of q , typically written as $q(\mu)$.

In Eq. (2.13) there are several different terms that are suppressed for $Q \gg \Lambda_{\text{QCD}}, m_N$:

- The function \mathcal{C} , the Wilson coefficient or perturbative kernel, will have $\mathcal{O}(\alpha_S)$ corrections. As α_S itself goes like $1/\log(Q/\Lambda_{\text{QCD}})$, these corrections to \mathcal{C} are suppressed for large Q . Since we can calculate \mathcal{C} in perturbation theory to a given order in α_S , it is possible to obtain such terms to a high degree of accuracy [51].
- There are target mass corrections that are $\mathcal{O}(m_N^2/Q^2)$, but which are attached to leading-order long-distance contributions. There are well-known methods to account for these contributions [52].
- Finally, there are higher-twist corrections^{††}. These are usually the hardest corrections to control since they contain their own non-perturbative contributions, distinct from those at leading-order. They are, however, more interesting, since these higher-twist structures provide us with interesting information about QCD dynamics.

However, at large energy scales, $Q^2 \gtrsim 10 \text{ GeV}^2$, we expect all these corrections to be minimal, and the long-distance contribution, q , can be determined from experiment. Alternatively, it is possible to constrain q from lattice QCD—see Section 3.2.

**The exception to this are processes such as $e^+e^- \rightarrow \text{hadrons}$ [50].

††The term ‘twist’ is used in two related but distinct ways in the literature. Either terms that are $Q^{2-\tau}$ suppressed are sometimes referred to as being of twist τ , with leading order terms being $\tau = 2$ and higher-twist being more suppressed [53]. On the other hand, ‘twist’ may refer to transformation properties of an operator [54]. The two definitions usually coincide. In this thesis, we use twist to refer to properties of the operators, and refer to terms that are explicitly Q^{-1} suppressed as ‘power-suppressed’.

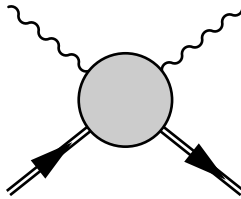


Figure 2.2: The Feynman diagram for generic Compton scattering. The shaded blob represents all photon-nucleon interactions.

In this thesis, we focus on the region $Q^2 \approx 2 - 12 \text{ GeV}^2$, which is what our lattice calculations can access. It is also a highly interesting region, as it encompasses the threshold of the perturbative region (i.e. where Eq. (2.13) becomes applicable), and hence helps us understand the transition from a hadronic to a quark-gluon description; or, using the terminology of the previous section, the transition from the confined to the asymptotically free region [44].

To give an example of Eq. (2.13), the Mellin moments of structure functions satisfy the following factorisation relation:

$$M_n(Q^2) = \sum_f c_n^f(\alpha_s(Q)) a_n^f + \mathcal{O}\left(\frac{\Lambda_{\text{QCD}}^2}{Q^2}, \frac{m_N^2}{Q^2}\right), \quad (2.14)$$

where, for our purposes, the n^{th} Mellin moment of a function $f(x)$ is defined as

$$M_n = \int_0^1 dx x^{n-1} f(x). \quad (2.15)$$

In Eq. (2.14), c_n is known as the Wilson coefficient, which is perturbatively calculable, and a_n is the parton distribution function moment, which contains the long-distance physics. This sort of factorisation theorem can be derived using the operator product expansion.

Using more modern methods of perturbative QCD [50], one can derive a factorisation theorem for the structure function $F(x, Q^2)$:

$$F_1(x, Q^2) = \sum_f \int_x^1 \frac{dy}{y} \mathcal{C}_f\left(\frac{x}{y}, \alpha_s(\mu), Q/\mu\right) q_f(y, \mu) + \mathcal{O}\left(\frac{\Lambda_{\text{QCD}}^2}{Q^2}, \frac{m_N^2}{Q^2}\right), \quad (2.16)$$

where again \mathcal{C} is short-distance and perturbatively calculable, while q_f is the long-distance PDF.

In Eq. (2.16), $q_f(y, \mu)$ is the *renormalised* PDF at renormalisation scale μ . Unlike Q which is fixed by the kinematics of the process, μ is arbitrary and is often chosen to be $\mu = Q$. We note that such renormalised PDFs do not have such a straightforward probability interpretation compared to the ‘bare’ PDFs of the leading-order parton model. As our focus in this thesis is the extraction of the amplitudes themselves—e.g. F_1 in Eq. (2.16)—we are not currently concerned with a perturbative matching of parton distributions or their renormalisation; see Refs. [15, 51, 55] for a treatment of perturbative QCD, and the renormalisation and scale dependence of parton distributions. Considering such details will become necessary as our calculations become more sophisticated.

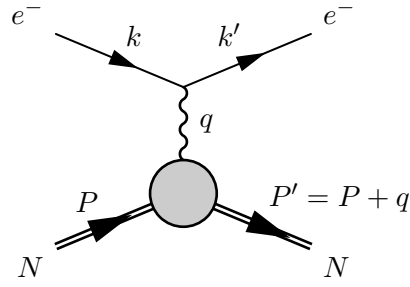


Figure 2.3: The Feynman diagram for elastic electron-nucleon scattering.

2.2 Compton Scattering

Our primary objective in this thesis is to calculate Compton amplitudes in lattice QCD. In particular, we will calculate the unpolarised off-forward Compton amplitude in Chapters 5 and 6, the polarised Compton amplitude in Chapter 7, and the Compton amplitude subtraction function in Chapter 8. The nucleon Compton amplitude is the amplitude for nucleon-photon scattering—see Fig. 2.2. It is typically measured experimentally from nucleon-electron scattering processes, such as deep-inelastic scattering (DIS) and deeply virtual Compton scattering (DVCS).

To begin this brief review of the physics of Compton scattering, we start with the simpler case of *elastic* nucleon-electron scattering, which is not a type of Compton scattering but which is highly related. Then, we review spin-averaged forward Compton scattering, introducing much of the relevant formalism as well. Further, we discuss polarised Compton scattering, the focus of Chapter 7, and finally we introduce off-forward Compton scattering, the focus of Chapters 5 and 6.

2.2.1 Elastic nucleon-electron scattering

Although we do not calculate elastic form factors (EFFs) in this thesis, we will refer to them frequently and so give a brief definition here. These form factors parameterise elastic^{‡‡} nucleon-electron scattering: $e^-(k) + N(P) \rightarrow e^-(k') + N(P')$ —Fig. 2.3.

The scattering matrix for this process is proportional to the matrix element for a single nucleon-photon interaction:

$$\langle P' | j^\mu(0) | P \rangle = \bar{u}(P') \left[\gamma^\mu F_1(Q^2) + \frac{i\sigma^{\mu\nu}(P' - P)_\nu}{2M} F_2(Q^2) \right] u(P), \quad (2.17)$$

where $\bar{u}(P')$ and $u(P)$ are Dirac spinors.

In this thesis, we only consider nucleons and hence define $|P\rangle$ as the nucleon state of momentum P_μ . The electromagnetic hadron current, j^μ , is

$$j^\mu(z) = \sum_f e_f \bar{\psi}_f(z) \gamma^\mu \psi_f(z), \quad (2.18)$$

where $\bar{\psi}_f$ and ψ_f are quark fields of flavour f , and $e_u = \frac{2}{3}$, $e_d = -\frac{1}{3}$ etc. for the charges of the quarks.

In Eq. (2.17), the Lorentz scalar functions $F_1(Q^2)$ and $F_2(Q^2)$ are the Dirac and Pauli electromagnetic form factors, respectively. They are non-perturbative quantities, and

^{‡‡}Elastic processes are those in which the initial states are the same as the final states.

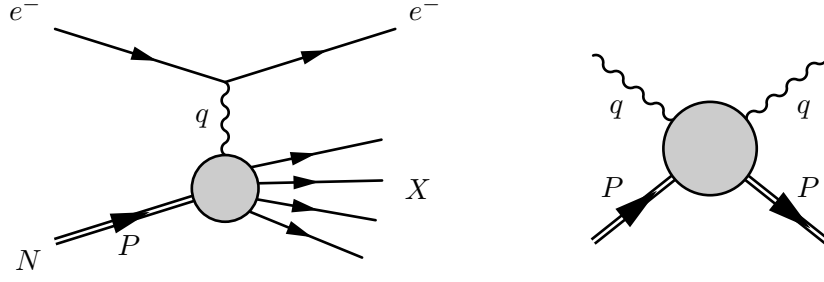


Figure 2.4: Left: the Feynman diagram for deep-inelastic scattering. Right: the Feynman diagram for forward Compton scattering.

therefore can only be measured from experiment or calculated from first principles on the lattice.

For EFFs, the standard notation is to define them as functions of $Q^2 = -q^2 = -(P' - P)^2$. From the Minkowski triangle inequality, we can show that q is a spacelike vector, and hence $Q^2 = -q^2 \geq 0$.

2.2.2 Spin-averaged forward Compton scattering

Now, we introduce the simplest and best-studied case of Compton scattering: forward, spin-averaged. Moreover, we use this section to introduce the theoretical tools—tensor decomposition, dispersion relations, operator product expansion and parton distributions—that form the basis of our theoretical parameterisation and interpretation of Compton amplitudes for this thesis. Finally, we note that this is a brief review of the topic; for more complete introductions see Refs. [47, 51, 56, 57].

We start by defining the forward^{§§} Compton amplitude:

$$T_{\mu\nu} \equiv i \int d^4z e^{iq \cdot z} \langle P | \mathcal{T} \{ j_\mu(z) j_\nu(0) \} | P \rangle, \quad (2.19)$$

where $\mathcal{T}\{\dots\}$ is the time-ordering operator, and q_μ is the virtual photon momentum (see Fig. 2.4 right).

Using the Ward identity $q_\mu T^{\mu\nu} = 0 = q_\nu T^{\mu\nu}$ and other discrete symmetries, the forward Compton amplitude can be decomposed into a sum of Lorentz invariant amplitudes multiplied by gauge invariant tensor structures:

$$\begin{aligned} T_{\mu\nu}(P, q) = & \left(-g_{\mu\nu} + \frac{q_\mu q_\nu}{q^2} \right) \mathcal{F}_1(\omega, Q^2) + \left(P_\mu - \frac{P \cdot q}{q^2} q_\mu \right) \left(P_\nu - \frac{P \cdot q}{q^2} q_\nu \right) \frac{\mathcal{F}_2(\omega, Q^2)}{P \cdot q} \\ & + \frac{i}{P \cdot q} \epsilon_{\mu\nu\rho\kappa} q^\rho \left(s^\kappa \tilde{g}_1(\omega, Q^2) + \left(s^\kappa - \frac{s \cdot q}{P \cdot q} P^\kappa \right) \tilde{g}_2(\omega, Q^2) \right), \end{aligned} \quad (2.20)$$

where we have introduced the spin vector

$$s_\mu \equiv \frac{1}{2} \bar{u}(p, s) \gamma_\mu \gamma_5 u(p, s), \quad (2.21)$$

^{§§}Forward scattering means that the momentum of the incoming and outgoing states is the same, while off-forward means the opposite.

and the kinematic scalars

$$Q^2 = -q^2, \quad \omega = \frac{2P \cdot q}{Q^2} = x^{-1}. \quad (2.22)$$

The momentum transfer, Q^2 , is the hard scale, while x is referred to as the *Bjorken scaling variable*, and $\omega = x^{-1}$. Note that it is common for $P \cdot q$ or $P \cdot q/m_N$ to be denoted as ν . However, we generally avoid this.

The forward virtual ($q^2 \neq 0$) Compton amplitude is never measured directly in experiment. Instead, it can be related to the process of deep-inelastic scattering (DIS), in which a high-energy electron scatters inelastically with a nucleon: $N + e^- \rightarrow X + e^-$ (see Fig. 2.4 left). More concretely, the hadronic tensor of inclusive*** DIS is given by

$$W_{\mu\nu} = \int d^4z e^{iq \cdot z} \langle P | j_\mu(z) j_\nu(0) | P \rangle. \quad (2.23)$$

Note that this is effectively Eq. (2.19) but here the currents are not time-ordered.

The hadronic tensor can likewise be decomposed in an identical way to Eq. (2.20), except with the replacements $\mathcal{F}_{1,2} \rightarrow F_{1,2}$ and $\tilde{g}_{1,2} \rightarrow g_{1,2}$.

The relationship between the Compton amplitude, Eq. (2.19), and the hadronic tensor, Eq. (2.23), can be made using the optical theorem:

$$2\text{Im}\mathcal{M}(P \rightarrow P) = \sum_X \int \frac{d^3P_X}{(2\pi)^3} \frac{1}{2P_X^0} (2\pi)^4 \delta^{(4)}(P - P_X) |\mathcal{M}(P \rightarrow X)|^2, \quad (2.24)$$

where $\mathcal{M}(P \rightarrow X)$ is the inclusive DIS amplitude, and $\mathcal{M}(P \rightarrow P)$ is the forward Compton scattering amplitude. The former is in terms of the hadronic tensor, while the latter is in terms of the Compton amplitude.

With some rearranging, the optical theorem can be written for the structure functions as

$$\text{Im}(\mathcal{F}_{1,2}) = 2\pi F_{1,2}, \quad \text{Im}(\tilde{g}_{1,2}) = 2\pi g_{1,2}. \quad (2.25)$$

After averaging over spins, only the spin-independent scalar amplitudes of the forward Compton amplitude, $\mathcal{F}_{1,2}$, survive. These amplitudes satisfy the following fixed- Q^2 dispersion integrals [58] (see Appendix B for a derivation):

$$\overline{\mathcal{F}}_1(\omega, Q^2) = \mathcal{F}_1(\omega, Q^2) - \mathcal{F}_1(0, Q^2) = 2\omega^2 \int_0^1 dx \frac{2xF_1(x, Q^2)}{1 - x^2\omega^2 - i\epsilon}, \quad (2.26)$$

$$\mathcal{F}_2(\omega, Q^2) = 4\omega \int_0^1 dx \frac{F_2(x, Q^2)}{1 - x^2\omega^2 - i\epsilon}, \quad (2.27)$$

where $F_{1,2}(x = \omega^{-1}, Q^2)$ are the DIS structure functions that parameterise the hadronic tensor, Eq. (2.23), not to be confused with the Dirac and Pauli EFFs, Eq. (2.17). In this thesis, while the forward spin-averaged Compton structure functions are not our main object of interest, they have been determined elsewhere using Feynman-Hellmann [36–38], and we will need them in Chapters 5 and 6 as the forward limit of our off-forward Compton amplitude.

***Inclusive processes are those in which the final state product is *not* specified, hence why Eq. (2.24) has a sum over X the final state.

Importantly, we note that Eq. (2.26) features a contribution from the *Compton amplitude subtraction function*:

$$S_1(Q^2) \equiv \mathcal{F}_1(\omega = 0, Q^2). \quad (2.28)$$

This subtraction function will be the focus of Chapter 8. Unlike $\overline{\mathcal{F}}_1$ and \mathcal{F}_2 , this object cannot be related directly to the experimental DIS structure functions. However, it is still a background for important experimental measurements, such as the proton charge radius [59, 60], and proton–neutron mass difference [61, 62].

For this thesis, the dispersion relations in Eqs. (2.26) and (2.27) are particularly useful because they relate the Compton structure functions at *any value of ω* to the DIS structure functions. This is important, as on the lattice we only have access to the unphysical region, $|\omega| \leq 1$. In particular, we can Taylor expand around $\omega = 0$ to get

$$\overline{\mathcal{F}}_1(\omega, Q^2) = 4 \sum_{n=1}^{\infty} \omega^{2n} \int_0^1 dx x^{2n-1} F_1(x, Q^2) = 2 \sum_{n=1}^{\infty} \omega^{2n} M_{2n}^{(1)}(Q^2), \quad (2.29)$$

$$\mathcal{F}_2(\omega, Q^2) = 4 \sum_{n=1}^{\infty} \omega^{2n-1} \int_0^1 dx x^{2n-2} F_2(x, Q^2) = 4 \sum_{n=1}^{\infty} \omega^{2n-1} M_{2n}^{(2)}(Q^2), \quad (2.30)$$

where $M_n^{(i)}(Q^2)$ are the Mellin moments, as defined in Eq. (2.15), of the structure functions. Note that a factor of two is absorbed by the moment in Eq. (2.29).

Since the DIS structure functions, $F_{1,2}$, are proportional to a positive definite scattering amplitude, they are positive definite functions. As such, their moments are monotonically decreasing with n :

$$M_n^{(i)} \geq M_{n+1}^{(i)} \geq 0, \quad \text{for any } n \in \mathbb{N} \text{ and } i = 1, 2. \quad (2.31)$$

More generally the moments of $F_{1,2}$ satisfy the Hausdorff moment criteria for positive-definite functions [63]:

$$(1 - S)^k M_n^i \geq 0, \quad \text{for any } n, k \in \mathbb{N} \text{ and } i = 1, 2,$$

where S is the operator $SM_n^{(i)} = M_{n+1}^{(i)}$.

Perturbative Compton scattering

For this thesis, we are primarily interested in the Compton amplitude for the high energy region, $Q^2 \gg \Lambda_{\text{QCD}}^2$, where perturbation theory is applicable, as discussed in Section 2.1. As such, we give a brief review of some basic tools in the perturbative expansion of this Compton amplitude.

In this high-energy region, there are strong constraints on our Lorentz scalars, Eq. (2.22). First, the virtual photon momentum, q_μ , must be a space-like vector, which can be shown using the Minkowski triangle inequality. Therefore, it follows $Q^2 = -q^2 \geq 0$.

Secondly, in inelastic scattering the mass of the intermediate state, m_X , must be greater than the ground state, m_N . Hence $m_X = (P + q)^2 > m_N^2$. With some manipulation, this becomes

$$P^2 + 2P \cdot q - Q^2 > P^2 \quad \Rightarrow \quad 2P \cdot q > Q^2 \quad \Rightarrow \quad \omega = \frac{2P \cdot q}{Q^2} > 1. \quad (2.32)$$

For time-ordered Compton scattering, we also have the crossed diagram: $m_X = (P - q)^2 > m_N^2$. And hence we have the limit $|\omega| > 1$, and consequently the Bjorken scaling variable $x = 1/\omega$ has the range $|x| < 1$.

Bjorken scaling and the naive parton model

In 1967, Bjorken predicted that the DIS cross section should exhibit a behaviour now known as ‘Bjorken scaling’ [5]: at fixed x and large Q^2 the DIS structure functions should behave like constants in Q^2 :

$$\lim_{Q^2 \rightarrow \infty} F_1(x, Q^2) = F_1(x), \quad \lim_{Q^2 \rightarrow \infty} P \cdot q F_2(x, Q^2) = P \cdot q F_2(x). \quad (2.33)$$

This behaviour was later confirmed by experiments performed at the Stanford linear accelerator (SLAC) [7], which paved the way for the discovery of QCD as the gauge theory of the strong force. Hence the *Bjorken limit* is

$$Q^2 \rightarrow \infty, \quad P \cdot q \rightarrow \infty, \quad x, \omega \text{ fixed to finite values.} \quad (2.34)$$

In coordinate space this limit corresponds to the current separation, z_μ , in Eq. (2.19) approaching a light-like vector [64,65]. As such, the nucleon in the Bjorken limit propagates along the light-cone.

In response to the SLAC experiments, Feynman [8] and Bjorken and Paschos [41] recognised that Bjorken scaling behaviour could be recovered if one assumed that the nucleon was composed of non-interacting fundamental particles, which they called partons. This led to the very simple model of the hadronic tensor, Eq. (2.23), as a sum of hadronic tensors, $W_f^{\mu\nu}$, for a given parton species, weighted by $q_f(x)$, the probability density to find a parton of species f and carrying a fraction, x , of the nucleon’s total momentum:

$$W^{\mu\nu} = \sum_f \int_0^1 dx' q_f(x') W_f^{\mu\nu}, \quad (2.35)$$

These probability densities, once cast into QCD language become parton distribution functions (PDFs), which we discuss throughout this thesis.

Using this simple model, one can derive [56] that the DIS structure functions become

$$F_1(x) = \frac{1}{2} \sum_f e_f^2 (q_f(x) + \bar{q}_f(x)), \quad F_2(x) = x \sum_f e_f^2 (q_f(x) + \bar{q}_f(x)). \quad (2.36)$$

where $\bar{q}_f(x)$ is the probability density of the anti-quark. Hence in the parton model, the structure functions are independent of Q^2 . Moreover, in the partonic picture the Bjorken scaling variable coincides with the parton momentum fraction, x .

Finally, we note that Eq. (2.36) implies the famous Callan-Gross relation [9]:

$$F_2(x) = 2xF_1(x). \quad (2.37)$$

The operator product expansion

The first connection between the emerging theory of QCD and the partonic description became possible with Wilson’s operator product expansion (OPE) [66]. For two operators,

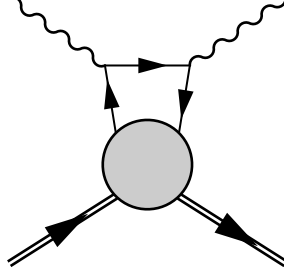


Figure 2.5: Feynman diagram showing the handbag diagram.

A and B , Wilson conjectured that at short distances

$$A(z)B(0) \xrightarrow{z \rightarrow 0} \sum_i c_i(z) \mathcal{O}_i(0). \quad (2.38)$$

The OPE is a coordinate space equivalent of the factorisation relation, Eq. (2.13), where the Wilson coefficients, c_i , describe the short-distance physics, and the operators, \mathcal{O}_i , describe the long-distance physics. More discussion of the OPE is given in Appendix C.

The OPE of the product of currents in Eq. (2.19) is

$$\begin{aligned} \mathcal{T}\{j^\mu(z)j^\nu(0)\} &\xrightarrow{z \rightarrow 0} (\partial_\mu \partial_\nu - g_{\mu\nu} \partial^2) \sum_{n=0,2,4}^{\infty} C_n^{(1)}(z^2) z_{\mu_1} \dots z_{\mu_n} \mathcal{O}_n^{\mu_1 \dots \mu_n}(0) \\ &+ (g_{\mu\kappa} \partial_\rho \partial_\nu + g_{\rho\nu} \partial_\mu \partial_\kappa - g_{\mu\kappa} g_{\nu\rho} \partial^2 - g_{\mu\nu} \partial_\rho \partial_\kappa) \sum_{n=0,2,4}^{\infty} C_n^{(2)}(z^2) z_{\mu_1} \dots z_{\mu_n} \mathcal{O}_{n+2}^{\mu\nu\mu_1 \dots \mu_n}(0), \\ &+ \text{anti-symmetric in } \mu \leftrightarrow \nu \text{ terms,} \end{aligned} \quad (2.39)$$

where the only QCD operators that contribute in the asymptotic limit of $z_\mu \rightarrow 0$ are the unpolarised twist-two operators,

$$\mathcal{O}_f^{(n)\mu_1 \dots \mu_n}(X) = \bar{\psi}_f(X) \gamma^{\{\mu_1} i \overleftrightarrow{D}^{\mu_2} \dots i \overleftrightarrow{D}^{\mu_n\}} \psi_f(X) - \text{traces}, \quad (2.40)$$

and the polarised twist-two operators, which are neglected in Eq. (2.39), are

$$\tilde{\mathcal{O}}_f^{(n)\mu_1 \dots \mu_n}(X) = \bar{\psi}_f(X) \gamma^{\{\mu_1} \gamma^5 i \overleftrightarrow{D}^{\mu_2} \dots i \overleftrightarrow{D}^{\mu_n\}} \psi_f(X) - \text{traces}, \quad (2.41)$$

where $\overleftrightarrow{D} = \frac{1}{2}(\vec{D} - \overleftarrow{D})$, for the covariant derivative defined in Eq. (2.8). See Appendix A for the symmetrisation convention of the Lorentz indices and the definition of \overleftrightarrow{D} .

In Eq. (2.39), the Fourier transform of the Wilson coefficients,

$$c_n^{(i)}(\alpha_S(Q)) = \int d^4 z e^{iq \cdot z} C_n^{(i)}(z^2), \quad (2.42)$$

can be calculated perturbatively, and have the form

$$c_n^{(i)}(\alpha_S(Q)) = \sum_f e_f^2 + \mathcal{O}(\alpha_S(Q)). \quad (2.43)$$

Hence this gives us the form of the Wilson coefficients in Eq. (2.14).

If we truncate all $\alpha_S(Q)$ corrections to the Wilson coefficients, Eq. (2.39) is equivalent to

$$\begin{aligned} \mathcal{T}\{j_\mu(z/2)j_\nu(-z/2)\} &= -2 \sum_f e_f^2 \frac{i}{2\pi^2} \frac{z^\rho}{(z^2 - i\epsilon)^2} \left(g_{\mu\rho}g_{\nu\kappa} + g_{\mu\kappa}g_{\nu\rho} - g_{\mu\nu}g_{\rho\kappa} \right) \\ &\times \sum_{n=1,3,5}^{\infty} \frac{(-i)^n}{n!} z_{\mu_1} \dots z_{\mu_n} \mathcal{O}_f^{(n+1)\kappa\mu_1 \dots \mu_n}, \end{aligned} \quad (2.44)$$

which is derived in Appendix C, and is the expression we will use for our OPE in Chapter 5. This is therefore an expression for the OPE in the absolute Bjorken limit, Eq. (2.34), which eliminates all terms suppressed by $1/Q^2$ and α_S . The Feynman diagram for this is given in Fig. 2.5, known as the ‘handbag diagram’. The perturbatively calculable ‘handle’ corresponds to the Wilson coefficient, while the non-perturbative structure is contained in the blob.

After putting Eq. (2.44) between two states and Fourier transforming, we get that the Compton structure functions are

$$\mathcal{F}_1(\omega, Q^2) = \sum_f e_f^2 \sum_{n=1}^{\infty} a_{2n}^f \omega^{2n}, \quad \mathcal{F}_2(\omega, Q^2) = 2x \sum_f e_f^2 \sum_{n=1}^{\infty} a_{2n}^f \omega^{2n}, \quad (2.45)$$

which are independent of Q^2 , as expected, and we have recovered the Callan-Gross relationship, Eq. (2.37). Note that we have defined the matrix element of the unpolarised operators as

$$\langle P | \mathcal{O}_f^{(n)\mu_1 \dots \mu_n} | P \rangle = P^{\mu_1} \dots P^{\mu_n} a_n^f - \text{traces}, \quad (2.46)$$

where the traces are terms proportional to $g^{\mu_i \mu_j}$ that give rise to m_N^2/Q^2 corrections [52], and a_n^f is the reduced matrix element, which contains the interesting non-perturbative information.

Finally, by comparing Eq. (2.29) to the OPE result, Eq. (2.45), we get a relation between the local QCD operator and the n even moments of structure functions:

$$2 \int_0^1 dx x^{n-1} F_1(x, Q^2) = \sum_f c_n^f(\alpha_S(Q^2)) a_n^f + (\text{higher-twist}), \quad (2.47)$$

where $c_n(\alpha_S(Q^2))$ has the form given in Eq. (2.43). This matches the type of factorisation relation we gave in Eq. (2.14).

Finally, interpreting F_1 at $\alpha_S = 0$ in terms of PDFs, Eq. (2.36), we have

$$2 \int_0^1 dx x^{n-1} F_1(x) = \sum_f e_f^2 \int_0^1 dx x^{n-1} (q_f(x) + \bar{q}_f(x)) = \sum_f e_f^2 a_n^f \quad (2.48)$$

This gives us the first link between the parton model and QCD operators: the Mellin moments of PDFs can be cast in terms of twist-two operators. Note that the OPE is an expansion in the unphysical region $|\omega| < 1$, which corresponds in coordinate space to the short-distance region $z_\mu \rightarrow 0$. As such, it does not complete our goal of finding a QCD operator description of the PDFs, only their moments.

Partons on the light-cone

To cast PDFs into the language of QCD operators we note that, as probability densities, the PDFs can be written as

$$q_f(x) = \int \frac{d^4 p_X}{(2\pi)^4} \sum_X |\langle X | \psi_f | P \rangle|^2 \delta(xP - p) = \langle P | \psi_f^\dagger \psi_f | P \rangle \delta(xP - p), \quad (2.49)$$

where p is the parton momentum and x is the fraction of the nucleon momentum carried by the parton.

However, the relation $p^\mu = xP^\mu$ is not completely correct. Rather, we are assuming that components of the parton momentum, p^μ , transverse to the nucleon's momentum are taken to be very small compared to the components parallel to the nucleon's momentum. This is not true in all frames—in the nucleon rest frame, for instance.

In the center of mass frame, where $q^\mu = (0, 0, 0, Q)$, the nucleon momentum is $P^\mu = (E, P^1, P^2, -\frac{P \cdot q}{Q})$. Since $P \cdot q \sim Q^2$ in the Bjorken limit, $P \cdot q/Q \sim Q$, which goes to infinity. Hence for large Q , we have $P^\mu \simeq (Q, 0, 0, -Q)$, a lightlike vector. Therefore, since the components of P_μ are the hard scale, all the transverse components of p_μ must be suppressed with respect to these. Hence we have $p \approx xP$ in this frame.

Since all our kinematics are dominated by light-like vectors in this frame, it is convenient to define a pair of collinear light-like vectors that span our kinematics: $n^\mu = \Lambda(1, 0, 0, 1)$ and $\bar{n}^\mu = (1, 0, 0, -1)/(2\Lambda)$, for Λ a parameter set so that $n \cdot P = 1$. Hence $P^\mu = \bar{n}^\mu + (M^2/2)n^\mu$. Therefore, the relationship between the parton and nucleon momentum is $p \cdot n = xP \cdot n$.

Another key assumption here is that the struck parton is on-shell. Roughly speaking, this follows from the fact that the parton is asymptotically free, and hence non-interacting; more detailed justifications are given elsewhere [15].

As such, we can write Eq. 2.49 more precisely:

$$q_f(x) = \int \frac{d^4 p_X}{(2\pi)^4} \sum_X |\langle X | \psi_f | P \rangle|^2 \delta(p \cdot n - xP \cdot n), \quad (2.50)$$

where the above equation describes a nucleon splitting into one constituent parton of momentum p , and the left-over parts of the nucleon X with momentum p_X .

After some manipulation, Eq. (2.50) gives us the definition of PDFs in terms of QCD operators:

$$q_f(x) = \int \frac{d\lambda}{2\pi} e^{i\lambda x} \langle P | \bar{\psi}_f(-\lambda n/2) \not{n} \psi_f(\lambda n/2) | P \rangle, \quad (2.51)$$

which is the probability amplitude for a quark to leave the hadron, propagate along the light-cone, and be reabsorbed.

More generally, we can introduce the non-local light-cone operator

$$\mathcal{O}_{\text{LC}}^f(x) = \int \frac{d\lambda}{2\pi} e^{i\lambda x} \bar{\psi}_f(-\lambda n/2) \Gamma \psi_f(\lambda n/2), \quad (2.52)$$

where Γ is a Dirac matrix; $\Gamma = \not{n}$ for unpolarised parton distributions. So that we can simply write^{†††}

$$q_f(x) = \frac{1}{2} \langle P | \mathcal{O}_{\text{LC}}^f(x) | P \rangle.$$

Finally, to come full circle, we can Taylor expand along the light-cone [56] to relate the local operators of Eq. (2.40) to the light-cone operator:

$$n_{\mu_1} \dots n_{\mu_m} \mathcal{O}_f^{\mu_1 \dots \mu_m} = \int_{-1}^1 dx x^{m-1} \mathcal{O}_{\text{LC}}^f(x), \quad (2.53)$$

for $\Gamma = \not{n}$. We can generalise this to other operators: for instance, if $\Gamma = \not{n} \gamma_5$ in the parton distribution, it can be related to the polarised local operators given in Eq. (2.41). Hence this is an extremely useful equation as it allows us to relate any parton distribution function to a basis of local operators.

2.2.3 Polarised forward Compton scattering

Now we can apply these tools and concepts to the polarised (spin-dependent) part of the forward Compton amplitude. We will calculate this Compton amplitude using lattice QCD in Section 7. Recall that we introduced a general tensor decomposition in Eq. (2.20), which contained the spin-independent structure functions, as well as the polarised structure functions, $\tilde{g}_{1,2}$. The polarised contributions correspond to the part of the Compton amplitude that is anti-symmetric under $\mu \leftrightarrow \nu$. Experimentally, these structure functions can be measured from polarised deep-inelastic scattering. For a more complete treatment of polarised forward Compton scattering see Refs. [57, 67].

Again, using the optical theorem, these Compton structure functions can be related to the DIS structure functions, $g_{1,2}$, by a dispersion relation (again, see Appendix B):

$$\tilde{g}_{1,2}(\omega, Q^2) = 4\omega \int_0^1 dx \frac{g_{1,2}(x, Q^2)}{1 - x^2 \omega^2 - i\epsilon}. \quad (2.54)$$

In contrast to Eq. (2.26), there is no subtraction function in this dispersion relation.

Then, as in the spin-averaged case, we can expand around $\omega = 0$ to relate this to the moments of the polarised DIS structure function:

$$\tilde{g}_{1,2}(\omega, Q^2) = 4 \sum_{n=1}^{\infty} \omega^{2n-1} \int_0^1 dx x^{2n-2} g_{1,2}(x, Q^2) = 4 \sum_{n=1}^{\infty} \omega^{2n-1} \tilde{M}_{2n-1}^{(1),(2)}(Q^2). \quad (2.55)$$

Note that, unlike the spin-averaged structure functions, the spin-dependent structure functions, $g_{1,2}$, are related to a difference of cross-sections, and are hence not guaranteed to be positive definite. Therefore, for the moments of the spin-dependent structure functions, there is no equivalent monotonic condition on the polarised moments, $\tilde{M}_n^{(1),(2)}(Q^2)$.

Perturbative expansion

We can apply the tools of the OPE and light-cone operators developed in Section 2.2.2 to gain physical insights into these polarised structure functions.

^{†††}In general, this equation contains a Wilson line to keep the operator gauge invariant. To simplify expressions for light-cone operators, we use light-cone gauge: $n_\mu A^\mu(x) = 0$ for the light-cone vector n_μ .

Operator product expansion

The OPE of the $\mu \leftrightarrow \nu$ antisymmetric component of the Compton amplitude is

$$\begin{aligned} \mathcal{T}\{j_\mu(z/2)j_\nu(-z/2)\} &= -2 \sum_f e_f^2 \frac{i}{2\pi^2} \frac{z^\rho}{(z^2 - i\epsilon)^2} i\epsilon_{\mu\nu\rho\kappa} \\ &\times \sum_{n=0,2,4}^{\infty} \frac{(-i)^n}{n!} z_{\mu_1} \dots z_{\mu_n} \tilde{\mathcal{O}}_f^{(n+1)\kappa\mu_1 \dots \mu_n}(0), \end{aligned} \quad (2.56)$$

where $\tilde{\mathcal{O}}_f^{(n+1)\kappa\mu_1 \dots \mu_n}(0)$ are the operators in Eq. (2.41), and we have also truncated $\alpha_S(Q)$ corrections to the Wilson coefficients.

Putting Eq. (2.56) between two equal momentum states and Fourier transforming we arrive at [57, 68]

$$\tilde{g}_1(\omega) = 4 \sum_f e_f^2 \sum_{n=1}^{\infty} \omega^{2n-1} \tilde{a}_{2n-1}^f, \quad \tilde{g}_2(\omega) = 8 \sum_f e_f^2 \sum_{n=1}^{\infty} \left(\frac{n-1}{1-2n} \right) \omega^{2n-1} \tilde{a}_{2n-1}^f, \quad (2.57)$$

where we have defined^{†††}

$$\langle P | \tilde{\mathcal{O}}_f^{(n)\mu_1 \dots \mu_n} | P \rangle = 4s^{\{\mu_1 P^{\mu_2} \dots P^{\mu_n}\}} \tilde{a}_n^f - \text{traces}, \quad (2.58)$$

for $\tilde{\mathcal{O}}_f^{(n)\mu_1 \dots \mu_n}$ the operators in Eq. (2.41), s^μ is the spin vector in Eq. (2.21), and \tilde{a}_n^f are the reduced matrix elements.

To compare to the moments of $g_{1,2}$, neglecting higher-twist corrections, we have

$$\tilde{M}_n^{(1)}(Q^2) = \sum_f c_n^{(1),f}(\alpha_S) \tilde{a}_n^f, \quad \tilde{M}_n^{(2)}(Q^2) = \left(\frac{1-n}{n} \right) \sum_f c_n^{(2),f}(\alpha_S) \tilde{a}_n^f, \quad (2.59)$$

where once again the Wilson coefficients, $c_n^{(1,2),f}$, go like Eq. (2.43). Therefore, we once again have the moments of the structure functions in terms of local operators.

Parton interpretation

The naive parton model prediction for the DIS structure functions is [57]

$$\begin{aligned} g_1(x) &= \frac{1}{2} \sum_f e_f^2 (\Delta q_f(x) + \Delta \bar{q}_f(x)), \\ g_2(x) &= 0, \end{aligned} \quad (2.60)$$

where we have used

$$\Delta q_f(x) \equiv q_f^\uparrow(x) - q_f^\downarrow(x),$$

and $q_f^\uparrow(x)$ is the probability density of finding the incident quark being flavour f with momentum fraction x and spin up.

^{†††}Note that we have defined the reduced matrix elements, \tilde{a}_n , to match that of Refs. [69, 70]. To compare to Manohar's convention [57], $\tilde{a}_n^{\text{Manohar}} = 2\tilde{a}_n$.

In terms of light-cone operators, Eq. (2.52), these quark helicity PDFs are

$$\Delta q_f(x) = \int \frac{d\lambda}{2\pi} e^{i\lambda x} \langle P | \bar{\psi}_f(-\lambda n/2) \not{n} \gamma_5 \psi_f(\lambda n/2) | P \rangle. \quad (2.61)$$

The g_1 structure function

We now discuss the physics of the g_1 structure function and its moments.

Interpretation of the first moment

From the definition of the local operators, Eq. (2.41), we can see that the $n = 1$ operator is simply the axial vector operator:

$$\tilde{\mathcal{O}}_f^{(1)\mu} = \bar{\psi}_f \gamma^\mu \gamma^5 \psi_f.$$

Given the partonic interpretation of the structure functions, Eq. (2.60), the first moment of g_1 is

$$\int_0^1 dx \left(q_f^\uparrow(x) - q_f^\downarrow(x) + \bar{q}_f^\uparrow(x) - \bar{q}_f^\downarrow(x) \right), \quad (2.62)$$

which is the contribution to the hadron's spin carried by quarks of flavour f .

Using the dispersion relation, Eq. (2.54), and the OPE, Eq. (2.57), we have the relation

$$4s^\mu \sum_f e_f^2 \tilde{a}_1^f = \sum_f e_f^2 \langle P | \bar{\psi}_f \gamma^\mu \gamma^5 \psi_f | P \rangle = 2s^\mu g_A, \quad (2.63)$$

where g_A is the axial coupling. Hence we can interpret the first moment as proportional to g_A , which is the contribution to the proton's spin carried by a certain quark species.

Moreover, by isospin symmetry, we have the following relation [57]:

$$\begin{aligned} \langle \text{proton} | \left(\bar{\psi}_u \gamma^\mu \gamma^5 \psi_u - \bar{\psi}_d \gamma^\mu \gamma^5 \psi_d \right) | \text{proton} \rangle &= \langle \text{proton} | \bar{\psi}_u \gamma^\mu \gamma^5 \psi_d | \text{neutron} \rangle \\ &= 2s^\mu g_A^{u-d}. \end{aligned} \quad (2.64)$$

Therefore, using these results we arrive at the Ellis-Jaffe sum rule [71]

$$2\tilde{M}_1^{(1)}(Q^2) = 2 \int_0^1 dx g_1(x, Q^2) = c_1(\alpha_S(Q)) g_A, \quad (2.65)$$

where we have reintroduced the Wilson coefficient $c_1 = \sum_f e_f^2 + \mathcal{O}(\alpha_S(Q))$. Unlike our other OPE results, where there are higher-order contributions from both the Wilson coefficients *and* higher-twist terms (refer to Eq. (2.13)), the Ellis-Jaffe sum rule only has higher-order contributions in the Wilson coefficient. This is because one cannot construct a gauge-invariant gluon operator to accompany the leading ω term [57].

The fact that $\tilde{M}_1^{(1)}(Q^2)$ contains no higher-order contributions other than the Wilson coefficient means that we can parameterise the moment as

$$2\tilde{M}_1^{(1),u-d}(Q^2) = \left(1 - \frac{\alpha_{g_1}(Q^2)}{\pi} \right) g_A^{u-d}. \quad (2.66)$$

In the above equation, α_{g_1} is defined as the ‘effective strong coupling’. Note that perturbative calculations of the strong coupling, $\alpha_S(Q^2)$, diverge as $Q \rightarrow \Lambda_{\text{QCD}}$; see Eq. (2.12). By contrast, if we define an effective coupling from an experimental observable, as in Eq. (2.66), we thereby extend the concept of a strong coupling to the $Q^2 < \Lambda_{\text{QCD}}^2$ region [72]. Therefore, one can use this effective strong coupling to study confinement as well as asymptotic freedom, and the transition between the two regions.

The g_2 structure function

Now we will discuss the g_2 structure function, and interpretations and predictions for its first and second moments.

Interpretation of the first moment

For $n = 1$, the OPE result, Eq. (2.57), predicts that the first moment of g_2 vanishes:

$$\lim_{Q^2 \rightarrow \infty} \tilde{M}_1^{(2)}(Q^2) = 0.$$

Of course, the OPE is only leading-twist and there may be higher-twist corrections to this.

However, it has been further argued that the first moment of g_2 vanishes *at all orders* [73]:

$$\tilde{M}_1^{(2)}(Q^2) = \int_0^1 dx g_2(x, Q^2) = 0. \quad (2.67)$$

This is known as the Burkhardt-Cottingham sum rule [74], which is derived using Regge theory, and is not completely model-independent. As such, we can test Eq. (2.67) at a given Q^2 using our lattice calculation.

Interpretation of the second moment

From the OPE result, Eq. (2.57), we have that the moments of g_2 can be completely determined by the moments of g_1 :

$$\tilde{g}_2(\omega) = 4 \sum_{n=1,3,5}^{\infty} \left(\frac{1-n}{n} \right) \omega^n \tilde{a}_n = -\tilde{g}_1(\omega) + \int_0^\omega d\omega' \frac{\tilde{g}_1(\omega')}{\omega'}. \quad (2.68)$$

By taking the imaginary part of Eq. (2.68) and changing the integration variable to $x = 1/\omega$, we arrive at the Wandzura-Wilczek (WW) relation for polarised DIS structure functions [75]:

$$g_2(x) = -g_1(x) + \int_x^1 dx' \frac{g_1(x')}{x'}. \quad (2.69)$$

And hence at leading-twist the g_2 structure function is completely determined by g_1 . However, the WW relation has higher-twist corrections to it. Again, we will test this relation for the $n = 3$ moment in our lattice calculation.

An OPE of the moments of g_2 including twist-three operators gives [70]

$$\int_0^1 dx x^{n-1} g_2(x, Q^2) = \frac{1-n}{n} \left[\tilde{a}_n - \frac{d_{n-1}}{4} \right], \quad (2.70)$$

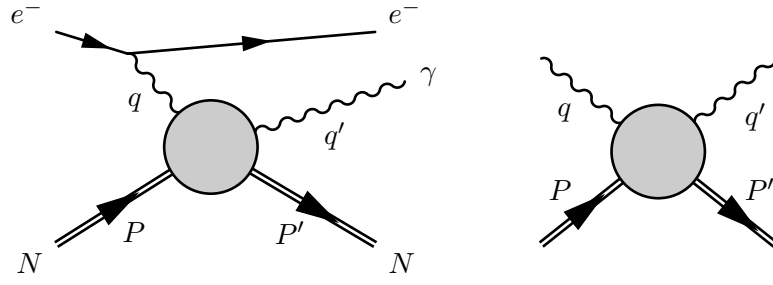


Figure 2.6: Left: the Feynman diagram for deeply virtual Compton scattering (DVCS). Right: the Feynman diagram for general off-forward Compton scattering.

where the \tilde{a}_n contribution is simply that from Eq. (2.57). And hence, the Wandzura-Wilczek breaking contribution is from the d_n terms. Moreover, these d_n contributions are twist-three in the operator sense but are not $1/Q^2$ suppressed.

The d_2 term in particular contains information about quark-gluon correlations in a nucleon [69,70,76]. To isolate d_2 from the structure function moments, we combine Eq. (2.70) and the OPE result Eq. (2.57) to get that^{§§§}

$$d_2(Q^2) \equiv 4\tilde{M}_3^{(1)}(Q^2) + 6\tilde{M}_3^{(2)}(Q^2). \quad (2.71)$$

Then, from Eqs. (2.70) and Eq. (2.57), we have that $d_2(Q^2) \rightarrow d_2$ as $Q^2 \rightarrow \infty$.

2.2.4 Off-forward Compton scattering

Finally, we look at the process of off-forward Compton scattering, which is used to access generalised parton distributions (GPDs). In Chapters 5 and 6, we calculate this amplitude in lattice QCD. The off-forward Compton amplitude (OFCA) is defined as

$$T_{\mu\nu} \equiv i \int d^4z e^{\frac{i}{2}(q+q')\cdot z} \langle P' | \mathcal{T} \{ j_\mu(z) j_\nu(0) \} | P \rangle, \quad (2.72)$$

which is similar to the forward Compton amplitude, Eq. (2.19), except that it describes a hadron with initial momentum P absorbing a photon with momentum q and after then emitting a photon with momentum q' so that the nucleon has final momentum P' —see Figure 2.6. This Compton amplitude, therefore, returns to the forward amplitude as $P' \rightarrow P$. Note, again, more complete treatments of this topic can be found in Refs. [56,77].

Due to momentum conservation, this process gives us three independent momentum vectors, which we will choose as

$$\bar{P} = \frac{1}{2}(P + P'), \quad \bar{q} = \frac{1}{2}(q + q'), \quad \Delta = P' - P = q - q'. \quad (2.73)$$

From these, we can form at most four linearly independent scalar variables. We choose two scaling variables and a soft and hard momentum transfer, given respectively as:

$$\bar{\omega} = \frac{2\bar{P} \cdot \bar{q}}{Q^2}, \quad \vartheta = -\frac{\Delta \cdot \bar{q}}{Q^2}, \quad t = \Delta^2, \quad \bar{Q}^2 = -\bar{q}^2. \quad (2.74)$$

^{§§§}Note, especially in experimental analysis, it is common to define $d_2 = 2\tilde{M}_3^{(1)} + 3\tilde{M}_3^{(2)}$ [44].

Here, we now have two scaling variables, $\bar{\omega}$ and ϑ , and two momentum transfers, \bar{Q}^2 and t . In the off-forward case, \bar{Q}^2 is the hard scale and is $\bar{Q}^2 \gg -t$. The variable $\bar{\omega}$ is simply ω in the limit that $t \rightarrow 0$. Similarly, $\bar{Q}^2 \rightarrow Q^2$ in the same limit. Moreover, the whole off-forward Compton amplitude reduces to the forward Compton amplitude for $t \rightarrow 0$.

We will use these momentum scalars in Chapter 5. We note that standard skewness variable in terms of these variables is $\xi = \vartheta/\bar{\omega}$.

Deeply virtual Compton scattering

The main experimental process to probe the OFCA and thereby GPDs is deeply virtual Compton scattering (DVCS): $e^- + N(P) \rightarrow e^- + \gamma(q') + N(P')$ (see Figure 2.6). In DVCS, the final state photon is on-shell, and hence we have the constraint that $q'^2 = 0$. After applying this constraint, $q'^2 = 0$, our Lorentz scalars become

$$\vartheta \simeq 1, \quad \bar{\omega} \simeq \xi^{-1}, \quad \bar{Q}^2 \simeq -\frac{q^2}{2}, \quad (2.75)$$

where \simeq in this context means “equal up to suppressed m_N^2/\bar{Q}^2 and t/\bar{Q}^2 terms”. Hence it is clear why DVCS is typically parameterised in terms of ξ , t , and $Q^2 = -q^2$.

We note also that there are a number of difficulties associated with extracting GPDs from experiment, as we will discuss in Chapter 5.

Generalised parton distributions

Generalised parton distributions (GPDs) are defined by the off-forward matrix element of the light-cone operator we saw in Eq. (2.52). For a light-like vector n^μ such that $n \cdot \bar{P} = 1^{****}$, we have [22, 78]

$$\begin{aligned} \int \frac{d\lambda}{2\pi} e^{i\lambda x} \langle P' | \bar{\psi}_f(-\lambda n/2) \not{n} \psi_f(\lambda n/2) | P \rangle &= H^f(x, \vartheta/\bar{\omega}, t) \bar{u}(P') \gamma^\mu n_\mu u(P) \\ &+ E^f(x, \vartheta/\bar{\omega}, t) \bar{u}(P') \frac{i\sigma^{\mu\nu} n_\mu \Delta_\nu}{2m_N} u(P). \end{aligned} \quad (2.76)$$

In contrast to the forward parton distributions, there are two GPDs, H^f and E^f , from the one light-cone operator. Due to the momentum transfer, the helicity of the nucleon can flip. As such, H^f and E^f are the helicity-conserving and -flipping GPDs, respectively.

If we calculate the OFCA for DVCS kinematics, we get [22, 78]

$$\begin{aligned} T^{\mu\nu}(P, q; P', q') &= \frac{1}{2} (g^{\mu\nu} - n^\mu \bar{n}^\nu - n^\nu \bar{n}^\mu) \int_{-1}^1 dx \left(\frac{1}{x - \xi + i\epsilon} + \frac{1}{x + \xi + i\epsilon} \right) \\ &\times \left[H(x, \xi, t) \bar{u}(P') \not{n} u(P) + E(x, \xi, t) \bar{u}(P') \frac{i\sigma^{\alpha\beta} \bar{n}_\alpha \Delta_\beta}{2M} u(P) \right], \end{aligned} \quad (2.77)$$

using n_μ and \bar{n}_μ , the light-like vectors defined in Section 2.2.2. The above equation is equivalent to the factorisation relation, Eq. (2.16), where the perturbative kernel is the $(x \pm \xi + i\epsilon)^{-1}$ terms, and the long-distance physics is contained in the GPDs.

****Using the standard Sudakov decomposition (see Appendix D), this gives us the familiar form of the skewness variable, $\xi = -n \cdot \Delta/2$. Note that occasionally definitions of ξ in terms of n_μ may differ by a factor of two or -1 .

It is also useful to relate GPDs to the local twist-two operators from Eq. (2.40). The off-forward nucleon matrix elements of these operators are [79]

$$\begin{aligned}
\langle P' | \mathcal{O}_f^{(n+1)\kappa\mu_1\dots\mu_n}(0) | P \rangle &= \bar{u}(P') \gamma^{\{\kappa} u(P) \sum_{i=0}^n A_{n+1,i}^f(t) \Delta^{\mu_1} \dots \Delta^{\mu_i} \bar{P}^{\mu_{i+1}} \dots \bar{P}^{\mu_n} \\
&+ \bar{u}(P') \frac{i\sigma^{\{\kappa\alpha} \Delta_\alpha}{2m_N} u(P) \sum_{i=0}^n B_{n+1,i}^f(t) \Delta^{\mu_1} \dots \Delta^{\mu_i} \bar{P}^{\mu_{i+1}} \dots \bar{P}^{\mu_n} \quad (2.78) \\
&+ C_{n+1}^f(t) \text{mod}(n, 2) \frac{\bar{u}(P') u(P)}{m_N} \Delta^{\{\kappa} \Delta^{\mu_1} \dots \Delta^{\mu_n\}} - \text{traces,}
\end{aligned}$$

where the Lorentz scalars $A_{n,i}^f$, $B_{n,i}^f$ and C_n^f are generalised form factors (GFFs).

Using Eqs. (2.76) and Eq. (2.78), as well as our relation between the light-cone and local twist-two operators, Eq. (2.53), we can relate the GPDs H and E to the GFFs:

$$\begin{aligned}
\int_{-1}^1 dx x^n H^f(x, \vartheta/\bar{\omega}, t) &= \sum_{j=0,2,4}^n (-2\vartheta/\bar{\omega})^j A_{n+1,j}^f(t) + \text{mod}(n, 2) (-2\vartheta/\bar{\omega})^{n+1} C_{n+1}^f(t), \\
\int_{-1}^1 dx x^n E^f(x, \vartheta/\bar{\omega}, t) &= \sum_{j=0,2,4}^n (-2\vartheta/\bar{\omega})^j B_{n+1,j}^f(t) - \text{mod}(n, 2) (-2\vartheta/\bar{\omega})^{n+1} C_{n+1}^f(t),
\end{aligned} \tag{2.79}$$

recalling that $\xi = \vartheta/\bar{\omega}$ in terms of the scalars defined at the start of this section. These equations are the famous ‘polynomiality’ of GPDs [79], which relates moments of GPDs to the GFFs.

Physical interpretation

From a hadronic structure perspective, GPDs provide us with a wealth of otherwise inaccessible physical information. Moreover, they can be related to forward PDFs and EFFs, thereby unifying seemingly unrelated quantities.

Relation to other observables

At $P' = P$ or equivalently $t = 0$, it is easy to see that Eqs. (2.51) and (2.76) coincide. Therefore, it is simple to show, noting $2P \cdot n = 2$, that

$$H^f(x, 0, 0) = q_f(x), \quad x > 0, \quad \text{and} \quad H^f(x, 0, 0) = -\bar{q}_f(-x), \quad x < 0, \tag{2.80}$$

where $\bar{q}_f(x)$ is the PDF for the anti-quark of flavour f .

Similarly, from the definition of elastic form factors in Section 2.2.1 that the GFFs from Eq. (2.78) can be associated with the Dirac and Pauli form factors (Eq. (2.17)) for $n = 1$:

$$A_{1,0}(t) = F_1(-t), \quad B_{1,0}(t) = F_2(-t),$$

where we note that Q^2 is positive in Eq. (2.17), while t is negative, hence the sign change.

Finally, for $n = 2$, these GFFs can be related to the quark contribution to the nucleon energy-momentum tensor (EMT) for a flavour of quark f [79]:

$$\begin{aligned} \langle P' | \mathcal{T}_f^{\mu\nu} | P \rangle = & \bar{u}(P') \left[A_{2,0}^f(t) \gamma^{\{\mu} \bar{P}^{\nu\}} + B_{2,0}^f(t) \frac{i\sigma^{\{\mu\alpha} \Delta_\alpha \bar{P}^{\nu\}}}{2M} \right. \\ & \left. + C_2^f(t) \frac{\Delta^\mu \Delta^\nu - g^{\mu\nu} \Delta^2}{M} \right] u(P). \end{aligned} \quad (2.81)$$

Physical information

As mentioned, GPDs contain an abundance of otherwise inaccessible physical information, including:

- **Spin structure:** Since the $n = 2$ moments parameterise the EMT, they can also be used to calculate the QCD angular momentum operator [22]:

$$\langle J_f^3 \rangle = \frac{1}{2} [A_{2,0}^f(0) + B_{2,0}^f(0)] = \frac{1}{2} \int_{-1}^1 dx x \left[H^f(x, \xi, t) + E^f(x, \xi, t) \right] \Big|_{t=0}. \quad (2.82)$$

This is the famous Ji sum rule. As we discussed previously, from the polarised forward structure functions we can determine the contribution to the nucleon's spin coming from its quarks, Eq. (2.62). Combining that result with the Ji sum rule it is possible to determine the contributions to the proton's spin from the orbital angular momentum of its constituents. Hence a measurement of GPDs would help to solve the long-standing 'proton spin puzzle' [16, 80, 81].

- **Mechanical properties:** Again, by their relation to the QCD energy-momentum tensor, GPDs can be related to the 'D-term', which coincides with the GFF C_2 in Eqs. (2.78). This D -term has been referred to as 'the last global unknown property' [24, 82, 83], and can provide semi-classical or 'mechanical' properties of hadrons, such as the distribution of shear forces and pressure in a hadron, and its mechanical radius. From analyses of the OFCA using dispersion relations, it has been shown that this D -term is experimentally accessible [84–87], and it was subsequently measured from DVCS [88, 89].
- **Spatial distributions:** Finally, it was shown by Burkardt [23, 90] that GPDs at zero skewness, $\xi = 0$, can be Fourier transformed to access spatial distributions:

$$q_f(x, \mathbf{b}_\perp) = \int \frac{d^2 \Delta_\perp}{(2\pi)^2} H^f(x, -\Delta_\perp^2) e^{-i\mathbf{b}_\perp \cdot \Delta_\perp}, \quad (2.83)$$

where H^f is the helicity conserving GPD and $q_f(x, \mathbf{b}_\perp)$ is the impact parameter dependent PDFs, defined as

$$q_f(x, \mathbf{b}_\perp) \equiv \langle P, \lambda | \int \frac{d\lambda}{2\pi} e^{i\lambda x} \bar{\psi}_f(-\lambda n/2 + \mathbf{b}_\perp) \not{n} \psi_f(\lambda n/2 + \mathbf{b}_\perp) | P, \lambda \rangle. \quad (2.84)$$

This is just the regular PDF definition, Eq. (2.52), except with the position of the quark fields shifted by some impact parameter vector, \mathbf{b}_\perp , for which $\mathbf{b}_\perp \cdot n = 0$. This object is commonly interpreted as the probability density of finding a quark with

momentum fraction x , at a displacement \mathbf{b}_\perp from the centre of mass of the struck hadron.

Hence a determination of GPDs can provide us with unprecedented information about the spatial structure of nucleons.

Note on off-forward formalism

Finally, we note that the formalism used to describe off-forward scattering presented here has been completely perturbative, in terms of the local twist-two operators, Eq. 2.40, and the light-cone operators, Eq. 2.52. By contrast, in the sections on the forward Compton amplitude, we also used the non-perturbative methods: the tensor decomposition, Eq. (2.20) and dispersion relations. In Chapter 5, we will derive the relevant tensor decomposition and dispersion relations for the off-forward Compton amplitude that are necessary to analyse our lattice results.

Lattice QCD

As we discussed in the previous chapter, at low energy scales the strong coupling is $\alpha_S \sim 1$, and hence standard perturbation theory cannot be applied to QCD. Even for high energy processes, where perturbation theory is applicable, there are still non-perturbative contributions to most cross sections. Therefore, for QCD calculations with non-perturbative contributions it is common to use a numerical approach: lattice QCD.

Lattice QCD was first formulated by Wilson [13], and involves calculating matrix elements of operators in a discrete spacetime of finite extent. As such, lattice QCD calculations have a finite number of degrees of freedom and are therefore amenable to numerical evaluation. Moreover, it is a completely first principles approach to the calculation of QCD operators, with improvable errors in the form of the lattice spacing (the distance between adjacent lattice sites) and finite volume corrections. Since lattice calculations often use heavier than physical quark masses as a way to reduce the numerical costs of the calculation, it is also necessary to correct for these unphysical masses.

Despite great successes in calculating a range of QCD quantities, lattice methods still face a range of persistent challenges. For the present thesis, one of our major obstacles stems from the ‘numerical sign problem’ associated with the evaluation of high-dimensional integrals [91, 92]. In lattice QCD the standard way to solve this sign problem is to use Euclidean instead of Minkowski spacetime*. However, it is not possible to directly calculate parton distributions or real-time scattering amplitudes in Euclidean spacetime. Instead, one can calculate related quantities in lattice QCD, which can then be used to constrain or ultimately determine the Minkowski space quantities.

Calculating partonic information from first principles is one of the most important topics in contemporary lattice QCD and is the central aim of this thesis. The earliest calculations of parton distributions moments were carried out in the 1980s [28, 29], but as yet $n = 3$ is the highest moment calculated with this method. Recent years have seen the development of new methods to go beyond the leading moments, the most prominent of which are the quasi- [32] and pseudo-distribution [33] approaches, among others [94, 95], including the Feynman-Hellmann Compton amplitude method presented in this thesis [36].

The structure of this chapter follows: in Section 3.1 we present a very brief description of the formulation of lattice QCD: Euclidean path integrals, the discretisation of the action, and a discussion of nucleon correlation functions. Then, in Section 3.2 we give an overview of the various methods to calculate partonic information in lattice QCD. The goal of this latter section is to give an idea of where our Feynman-Hellmann Compton amplitude method fits into the field, the shared difficulties and the contrasts.

*For calculations at finite baryon density, a related sign problem persists even in Euclidean spacetime [93].

3.1 Formulation of Lattice QCD

3.1.1 Euclidean path integrals

In the path integral formalism of quantum field theory, the vacuum expectation value of an operator is given by

$$\langle \Omega | \mathcal{O} | \Omega \rangle = \frac{\int \mathcal{D}A_\mu \mathcal{D}\bar{\psi} \mathcal{D}\psi \mathcal{O} e^{iS_{\text{QCD}}}}{\int \mathcal{D}A_\mu \mathcal{D}\bar{\psi} \mathcal{D}\psi e^{iS_{\text{QCD}}}}, \quad (3.1)$$

where $|\Omega\rangle$ is the vacuum state and $\mathcal{D}\phi$ is the functional volume element for some field ϕ .

The full QCD action is $S_{\text{QCD}} = S_F + S_G$, where[†]

$$S_F = \int d^4z \sum_f \bar{\psi}_f(z) (\not{D} - m_f) \psi_f(z), \quad S_G = - \int d^4z \frac{1}{4} F^{\mu\nu}(z) F_{\mu\nu}(z). \quad (3.2)$$

Here, we have broken up the QCD Lagrangian density from Eq. 2.10.

Due to the highly oscillatory factor of $e^{iS_{\text{QCD}}}$ in Eq. (3.1), the numerical evaluation of this equation is near impossible on classical computers—the so-called ‘numerical sign problem’. Instead, we can use the property of analytic continuity to ‘Wick rotate’:

$$t \rightarrow -i\tau \quad \Rightarrow \quad e^{iS_{\text{QCD}}} \rightarrow e^{-S_{\text{QCD}}^E}. \quad (3.3)$$

Under this transformation, the invariant length of some spacetime vector, z_μ , is

$$z^2 = -\tau^2 - |\mathbf{z}|^2 < 0. \quad (3.4)$$

Hence after the Wick rotation we are working in a Euclidean spacetime: the spatial and temporal components of the invariant length have the same sign.

In the literature the convention is to change the elements of a Lorentz vector in coordinate space, x_μ , and in momentum space, p_μ , like so:

$$x_0 \rightarrow -ix_4, \quad p_0 \rightarrow ip_4, \quad (3.5)$$

which means that the temporal/energy component moves to the end of the four-vector. Note that the opposing sign on the momentum vector keeps Fourier transforms well-defined.

As such, the new Euclidean action is

$$S_F^E = \int d^4z \sum_f \bar{\psi}_f(z) (D_\mu \gamma_\mu^E + m_f) \psi_f(z), \quad S_G^E = \int d^4z \frac{1}{4} F_{\mu\nu}(z) F_{\mu\nu}(z), \quad (3.6)$$

where the Dirac matrices are changed to $\gamma_\mu^E = (\gamma^0, -i\gamma^i)$ to satisfy the Euclidean Clifford algebra: $\{\gamma_\mu, \gamma_\nu\} = 2\delta_{\mu\nu}\mathbb{I}$.

[†]In this chapter we generally suppress all colour indices. Moreover, where we wrote $t^a A_\mu^a(z)$ for the product of the SU(3) generator and gauge field, we now simply write $A_\mu(z)$.

And the Euclidean path integral is

$$\langle \Omega | \mathcal{O} | \Omega \rangle = \frac{\int \mathcal{D}A_\mu \mathcal{D}\bar{\psi} \mathcal{D}\psi \mathcal{O} e^{-S_F^E - S_G^E}}{\int \mathcal{D}A_\mu \mathcal{D}\bar{\psi} \mathcal{D}\psi e^{-S_F^E - S_G^E}}. \quad (3.7)$$

Defining the fermion operator as

$$M = \not{D} - m_f, \quad (3.8)$$

one can show that Eq. (3.7) becomes [96]

$$\langle \Omega | \mathcal{O} | \Omega \rangle = \frac{\int \mathcal{D}A_\mu \det[M] \mathcal{O} e^{-S_G^E}}{\int \mathcal{D}A_\mu \det[M] e^{-S_G^E}}. \quad (3.9)$$

Hence, in contrast to the oscillatory $e^{iS_{\text{QCD}}}$ in Eq. (3.1), we have the weight $\det[M]e^{-S_G^E}$ that accompanies the operator. This distribution is far simpler to sample, and hence the Wick rotation is crucial to making lattice QCD numerically feasible.

However, since we live in a world with real and not imaginary time, the Wick rotation does not come without consequences. As shown in Eq. (3.4), all the coordinate space separations in this formulation are spacelike: $z^2 < 0$. By contrast the parton distributions discussed in the previous chapter are defined as light-like correlation functions, Eq. (2.52). Similarly, a direct calculation of the Compton scattering amplitude requires real time—see Section 4.2. Therefore, this forms a central difficulty of our calculation: although the Wick rotation is necessary to make lattice calculations computationally feasible, it also makes the direct calculation of parton distributions and scattering amplitudes impossible. We discuss this problem and some solutions in Section 3.2.

3.1.2 Discretisation

Even after the Wick rotation, the integral in Eq. (3.9) still has an infinite number of degrees of freedom. Therefore, to make the evaluation of this path integral possible on a computer, we need to reduce it to a finite number of degrees of freedom. We do this by working in a discrete spacetime with a finite extent: the lattice. The discretisation of the Euclidean action, Eq. (3.6), is a highly involved exercise. Here, we give a brief overview of the discretisation used for our calculations—more complete treatments can be found in Refs. [96–99].

Discretisation begins by replacing our continuous infinite spacetime with a bounded discrete set of points. Hence a given spacetime vector, z_μ , becomes

$$z_\mu = an_\mu,$$

where a is the lattice spacing and the elements of n_μ are in $\{0, 1, 2, \dots, N - 1\}$ for N the number of points in a given direction. The spatial extent is $L = aN$, and typically we choose L the same in all spatial directions and the temporal extent to be $T = 2L$.

Due to the limited spacetime extent and periodic boundary conditions, the three momentum, \mathbf{p} , are quantised on the lattice like so:

$$\mathbf{p} = \frac{2\pi}{L} \mathbf{n}, \quad (3.10)$$

where the elements of \mathbf{n} are in $\{-N/2 + 1, -N/2 + 2, \dots, 0, 1, \dots, N/2\}$ for N again the number of spacetime points in a given direction. Therefore, there are the same number of momentum values as spacetime sites for a given direction.

The lattice QCD action

Now we would like to quantise the Euclidean QCD action; we will do this separately for the gauge and fermion components given in Eq. (3.6).

Recall from Chapter 2 that the SU(3) symmetry of QCD is *local*, and hence operators at different spacetime points have different gauge spaces. As such, we introduced the Wilson line, $U(z, z')$, as a way of ‘comparing’ two operators in different gauge spaces. For the discretised theory we introduce the analogue of the Wilson line, the ‘link variable’:

$$U_\mu(z) \equiv U(z, z + a\hat{\mu}) = e^{igaA_\mu(z)}, \quad (3.11)$$

where $\hat{\mu}$ is the unit vector in the μ direction. Note that the link variable pointing in the $-\hat{\mu}$ direction is $U_{-\mu}(z) = U_\mu^\dagger(z - a\hat{\mu})$.

Then, the discretised covariant derivative acting on a quark field is

$$D_\mu\psi(z) = \frac{U_\mu(z)\psi(z + a\hat{\mu}) - U_\mu^\dagger(z - a\hat{\mu})\psi(z - a\hat{\mu})}{2a}. \quad (3.12)$$

Unlike in the continuum case (Eq. 2.8), we cannot take a to be infinitesimal, and therefore we do not have the straightforward relationship between the covariant derivative and the gauge boson fields A_μ as in Eq. 2.8. This suggests that gauge invariant quantities on the lattice must be constructed from the link variables rather than A_μ directly.

Gauge component

Since one can show that a closed loop of link variables is gauge invariant [99], we start with the simplest such loop, the plaquette:

$$\mathcal{P}_{\mu\nu}(z) \equiv U_\nu^\dagger(z)U_\mu^\dagger(z + a\hat{\nu})U_\nu(z + a\hat{\mu})U_\mu(z). \quad (3.13)$$

Then, using the identity $e^a e^b = \exp\left\{a + b + \frac{1}{2}[a, b] + \dots\right\}$ and Taylor expanding the vector fields, one can derive that

$$\mathcal{P}_{\mu\nu}(z) = e^{ia^2g^2G_{\mu\nu}(z) + \mathcal{O}(a^3)}, \quad (3.14)$$

where $G_{\mu\nu}$ is a discretisation of the QCD field strength tensor, $F_{\mu\nu}$, from Eq. 2.9. This suggests the Wilson gauge action as a suitable discretisation [13]:

$$S_G = \frac{2}{g^2} \sum_{\text{sites}} \sum_{\mu < \nu} \text{Re trace}[\mathbb{I} - \mathcal{P}^{\mu\nu}(z)]. \quad (3.15)$$

This recovers the Euclidean gauge action, S_G in Eq. (3.6), as $a \rightarrow 0$. There are improvements in the $\mathcal{O}(a^2)$ corrections that can be made to this action. For our calculations we use the Symanzik-improved gluon action [27], for which a more detailed treatment can be found in Ref. [99].

Fermion component

At first glance, building a gauge invariant fermion action seems much simpler than the gauge action, using the covariant derivative in Eq. (3.12):

$$S_F^{\text{naive}} = \sum_{\text{sites}} \left[\bar{\psi}(z) \gamma_\mu \frac{U_\mu(z) \psi(z + a\hat{\mu}) - U_\mu^\dagger(z - a\hat{\mu}) \psi(z - a\hat{\mu})}{2a} + m \bar{\psi}(z) \psi(z) \right], \quad (3.16)$$

which has $\mathcal{O}(a^2)$ errors.

However, this naive fermion action suffers from a difficulty known as ‘fermion doubling’: due to the nature of momentum on the lattice, the massless fermion propagator has 16 poles, leading to 16 fermion species, where there should be only two. This doubling can be removed by the addition of the ‘Wilson term’ to Eq. (3.16) [96, 97, 99]. However, this Wilson term introduces $\mathcal{O}(a)$ errors, which can be improved by the inclusion of the Sheikholeslami-Wolhart (or ‘clover’) term [100].

We simply quote the Wilson fermion action below [‡]:

$$S_F^W = \sum_{n,m} \bar{\psi}(z_n) M^W(n, m) \psi(z_m), \quad (3.17)$$

where $M^W(n, m)$ is the Wilson fermion matrix[§], a discretisation of the fermion operator introduced in Eq. (3.8):

$$M^W(n, m) = (m_0 + 4r) \delta_{n,m} - \frac{1}{2a} \sum_{\mu} \left[(r - \gamma_\mu) U_\mu(z_n) \delta_{n+\hat{\mu}, m} + (r + \gamma_\mu) U_\mu(z_n - a\hat{\mu})^\dagger \delta_{n-\hat{\mu}, m} \right], \quad (3.18)$$

where m_0 is the bare fermion mass, and we typically set $r = 1$.

Although we do not write it out here, the Wilson action is often expressed in terms of the ‘hopping parameter’, κ :

$$\kappa = \frac{1}{2m_0 a + 8r}. \quad (3.19)$$

This parameter is used to tune quark masses and is one of the fundamental inputs into lattice calculations.

3.1.3 Determining matrix elements

We now return to our path integral, Eq. (3.9), which in terms of the gauge links is**

$$\langle \Omega | \mathcal{O} | \Omega \rangle = \frac{\int \mathcal{D}U \det[M[U, \bar{\psi}, \psi]] \mathcal{O}[U, \bar{\psi}, \psi] e^{-S_G^E[U]}}{\int \mathcal{D}U \det[U, \bar{\psi}, \psi] e^{-S_G^E[U]}}, \quad (3.20)$$

where we have written out the dependence on the gauge links U , and the fermion fields, $\bar{\psi}$ and ψ . The sea quark contributions are contained entirely within $\det[M[U, \bar{\psi}, \psi]]$, and the valence quarks in the operator, $\mathcal{O}[U, \bar{\psi}, \psi]$.

[‡]Note that there are other possible discretisations of the fermion action [96, 97].

[§]For z_n or z_m , the index refers to the lattice site, not the component of the Lorentz vector.

**Here, we suppress the Lorentz index on the gauge links, and write them simply as U .

Gauge fields

To approximate this integral, we generate gauge links with the acceptance probability of $\det[M]e^{-S_G}$, for discretised M and S_G as described above. Gauge field generation is typically the most computationally expensive part of the lattice process and is performed with Hamiltonian Monte Carlo [101], although exploratory studies have tested the ability of machine learning techniques to improve the accuracy and computational cost of gauge field generation [102].

As the field configurations are generated to conform to this probability distribution, we can approximate the path integral as

$$\langle \Omega | \mathcal{O} | \Omega \rangle \approx \langle \mathcal{O} \rangle_U \equiv \frac{1}{N_{\text{conf}}} \sum_{i=1}^{N_{\text{conf}}} \mathcal{O}[U^i], \quad (3.21)$$

where U^i is the i^{th} configuration of the gauge links, and we have defined $\langle \dots \rangle_U$ as the average over all the gauge configurations. A set of gauge configurations is known as an ‘ensemble’, and hence Eq. (3.21) is also called an ‘ensemble average’.

A fundamental input into gauge field generation is the parameter $\beta \equiv 6/g^2$, where g is bare the QCD coupling strength. As such, like κ , the β parameter is used to label the gauge ensembles in this thesis.

Fermions

For the quark fields in our operator, \mathcal{O} , we perform all Wick contractions, which gives the fermion part of the operator in terms of quark propagators. Since the continuum quark propagator is the Green’s function (i.e. functional inverse) of the Fermion operator, for discrete spacetime the lattice quark propagator is the inverse of the fermion matrix:

$$S_f(z_n, z_m) = [M_f^W]_{nm}^{-1}, \quad (3.22)$$

for M_f^W as in Eq. (3.18) for a quark of a single flavour.

The inversion of the sparse matrix in Eq. (3.18) is typically the second most computationally expensive procedure in a lattice calculation. However, as the masses of the quarks increase, the numerical cost of this inversion decreases^{††}. Therefore, in this thesis, our lattice calculations use unphysically large quark masses. Although, lattice calculations at the physical masses are becoming more common.

As an example, consider the nucleon two-point correlation function (also referred to as a ‘correlator’):

$$\langle \Omega | \chi_\alpha(z') \chi_\beta^\dagger(z) | \Omega \rangle, \quad (3.23)$$

where the proton interpolating operators are

$$\begin{aligned} \chi_\alpha(z) &= \epsilon^{ijk} [\psi_u]_\alpha^i(z) \left([\psi_u]_\beta^j(z) [C\gamma_5]_{\beta\gamma} [\psi_d]_\gamma^k(z) \right), \\ \chi_\alpha^\dagger(z) &= \epsilon^{ijk} \left([\bar{\psi}_u]_\beta^i(z) [C\gamma_5]_{\beta\gamma} [\bar{\psi}_d]_\gamma^j(z) \right) [\bar{\psi}_u]_\alpha^k(z). \end{aligned} \quad (3.24)$$

^{††}Roughly speaking, we can see this in Eq. (3.18): as m_0 becomes increasingly large, the diagonal mass contribution dominates the non-diagonal kinetic contribution. In the limit of infinite quark mass, therefore, we have a diagonal matrix, for which it is trivial to find the inverse.

Here, i, j, k are fermion colour indices and α, β, γ are Dirac indices. Note that C is the charge conjugation matrix.

By taking all possible Wick contractions in Eq. (3.23), we find that this expectation value can be computed from the ensemble average of quark propagators:

$$\begin{aligned} \langle \chi_\alpha(z') \chi_\beta^\dagger(z) \rangle_U &= \epsilon^{ijk} \epsilon^{i'j'k'} [C\gamma_5]_{\gamma\delta} [C\gamma_5]_{\sigma\rho} \left\langle \left[[S_u(z', z)]_{\alpha\sigma}^{ii'} [S_u(z', z)]_{\gamma\beta}^{jj'} [S_d(z', z)]_{\delta\rho}^{kk'} \right. \right. \\ &\quad \left. \left. - [S_u(z', z)]_{\alpha\beta}^{ij'} [S_u(z', z)]_{\gamma\sigma}^{j'i'} [S_d(z', z)]_{\delta\rho}^{k'k'} \right] \right\rangle_U. \end{aligned} \quad (3.25)$$

Similarly, one can use operators that couple to pion fields and proceed in an identical way; however, all the lattice QCD calculations in this thesis are for nucleons only.

3.1.4 Correlation functions

We now give a brief overview of the calculation of nucleon two- and three-point hadron correlation functions in lattice QCD.

Two-point functions

Among the most common applications of lattice QCD is the calculation of two-point functions, from which one can determine part of the energy spectrum of hadrons. These methods are also important for this thesis, as the Feynman-Hellmann method is based on the calculation of two-point functions, where the action has been modified by the addition of perturbing background fields.

We start with the nucleon two-point function, given in Eq. (3.23). The eigenstates of the QCD Hamiltonian are $\{|X(\mathbf{p})\rangle\}$, where X is the hadronic state and \mathbf{p} is the momentum, whose components are quantised as in Eq. (3.10). These states satisfy the normalisation conditions

$$H_{\text{QCD}}|X(\mathbf{p})\rangle = E_X(\mathbf{p})|X(\mathbf{p})\rangle, \quad \langle Y(\mathbf{p}')|X(\mathbf{p})\rangle = 2E_X(\mathbf{p})L^3\delta_{X,Y}\delta_{\mathbf{p}',\mathbf{p}}. \quad (3.26)$$

We then define $\mathcal{G}(\tau, \mathbf{p})$ the Fourier-projected two-point function^{‡‡}:

$$\mathcal{G}(\Gamma, \tau, \mathbf{p}) \equiv \Gamma_{\beta\alpha} \sum_{\mathbf{z}} e^{-i\mathbf{p}\cdot\mathbf{z}} \langle \Omega | \chi_\alpha(\tau, \mathbf{z}) \chi_\beta^\dagger(0) | \Omega \rangle, \quad (3.27)$$

where Γ is a spin-parity projector, a matrix in Dirac space, and there is an implicit sum over α and β . This correlation function is illustrated on the left panel of Fig. 3.1.

In the rest frame, $\mathbf{p} = 0$, the choice of Γ isolates different spin-parity states:

$$\begin{aligned} \Gamma = \text{diag}(1, 0, 0, 0) &\rightarrow \text{spin up, positive parity,} \\ \Gamma = \text{diag}(0, 1, 0, 0) &\rightarrow \text{spin down, positive parity,} \\ \Gamma = \text{diag}(0, 0, 1, 0) &\rightarrow \text{spin up, negative parity,} \\ \Gamma = \text{diag}(0, 0, 0, 1) &\rightarrow \text{spin down, negative parity.} \end{aligned}$$

^{‡‡}By translational invariance, we can fix the initial position of the creation operator at $z_\mu = 0$ without loss of generality.

As such,

$$\Gamma_{\text{unpol}} = \frac{1}{2}(\mathbb{I} + \gamma_4), \quad (3.28)$$

picks out the average of the spin up and down, and is therefore most commonly used for nucleon two-point functions. We will discuss different spin-parity projectors in Chapters 4–7; however, for the rest of this chapter we will suppress them in our expressions.

Then inserting a complete set of states^{§§}

$$\begin{aligned} \mathcal{G}(\tau, \mathbf{p}) &= \sum_{X, \mathbf{p}'} \sum_{\mathbf{z}} e^{-i\mathbf{p}\cdot\mathbf{z}} \langle \Omega | \chi(\tau, \mathbf{z}) \frac{|X(\mathbf{p}')\rangle \langle X(\mathbf{p}')|}{\langle X(\mathbf{p}') | X(\mathbf{p}') \rangle} \chi^\dagger(0) | \Omega \rangle \\ &= \sum_{X, \mathbf{p}'} \sum_{\mathbf{z}} e^{-i\mathbf{p}\cdot\mathbf{z}} \langle \Omega | e^{H\tau - i\hat{\mathbf{p}}\cdot\mathbf{z}} \chi(0) e^{-H\tau + i\hat{\mathbf{p}}\cdot\mathbf{z}} \frac{|X(\mathbf{p}')\rangle \langle X(\mathbf{p}')|}{\langle X(\mathbf{p}') | X(\mathbf{p}') \rangle} \chi^\dagger(0) | \Omega \rangle \\ &= \sum_{X, \mathbf{p}'} e^{-E_X(\mathbf{p}')\tau} \sum_{\mathbf{z}} e^{-i(\mathbf{p}-\mathbf{p}')\cdot\mathbf{z}} \langle \Omega | \chi(0) \frac{|X(\mathbf{p}')\rangle \langle X(\mathbf{p}')|}{\langle X(\mathbf{p}') | X(\mathbf{p}') \rangle} \chi^\dagger(0) | \Omega \rangle \\ &= \sum_X e^{-E_X(\mathbf{p})\tau} \frac{|\langle \Omega | \chi(0) | X(\mathbf{p}) \rangle|^2}{\langle X(\mathbf{p}) | X(\mathbf{p}) \rangle}, \end{aligned} \quad (3.29)$$

where we have used the translational invariance of operators after the Wick rotation:

$$\mathcal{O}(\mathbf{z}, \tau) = e^{H\tau - i\hat{\mathbf{p}}\cdot\mathbf{z}} \mathcal{O}(0) e^{-H\tau + i\hat{\mathbf{p}}\cdot\mathbf{z}}. \quad (3.30)$$

For simplicity, we write Eq. (3.29) as

$$\mathcal{G}(\tau, \mathbf{p}) = \sum_X A_X(\mathbf{p}) e^{-E_X(\mathbf{p})\tau}. \quad (3.31)$$

Therefore, for large τ , the term in the sum of X with the lowest energy will dominate: the nucleon. Hence

$$\mathcal{G}(\tau, \mathbf{p}) \approx A_N(\mathbf{p}) e^{-E_N(\mathbf{p})\tau}, \quad \tau \gg a. \quad (3.32)$$

Excited nucleon states may still contribute significantly if the Euclidean time is not sufficiently large or if the mass splitting is too fine. As such, it is important to keep $a > 1/\Delta E$, where ΔE is the smallest relevant mass splitting. We will explore analogous excited states that appear in Feynman-Hellmann in Chapter 4.

Equation (3.32) allows us to extract the ground state nucleon. In particular, we define the ‘effective mass’:

$$\Delta E_{\text{eff}}(\tau) \equiv \frac{1}{\delta\tau} \log \left(\frac{\mathcal{G}(\tau, \mathbf{p})}{\mathcal{G}(\tau + \delta\tau, \mathbf{p})} \right). \quad (3.33)$$

This quantity is useful for helping lattice practitioners assess the quality of the ground state saturation in their correlation functions.

^{§§}Technically, in this operator formalism we also need to include an inverse factor of the partition function, $\mathcal{Z}_T = \sum_X e^{-E_X T}$, and the backwards propagating state [99]. However, both of these contributions are highly suppressed for $T \gg 1/E_X$.

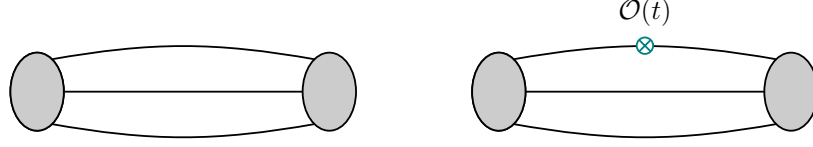


Figure 3.1: Lattice diagrams of two-point (left) and connected three-point (right) correlation functions. The connected quark propagators are the solid lines, while the grey blobs are the source and sink—time increases left to right. The circled cross in the three-point function represents the insertion of the operator.

For the correlator, Eq. (3.32), we note that large momenta make it difficult to extract the ground state: at $\mathbf{p} = 0$ the mass splitting is well defined:

$$E_N = m_N \leq E_{N_1} = m_{N_1} \leq \dots$$

However, for non-zero momenta we have

$$E_N = \sqrt{m_N^2 + \mathbf{p}^2} \leq E_{N_1} = \sqrt{m_{N_1}^2 + \mathbf{p}^2} \leq \dots$$

And hence as $|\mathbf{p}| \sim m_X$, the mass splitting becomes increasingly small and so it is harder to isolate the ground state. This is a persistent problem in our calculation and other calculations of partonic quantities on the lattice, as we discuss in Section 3.2.

Three-point functions

The three-point correlation function,

$$\langle \Omega | \chi(z') \mathcal{O}(y) \chi^\dagger(z) | \Omega \rangle, \quad (3.34)$$

is another extremely important correlation function, which is central to studies of hadron structure in lattice QCD—see the right panel of Fig. 3.1. Using this correlation function, one can determine the matrix element $\langle N | \mathcal{O}(0) | N \rangle$, where we have used nucleon states, but in principle other states are possible. As such, this type of calculation has allowed for first principles determinations of electromagnetic form factors [103], scalar, tensor and axial charges [104], and the moments of parton distribution functions [105], among others.

By Fourier transforming Eq. (3.34) and setting the source point to be at the origin, we get

$$\mathcal{G}_{3\text{-pt}}(\tau, t) = \sum_{\mathbf{z}, \mathbf{y}} e^{-i\mathbf{p} \cdot (\mathbf{z} - \mathbf{y})} e^{-i\mathbf{p} \cdot \mathbf{y}} \langle \Omega | \chi(\tau, \mathbf{z}) \mathcal{O}(t, \mathbf{y}) \chi^\dagger(0) | \Omega \rangle. \quad (3.35)$$

Again, inserting a complete sets of states and using translational invariance as in Eq. (3.29), we have

$$\begin{aligned} \mathcal{G}_{3\text{-pt}}(\mathbf{p}, \mathbf{p}; \tau, t) &= \sum_{X, Y} \frac{e^{-E_X(\mathbf{p})(\tau-t)} e^{-E_Y(\mathbf{p})t}}{\langle X(\mathbf{p}') | X(\mathbf{p}') \rangle \langle Y(\mathbf{p}) | Y(\mathbf{p}) \rangle} \\ &\times \langle \Omega | \chi(0) | X(\mathbf{p}) \rangle \langle X(\mathbf{p}) | \mathcal{O}(0) | Y(\mathbf{p}) \rangle \langle Y(\mathbf{p}) | \chi^\dagger(0) | \Omega \rangle. \end{aligned} \quad (3.36)$$

Then, by taking the ratio of the above expression with the two-point function, Eq. (3.27), for forward kinematics we have

$$\frac{\mathcal{G}_{3\text{-pt}}(\mathbf{p}, \mathbf{p}; \tau, t)}{\mathcal{G}(\mathbf{p}, \tau)} \propto \langle N(\mathbf{p}) | \mathcal{O}(0) | N(\mathbf{p}) \rangle, \quad \text{for } \tau - t \gg a, t \gg a. \quad (3.37)$$

It is necessary to take both $\tau - t \gg a$ and $t \gg a$ in order to isolate the nucleon ground states (or other ground-state hadron). Therefore, three-point calculations require careful control of contributions from excited states [106]. As with two-point functions, higher sink momentum makes extracting the ground state more difficult.

Four-point functions

One can generalise this method to calculate four-point functions:

$$\langle \Omega | \chi(z') \mathcal{O}_1(y') \mathcal{O}_2(y) \chi^\dagger(z) | \Omega \rangle. \quad (3.38)$$

This type of matrix element is extremely important to the current study, as our Feynman-Hellmann method is one approach to circumvent the many difficulties associated with a direct calculation of four-point functions.

The standard way of performing the partial Fourier transform is then

$$\begin{aligned} & \mathcal{G}_{4\text{-pt}}(\tau, t_1, t_2; \mathbf{p}, \mathbf{k}, \mathbf{k}') \\ &= \sum_{\mathbf{z}, \mathbf{y}', \mathbf{y}} e^{-i\mathbf{p} \cdot (\mathbf{z} - \mathbf{y}')} e^{-i\mathbf{k}' \cdot (\mathbf{y}' - \mathbf{y})} e^{-i\mathbf{k} \cdot \mathbf{y}} \langle \Omega | \chi(\mathbf{z}, \tau) \mathcal{O}_1(\mathbf{y}', t_2) \mathcal{O}_2(\mathbf{y}, t_1) \chi^\dagger(0) | \Omega \rangle. \end{aligned} \quad (3.39)$$

Therefore, to isolate the ground state at the source and sink we need $\tau - t_2 \gg a$ and $t_1 \gg a$. To get ground state saturation in the intermediate state (i.e. between t_1 and t_2), we need $t_2 - t_1 \gg a$. For low-energy observables, where we are only interested in the nucleon pole contribution, it is necessary to ensure ground state saturation [107, 108]. On the other hand, for high-energy observables, such as the hadronic tensor, ground state saturation is *not* desirable [109]. In either case, four-point functions require a much more careful treatment of excited states than two- and three-point functions, and may require a lattice with a larger temporal extent.

An example of an operator that is commonly used in hadron structure studies of four- and three-point functions, and which will be used in this thesis, is the vector current: $j_\mu(z) = \bar{\psi}(z) \gamma_\mu \psi(z)$.

On the lattice, we discretise this either with the local vector current:

$$j_\mu^{\text{loc}}(z_n) = Z_V \bar{\psi}(z_n) \gamma_\mu \psi(z_n), \quad (3.40)$$

where Z_V is the multiplicative renormalisation factor.

Or the conserved vector current, which is a Noether current on the lattice [99]:

$$j_\mu^{\text{con}}(z_n) = \frac{1}{2} \left(\bar{\psi}(z_n + a\hat{\mu})(r + \gamma_\mu) U_\mu^\dagger(z_n) \psi(z_n) - \bar{\psi}(z_n)(r - \gamma_\mu) U_\mu(z_n) \psi(z_n + a\hat{\mu}) \right). \quad (3.41)$$

3.2 Lattice Parton Distributions

The calculation of partonic information from first principles QCD is the central goal of this thesis, and is among the most important and difficult areas in all lattice QCD—see reviews [105, 110, 111].

Recall the definition of the standard parton distribution function in terms of a light-cone operator, Eq. (2.51):

$$q_f(x) = \int \frac{d\lambda}{2\pi} e^{i\lambda x} \langle P | \bar{\psi}_f(-\lambda n/2) \not{n} \psi_f(\lambda n/2) | P \rangle,$$

where n_μ is a light-like vector. As discussed in Section 3.1, the Euclidean signature of spacetime on the lattice (Eq. (3.4)) prevents the calculation of light-like correlation functions, and hence prevents the direct calculation of parton distributions. Since a direct determination is impossible, there is an abundance of methods to indirectly access partonic information on the lattice. Our Feynman-Hellmann Compton amplitude method is just one such method. In this section we give a brief review of the other main approaches.

3.2.1 Lattice OPE

Recall from Chapter 2 that we can relate the Mellin moments of parton distributions to local operators. In the case of the unpolarised PDF this is:

$$a_n^f = 2 \int_{-1}^1 dx x^{n-1} q_f(x),$$

where a_n^f are the reduced matrix elements of the twist-two operators defined in Eq. (2.40):

$$\langle P | \mathcal{O}_f^{(n)\mu_1 \dots \mu_n} | P \rangle = a_n^f P^{\mu_1} \dots P^{\mu_n} - \text{traces}.$$

This is important from the perspective of lattice calculations, as local operators by definition do not depend on a coordinate space separation. As such, the matrix elements of local operators are the same in Euclidean and Minkowski space. Therefore, we can calculate the moments of parton distributions using the three-point function formalism described above. For instance, for the operator $\mathcal{O}^{(2)\mu\nu}$, the unrenormalised matrix element can be calculated like so:

$$\frac{\mathcal{G}_{3\text{-pt}}(\mathbf{p}; \tau, t)}{\mathcal{G}(\mathbf{p}, \tau)} \propto \langle N(\mathbf{p}) | \mathcal{O}^{(2)\mu\nu} | N(\mathbf{p}) \rangle = (P^\mu P^\nu - \text{traces}) a_2^{\text{bare}}. \quad (3.42)$$

However, renormalising the matrix element in Eq. (3.42) becomes extremely complicated due to operator mixing induced by the broken Lorentz symmetry on the lattice. The twist-two local operators defined in Eq. 2.40 belong to an irreducible representation of the Lorentz group (some further discussion is given in Appendix C). Since lattice QCD is formulated on a hypercubic grid of points, it breaks Lorentz symmetry. Instead of the usual continuum orthogonal group $O(4)$ of transformations, only a finite subgroup, the hypercubic subgroup, survives. As a result, the usual leading-twist operators mix under renormalisation with other operators on the lattice [30, 31]. If an operator mixes with

lower dimensional operators, these operators contain coefficients of $1/a$, which can make such calculations harder when extrapolating to the continuum [112, 113].

For the lowest $n = 2$ operator, this mixing can be controlled systematically by subtracting off the divergent unphysical operator [112], but as n gets larger the mixing becomes harder to control [113]. Therefore, few studies go beyond the $n = 3$ moment. This is problematic, since the number of moments needed to reconstruct parton distributions is much higher: some estimates are $n \sim 50$ moments [114], while a lower number, $n \sim 10$, is possible if one makes certain assumptions about the parton distribution [115].

The first numerical calculations of lattice parton distribution moments were performed in the late 1980s [28, 29], making it by far the oldest and most developed method to determine partonic information in lattice QCD. While there are ongoing efforts to extend this method to higher moments [116, 117], this approach remains limited, which has led to other methods to calculate lattice parton distributions.

For the present thesis, we are most interested in the calculation of the nucleon spin-dependent and off-forward moments. In the case of spin-dependent PDFs, there have been numerous calculations of the first moment [104], which is simply the axial charge, Eq. (2.64). Moreover, there have been lattice calculations of d_2 [118–121], the quantity from Eq. (2.70). For the off-forward Compton amplitude, there have been many calculations of the $n = 1, 2, 3$ moments [122–133], but no higher than this.

3.2.2 Quasi- and pseudo-distributions

Since the 2010s, there has been a wave of new methods proposed to calculate the x dependence of parton distributions in lattice QCD. Among the most prominent of these are the quasi-distribution [32] and the pseudo-distribution approaches [33]^{***}. Both of these methods start by calculating the same lattice correlation function:

$$\langle \Omega | \chi(\mathbf{z}', \tau) \mathcal{O}(\mathbf{y}', \mathbf{y}, t) \chi^\dagger(\mathbf{z}, 0) | \Omega \rangle, \quad (3.43)$$

where the operator here is

$$\mathcal{O}(\mathbf{y}', \mathbf{y}, t) = \bar{\psi}(\mathbf{y}', t) \Gamma U(\mathbf{y}', \mathbf{y}; t, t) \psi(\mathbf{y}, t), \quad (3.44)$$

noting that $U(\mathbf{y}', \mathbf{y}; t, t)$ is the Wilson line (Eq. (2.4)) from the point (\mathbf{y}, t) to (\mathbf{y}', t) and Γ is some Dirac matrix. On the lattice, this is discretised in terms of the link variable, Eq. (3.11). See Fig. 3.2 for a lattice diagram of this correlation function.

A key feature of the operator in Eq. (3.44) is that it is non-local in space, but local in time. This confers two advantages: (1) like local operators, the matrix elements of equal-time operators are the same in Minkowski and Euclidean space [135]; and (2) with only a single time coordinate, one can ensure ground state saturation of the matrix element in effectively the same way as three-point functions, Eq. (3.36), thereby avoiding the many difficulties of directly calculating four-point functions.

The extracted matrix element from the correlation function in Eq. (3.43) is

$$\langle P | \bar{\psi}(z) \gamma_\mu U(z, 0) \psi(0) | P \rangle = 2P_\mu h(P \cdot z, z^2) + z_\mu \bar{h}(P \cdot z, z^2), \quad (3.45)$$

^{***}There are also calculations of coordinate space current-current operators [34, 35, 134], which are calculated and analysed in an analogous way to the pseudo-distributions.

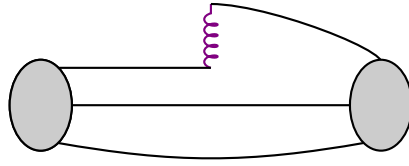


Figure 3.2: Lattice diagram of the correlation function for quasi- and pseudo-distributions, Eq. (3.43). The coiled line represents the gauge link of length z .

where we have limited ourselves to $\Gamma = \gamma_\mu$, and no momentum transfer. Since our operator in Eq. (3.44) is local in time, the separation is purely spatial; the convention in the literature is to choose this separation purely in the $\hat{\mathbf{e}}_3$ direction^{††} $z_\mu = (0, 0, z, 0)$. Hence our two Lorentz scalars become $P \cdot z = -zP_z$ and $z \cdot z = -z^2$.

We can see that the operator in Eq. (3.45) is similar to the coordinate space correlation in the light-cone definition of the PDF, Eq. (2.52):

$$\langle P | \bar{\psi}(-\lambda n/2) \gamma_\mu n^\mu U(-\lambda n/2, \lambda n/2) \psi(\lambda n/2) | P \rangle.$$

In fact, the form factor $h(P \cdot z, z^2)$ is proportional to this matrix element if z_μ is a light-like vector. As such, $h(P \cdot z, z^2)$ gives us the spacelike (or Euclidean) analogue of the light-like parton distribution. The form factor $\bar{h}(P \cdot z, z^2)$ is purely higher-twist, and must be removed.

Constructing the distributions and light-cone matching

The difference between the quasi and pseudo approaches then arises purely from what one does with the form factor $h(P \cdot z, z^2)$. The quasi-distribution is defined by integrating over the spatial separation, z [32]:

$$\mathcal{Q}(x, P_z) = \mathcal{N}_Q \int_{-\infty}^{\infty} \frac{dz}{2\pi} e^{-ixP_z z} h(P \cdot z, z^2), \quad (3.46)$$

where \mathcal{N}_Q is a normalisation factor.

To match this quasi-distribution to the light-cone parton distribution, $q(x)$, one uses large momentum effective theory (LaMET) [32, 136]. The general form of the relation between the PDF and the quasi-distribution is [137, 138]

$$\mathcal{Q}(x, P_z) = \int \frac{dy}{|y|} \mathcal{C}_Q \left(\frac{x}{y}, \frac{1}{xP_z} \right) q(y) + \mathcal{O} \left(\frac{\Lambda_{\text{QCD}}^2}{P_z^2 x^2 (1-x)} \right). \quad (3.47)$$

Note that this is a factorisation theorem of the form in Eq. (2.16). The kernel \mathcal{C}_Q can be calculated to a given order in perturbation theory. The higher-twist corrections on the other hand must be sufficiently suppressed by large momentum: $P_z \gg \Lambda_{\text{QCD}}$.

By contrast, the pseudo-distribution is defined by integrating over the variable zP_z :

$$\mathcal{P}(x, z) = \mathcal{N}_P \int_{-\infty}^{\infty} \frac{dzP_z}{2\pi} e^{-ixP_z z} h(P \cdot z, z^2). \quad (3.48)$$

^{††}Hopefully this does not cause confusion: in general for this thesis we use z_μ as a generic spacetime coordinate; for this brief discussion of quasi- and pseudo-distributions we use^{†††} $z_\mu = (0, 0, z, 0)$.

Then, the pseudo-distributions are related to the PDF by a similar factorisation theorem [137, 138]

$$\mathcal{P}(x, z) = \int \frac{dy}{|y|} \mathcal{C}_P\left(\frac{x}{y}, z^2\right) q(y) + \mathcal{O}(z^2 \Lambda_{\text{QCD}}^2 (1-x)). \quad (3.49)$$

Once again, the perturbative kernel can be calculated in perturbation theory, while higher-twist corrections need to be suppressed by short-distances: $z \ll 1/\Lambda_{\text{QCD}}$.

Challenges

From Eqs. (3.46)—(3.49) we can see the contrasting difficulties in the quasi and pseudo approaches:

- **Integration:** In constructing the quasi- and pseudo-distributions from $h(P \cdot z, z^2)$ —Eqs. (3.46) and (3.48), respectively—the quasi method has an advantage [139, 140]. For the quasi-distribution, Eq. (3.46) is approximated by a sum over a range of separations $|z| \leq z_{\text{max}}$ for $z_{\text{max}} \sim 10a$ [141]. Since $h(P \cdot z, z^2)$ decays exponentially with z [142], a finite extent in this sum is justified [141, 143].

By contrast, to attain the full range of zP_z for the pseudo-distribution integral, Eq. (3.48), one needs to access very large values of the sink momentum, P_z , which are not feasible in current calculations [139, 144]. As the full domain of the integrand in Eq. (3.48) is not accessible, the pseudo-distribution approach is faced with an ill-conditioned ‘inverse problem’^{§§§}.

- **Higher-twist:** On the other hand, for the control of higher-twist contributions, pseudo-distributions have an advantage. As quasi-distributions require $P_z \gg \Lambda_{\text{QCD}}$ to suppress higher-twist corrections, the large sink momentum decreases the quality of the signal. Moreover, due to the factors of $1/x^2$ and $1/(1-x)$ in the quasi-distribution higher-twist corrections, it is often very difficult to determine the physical parton distribution outside of some intermediate range of $0 < x_{lb} < x < x_{ub} < 1$. By contrast, from Eq. (3.49) the higher-twist corrections to pseudo-distributions are suppressed by short-distance: $z^2 \ll 1/\Lambda_{\text{QCD}}$. Hence large momentum is not necessary. Moreover, there are no divergent $1/x^2$ or $1/(1-x)$ terms in the higher-twist corrections—on the contrary, the higher-twist corrections are *suppressed* for $x \sim 1$.

Therefore, in different ways, both methods face the challenge of accessing high sink momentum. Moreover, both methods face difficulties of renormalisation and operator-mixing—see reviews [105, 110, 111]. However, impressive advances have been made for quasi- and pseudo-distribution calculations, which appear to be approaching phenomenological PDFs [145].

Since the present thesis is most concerned with the calculation of generalised parton distributions and polarised PDFs, we note that there have already been a number of numerical calculations of quasi-GPDs [146–149], and very recently of pseudo-GPDs as well [150]. For polarised PDFs, there have been a number of studies in both formalisms [151–154].

^{§§§}It has also been argued that the quasi-distribution approach suffers from a related inverse problem, since they approximate the continuous integral by a finite number of points [139].

3.2.3 Two current operators

Now we look at calculations of the matrix element of the product of currents, $j_\mu(z)j_\nu(0)$. These calculations include Compton amplitudes (time-ordered currents), as calculated in this thesis, or a hadronic tensor (single time-ordering). This type of calculation has two main advantages over the lattice OPE, quasi and pseudo approaches: (1) there are fewer difficulties with renormalisation and operator mixing, as the product of currents has a well-defined continuum limit^{****}; and (2) as this is a discretisation of the operator for physical particle scattering, we can access highly important non-leading-twist information that is otherwise inaccessible^{†††}.

Nucleon hadronic tensor

The calculation of the nucleon hadronic tensor, Eq. (2.23), using the direct evaluation of four-point functions has been an ongoing area of study for a number of years [94, 107, 109, 155–157]. The necessary four-point function is

$$\mathcal{G}_{4\text{-pt}}(\tau, t_1, t_2; \mathbf{p}, \mathbf{q}) = \sum_{\mathbf{z}, \mathbf{y}', \mathbf{y}} e^{-i\mathbf{p}\cdot\mathbf{z}} e^{-i\mathbf{q}\cdot(\mathbf{y}'-\mathbf{y})} \langle \Omega | \chi(\mathbf{z}, \tau) j_\mu(\mathbf{y}', t_2) j_\nu(\mathbf{y}, t_1) \chi^\dagger(0) | \Omega \rangle. \quad (3.50)$$

As discussed in Section 3.1, it is difficult to ensure ground state saturation at the source and sink for four-point functions. For the hadronic tensor, we do not need ground state saturation in the intermediate state, and as such the temporal separation between the two currents, $\Delta t = t_2 - t_1$, does not need to be extremely large.

Then, by taking a ratio of four- and two-point functions, $\mathcal{G}_{4\text{-pt}}/\mathcal{G}_{2\text{-pt}}$, one can isolate

$$W_{\mu\nu}(\Delta t) = \int d(\Delta t) e^{-q_0 \Delta t} W_{\mu\nu}^M, \quad (3.51)$$

where $W_{\mu\nu}^M$ is the Minkowski hadronic tensor, Eq. (2.23). As in the discussion of pseudo-distributions, solving the above equation for the Minkowski hadronic tensor constitutes an ill-conditioned inverse problem. Attempts have been made to solve this problem using similar approaches to work on pseudo-distributions [109]. However, due to difficulties associated with the calculation of four-point functions, as discussed in Section 3.1, these calculations have not gone beyond preliminary tests^{†††}.

Heavy-quark OPE

Another four-point function approach is the heavy-quark OPE (HOPE) method, in which intermediate propagator between y and y' is calculated with an unphysical heavy quark [95, 158, 159]. As discussed in Section 3.1, at heavier quark masses the inversion is much cheaper, making this calculation cheaper than a standard four-point function. Moreover, the heavy quark mass suppresses higher-twist corrections [158].

^{****}While in principle the continuum limit of our Compton amplitude has no operator mixing problems, at finite lattice spacings such problems may exist—see Chapter 8

^{†††}This second advantage does not apply to the heavy-quark OPE method.

^{††††}There are also calculations of four-point functions for low Q^2 , which appear to be successful for exploratory calculations [107, 108]. However, since these are low-energy, they do not investigate partonic information and we do not discuss them in this review.

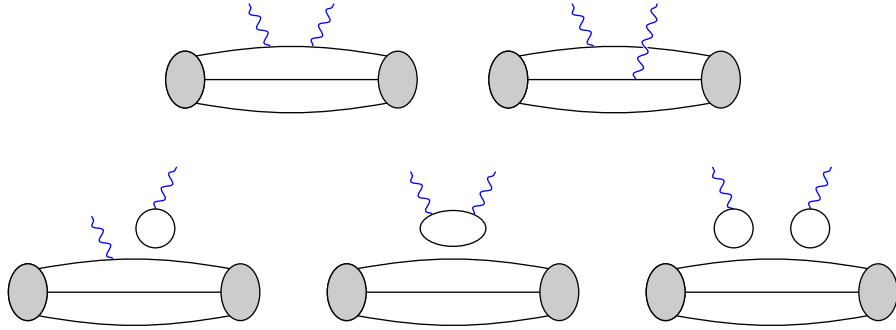


Figure 3.3: Lattice diagrams showing the type of contributions necessary for the calculation of the hadronic tensor. The blue photon line in the three-point function represents the insertion of a vector current.

While the calculation of the nucleon hadronic tensor from this method has been proposed [160], numerical efforts have focused on the pion distribution amplitude, which only requires a three-point function to calculate:

$$\begin{aligned} \mathcal{G}_{\text{HOPE}}(\tau, t_1, t_2; \mathbf{p}, \mathbf{q}) \\ = \sum_{\mathbf{z}, \mathbf{y}', \mathbf{y}} e^{-i\mathbf{q}\cdot(\mathbf{y}'-\mathbf{y})} e^{i\mathbf{p}\cdot\mathbf{z}} \langle \Omega | \psi(\mathbf{y}', t_2) \gamma_\mu \Psi(\mathbf{y}', t_2) \Psi(\mathbf{y}, t_1) \gamma_\nu \psi(\mathbf{y}, t_1) \chi^\dagger(\mathbf{z}, \tau) | \Omega \rangle. \end{aligned} \quad (3.52)$$

Note that here the interpolating operators are for pions, and $\Psi(z)$ is the heavy quark field. By focusing on the distribution amplitude, one avoids difficulties associated with the calculation of four-point functions; however, extending this work to the nucleon hadronic tensor would require the direct calculation of four-point functions [95]. Although solving for the associated Minkowski space distribution from Eq. (3.52) also constitutes an inverse problem, so far work in this area has focused on the extraction of moments [159].

In relation to the spin-dependent and off-forward amplitudes that we are interested in, there is so far no comparable work from other four-point function methods. As such, the work presented in this thesis is the first calculation of these amplitudes from a two-current approach.

3.2.4 Comparisons

Although the lattice parton methods presented here appear to be drastically different, they share a few common features that we now discuss. It is important to understand these generalities, as our own Feynman-Hellmann Compton amplitude method shares these features as well. Moreover, in zooming out and understanding the general structure of these methods, we can better compare their relative merits and disadvantages.

A unifying feature of quasi, pseudo and two-current approaches is the relation between a Euclidean (spacelike separated) distribution, $\mathcal{F}^E(\xi)$, and the desired Minkowski parton distribution/structure function, $\mathcal{F}^M(x)$:

$$\mathcal{F}^E(\xi) = \int dx K(x, \xi) \mathcal{F}^M(x), \quad (3.53)$$

where we have neglected higher-twist contributions. This difficulty traces its origin to the Wick rotation, Eq. (3.3), without which we would be able to directly calculate $\mathcal{F}^M(x)$.

All methods have some difficulty associated with ‘undoing’ this equation to obtain $\mathcal{F}^M(x)$. For the quasi-distribution approach, these difficulties are associated with controlling higher-twist terms, especially the $1/x$ and $1/(1-x)$ divergences. For the pseudo-distribution and two-current approaches, the difficulty lies mostly in the ill-conditioned inverse problem [109, 139, 159]—our Feynman-Hellmann Compton amplitude method suffers from the same problem [161].

To tame this inverse problem, there are primarily three approaches that are considered:

- Model-independent inversions using Backus-Gilbert, singular value decomposition, and machine learning [109, 139, 161, 162]. This sort of reconstruction is most desirable, since one reconstructs the original distribution with minimal assumptions. However, it requires extremely clean data, which may be difficult for lattice QCD calculations especially at high momentum.
- Using a model-dependent parameterisation [139, 161]. While a parameterisation gives us a great deal more traction over the inverse problem, it is typically less desirable as we are assuming more about the distribution we want to extract. We will explore such a fit in Chapter 6.
- Taylor expanding the kernel, $K(x, \xi)$, in ξ , which is equivalent to an OPE on the operator level. This sort of approach is the emphasis of the HOPE method [159] and is also used for pseudo-distributions [145]. We also use this for Chapters 5–7, and was used in our previous calculations [37, 38]. Although this does not give a complete reconstruction of the desired Minkowski space amplitude, the determination of moments is far more numerically stable, and the moments themselves contain interesting physical information. Moreover, it is usually easier to access higher moments this way than through the lattice OPE method.

Finally, we note a key difference between approaches that use a discretisation of physical currents (such as ours and the hadronic tensor method), and approaches that calculate an unphysical operator (such as the HOPE, quasi-distribution and pseudo-distribution methods).

For the discretisation of a physical operator, our higher-twist corrections are physical up to discretisation artefacts, and therefore represent useful and interesting information. As such, it is desirable to extract the Minkowski distribution *with its* Λ^2/Q^2 *corrections*:

$$\mathcal{F}^E(\xi, \Lambda^2/Q^2) = \int dx K(x, \xi) \mathcal{F}^M(x, \Lambda^2/Q^2). \quad (3.54)$$

By contrast, for methods that calculate an unphysical operator, we have instead

$$\mathcal{F}^E(\xi, \Lambda/\mu) = \int dx K(x, \xi, \Lambda/\mu) \mathcal{F}^M(x) + \mathcal{O}\left(\frac{\Lambda}{\mu}\right). \quad (3.55)$$

The Λ/μ corrections are simply a systematic error and must be controlled by a mixture of perturbative calculation of the kernel K and extrapolation to $\mu \rightarrow \infty$.

Lattice Feynman-Hellmann

In lattice field theory, Feynman-Hellmann* (FH) is a powerful method that offers an alternative to the direct evaluation of n -point functions. In this method, a background field with some weak coupling, λ , is added to the regular Lagrangian. Two-point functions computed in the presence of this background field can then be related to three- and four-point (and in principle n -point) functions. In analogy to the original Feynman-Hellmann theorem [163, 164],

$$\frac{\partial E_\lambda}{\partial \lambda} = \langle n | \frac{\partial H_\lambda}{\partial \lambda} | n \rangle, \quad (4.1)$$

where E_λ is the perturbed energy and H_λ is the perturbed Hamiltonian, lattice Feynman-Hellmann methods relate the perturbed two-point function to the desired n -point function by a derivative with respect to the perturbing parameter, λ .

In the case of three-point functions, Feynman-Hellmann has been applied with success to a wide range of matrix elements, including sigma terms [165–168], electromagnetic form factors, [169], the axial and tensor charges [170–174], and the energy-momentum tensor [175], among others. It has been argued that Feynman-Hellmann evaluation of three-point functions may increase control of excited-state contamination compared to a direct evaluation [173]. Moreover, certain properties such as large current momentum are easier to access with FH [169].

For the present thesis, we are interested in applying Feynman-Hellmann to calculate four-point functions, particularly Compton amplitudes. For the case of four-point functions, Feynman-Hellmann is vastly more computationally efficient than the direct evaluation. In fact, a comparable evaluation of the Compton amplitude through the direct evaluation of four-point functions is so computationally expensive that it has never been implemented[†].

The evaluation of four-point functions using Feynman Hellmann is an active area of research, led by the CSSM/QCDSF collaboration. This was first applied to the simplest case: the unpolarised forward Compton structure functions [36–38, 161, 176]. The leading Mellin moments determined from these calculations show good agreement with both phenomenology and other lattice studies. The aim of the present work is to extend this method to other more involved cases, such as the off-forward Compton amplitude [39] (Chapters 5 and 6), the polarised forward Compton amplitude (Chapter 7), and the subtraction function [40] (Chapter 8). In all these cases, unlike the unpolarised forward case,

*Similar to, if not indistinguishable from, background field methods.

[†]The hadronic tensor method is the closest to a direct four-point function evaluation of the Compton amplitude. Nonetheless, this method still calculates quite a different quantity to our Compton amplitude.

we use two different currents. As such, the Feynman-Hellmann relations for this chapter are for the second-order in λ , mixed current case.

Furthermore, apropos the arguments in Chapter 3, we note that what we can calculate on the lattice is the Euclidean Compton amplitude. In this chapter, we will discuss under what conditions we can relate this to the Minkowski Compton amplitude. In principle, we can reconstruct the Minkowski from the Euclidean; however, due to the well-known inverse problem, a complete reconstruction is made difficult by the numerically unstable solutions [161].

The outline of this chapter is as follows: in Section 4.1, we will derive our chosen Feynman-Hellmann identities using a Dyson series. In Section 4.2, we first explain the implementation of Feynman-Hellmann in lattice QCD. Then, we discuss the interpretation of the Euclidean Compton amplitude, its relation to the Minkowski Compton amplitude, and the associated inverse problem.

Motivation

A straightforward discretisation of the Compton amplitude (Eq. (2.19)) is

$$T_{\mu\nu} = \sum_{z, z'} e^{iq \cdot (z - z')} \langle N | \mathcal{T} \{ j_\mu(z) j_\nu(z') \} | N \rangle, \quad (4.2)$$

where we drop the factor of i due to the Wick rotation to Euclidean space. To evaluate this matrix element directly would require the calculation of a four-point function,

$$\langle \Omega | \chi(\tau, \mathbf{z}) j_\mu(t_2, \mathbf{y}_2) j_\nu(t_1, \mathbf{y}_1) \chi^\dagger(0) | \Omega \rangle, \quad (4.3)$$

which, as discussed in Section 3.1, demands very careful treatment of excited states to ensure ground-state saturation at the source and sink. Moreover, note that Eq. (4.2) requires a sum over time-slices on which the currents are inserted. Hence we would need to calculate the four-point function for each pair of time-slices, t_1 and t_2 , in our integration region, increasing the computational costs by a factor of $\mathcal{O}(N_T^2)$, for N_T the number of time-slices. This sort of calculation is so costly that it has never been performed.

Instead, four-point functions are typically calculated at a *fixed* time separation [94, 95], as discussed in the previous chapter. This approach still suffers from the difficulties associated with isolating the ground state in four-point functions[‡]. Moreover, without the sum over time-slices one is left with

$$\begin{aligned} & \sum_{\mathbf{z}} e^{i\mathbf{q} \cdot \mathbf{z}} \langle N | j_\mu(\mathbf{z}, t_2) j_\nu(0, t_1) | N \rangle \\ &= \sum_X \frac{e^{-(E_X - E_N - q_0)(t_2 - t_1)}}{2E_X} \langle N | j_\mu(0) | X \rangle \langle X | j_\nu(0) | N \rangle \delta_{p_X, p+q}. \end{aligned} \quad (4.4)$$

And therefore, even if one can ensure ground state saturation, a variation in $t_2 - t_1$ is still necessary to extract partonic information [159]. Therefore, multiple four-point functions must be calculated and further analysis performed to determine the amplitude.

[‡]As discussed previously, there are also calculations of the low-energy hadronic tensor from four-point functions, for which excited states are easier to control [107, 108]. However, the hadronic information that these studies aim to determine is quite different to our own.

Feynman-Hellmann

By contrast, using Feynman-Hellmann methods we can calculate the discretised Compton amplitude, Eq. (4.2), with its sum over time-slices, using only a two-point function. This is remarkably useful, since the excited state contributions of two-point functions are typically much easier to handle than three- and four-point functions [106], and moreover it gives us the desired Compton amplitude, Eq. (4.2), without any further need to vary time-slices.

To give an idea of how this is possible, we consider a simple example of the forward spin-independent Compton amplitude for a structureless fermion. We start with the perturbed fermion propagator:

$$S_\lambda(z_n, z_m) = [M - \lambda \mathcal{O}_q]_{nm}^{-1}, \quad (4.5)$$

where M is the fermion matrix, Eq. (3.18), λ a small coupling and \mathcal{O}_q the perturbing matrix.

Then, by a matrix geometric series[§], we can expand Eq. (4.5) about $\lambda = 0$:

$$S_\lambda = \underbrace{S}_{\text{unperturbed}} + \lambda \underbrace{S \mathcal{O}_q S}_{\text{three-point}} + \lambda^2 \underbrace{S \mathcal{O}_q S \mathcal{O}_q S}_{\text{four-point}} + \mathcal{O}(\lambda^3), \quad (4.6)$$

where $S = M^{-1}$ is the unperturbed propagator.

The four-point function of Eq. (4.6) can then be related to the second derivative of the propagator with respect to λ . If we choose diagonal perturbing matrices of the form

$$\mathcal{O}_q(n, m) = 2\delta_{n,m} \cos(\mathbf{q} \cdot \mathbf{z}_n) \gamma_3,$$

then we have that this derivative is

$$\left. \frac{\partial^2 S_\lambda(z, 0)}{\partial \lambda^2} \right|_{\lambda=0} = 8 \sum_{y_1, y_2} \cos(\mathbf{q} \cdot \mathbf{y}_1) \cos(\mathbf{q} \cdot \mathbf{y}_2) S(z, y_2) \gamma_3 S(y_2, y_1) \gamma_3 S(y_1, 0), \quad (4.7)$$

which can be expressed in terms of operators as

$$\left. \frac{\partial^2 S_\lambda(z, 0)}{\partial \lambda^2} \right|_{\lambda=0} = 8 \sum_{\substack{\mathbf{y}_1, \mathbf{y}_2 \\ t_1, t_2}} \cos(\mathbf{q} \cdot \mathbf{y}_1) \cos(\mathbf{q} \cdot \mathbf{y}_2) \langle \Omega | \psi(\tau, \mathbf{z}) j_3(t_2, \mathbf{y}_2) j_3(t_1, \mathbf{y}_1) \bar{\psi}(0) | \Omega \rangle, \quad (4.8)$$

which is a four-point function with a sum over all the spatial coordinates, $\mathbf{y}_{1,2}$, as well as the temporal coordinates, $t_{1,2}$.

In this simple example we can see the two main advantages of second-order Feynman-Hellmann: (1) we only need to determine two-point functions, meaning we do not face any of the aforementioned difficulties associated with direct four-point calculations, and (2) the four-point functions we determine have a sum over the time-slices on which the currents are inserted. The sum over time slices means that we can directly access a discretisation of the amplitude, as in Eq. (4.2), without needing further calculations to vary the time separation between the two currents.

[§]One can show that, for two $n \times n$ matrices A and B , we have $(A - B)^{-1} = A^{-1} \sum_{k=0}^{\infty} (BA^{-1})^k$ so long as each of the eigenvalues of $A^{-1}B$ are less than one [177].

This gives us the remarkable property of being able to determine the Compton amplitude from a two-point function—a great advantage in computational cost and control of excited states.

4.1 Feynman-Hellmann Derivation

In this section, we derive Feynman-Hellmann relations that allow us to relate derivatives of our perturbed two-point functions to four-point functions. These relations have the form

$$\left. \frac{\partial^2}{\partial \lambda_1 \partial \lambda_2} \frac{\mathcal{G}_\lambda(\tau)}{\mathcal{G}_0(\tau)} \right|_{\lambda=0} \simeq \frac{\tau}{2E_N} T, \quad (4.9)$$

where T is a Compton amplitude, which we will show is attached to a linear in τ contribution. This derivation is in continuum spacetime—the lattice implementation is discussed in Section 4.2, and in Chapter 8 we explore discretisation artefacts arising in the lattice Feynman-Hellmann method.

Previous Feynman-Hellmann proofs [37, 178] have used the following steps:

1. Describe the perturbation to the lattice action: $S_\lambda = S_{\text{QCD}} + \lambda V$.
2. Take the derivative of the perturbed correlator as expressed in terms of the path integral

$$\mathcal{G}_\lambda = \langle \mathcal{O} \rangle = \frac{\int \mathcal{D}\phi \mathcal{O} e^{-S_\lambda}}{\int \mathcal{D}\phi e^{-S_\lambda}},$$

with respect to λ . Recall the notation of Eq. (3.7).

3. Take the derivative of the same correlator expressed as

$$\mathcal{G}_\lambda(\tau) = A_\lambda e^{-E_\lambda \tau}.$$

This is the form of Eq. (3.32), except with perturbed energies and overlaps.

4. Equate the two derivatives to derive an equation of the form

$$\left. \frac{\partial^2 E_\lambda}{\partial \lambda^2} \right|_{\lambda=0} \propto T.$$

However, in the second step we need to show that there is a well-defined perturbed energy, E_λ . In the case of off-forward first order [169] and second-order FH [56], where there are degeneracies in the spectrum of unperturbed energies, this means that there are two corresponding low-lying perturbed energies. It is then necessary to show that the correct low-lying perturbed energy is being extracted, a task that is often quite difficult [56]. By contrast, the Dyson series approach is simply a perturbative expansion of the perturbed correlator, which does not require us to assume anything about the perturbed energy spectrum. As such, we apply the Dyson series expansion for our Feynman-Hellmann proof here.

4.1.1 Mixed currents: the general case

The Feynman-Hellmann relations we will use in the present thesis all have mixed-currents; that is, in the two-current operator such as Eq. (2.19), the two currents will differ by momentum transfer, Lorentz index or another property. The general form of such an operator is given below:

$$\langle \text{out} | \mathcal{J}_1 \mathcal{J}_2 | \text{in} \rangle.$$

As such, here we give a derivation of a general Feynman-Hellmann relation for these mixed-current operators.

To begin, note that for mixed-current operators we need to add two perturbing background fields to the QCD Lagrangian:

$$\mathcal{L}_{\text{FH}}(z) = \mathcal{L}_{\text{QCD}}(z) + \lambda_1 \mathcal{O}_1(z) + \lambda_2 \mathcal{O}_2(z), \quad (4.10)$$

where $\lambda_{1,2}$ are our FH couplings and $\mathcal{O}_{1,2}$ are our background field operators.

As long as $\mathcal{O}_{1,2}$ contain no derivatives of particle fields, the Legendre transformation to the Hamiltonian density is simply

$$\mathcal{H}_{\text{FH}}(z) = \mathcal{H}_{\text{QCD}}(z) - \lambda_1 \mathcal{O}_1(z) - \lambda_2 \mathcal{O}_2(z).$$

And hence the perturbed Hamiltonian is

$$H_{\text{FH}} = H_{\text{QCD}} - \lambda_1 V_1 - \lambda_2 V_2, \quad (4.11)$$

where

$$V_{1,2} \equiv \int d^3z \mathcal{O}_{1,2}(\mathbf{z}).$$

In general,

$$\mathcal{O}_{1,2}(\mathbf{z}) = (e^{i\mathbf{q}_{1,2} \cdot \mathbf{z}} \pm e^{-i\mathbf{q}_{1,2} \cdot \mathbf{z}}) J(\mathbf{z}), \quad (4.12)$$

for some time-independent current $J(\mathbf{z})$.

We can see from Eq. (4.12) that our background fields will transfer some momenta $\mathbf{q}_{1,2}$. For forward scattering, we want $\mathbf{q}_1 = \mathbf{q}_2$, while for off-forward $\mathbf{q}_1 \neq \mathbf{q}_2$. Between two states $|X(\mathbf{p}_X)\rangle$ and $|Y(\mathbf{p}_Y)\rangle$, where the momentum \mathbf{p}_Y is not fixed, we can see that the background fields transfer momentum in the following way:

$$\begin{aligned} \langle X(\mathbf{p}_X) | V_n | Y(\mathbf{p}_Y) \rangle &= \int d^3z (e^{i\mathbf{q} \cdot \mathbf{z}} \pm e^{-i\mathbf{q} \cdot \mathbf{z}}) e^{i(\mathbf{p}_Y - \mathbf{p}_X) \cdot \mathbf{z}} \langle X(\mathbf{p}_X) | J(0) | Y(\mathbf{p}_Y) \rangle \\ &= \langle X(\mathbf{p}_X) | J(0) | Y(\mathbf{p}_Y) \rangle (2\pi)^3 (\delta^{(3)}(\mathbf{p}_X - \mathbf{q} - \mathbf{p}_Y) \pm \delta^{(3)}(\mathbf{p}_X + \mathbf{q} - \mathbf{p}_Y)). \end{aligned} \quad (4.13)$$

Therefore, our choice of momentum transfer in the background field is what determines the energy $E_Y(\mathbf{p}_Y)$. As we will see, this is an extremely important point in determining the Euclidean time dependence of the perturbed two-point function, and we will need to be careful in how we choose the momenta transferred by our background fields.

This perturbed Hamiltonian is the starting point of our Dyson transfer proof, as we can use it to expand the *perturbed* time evolution operator, $e^{-H_{\text{FH}}\tau}$, with a Dyson series^{**}:

$$e^{-H_{\text{FH}}\tau} = e^{-H_{\text{QCD}}\tau} \left[1 + \sum_{n=1}^2 \lambda_n \int_0^\tau d\tau' e^{H_{\text{QCD}}\tau'} V_n e^{-H_{\text{QCD}}\tau'} + \sum_{n,m=1}^2 \lambda_n \lambda_m \int_0^\tau d\tau' \int_0^{\tau'} d\tau'' e^{H_{\text{QCD}}\tau'} V_n e^{-H_{\text{QCD}}(\tau'-\tau'')} V_m e^{-H_{\text{QCD}}\tau''} \right] + \mathcal{O}(\lambda^3), \quad (4.14)$$

where we note that $V(\tau) = e^{H_{\text{QCD}}\tau} V e^{-H_{\text{QCD}}\tau}$, and so our currents pick up time dependence.

By using the perturbed Lagrangian in Eq. (4.10), we calculate perturbed nucleon two-point functions (correlators):

$$\mathcal{G}_\lambda(\tau, \mathbf{p}') = \Gamma_{\beta\alpha} \int d^3z e^{-i\mathbf{p}'\cdot\mathbf{z}} {}_\lambda\langle\Omega|\chi_\alpha(\mathbf{z}, \tau)\chi_\beta^\dagger(0)|\Omega\rangle_\lambda, \quad (4.15)$$

where $\lambda = (\lambda_1, \lambda_2)$, and Γ is the spin-parity projector. Note that the perturbed vacuum, $|\Omega\rangle_\lambda$, is simply the eigenstate of the perturbed Hamiltonian, H_{FH} , with eigenvalue zero.

Therefore, expressed in terms of the momentum eigenstates, the perturbed vacuum is

$$|\Omega\rangle_\lambda = c_1|\Omega\rangle + \mathcal{O}(\lambda), \quad (4.16)$$

where c_1 is $\mathcal{O}(1)$ and all other terms are $\mathcal{O}(\lambda)$.

Recall the Euclidean translational invariance, Eq. (3.30), which gives us $\chi(\mathbf{z}, \tau) = e^{H_{\text{FH}}\tau - i\hat{\mathbf{P}}\cdot\mathbf{z}} \chi(0) e^{-H_{\text{FH}}\tau + i\hat{\mathbf{P}}\cdot\mathbf{z}}$, for the perturbed Hamiltonian. And then recall the identity in the space of momentum eigenstates, Eq. (A.3):

$$\mathbb{I} = \sum_{X,s} \int \frac{d^3p}{(2\pi)^3} \frac{1}{2E_X(\mathbf{p})} |X(\mathbf{p}, s)\rangle \langle X(\mathbf{p}, s)|.$$

Hence we can insert two identities into Eq. (4.15) and take the spacetime-dependence out of the interpolating operators. After evaluating the integral over spatial coordinate, \mathbf{z} , to get a delta function, and then performing the integral over \mathbf{p}' , we get

$$\mathcal{G}_\lambda(\tau, \mathbf{p}') = \Gamma_{\beta\alpha} \frac{1}{4} \sum_{s,s'} \sum_{X,Y} \int \frac{d^3p}{(2\pi)^3} {}_\lambda\langle\Omega|\chi(0)|X(\mathbf{p}', s')\rangle \langle X(\mathbf{p}', s')| e^{-H_{\text{FH}}\tau} |Y(\mathbf{p}, s)\rangle \langle Y(\mathbf{p}, s)|\chi^\dagger(0)|\Omega\rangle_\lambda. \quad (4.17)$$

Note that states and energies without a λ subscript are unperturbed. For the sake of brevity, we will suppress spin-dependence from here on, and introduce it in the final expressions.

^{**}This relation can be proven by applying the identity $e^{-(A+B)\tau} = e^{-A\tau} + e^{-A\tau} \int_0^\tau e^{A\tau'} B e^{-(A+B)\tau'} d\tau'$ iteratively and taking the matrix elements of B to be small.

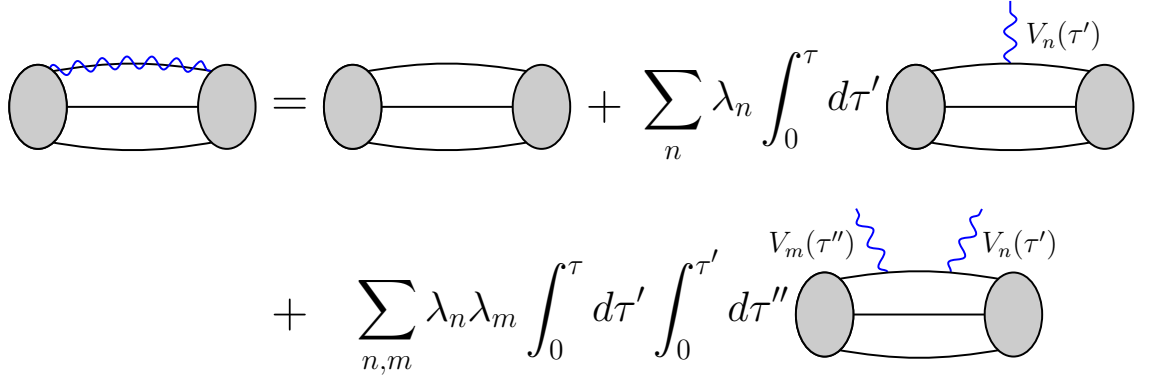


Figure 4.1: Lattice diagram of the expansion of the perturbed correlator, Eq. (4.18). The propagator with a photon line overlaid on the quark line represents the perturbed propagator, where the perturbation is applied to the singly represented quark.

By inserting Eq. (4.14) into Eq. (4.17), we get

$$\begin{aligned}
\mathcal{G}_\lambda(\tau, \mathbf{p}') &= \sum_{X,Y} \int \frac{d^3 p}{(2\pi)^3} \frac{1}{4E_X(\mathbf{p}')E_Y(\mathbf{p})} \lambda \langle \Omega | \chi(0) | X(\mathbf{p}') \rangle \langle Y(\mathbf{p}) | \chi^\dagger(0) | \Omega \rangle_\lambda \\
&\times \langle X(\mathbf{p}') | e^{-H_{\text{QCD}}\tau} \left[1 + \sum_{n=1}^2 \lambda_n \int_0^\tau d\tau' e^{H_{\text{QCD}}\tau'} V_n e^{-H_{\text{QCD}}\tau'} \right. \\
&+ \left. \sum_{n,m=1}^2 \lambda_n \lambda_m \int_0^\tau d\tau' \int_0^{\tau'} d\tau'' e^{H_{\text{QCD}}\tau'} V_n e^{H_{\text{QCD}}(\tau''-\tau')} V_m e^{-H_{\text{QCD}}\tau''} + \mathcal{O}(\lambda^3) \right] | Y(\mathbf{p}) \rangle.
\end{aligned} \tag{4.18}$$

This equation is represented visually in Fig. 4.1.

Taking a step back for a moment, we note that we are interested in the $\lambda_1 \lambda_2$ term, as this gives us the mixed-current operator. The $(\lambda_1)^2$ and $(\lambda_2)^2$ contributions will give us terms for which both currents are the same, such as in the $\mu = \nu$ term of the forward Compton amplitude.

It is convenient to define the perturbed overlap:

$$\begin{aligned}
\mathcal{Z}_\lambda^X(\mathbf{p}) &\equiv \lambda \langle \Omega | \chi(0) | X(\mathbf{p}) \rangle \\
&= \mathcal{Z}^X(\mathbf{p}) + \lambda_1 \mathcal{Z}_{1,0}^X(\mathbf{p}) + \lambda_2 \mathcal{Z}_{0,1}^X(\mathbf{p}) + \mathcal{O}(\lambda^2).
\end{aligned} \tag{4.19}$$

Evaluating Dyson series terms

We now want to evaluate the matrix elements of each of the terms in the Dyson expansion, Eq. (4.15), for each order of λ in the perturbed time-evolution operator. In particular, we want to show that the $\lambda_1 \lambda_2$ term is proportional to the mixed-current Compton amplitude, and moreover that this term is enhanced by a linear factor of the Euclidean sink time, τ . We refer to terms that are linear in τ as ‘ τ -enhanced’. On the other hand, we want to show that all terms that are not the Compton amplitude are either constant or exponentially suppressed in τ .

For simplicity of notation, we decompose the perturbed nucleon correlator as

$$\mathcal{G}_\lambda = \mathcal{G}^{(0)} + \mathcal{G}^{(1)} + \mathcal{G}^{(2)} + \mathcal{O}(\lambda^3), \quad (4.20)$$

where $\mathcal{G}^{(n)}$ is the contribution with n insertions of the current, which corresponds to the $\mathcal{O}(\lambda^n)$ term in the Dyson series.

Note that, just like the unperturbed two-point function and three- and four-point functions, we ensure ground state saturation at the source with

$$\sum_X \langle X(\mathbf{p}') | e^{-H_{\text{QCD}}\tau} \stackrel{\tau \gg a}{\simeq} \langle N(\mathbf{p}') | e^{-E_N\tau}.$$

However, we have summed over the current insertion times. Therefore, ground state saturation at the source needs to be ensured with kinematic choices that we outline below.

No insertion

We start with the $\mathcal{O}(\lambda^0)$ term of the Dyson series, which has no insertion of the current. Using the state normalisation, Eq. (A.4), this is

$$\mathcal{G}^{(0)} = \sum_X e^{-E_X(\mathbf{p}')\tau} \frac{|\mathcal{Z}_\lambda^X(\mathbf{p}')|^2}{2E_X(\mathbf{p}')} \stackrel{\tau \gg a}{\simeq} e^{-E_N(\mathbf{p}')\tau} \frac{|\mathcal{Z}_\lambda^N(\mathbf{p}')|^2}{2E_N(\mathbf{p}')}. \quad (4.21)$$

Once we divide out by our unperturbed correlator for the same momentum, Eq. (3.32), this term will be constant in τ .

Even though this term has no insertions (i.e. it is $\mathcal{O}(\lambda^0)$ in the Dyson series), due to the factors of \mathcal{Z}_λ^N it contains all orders of λ :

$$\mathcal{Z}_\lambda^N (\mathcal{Z}_\lambda^N)^* = (\mathcal{Z}^N + \lambda_1 \mathcal{Z}_{1,0}^N + \lambda_2 \mathcal{Z}_{0,1}^N + \dots) (\mathcal{Z}^N + \lambda_1 \mathcal{Z}_{1,0}^N + \lambda_2 \mathcal{Z}_{0,1}^N + \dots)^*. \quad (4.22)$$

Therefore, even when we isolate the $\lambda_1 \lambda_2$ term, there is a residual contribution from $\mathcal{G}^{(0)}$.

Single insertion

Next, we look at the $\mathcal{O}(\lambda)$ term of the Dyson series, which has a single insertion of the current.

Now, our choice of our background fields, $V_{1,2}$, determines what momenta \mathbf{p} the source may have. As long as we choose $V_{1,2}$ such that $E_Y(\mathbf{p}) \neq E_N(\mathbf{p}')$ for all Y , the $\mathcal{O}(\lambda)$ term from the Dyson series is

$$\begin{aligned} \mathcal{G}^{(1)} &= \sum_{X,Y} \int \frac{d^3p}{(2\pi)^3} \frac{\mathcal{Z}_\lambda^X(\mathbf{p}') (\mathcal{Z}_\lambda^Y(\mathbf{p}))^*}{4E_X(\mathbf{p}') E_Y(\mathbf{p})} \\ &\times \sum_{n=1}^2 \lambda_n e^{-E_X(\mathbf{p}')\tau} \frac{1 - e^{-(E_Y(\mathbf{p}) - E_X(\mathbf{p}'))\tau}}{E_Y - E_X} \langle X(\mathbf{p}') | V_n | Y(\mathbf{p}) \rangle. \end{aligned} \quad (4.23)$$

Now, we can take the large Euclidean time limit $\sum_X e^{-E_X \tau} \stackrel{\tau \gg a}{\simeq} e^{-E_N \tau}$. Moreover, we will apply Eq. (4.13) to Eq. (4.23) to get

$$\begin{aligned} \mathcal{G}^{(1)} \stackrel{\tau \gg a}{\simeq} e^{-E_N(\mathbf{p}')\tau} \sum_{n=1}^2 \lambda_n \sum_Y \frac{\mathcal{Z}_\lambda^N(\mathbf{p}')(\mathcal{Z}_\lambda^Y(\mathbf{p}' + \mathbf{q}_n))^*}{4E_N(\mathbf{p}')E_Y(\mathbf{p}' + \mathbf{q}_n)} \\ \times \frac{1 - e^{-(E_Y(\mathbf{p}' + \mathbf{q}_n) - E_N(\mathbf{p}'))\tau}}{E_Y(\mathbf{p}' + \mathbf{q}_n) - E_N(\mathbf{p}')} \langle N(\mathbf{p}') | J_n(0) | Y(\mathbf{p}' + \mathbf{q}_n) \rangle \pm (\mathbf{q}_n \rightarrow -\mathbf{q}_n). \end{aligned} \quad (4.24)$$

Again, once we divide out by the unperturbed correlator, this will have τ dependence dominated by $1 - e^{-(E_Y(\mathbf{p}' \pm \mathbf{q}_n) - E_N(\mathbf{p}'))\tau}$. Therefore, we must choose our background fields such that $E_Y(\mathbf{p}' \pm \mathbf{q}_n) > E_N(\mathbf{p}')$ for all Y . Even near-degeneracies here can make fitting difficult, a fact we will discuss further in Chapter 6. On the other hand, if we had chosen $V_{1,2}$ such that $E_Y(\mathbf{p}' \pm \mathbf{q}_n) = E_N(\mathbf{p}')$ for some Y , it is straightforward to see that Eq. (4.24) would have contributions linear in Euclidean time dependence.

Since the nucleon is the ground state of the spectrum, to ensure that $E_Y(\mathbf{p}' \pm \mathbf{q}_n) > E_N(\mathbf{p}')$, it is sufficient to keep the following condition:

$$|\mathbf{p}' \pm \mathbf{q}_n| > |\mathbf{p}'|, \quad \text{for both momenta } \mathbf{q}_{1,2}. \quad (4.25)$$

As in the zeroth order case, although Eq. (4.23) only has one insertion, it may contain higher orders of λ due the factors of \mathcal{Z}_λ^N . For example,

$$\lambda_1 \mathcal{Z}_\lambda^N (\mathcal{Z}_\lambda^N)^* = \lambda_1 (\mathcal{Z}^N + \lambda_1 \mathcal{Z}_{1,0}^N + \lambda_2 \mathcal{Z}_{0,1}^N + \dots) (\mathcal{Z}^N + \lambda_1 \mathcal{Z}_{1,0}^N + \lambda_2 \mathcal{Z}_{0,1}^N + \dots)^*, \quad (4.26)$$

meaning that the $\mathcal{G}^{(1)}$ expression contains all powers of λ beyond $\mathcal{O}(\lambda)$. Therefore, it also contributes to the $\lambda_1 \lambda_2$ term.

Double insertion

And finally, the term we are interested in is that with two insertions of the current:

$$\begin{aligned} \mathcal{G}^{(2)} = \sum_{X,Y} \int \frac{d^3 p}{(2\pi)^3} \frac{\mathcal{Z}_\lambda^X(\mathbf{p}')(\mathcal{Z}_\lambda^Y(\mathbf{p}))^*}{4E_X(\mathbf{p}')E_Y(\mathbf{p})} e^{-E_X(\mathbf{p}')\tau} \\ \times \sum_{n,m=1}^2 \lambda_n \lambda_m \langle X(\mathbf{p}') | \int_0^\tau d\tau' \int_0^{\tau'} d\tau'' e^{H_{\text{QCD}}\tau'} V_n e^{H_{\text{QCD}}(\tau'' - \tau')} V_m e^{-H_{\text{QCD}}\tau''} | Y(\mathbf{p}) \rangle. \end{aligned} \quad (4.27)$$

After inserting a complete set of states and taking large Euclidean time, Eq. (4.27) becomes

$$\begin{aligned} \mathcal{G}^{(2)} \stackrel{\tau \gg a}{\simeq} \sum_Y \int \frac{d^3 p}{(2\pi)^3} \frac{\mathcal{Z}_\lambda^X(\mathbf{p}')(\mathcal{Z}_\lambda^Y(\mathbf{p}))^*}{4E_N(\mathbf{p}')E_Y(\mathbf{p})} e^{-E_N(\mathbf{p}')\tau} \\ \times \sum_{n,m=1}^2 \lambda_n \lambda_m \int_0^\tau d\tau' \int_0^{\tau'} d\tau'' e^{-(E_Z(\mathbf{p}_Z) - E_N(\mathbf{p}'))\tau' + (E_Z(\mathbf{p}_Z) - E_Y(\mathbf{p}))\tau''} \\ \times \sum_Z \int \frac{d^3 p_Z}{(2\pi)^3} \frac{1}{2E_Z(\mathbf{p}_Z)} \langle N(\mathbf{p}') | V_n | Z(\mathbf{p}_Z) \rangle \langle Z(\mathbf{p}_Z) | V_m | Y(\mathbf{p}) \rangle. \end{aligned} \quad (4.28)$$

Focusing solely on the Euclidean time-dependence for a moment, we see that, if we choose our background fields, $V_{1,2}$, such that $E_Y(\mathbf{p}) = E_N(\mathbf{p}')$, then

$$\begin{aligned} & \int_0^\tau d\tau' \int_0^{\tau'} d\tau'' e^{-(E_Z(\mathbf{p}_Z) - E_N(\mathbf{p}'))\tau'} e^{(E_Z(\mathbf{p}_Z) - E_Y(\mathbf{p}))\tau''} \\ &= \frac{1}{E_Z(\mathbf{p}_Z) - E_N(\mathbf{p}')} \left(\tau + \frac{e^{-(E_Z(\mathbf{p}_Z) - E_N(\mathbf{p}'))\tau} - 1}{E_Z(\mathbf{p}_Z) - E_N(\mathbf{p}')} \right). \end{aligned} \quad (4.29)$$

And if $E_Y(\mathbf{p}) \neq E_N(\mathbf{p}')$,

$$\begin{aligned} & \int_0^\tau d\tau' \int_0^{\tau'} d\tau'' e^{-(E_Z(\mathbf{p}_Z) - E_N(\mathbf{p}'))\tau'} e^{(E_Z(\mathbf{p}_Z) - E_Y(\mathbf{p}))\tau''} \\ &= \frac{1}{E_Z(\mathbf{p}_Z) - E_Y(\mathbf{p})} \left(\frac{e^{-(E_Z(\mathbf{p}_Z) - E_N(\mathbf{p}'))\tau} - 1}{E_Z(\mathbf{p}_Z) - E_N(\mathbf{p}')} - \frac{e^{-(E_Y(\mathbf{p}) - E_N(\mathbf{p}'))\tau} - 1}{E_Y(\mathbf{p}) - E_N(\mathbf{p}')} \right). \end{aligned} \quad (4.30)$$

Therefore, the perturbed correlator is the sum of Eqs. (4.21), (4.24), (4.28), as given in the decomposition, Eq. (4.20).

4.1.2 Off-forward momentum

Now we can get more specific with the type of Compton amplitude we want to calculate. We start with the off-forward Compton amplitude (OFCA), defined in Eq. (2.72):

$$T_{\mu\nu} = i \int d^4z e^{\frac{i}{2}(q+q')\cdot z} \langle P' | \mathcal{T} \{ j_\mu(z) j_\nu(0) \} | P \rangle.$$

In contrast to the forward Compton amplitude we discussed in Section 2.2.2, there is a net momentum transfer between the initial and final states—see Chapter 5.

To calculate this Compton amplitude, we choose the two background fields

$$\mathcal{O}_1(\mathbf{z}) = (e^{i\mathbf{q}_1 \cdot \mathbf{z}} + e^{-i\mathbf{q}_1 \cdot \mathbf{z}}) j_k(\mathbf{z}), \quad \mathcal{O}_2(\mathbf{z}) = (e^{i\mathbf{q}_2 \cdot \mathbf{z}} + e^{-i\mathbf{q}_2 \cdot \mathbf{z}}) j_k(\mathbf{z}), \quad (4.31)$$

where $\mathbf{q}_1 \neq \mathbf{q}_2$ and $j_\mu(z) = \bar{\psi}(z) \gamma_\mu \psi(z)$ is the vector current. Importantly, we will choose our two inserted momenta, $\mathbf{q}_{1,2}$, such that

$$|\mathbf{p}'| = |\mathbf{p}' + \mathbf{q}_1 - \mathbf{q}_2|, \quad (4.32)$$

for our sink momentum \mathbf{p}' . In terms of the off-forward kinematics we introduced in Section 2.2.4, the soft-momentum transfer is $\Delta = \mathbf{q}_1 - \mathbf{q}_2$. Hence the condition in Eq. (4.32) keeps us in a frame where the incoming/outgoing energy are equal. This equal energy condition is key to extracting our τ -enhanced contribution and the OFCA.

Therefore, for these background fields using Eq. (4.13), the four-point function of Eq. (4.28) becomes

$$\begin{aligned} & \langle N(\mathbf{p}') | V_n | Z(\mathbf{p}_Z) \rangle \langle Z(\mathbf{p}_Z) | V_m | Y(\mathbf{p}) \rangle \\ &= \langle N(\mathbf{p}') | j_k(0) | Z(\mathbf{p}_Z) \rangle \langle Z(\mathbf{p}_Z) | j_k(0) | Y(\mathbf{p}) \rangle \Delta_{nm}, \end{aligned} \quad (4.33)$$

where

$$\begin{aligned} \Delta_{ij} \equiv & (2\pi)^6 \left[\delta^{(3)}(\mathbf{p}' - \mathbf{q}_i - \mathbf{p}_Z) + \delta^{(3)}(\mathbf{p}' + \mathbf{q}_i - \mathbf{p}_Z) \right] \\ & \times \left[\delta^{(3)}(\mathbf{p} - \mathbf{q}_n - \mathbf{p}_Z) + \delta^{(3)}(\mathbf{p} + \mathbf{q}_n - \mathbf{p}_Z) \right]. \end{aligned} \quad (4.34)$$

These delta functions ensure that our intermediate momenta are always $\mathbf{p}_X = \mathbf{p}' \pm \mathbf{q}_n$. Similarly, our source momenta must be $\mathbf{p} = \mathbf{p}'(\pm)\mathbf{q}_n(\pm)\mathbf{q}_m$, which gives 16 total terms and nine unique source momenta: $\mathbf{p}' \pm (\mathbf{q}_1 - \mathbf{q}_2)$, $\mathbf{p}' \pm (\mathbf{q}_1 + \mathbf{q}_2)$, $\mathbf{p}' \pm 2\mathbf{q}_1$, $\mathbf{p}' \pm 2\mathbf{q}_2$, \mathbf{p}' .

Exponential in τ contributions

As in our discussion of the unperturbed two-point function in Chapter 3, the perturbed two-point function has excited state contaminations that we must take into account in our calculations. These take the form of terms that are exponentials in τ . In particular, we need to carefully choose our kinematics so that these terms are sufficiently suppressed.

To begin, we look at the exponential terms in Eqs. (4.29) and (4.30). After evaluating the delta functions discussed above, these will become either of the form

$$\frac{e^{-(E_X(\mathbf{p}' \pm \mathbf{q}_n) - E_N(\mathbf{p}))\tau}}{E_X(\mathbf{p}' \pm \mathbf{q}_n) - E_N(\mathbf{p})}, \quad \text{for } n = 1, 2 \text{ and some state } X. \quad (4.35)$$

Note that this is no different from the exponential contributions from the $\mathcal{O}(\lambda)$ contributions in Eq. (4.24), and these will be suppressed as long as the condition of Eq. (4.25) is satisfied.

On the other hand, there are contributions that behave like

$$\frac{e^{-(E_X(\mathbf{p}'(\pm)\mathbf{q}_n(\pm)\mathbf{q}_m) - E_N(\mathbf{p}))\tau}}{E_X(\mathbf{p}'(\pm)\mathbf{q}_n(\pm)\mathbf{q}_m) - E_N(\mathbf{p})}, \quad \text{for } n, m = 1, 2 \text{ and some state } X. \quad (4.36)$$

This second type Feynman-Hellmann excited state is relatively easy to avoid, if one chooses kinematics such that $E_X(\mathbf{p}'(\pm)\mathbf{q}_n(\pm)\mathbf{q}_m) > E_N(\mathbf{p}')$. Again, since the nucleon is the ground state, it is sufficient to keep

$$|\mathbf{p}'(\pm)\mathbf{q}_n(\pm)\mathbf{q}_m| > |\mathbf{p}'|, \quad \text{for all combinations } (\pm)\mathbf{q}_n(\pm)\mathbf{q}_m \text{ except } \mathbf{q}_1 - \mathbf{q}_2. \quad (4.37)$$

The conditions in Eqs. (4.25) and (4.37), respectively, only account for one and two insertions of the current. On the other hand, our calculation will have contributions from all orders of λ , which encompass all possible insertions of the momentum $\mathbf{q}_{1,2}$.

Therefore, we can generalise the conditions in Eqs. (4.25) and (4.37), and include the condition in Eq. (4.32) with

$$\begin{aligned} & |\mathbf{p}' + \mathbf{q}_1 - \mathbf{q}_2| = |\mathbf{p}'|, \\ & |\mathbf{p}' + n\mathbf{q}_1 + m\mathbf{q}_2| > |\mathbf{p}'|, \quad \text{for all other } n, m \in \mathbb{Z}. \end{aligned} \quad (4.38)$$

Physically, the first equation corresponds to keeping us in an equal energy frame, while the second equation corresponds to keeping the intermediate state off-shell.

Even if we satisfy the conditions in Eq. (4.38), there are still kinematic limits we need to be careful of. For instance, if $E_X(\mathbf{p}' + n\mathbf{q}_1 + m\mathbf{q}_2) \approx E_N(\mathbf{p}')$, we still have

$$\frac{e^{-(E_X(\mathbf{p}'(\pm)\mathbf{q}_n(\pm)\mathbf{q}_m) - E_N(\mathbf{p}))\tau}}{E_X(\mathbf{p}'(\pm)\mathbf{q}_n(\pm)\mathbf{q}_m) - E_N(\mathbf{p})} \sim \tau. \quad (4.39)$$

In other words, for sufficiently small τ these near-degenerate contributions behave like the τ -enhanced contributions that we are interested in.

In particular, we are interested in three different kinematic limits that induce near-degeneracies and hence large FH excited terms:

- In both the forward and off-forward case, when the hard scale (Q^2 or \bar{Q}^2) is much less than m_N^2 , the nucleon mass squared, then we have

$$E_N(\mathbf{p}' \pm \mathbf{q}_i) \approx E_N(\mathbf{p}'),$$

which causes the excited states in Eq. (4.35) to blow up.

- In the cases where $\omega \rightarrow \pm 1$ (or in the off-forward case $\bar{\omega} \rightarrow \pm 1$), we have

$$E_N(\mathbf{p}' \pm 2\mathbf{q}_i) \approx E_N(\mathbf{p}') \quad \text{or} \quad E_N(\mathbf{p}' + \mathbf{q}_1 - \mathbf{q}_2) \approx E_N(\mathbf{p}'),$$

causing the excited states in Eq. (4.36) to blow up.

- Finally there is a case that is unique to off-forward kinematics. If $|t| \ll m_N^2$, then

$$E_N(\mathbf{p}' + \mathbf{q}_1 - \mathbf{q}_2) \approx E_N(\mathbf{p}'),$$

again, this causes excited states in Eq. (4.36) to blow up.

To summarise, we have unsuppressed FH excited terms in the kinematics

$$Q^2, \bar{Q}^2 \ll m_N^2, \quad \omega, \bar{\omega} \rightarrow \pm 1, \quad |t| \ll m_N^2. \quad (4.40)$$

As such, in the following chapters we will either avoid these kinematic limits, or where they are unavoidable, discuss difficulties induced by these excited states.

τ -enhanced contributions

As mentioned, the contributions we are interested in are the τ -enhanced (that is, linear in Euclidean time) contributions. As long as we choose momenta that obey the conditions in Eqs. (4.25) and (4.38), the dominant contribution will be the linear in τ term of Eq. (4.29), arising in the case that $E_Y(\mathbf{p}) = E_N(\mathbf{p}')$. The only kinematics for which we will get $E_N(\mathbf{p}) = E_N(\mathbf{p}')$ are if $\mathbf{q}_i = \mathbf{q}_n$, in which case $\mathbf{p} = \mathbf{p}'$ and we have the forward Compton amplitude. Otherwise, we need that $\mathbf{p}' = \mathbf{p} + \mathbf{q}_1 - \mathbf{q}_2$, since we have chosen our momentum insertions so that $|\mathbf{p}| = |\mathbf{p} + \mathbf{q}_1 - \mathbf{q}_2|$.

Therefore, the τ -enhanced contribution of Eq. (4.28) is proportional to

$$\sum_Z \int \frac{d^3p}{(2\pi)^3} \int \frac{d^3p_Z}{(2\pi)^3} \frac{1}{2E_Z(\mathbf{p}_Z)} \frac{\langle N(\mathbf{p}') | j_k(0) | Z(\mathbf{p}_Z) \rangle \langle Z(\mathbf{p}_Z) | j_k(0) | N(\mathbf{p}) \rangle}{E_Z(\mathbf{p}_Z) - E_N(\mathbf{p}')} \Delta_{nm}. \quad (4.41)$$

It is convenient to define the operator

$$\hat{\mathcal{O}}_{\mu\nu}(\mathbf{p}, \mathbf{q}) \equiv \sum_X \frac{1}{2E_X(\mathbf{p} + \mathbf{q})} \frac{j_\mu(0)|X(\mathbf{p} + \mathbf{q})\rangle \langle X(\mathbf{p} + \mathbf{q})|j_\nu(0)}{E_X(\mathbf{p} + \mathbf{q}) - E_N(\mathbf{p})}.$$

After evaluating all the delta functions in Eq. (4.41) and keeping only the terms for which $|\mathbf{p}'| = |\mathbf{p}|$, we get

$$\begin{aligned} & (\lambda_1)^2 \left(\langle N(\mathbf{p}') | \hat{\mathcal{O}}_{kk}(\mathbf{p}', -\mathbf{q}_1) | N(\mathbf{p}') \rangle + \langle N(\mathbf{p}') | \hat{\mathcal{O}}_{kk}(\mathbf{p}', \mathbf{q}_1) | N(\mathbf{p}') \rangle \right) \\ & + (\lambda_2)^2 \left(\langle N(\mathbf{p}') | \hat{\mathcal{O}}_{kk}(\mathbf{p}', -\mathbf{q}_2) | N(\mathbf{p}') \rangle + \langle N(\mathbf{p}') | \hat{\mathcal{O}}_{kk}(\mathbf{p}', \mathbf{q}_2) | N(\mathbf{p}') \rangle \right) \\ & + \lambda_1 \lambda_2 \left(\langle N(\mathbf{p}') | \hat{\mathcal{O}}_{kk}(\mathbf{p}', \mathbf{q}_1) | N(\mathbf{p}') \rangle + \langle N(\mathbf{p}') | \hat{\mathcal{O}}_{kk}(\mathbf{p}', -\mathbf{q}_2) | N(\mathbf{p}') \rangle \right). \end{aligned} \quad (4.42)$$

where \mathbf{p} now has a fixed value determined by $\mathbf{p}' = \mathbf{p} + \mathbf{q}_1 - \mathbf{q}_2$. Noting that the $\mu = \nu = k$ component of the forward Compton amplitude is

$$T_{\mu\nu}(\mathbf{p}, \mathbf{q}) = \langle N(\mathbf{p}) | \hat{\mathcal{O}}_{\mu\nu}(\mathbf{p}, \mathbf{q}) | N(\mathbf{p}) \rangle + \langle N(\mathbf{p}) | \hat{\mathcal{O}}_{\nu\mu}(\mathbf{p}, -\mathbf{q}) | N(\mathbf{p}) \rangle. \quad (4.43)$$

And the OFCA is

$$T_{\mu\nu}(\mathbf{p}, \mathbf{p}'; \mathbf{q}, \mathbf{q}') = \langle N(\mathbf{p}') | \hat{\mathcal{O}}_{\mu\nu}(\mathbf{p}', \mathbf{q}) | N(\mathbf{p}') \rangle + \langle N(\mathbf{p}') | \hat{\mathcal{O}}_{\nu\mu}(\mathbf{p}', -\mathbf{q}') | N(\mathbf{p}') \rangle. \quad (4.44)$$

It is clear from this form of the Compton amplitudes, with the spacetime dependence integrated out, that our Compton amplitude will not vary with τ . However, practically speaking a fit in τ will be sensitive to excited state contributions as outlined in this section.

Therefore, Eq. (4.28) becomes

$$\begin{aligned} \mathcal{G}^{(2)} \stackrel{\tau \gg a}{\simeq} & \frac{\mathcal{Z}_\lambda^N(\mathbf{p}')}{2E_N(\mathbf{p}')} \frac{\tau e^{-E_N(\mathbf{p}')\tau}}{2E_N(\mathbf{p}')} \left[[(\lambda_1)^2 T_{kk}(\mathbf{p}', \mathbf{q}_1) + (\lambda_2)^2 T_{kk}(\mathbf{p}', \mathbf{q}_2)] (\mathcal{Z}_\lambda^N(\mathbf{p}'))^* \right. \\ & \left. + \lambda_1 \lambda_2 T_{kk}(\mathbf{p}, \mathbf{p}'; \mathbf{q}_1, \mathbf{q}_2) (\mathcal{Z}_\lambda^N(\mathbf{p}))^* \right] + \text{exponentially suppressed terms.} \end{aligned} \quad (4.45)$$

Hence, using Eqs. (4.21), (4.24), (4.45), the perturbed correlator is

$$\begin{aligned} \mathcal{G}_\lambda(\tau, \mathbf{p}) \stackrel{\tau \gg a}{\simeq} & e^{-E_N(\mathbf{p}')\tau} \left\{ \frac{|\mathcal{Z}_\lambda^N(\mathbf{p}')|^2}{2E_N(\mathbf{p}')} + \sum_{n=1}^2 \lambda_n A_{\text{ND},n}^{(1)}(\boldsymbol{\lambda}) e^{-(E_N(\mathbf{p}' \pm \mathbf{q}_n) - E_N(\mathbf{p}'))\tau} \right. \\ & + \lambda_1 \lambda_2 A_{\text{ND}}^{(2)}(\boldsymbol{\lambda}) e^{-(E_N(\mathbf{p}' - \boldsymbol{\Delta}) - E_N(\mathbf{p}'))\tau} + \\ & \left. \frac{\tau}{2E_N(\mathbf{p}')} \frac{\mathcal{Z}_\lambda^N(\mathbf{p}')}{2E_N(\mathbf{p}')} \left[[(\lambda_1)^2 T_{kk}(\mathbf{p}', \mathbf{q}_1) + (\lambda_2)^2 T_{kk}(\mathbf{p}', \mathbf{q}_2)] (\mathcal{Z}_\lambda^N(\mathbf{p}'))^* \right. \right. \\ & \left. \left. + \lambda_1 \lambda_2 T_{kk}(\mathbf{p}, \mathbf{p}'; \mathbf{q}_1, \mathbf{q}_2) (\mathcal{Z}_\lambda^N(\mathbf{p}))^* \right] + \mathcal{O}(\lambda^3) \right\}, \end{aligned} \quad (4.46)$$

where we have collected the matrix elements we are not interested in as $A(\boldsymbol{\lambda})$, noting that these coefficients contain all powers of $\lambda_{1,2}$; the $A_{\text{ND}}^{(1)}$ terms are the near-degenerate terms arising from one insertion of the current, while $A_{\text{ND}}^{(2)}$ are near-degenerate terms from two insertions.

In principle, we could perform multi-state fits in Euclidean time that incorporate these near-degenerate terms. Similar multi-state fits were performed for a Feynman-Hellmann calculation of the axial coupling [173]. However, this would require significant work to extend it to the more complicated case of second-order with momentum transfer. Instead, our discussion of near-degeneracies here is simply to help us understand the kinematics that are susceptible to excited state contaminations.

Now if our near-degeneracies are sufficiently suppressed, Eq. (4.46) becomes

$$\begin{aligned} \mathcal{G}_\lambda(\tau, \mathbf{p}) &\stackrel{\tau \gg a}{\simeq} e^{-E_N(\mathbf{p}')\tau} \left\{ \frac{|\mathcal{Z}_\lambda^N(\mathbf{p}')|^2}{2E_N(\mathbf{p}')} \right. \\ &+ \frac{\tau}{2E_N(\mathbf{p}')} \frac{\mathcal{Z}_\lambda^N(\mathbf{p}')}{2E_N(\mathbf{p}')} \left[[(\lambda_1)^2 T_{kk}(\mathbf{p}', \mathbf{q}_1) + (\lambda_2)^2 T_{kk}(\mathbf{p}', \mathbf{q}_2)] (\mathcal{Z}_\lambda^N(\mathbf{p}'))^* \right. \\ &\left. \left. + \lambda_1 \lambda_2 T_{kk}(\mathbf{p}, \mathbf{p}'; \mathbf{q}_1, \mathbf{q}_2) (\mathcal{Z}_\lambda^N(\mathbf{p}))^* \right] + \mathcal{O}(\lambda^3) \right\}, \end{aligned} \quad (4.47)$$

And we note that if $\lambda^2 \tau \ll a$, then we can re-sum this as an exponential^{††}

$$\begin{aligned} \mathcal{G}_\lambda(\tau, \mathbf{p}) &\stackrel{\tau \gg a}{\simeq} \frac{|\mathcal{Z}_\lambda^N(\mathbf{p}')|^2}{2E_N(\mathbf{p}')} \exp \left\{ - \left(E_N(\mathbf{p}') + \frac{1}{2E_N(\mathbf{p}')} \left[[(\lambda_1)^2 T_{kk}(\mathbf{p}', \mathbf{q}_1) + (\lambda_2)^2 T_{kk}(\mathbf{p}', \mathbf{q}_2)] \right. \right. \right. \\ &\left. \left. \left. + \lambda_1 \lambda_2 T_{kk}(\mathbf{p}, \mathbf{p}'; \mathbf{q}_1, \mathbf{q}_2) + \mathcal{O}(\lambda^3) \right] \right) \tau \right\}. \end{aligned} \quad (4.48)$$

This parameterisation gives us the form $\mathcal{G}_\lambda = A_\lambda e^{-E_\lambda \tau}$ present in many Feynman-Hellmann derivations.

Now we are ready to derive a Feynman-Hellmann relation of the form in Eq. (4.9). Using the contributions to the perturbed correlator, Eq. (4.46), the second-order mixed derivative of the correlator is

$$\begin{aligned} \frac{\partial^2}{\partial \lambda_1 \partial \lambda_2} \frac{\mathcal{G}_\lambda(\tau)}{\mathcal{G}_0(\tau)} \Big|_{\lambda=0} &\stackrel{\tau \gg a}{\simeq} B_{\text{int}} + \sum_{i=1,2} B_{\text{ND},i}^{(1)} e^{-(E_N(\mathbf{p}' \pm \mathbf{q}_i) - E_N(\mathbf{p}'))\tau} \\ &+ B_{\text{ND}}^{(2)} e^{-(E_N(\mathbf{p}' - \mathbf{\Delta}) - E_N(\mathbf{p}'))\tau} + \frac{\tau}{2E_N(\mathbf{p}')} T_{kk}(\mathbf{p}, \mathbf{p}'; \mathbf{q}_1, \mathbf{q}_2), \end{aligned} \quad (4.49)$$

where

$$B_{\text{int}} = \frac{\partial^2}{\partial \lambda_1 \partial \lambda_2} \frac{|\mathcal{Z}_\lambda^N(\mathbf{p}')|^2}{2E_N(\mathbf{p}')} \Big|_{\lambda=0}, \quad B_{\text{ND}} = \frac{\partial^2 A_{\text{ND}}(\lambda)}{\partial \lambda_1 \partial \lambda_2} \Big|_{\lambda=0},$$

for each of the coefficients in Eq. (4.46). Recall from Eqs. (4.22) and (4.26) that the zero and single current insertion contributions still contain $\lambda_1 \lambda_2$ terms.

Again, if τ is sufficiently large or our kinematics otherwise keep these terms suppressed, we arrive at the very simple Feynman-Hellmann relation:

$$\frac{\partial^2}{\partial \lambda_1 \partial \lambda_2} \frac{\mathcal{G}_\lambda(\tau)}{\mathcal{G}_0(\tau)} \Big|_{\lambda=0} \stackrel{\tau \gg a}{\simeq} B_{\text{int}} + \frac{\tau}{2E_N(\mathbf{p}')} T_{kk}(\mathbf{p}, \mathbf{p}'; \mathbf{q}_1, \mathbf{q}_2). \quad (4.50)$$

^{††}This reparameterisation assumes $\mathcal{Z}_\lambda^N(\mathbf{p}') \approx \mathcal{Z}_\lambda^N(\mathbf{p})$.

Note that we could have used Eq. (4.48) to derive

$$\left. \frac{\partial^2 E_\lambda}{\partial \lambda_1 \partial \lambda_2} \right|_{\lambda=0} = -\frac{T_{kk}(\mathbf{p}, \mathbf{p}'; \mathbf{q}_1, \mathbf{q}_2)}{2E_N(\mathbf{p}')}, \quad (4.51)$$

which is the standard form of FH relation that is derived in Refs. [37, 178, 179]. However, in this thesis we will use the correlator derivative, Eq. (4.50), instead of this energy shift.

In practice, we approximate the derivative of the correlator using

$$\left. \frac{\partial^2 \mathcal{G}_\lambda}{\partial \lambda_1 \partial \lambda_2} \right|_{\lambda=0} = \frac{\mathcal{G}_{(\lambda, \lambda)} + \mathcal{G}_{(-\lambda, -\lambda)} - \mathcal{G}_{(\lambda, -\lambda)} - \mathcal{G}_{(-\lambda, \lambda)}}{4\lambda^2} + \mathcal{O}(\lambda^2). \quad (4.52)$$

And hence it is convenient to define

$$R_\lambda \equiv \frac{\mathcal{G}_{(\lambda, \lambda)} + \mathcal{G}_{(-\lambda, -\lambda)} - \mathcal{G}_{(\lambda, -\lambda)} - \mathcal{G}_{(-\lambda, \lambda)}}{\mathcal{G}_{(0, 0)}}. \quad (4.53)$$

If we are dealing with a nucleon, our correlator is also carrying a pair of Dirac indices that are traced over with a spin-parity projector (recall Eqs. (4.15) and (4.7)). Hence Eq. (4.50) with the spin-parity projections becomes^{‡‡}

$$\left. \frac{\partial^2}{\partial \lambda_1 \partial \lambda_2} \frac{\Gamma^{\beta\alpha} \sum_{s, s'} \mathcal{G}_\lambda^{\alpha\beta}(\tau)}{\Gamma_{\text{unpol}}^{\beta\alpha} \sum_{s, s'} \mathcal{G}_0^{\alpha\beta}(\tau)} \right|_{\lambda=0} \stackrel{\tau \gg a}{\simeq} \frac{\tau}{2E_N(\mathbf{p}')} \frac{\sum_{s, s'} \text{tr}[\Gamma u(p', s') T_{kk} \bar{u}(p, s)]}{\sum_s \text{tr}[\Gamma_{\text{unpol}} u(p', s) \bar{u}(p', s)]}, \quad (4.54)$$

dropping the τ independent intercept term.

Hence it is useful to define

$$\mathcal{R}_{\mu\nu}^\Gamma \equiv \frac{\sum_{s, s'} \text{tr}[\Gamma u(P', s') T_{\mu\nu} \bar{u}(P, s)]}{\sum_s \text{tr}[\Gamma_{\text{unpol}} u(P', s) \bar{u}(P', s)]}, \quad (4.55)$$

where we always use the unpolarised spin-parity projector, Eq. (3.28), for the denominator. By varying the spin-parity projector in the numerator, we can isolate different components of the off-forward Compton amplitude—we will discuss this in more detail in Chapter 6.

4.1.3 Spin-dependent forward

Next, we derive a FH relation for the spin-dependent structure functions of the forward Compton amplitude, Eq. (2.19). These structure functions, $\tilde{g}_{1,2}$ of Eq. (2.20), only exist in the $\mu \neq \nu$ component of the forward Compton amplitude, and moreover they are odd under $q \rightarrow -q$. Therefore, the cosine phases we used in the previous section, Eq. (4.12), will annihilate our Compton amplitude. As such, we need to extract a signal that is odd under $\mathbf{q} \rightarrow -\mathbf{q}$.

If we naively use cosine phases, $e^{i\mathbf{q}\cdot\mathbf{z}} + e^{-i\mathbf{q}\cdot\mathbf{z}}$, on both currents, then the final product will be even in \mathbf{q} . Similarly, if both currents have the sine combination, $e^{i\mathbf{q}\cdot\mathbf{z}} - e^{-i\mathbf{q}\cdot\mathbf{z}}$, we will also have only even in \mathbf{q} contributions, since

$$\sum_{\mathbf{z}, \mathbf{y}} \sin(\mathbf{q} \cdot \mathbf{z}) \sin(\mathbf{q} \cdot \mathbf{y})$$

^{‡‡}For the energy shift parameterisation, Eq. (4.51), an equivalent of the spin-parity trace can be achieved by taking a combination of spin up and down correlators in a ratio [179].

is still even under $\mathbf{q} \rightarrow -\mathbf{q}$.

Instead, by having one current carrying the sine combination and the other the cosine, we isolate a contribution that is odd under $\mathbf{q} \rightarrow -\mathbf{q}$, as we would like. Hence we choose the perturbing operators:

$$\mathcal{O}_1(\mathbf{z}) = (e^{i\mathbf{q}\cdot\mathbf{z}} + e^{-i\mathbf{q}\cdot\mathbf{z}})j_1(\mathbf{z}), \quad \mathcal{O}_2(\mathbf{z}) = i(e^{i\mathbf{q}\cdot\mathbf{z}} - e^{-i\mathbf{q}\cdot\mathbf{z}})j_2(\mathbf{z}), \quad (4.56)$$

noting that the sine phases have a factor of i to keep them Hermitian, and hence our overall Compton amplitude real. Note also that now our background fields have the same momentum, \mathbf{q} , as we are interested in the forward Compton amplitude.

Exponential in τ contributions

The forward case is somewhat simpler in terms of kinematic constraints: there is no need for the constraint in Eq. (4.32), since there is only one inserted momentum. Since there is only one momentum, the condition in Eq. (4.38) becomes

$$|\mathbf{p} + n\mathbf{q}| > |\mathbf{p}|, \quad \text{for } n \in \mathbb{Z} \setminus \{0\}. \quad (4.57)$$

As discussed, we have poorly suppressed FH excited states arising for the kinematics $Q^2 \ll m_N^2$ and $\omega \rightarrow \pm 1$.

τ -enhanced contributions

Hence, for the spin dependent forward, the τ -enhanced contribution of Eq. (4.28) is proportional to

$$\sum_Z \int \frac{d^3p}{(2\pi)^3} \int \frac{d^3p_Z}{(2\pi)^3} \frac{1}{2E_Z(\mathbf{p}_Z)} \frac{\langle N(\mathbf{p})|j_n(0)|Z(\mathbf{p}_Z)\rangle \langle Z(\mathbf{p}_Z)|j_m(0)|N(\mathbf{p}_s)\rangle}{E_Z(\mathbf{p}_Z) - E_N(\mathbf{p})} \tilde{\Delta}_{nm}, \quad (4.58)$$

where, using Eq. (4.13),

$$\begin{aligned} \tilde{\Delta}_{nm} \equiv & (2\pi)^6 (i)^{\delta_{n,2}} \left[\delta^{(3)}(\mathbf{p} - \mathbf{q} - \mathbf{p}_Z) + (-1)^{\delta_{n,2}} \delta^{(3)}(\mathbf{p} + \mathbf{q} - \mathbf{p}_Z) \right] \\ & \times (i)^{\delta_{m,2}} \left[\delta^{(3)}(\mathbf{p}_s - \mathbf{q} - \mathbf{p}_Z) + (-1)^{\delta_{m,2}} \delta^{(3)}(\mathbf{p}_s + \mathbf{q} - \mathbf{p}_Z) \right], \end{aligned} \quad (4.59)$$

where \mathbf{p}_s is the source momentum.

Again, we evaluate the delta functions in Eq. (4.59), but this time keep only the contributions for which $\mathbf{p} = \mathbf{p}_s$:

$$\begin{aligned} & (\lambda_1)^2 \left(\langle N(\mathbf{p})|\hat{\mathcal{O}}_{11}(\mathbf{p}, \mathbf{q})|N(\mathbf{p})\rangle + \langle N(\mathbf{p})|\hat{\mathcal{O}}_{11}(\mathbf{p}', -\mathbf{q})|N(\mathbf{p})\rangle \right) \\ & + (\lambda_2)^2 \left(\langle N(\mathbf{p})|\hat{\mathcal{O}}_{22}(\mathbf{p}, \mathbf{q})|N(\mathbf{p})\rangle + \langle N(\mathbf{p})|\hat{\mathcal{O}}_{22}(\mathbf{p}, -\mathbf{q})|N(\mathbf{p})\rangle \right) \\ & + i\lambda_1\lambda_2 \left(\langle N(\mathbf{p})|\hat{\mathcal{O}}_{12}(\mathbf{p}, \mathbf{q})|N(\mathbf{p})\rangle + \langle N(\mathbf{p})|\hat{\mathcal{O}}_{21}(\mathbf{p}, \mathbf{q})|N(\mathbf{p})\rangle \right) \\ & - i\lambda_1\lambda_2 \left(\langle N(\mathbf{p})|\hat{\mathcal{O}}_{12}(\mathbf{p}, -\mathbf{q})|N(\mathbf{p})\rangle + \langle N(\mathbf{p})|\hat{\mathcal{O}}_{21}(\mathbf{p}, -\mathbf{q})|N(\mathbf{p})\rangle \right). \end{aligned} \quad (4.60)$$

From Eq. (4.43), the last two lines of Eq. (4.60) are $T_{12}(p, q) - T_{21}(p, -q)$. Since we are interested in isolating the $q \rightarrow -q$ odd contribution, we can rewrite this as $T_{12}(p, q) - T_{21}(p, -q) = 2T_{12}(p, q)$. Hence Eq. (4.28) becomes

$$\mathcal{G}^{(2)} \stackrel{\tau \gg a}{\simeq} \frac{|\mathcal{Z}_\lambda^N(\mathbf{p})|^2}{2E_N(\mathbf{p})} \frac{\tau e^{-E_N(\mathbf{p})\tau}}{2E_N(\mathbf{p})} \left[(\lambda_1)^2 T_{11}(\mathbf{p}, \mathbf{q}) + (\lambda_2)^2 T_{22}(\mathbf{p}, \mathbf{q}) + 2i\lambda_1\lambda_2 T_{12}(\mathbf{p}, \mathbf{q}) \right] + \text{exponentially suppressed terms.} \quad (4.61)$$

Again, in analogy to the OFCA section, we will drop all the terms except the most dominant to get

$$\frac{\partial^2}{\partial\lambda_1\partial\lambda_2} \frac{\mathcal{G}_\lambda(\tau)}{\mathcal{G}_0(\tau)} \Big|_{\lambda=0} \stackrel{\tau \gg a}{\simeq} B_{\text{int}} + B_{\text{ND}}^{(1)} e^{-(E_N(\mathbf{p}\pm\mathbf{q}) - E_N(\mathbf{p}))\tau} + \frac{i\tau}{E_N(\mathbf{p})} T_{12}(\mathbf{p}, \mathbf{q}). \quad (4.62)$$

We note that, since we do not have off-forward kinematics, we only have the near-degeneracies from a single insertion of the current, $B_{\text{ND}}^{(1)}$. Then, for sufficiently suppressed near-degeneracies, we have

$$\frac{\partial^2}{\partial\lambda_1\partial\lambda_2} \frac{\mathcal{G}_\lambda(\tau)}{\mathcal{G}_0(\tau)} \Big|_{\lambda=0} \stackrel{\tau \gg a}{\simeq} B_{\text{int}} + \frac{i\tau}{E_N(\mathbf{p})} T_{12}(\mathbf{p}, \mathbf{q}). \quad (4.63)$$

Since the spin dependent structure component of the Compton amplitude is itself imaginary, the factor of i keeps the whole signal real.

As in the case of the OFCA, we will introduce the spins and Dirac indices again to get

$$\frac{\partial^2}{\partial\lambda_1\partial\lambda_2} \frac{\Gamma^{\beta\alpha} \sum_{s,s'} \mathcal{G}_\lambda^{\alpha\beta}(\tau)}{\Gamma_{\text{unpol}}^{\beta\alpha} \sum_{s,s'} \mathcal{G}_0^{\alpha\beta}(\tau)} \Big|_{\lambda=0} \stackrel{\tau \gg a}{\simeq} \frac{i\tau}{E_N(\mathbf{p})} \frac{\sum_{s,s'} \text{tr}[\Gamma u(p, s') T_{12} \bar{u}(p, s)]}{\sum_s \text{tr}[\Gamma_{\text{unpol}} u(p, s) \bar{u}(p, s)]}. \quad (4.64)$$

We always use the unpolarised spin-parity projector for the correlator on the denominator. Again, we can vary Γ in the numerator to isolate different components of the spin-dependent Compton amplitude.

Again, as in the off-forward case, we can express the perturbed correlator in the form $\mathcal{G}_\lambda = A_\lambda e^{-E_\lambda\tau}$ as long as $\lambda^2\tau \ll a$, and derive the Feynman-Hellmann relation in terms of the energy-shift:

$$\frac{\partial^2 E_\lambda}{\partial\lambda_1\partial\lambda_2} \Big|_{\lambda=0} = \frac{iT_{12}(\mathbf{p}, \mathbf{q})}{E_N(\mathbf{p})}. \quad (4.65)$$

Since T_{12} is imaginary, the energy shift is real.

4.2 Implementation and Interpretation

4.2.1 Implementation

In the previous section, we presented some useful Feynman-Hellmann relations, Eqs. (4.50) and (4.63), derived in continuum quantum field theory, that relate perturbed two-point functions to four-point functions. Here, we will discuss how these perturbed two-point

functions are calculated in practice, as well as some of the differences to be mindful of between the continuum derivations presented in the previous section and the discretised implementation.

Although we started with a perturbed Lagrangian, Eq. (4.10), in most implementations of Feynman-Hellmann we do not directly perturb the lattice action, which would require the generation of new gauge configurations, a highly computationally expensive task. Instead, we calculate perturbed quark propagators as discussed at the start of this chapter.

Local current

The first case we consider is that in which the vector currents in our lattice Compton amplitude, Eq. (4.2), are the local vector current^{§§}, Eq. (3.40):

$$j_\mu^{\text{loc}}(z_n) = Z_V \bar{\psi}(z_n) \gamma_\mu \psi(z_n).$$

Recall the unperturbed fermion matrix from Eq. (3.18), M . We perturb this with two perturbing matrices, $\mathcal{O}_{1,2}$:

$$M_\lambda = M - \lambda_1 \mathcal{O}_1 - \lambda_2 \mathcal{O}_2. \quad (4.66)$$

For the off-forward Compton amplitude, we choose the matrices

$$[\mathcal{O}_1]_{n,m} = \delta_{n,m} (e^{i\mathbf{q}_1 \cdot \mathbf{z}_n} + e^{-i\mathbf{q}_1 \cdot \mathbf{z}_n}) \gamma \cdot \hat{\mathbf{e}}, \quad [\mathcal{O}_2]_{n,m} = \delta_{n,m} (e^{i\mathbf{q}_2 \cdot \mathbf{z}_n} + e^{-i\mathbf{q}_2 \cdot \mathbf{z}_n}) \gamma \cdot \hat{\mathbf{e}}, \quad (4.67)$$

where $\hat{\mathbf{e}}$ is a unit three-vector that picks out the direction of our current. For Chapter 5, we always choose $\hat{\mathbf{e}} = (0, 0, 1)$. However, for Chapter 6, we will choose directions such as $\hat{\mathbf{e}} = \frac{1}{\sqrt{2}}(1, -1, 0)$ to isolate certain contributions from the OFCA.

On the other hand, for the spin-dependent forward Compton amplitude, we choose

$$[\mathcal{O}_1]_{n,m} = \delta_{n,m} (e^{i\mathbf{q} \cdot \mathbf{z}_n} + e^{-i\mathbf{q} \cdot \mathbf{z}_n}) \gamma_1, \quad [\mathcal{O}_2]_{n,m} = \delta_{n,m} i (e^{i\mathbf{q} \cdot \mathbf{z}_n} - e^{-i\mathbf{q} \cdot \mathbf{z}_n}) \gamma_2. \quad (4.68)$$

These perturbing matrices correspond directly to discretised versions of the background fields in Eqs. (4.31) and (4.56) by $\hat{\mathcal{O}} = \bar{\psi} \mathcal{O} \psi$.

Then, the perturbed quark propagators are simply

$$S_\lambda(z_n, z_m) = [M - \lambda_1 \mathcal{O}_1 - \lambda_2 \mathcal{O}_2]_{n,m}^{-1}. \quad (4.69)$$

In terms of these quark propagators, the perturbed proton correlators are calculated exactly as in the unperturbed case, Eq. (3.25), with one or more of the quark propagators replaced by perturbed quark propagators:

$$\mathcal{G}_\lambda^{uu} \sim \langle S_\lambda^u S_\lambda^u S^d \rangle_U, \quad \mathcal{G}_\lambda^{dd} \sim \langle S^u S^u S_\lambda^d \rangle_U, \quad \mathcal{G}_\lambda^{ud} \sim \langle S_\lambda^u S_\lambda^u S_\lambda^d \rangle_U, \quad (4.70)$$

where $\langle \dots \rangle_U$ represents gauge ensemble averaging as in Eq. (3.25).

^{§§}For an implementation with the conserved current, Eq. (3.41), see Refs. [40, 178].

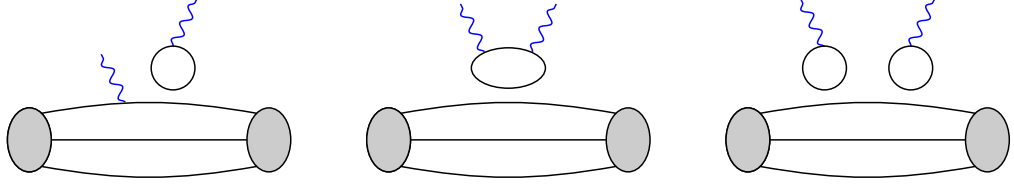


Figure 4.2: Lattice diagrams showing the type of disconnected contributions that are missing from our calculation. These disconnected contributions correspond to one or both of the photons interacting with a sea quark.

Then, our FH relations in Eqs. (4.50) and (4.63) may be applied to these objects. For the flavour diagonal ($f = f'$) we have, up to the intercept term,

$$\left. \frac{\partial^2}{\partial \lambda_1 \partial \lambda_2} \frac{\mathcal{G}_\lambda^{ff}(\tau)}{\mathcal{G}_0(\tau)} \right|_{\lambda=0} \simeq \frac{\tau}{2E_N} T_{kk}^{ff},$$

where $T_{\mu\nu}^{ff}$ is the OFCA with both currents have flavour f , neglecting charge.

For the case where the perturbation is applied to both flavours (see Eq. (4.70)), we have

$$\left. \frac{\partial^2}{\partial \lambda_1 \partial \lambda_2} \frac{\mathcal{G}_\lambda^{ud}(\tau)}{\mathcal{G}_0(\tau)} \right|_{\lambda=0} \simeq \frac{\tau}{2E_N} \left(T_{kk}^{uu} + T_{kk}^{dd} + T_{kk}^{ud} \right),$$

where $T_{\mu\nu}^{ud}$ is the mixed flavour OFCA:

$$T_{\mu\nu}^{ud} \equiv i \int d^4 z e^{\frac{i}{2}(q+q') \cdot z} \langle P' | \mathcal{T} \{ j_\mu^u(z) j_\nu^d(0) \} | P \rangle.$$

Therefore, to isolate this flavour contribution, we must take

$$\left. \frac{\partial^2}{\partial \lambda_1 \partial \lambda_2} \frac{\mathcal{G}_\lambda^{ud}(\tau) - \mathcal{G}_\lambda^{uu}(\tau) - \mathcal{G}_\lambda^{dd}(\tau)}{\mathcal{G}_0(\tau)} \right|_{\lambda=0} \simeq \frac{\tau}{2E_N} T_{kk}^{ud}. \quad (4.71)$$

Then, if we are only considering the up and down quarks, the proton Compton amplitude is

$$T_{\mu\nu}^p = \frac{4}{9} T_{\mu\nu}^{uu} + \frac{1}{9} T_{\mu\nu}^{dd} - \frac{2}{9} T_{\mu\nu}^{ud}.$$

Analogous expressions are applicable to the spin-dependent Compton amplitude, except using the Feynman-Hellmann relation in Eq. (4.63).

In this thesis we do not determine the $T_{\mu\nu}^{ud}$ contribution, as this is generally highly suppressed [38].

Disconnected contributions

As the perturbation is only applied to the quark propagators, it only affects the valence quarks. In order to apply the perturbation to the sea quarks too, one would need to generate new gauge configurations, as was performed in Refs. [180, 181]. In this case, the

gauge links are generated according to the *perturbed* weight:

$$\det \left[M[U] - \lambda_1^{\text{sea}} \mathcal{O}_1 - \lambda_2^{\text{sea}} \mathcal{O}_2 \right] e^{-S_G[U]}, \quad (4.72)$$

whereas in our calculation we have set $\lambda_{\text{sea}} = 0$.

Alternatively, the sea quark contributions could be approximated by a reweighting of the unperturbed configurations similar to techniques applied to finite density calculations [182].

It is far cheaper computationally to calculate without perturbing the sea quarks. However, it means that our Compton amplitudes are missing disconnected contributions, which are illustrated in Fig. 4.2. This sort of calculation is common in lattice QCD, particularly exploratory studies, as it is generally assumed that sea quark contributions to most observables are minor. Moreover, as all of our calculations will be at the SU(3) flavour symmetric point, the isovector (up quark minus down quark) contributions will be independent of sea quarks, whether our calculation includes them or not. Hence our isovector results will not require sea quark contributions.

4.2.2 Interpretation

Once we have calculated a Compton amplitude on the Euclidean lattice, our work has only just begun. As discussed in Chapter 3, the Wick rotation in Eq. (3.3) makes the calculation of real time scattering amplitudes impossible.

For instance, we can write the Minkowski Compton amplitude as

$$T_{\mu\nu}^M = i \sum_X \int d^3z \int_0^\infty dt e^{i(q_0 + E_N - E_X + i\varepsilon)t} e^{-i(\mathbf{q} + \mathbf{P} - \mathbf{P}_X) \cdot \mathbf{z}} \langle P | j_\mu(0) | X \rangle \langle X | j_\nu(0) | X \rangle, \quad (4.73)$$

up to the crossed term: $\mu \leftrightarrow \nu$ and $q \rightarrow -q$.

By contrast, when we Wick rotate Eq. (4.73), we get the Euclidean Compton amplitude:

$$T_{\mu\nu}^E = \sum_X \int d^3z \int_0^\infty d\tau e^{(q_0 + E_N - E_X)\tau} e^{-i(\mathbf{q} + \mathbf{P} - \mathbf{P}_X) \cdot \mathbf{z}} \langle P | j_\mu(0) | X \rangle \langle X | j_\nu(0) | X \rangle, \quad (4.74)$$

again, up to the crossed term. So if $\Delta E < 0$,

$$\lim_{\varepsilon \rightarrow 0^+} i \int_0^\infty dt e^{i(\Delta E + i\varepsilon)t} = \int_0^\infty d\tau e^{\Delta E \tau}, \quad (4.75)$$

and hence Eqs. (4.73) and (4.74) can be equated with one another [37, 135]. However, if $\Delta E \geq 0$, then Eq. (4.75) is no longer valid and we cannot equate our Euclidean and Minkowski amplitudes.

In our Feynman-Hellmann calculations, we set $q_0 = 0$. And hence to equate the Euclidean and Minkowski Compton amplitudes we must have $E_N - E_X < 0$. Note that this condition is already encompassed by the kinematic constraints in Eq. (4.38).

The condition $E_N - E_X < 0$ implies that

$$\sqrt{m_X^2 + (\mathbf{p} \pm \mathbf{q})^2} > \sqrt{m_N^2 + \mathbf{p}^2} \quad \Rightarrow \quad m_X^2 + (\mathbf{p} \pm \mathbf{q})^2 > m_N^2 + \mathbf{p}^2. \quad (4.76)$$

Since $m_X > m_N$ for all $X \neq N$, then our strongest constraint on \mathbf{p} is for $X = N$:

$$m_N^2 + (\mathbf{p} \pm \mathbf{q})^2 > m_N^2 + \mathbf{p}^2 \quad \Rightarrow \quad \pm 2\mathbf{p} \cdot \mathbf{q} + \mathbf{q}^2 > 0. \quad (4.77)$$

Recall the inverse Bjorken scaling variable, Eq. (2.22). Noting that $Q^2 = \mathbf{q}^2$, while $P \cdot q = -\mathbf{p} \cdot \mathbf{q}$, this condition implies that to equate the Euclidean and Minkowski Compton amplitudes we must have

$$-1 < \omega < 1. \quad (4.78)$$

This is in contrast to the physical region of the Compton amplitude $|\omega| > 1$, Eq. (2.32). We note that, while it is possible to calculate $|\omega| \geq 1$ values, we do not analyse these, since we cannot directly relate them to the Minkowski amplitude***.

4.2.3 Inverse problem

As we saw, the Wick rotation leads to the necessity to keep ω in an unphysical region. Therefore, as in the other lattice parton methods discussed in Section 3.2, the Euclidean spacetime leads to an ill-conditioned ‘inverse problem’ [161]. Moreover, as with the pseudo-distribution, HOPE and hadronic tensor inverse problems, we have a similar set of tools with which to tame this difficulty.

To see how this inverse problem arises, we start with the dispersion relation, Eq. (2.26):

$$\bar{\mathcal{F}}_1(\omega, Q^2) = 2\omega^2 \int_0^1 dx \frac{2x}{1 - (\omega x)^2} F_1(x, Q^2) = \int_0^1 dx K(\omega, x) F_1(x, Q^2). \quad (4.79)$$

If $|\omega| < 1$, the physical structure function F_1 and the amplitude we get from the lattice calculation, $\bar{\mathcal{F}}_1$, are related through a Fredholm integral equation of the first kind, which is numerically unstable and does not always have unique solutions.

In Section 3.2, we discussed standard methods to tame these inverse problems used in other lattice calculations of partonic quantities. A previous attempt at direct inversion through singular value decomposition failed for our forward Compton amplitude data [161], as this type of method is extremely sensitive to systematic errors, noisy data points and a limited number of ω values—all of which are present in our lattice data. Therefore, in this thesis we use the follow methods:

- In Chapters 5–7, we extract the moments of the relevant amplitudes. To demonstrate this for the unpolarised forward Compton amplitude, recall Eq. (2.29) where we Taylor expand about $\omega = 0$:

$$\bar{\mathcal{F}}_1(\omega, Q^2) = 2 \sum_{n=1}^{\infty} \omega^{2n-1} M_{2n-1}(Q^2),$$

where

$$M_n(Q^2) \equiv 2 \int_0^1 dx x^{n-1} F_1(x, Q^2).$$

We will use similar moment expansions for the off-forward and polarised Compton amplitudes.

***One can derive analogous relations showing that the off-forward analogue must be kept $|\bar{\omega}| \lesssim 1$ [56].

The extraction of moments is numerically very stable, and the moments themselves provide interesting physical information. However, since we are limited to $|\omega| < 1$, for ω^N as N becomes larger, these higher moments are more suppressed. Moreover, the higher ω values require higher sink momentum values. As discussed in Chapter 3, high sink momentum decreases the quality of the signal. Therefore, we are limited in the number of moments we can meaningfully constrain.

- Furthermore, in Chapter 6, we use a phenomenological parameterisation of generalised parton distributions with a limited number of parameters, similar to Ref. [161]. While sacrificing some model-independence, this gives us much more traction on the inversion.

Now that we have derived the relevant Feynman-Hellmann relations, and outlined the processes of implementing and interpreting these results, we are ready to apply this formalism to numerical calculations.

The Off-Forward Compton Amplitude: Part I

In the previous chapter, we outlined how to use Feynman-Hellmann to calculate the off-forward Compton amplitude (OFCA). Here, we apply this formalism to a lattice QCD calculation of the OFCA, and show how to use this amplitude to determine properties of generalised parton distributions (GPDs). GPDs are observables that have generated a great deal of interest, theoretical and experimental, in recent years. They contain a staggering amount of physical information, including the spin decomposition [22] and the spatial distributions [23] of quarks and gluons within a hadron. More recent research has shown that GPDs can be used to access the ‘mechanical’ properties of hadrons: their internal pressure, energy and force distributions [83, 88].

Experimental determinations of GPDs require measurements of exclusive, hard scattering processes like deeply virtual Compton scattering (DVCS) and deeply virtual meson production (DVMP). In these processes, the quantity of interest is the off-forward Compton amplitude as this can be related to GPDs at high energies. Such experiments have been performed at HERA [183–187], COMPASS [188], JLab [189–192], and in the future at the Brookhaven electron-ion collider [25].

However, experimental determinations of GPDs suffer from a number of kinematic difficulties related to the high-dimensionality of off-forward scattering*, including the deconvolution problem, and the necessity to span kinematics. As such, most experimental extractions of GPDs use simple parameterisations that bring a great deal of model dependence [193, 194]. Therefore, lattice QCD studies can provide first principles information on GPDs to guide or constrain experimental determinations.

Historically, lattice QCD calculations of GPD properties have been limited to three-point studies of their Mellin moments [122–133]. However, as discussed in Section 3.2, the $n = 3$ moments are the highest so far computed [127]. There have also been calculations of quasi-GPDs [146–149], and a test calculation of pseudo-GPDs [195]. These latter two methods aim to reconstruct the light-cone distributions, whereas here we calculate a discretisation of the Compton amplitude, which can be more directly related to experiment.

The structure of this chapter is as follows: in Section 5.1 we derive a parameterisation of the OFCA that is suitable to compare to our lattice calculation. Since we calculate the full Compton amplitude including all higher-twist corrections, we need a non-perturbative

*In other words, off-forward scattering is a function of four scalar variables, whereas forward scattering is a function of two.

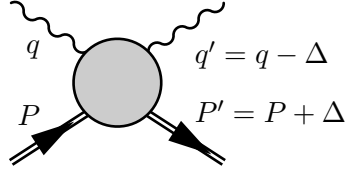


Figure 5.1: The Feynman diagram for off-forward $\gamma^*(q) + N(P) \rightarrow \gamma^*(q') + N(P')$ scattering.

tensor decomposition where we know the partonic interpretation of each of the amplitudes in the $\bar{Q}^2 \rightarrow \infty$ limit. This is different to the perturbative matching for quasi- and pseudo-parton distributions: as discussed in Section 4.2, we wish to determine the Compton amplitude *with* its power corrections, but still know the asymptotic limit of the structures.

Then in Section 5.2 we use the FH method to calculate the OFCA for two values of the soft momentum transfer: $t = -1.10, -2.20 \text{ GeV}^2$. Further, we use zero-skewness ($\xi = 0$) kinematics; this reduces the number of variables we need to span and is physically interesting [23]. We then apply the aforementioned parameterisation to interpret the OFCA we calculate in terms of GPDs. In particular, following the discussion of Section 4.2, we extract the $n = 2, 4$ Mellin moments of the OFCA, which can be interpreted in the high-energy limit as the corresponding moments of GPDs.

5.1 Theoretical Parameterisation

We start with the off-forward Compton amplitude (OFCA) from Eq. (2.72):

$$T_{\mu\nu} \equiv i \int d^4z e^{\frac{i}{2}(q+q')\cdot z} \langle P' | \mathcal{T} \{ j_\mu(z) j_\nu(0) \} | P \rangle,$$

which describes hadron-photon scattering with some momentum transfer between initial and final states—see Fig. 5.1.

Recall from Eq. (2.73) that we have three linearly independent momentum vectors:

$$\bar{P} = \frac{1}{2}(P + P'), \quad \bar{q} = \frac{1}{2}(q + q'), \quad \Delta = P' - P = q - q'.$$

From these, we form the following scalar variables, given in Eq. (2.74):

$$\bar{\omega} = \frac{2\bar{P} \cdot \bar{q}}{\bar{Q}^2}, \quad \vartheta = -\frac{\Delta \cdot \bar{q}}{\bar{Q}^2}, \quad t = \Delta^2, \quad \bar{Q}^2 = -\bar{q}^2.$$

The $t \rightarrow 0$ limit recovers the forward Compton amplitude, Eq. (2.19). In terms of the forward Compton scattering scalars (Eq. (2.22)), the scalars of Eq. (2.74) are in the forward limit

$$\lim_{t \rightarrow 0} \bar{\omega} \rightarrow \omega, \quad \lim_{t \rightarrow 0} \bar{Q}^2 \rightarrow Q^2, \quad \lim_{t \rightarrow 0} \vartheta \rightarrow 0.$$

Most studies of the OFCA use the ‘skewness’ variable, which in covariant kinematics is $\xi = -\frac{\Delta \cdot \bar{q}}{2\bar{P} \cdot \bar{q}} = \vartheta/\bar{\omega}$. Hence $\vartheta = 0$, $\bar{\omega} \neq 0$ implies that $\xi = 0$.

In analogy to Section 2.2.2, the generalised Bjorken limit can be defined as

$$\bar{Q}^2 \rightarrow \infty, \quad \bar{\omega}, \vartheta \text{ fixed.} \quad (5.1)$$

5.1.1 Motivation

In the existing literature on the OFCA, there are primarily two types of works. First, there are perturbative expansions of the OFCA for DVCS kinematics [22], which we saw in Eq. (2.77):

$$T^{\mu\nu} = -\frac{1}{2}(n^\mu \bar{n}^\nu + n^\nu \bar{n}^\mu - g^{\mu\nu}) \int_{-1}^1 dx \left(\frac{1}{x - \xi + i\epsilon} + \frac{1}{x + \xi + i\epsilon} \right) \\ \times \left[H(x, \xi, t) \bar{u}(P') \not{n} u(P) + E(x, \xi, t) \bar{u}(P') \frac{i\sigma^{\alpha\beta} \bar{n}_\alpha \Delta_\beta}{2m_N} u(P) \right].$$

These expansions use light-cone vectors, n_μ and \bar{n}_μ , and parameterise the non-perturbative structures in terms of convolutions of GPDs. Hence they are easy to relate to GPDs, but are only applicable to highly-boosted hadrons in Minkowski spacetime. This is not simply a matter of Lorentz-transforming back to another frame, since expressions such as Eq. (2.77) explicitly drop terms that are small in the infinite momentum frame, but may be non-negligible in other frames. For instance, in the infinite momentum frame there are only three possible Lorentz vectors with which to build tensor structures (see Appendix D), while in a generic frame for a spin 1/2 particle we have \bar{P} , \bar{q} , Δ as well as the Dirac bilinears. Therefore, although it is possible to derive the light-cone expansion from a covariant expansion, it is in general not possible to go the other way.

Second, there are older papers that attempt a complete non-perturbative tensor decomposition of the amplitude [196–199]:

$$T^{\mu\nu} = \sum_{i=1}^{18} \mathcal{A}_i(\bar{\omega}, \vartheta, t, \bar{Q}^2) L_i^{\mu\nu}, \quad (5.2)$$

where \mathcal{A}_i are scalar amplitudes, and $L_i^{\mu\nu}$ are gauge-invariant tensors. We have already seen a tensor decomposition like this for the forward Compton amplitude, Eq. (2.20). However, while the forward Compton amplitude can be parameterised by only four independent structures, the off-forward needs 18.

Although Eq. (5.2) can be compared to our lattice calculation[†], it would not be immediately clear how to interpret the scalar amplitudes, \mathcal{A}_i , in terms of GPDs. Existing tensor decompositions, especially Perrottet’s [196] and Tarrach’s work [197], are concerned with finding the most general possible form of the Compton amplitude, which means eliminating kinematic zeros and poles[‡]. However, since these works predate knowledge of GPDs, they are typically not interested in connecting their scalar amplitudes to physical observables, especially not GPDs.

In principle the perturbative light-cone expansion in terms of GPDs and the tensor decompositions describe the same object. Therefore, we expect that at high energies

[†]Up to $\mathcal{O}(a)$ differences between the lattice and continuum Ward identities.

[‡]For instance, a tensor structure of the form $\frac{1}{p \cdot q} \mathcal{A}$ has a kinematic pole at $p \cdot q = 0$, while $p \cdot q \mathcal{A}$ has a kinematic zero at the same point. However, this does not necessarily imply that the tensor structure \mathcal{A} goes to infinity or zero as $p \cdot q \rightarrow 0$, as \mathcal{A} itself may contain powers of $p \cdot q$. As such, these kinematic poles/zeros are undesirable for the most general tensor decomposition.

($\bar{Q}^2 \gg \Lambda_{\text{QCD}}^2$) the amplitudes of Eq. (5.2) are dominated by convolutions of GPDs [22,200]:

$$\mathcal{A} \simeq \int dx G(x, \vartheta/\bar{\omega}, t) \left[\frac{\bar{\omega}}{1+x\bar{\omega}-i\epsilon} \pm \frac{\bar{\omega}}{1-x\bar{\omega}-i\epsilon} \right],$$

where G is a GPD. Or, in the Euclidean region, $|\bar{\omega}| < 1$,

$$\mathcal{A} \simeq \sum_n \bar{\omega}^n \int dx x^{n-1} G(x, \vartheta/\bar{\omega}, t).$$

However, because light-cone perturbative expansion cannot be matched to the existing tensor decompositions, we need to do some of this work ourselves.

As such, in this section our ultimate aim is to derive a form of the OFCA that can be compared to our lattice calculation *and* can be related to leading-twist GPDs. The steps involved in this procedure are

1. Perform a perturbative expansion of the OFCA that is Lorentz covariant—i.e. valid in any frame. This means that, rather than using formalisms that require light-cone kinematics [201,202], we use the short-distance operator product expansion (OPE), discussed in Chapter 2 and Appendix C.
2. Start with a given tensor decomposition—we will use Tarrach’s [197]—and, with various Gordon-type identities [203], transform this basis into one that matches the OPE from the previous step[§].

As such this will give us the leading-twist content of all 18 scalar amplitudes of the OFCA, which allows us to interpret our lattice results in terms of GPDs. However, recall that the point is not a perturbative matching from our lattice results to GPDs. Instead, we want to know what the invariant amplitudes \mathcal{A} are in the partonic limit, but we are still interested in the finite $1/\bar{Q}^2$ corrections.

5.1.2 Operator product expansion

A suitable tool for a perturbative expansion of the OFCA is the short-distance operator product expansion (OPE). This recommends itself to comparison with a lattice calculation for two main reasons: (1) it does not rely on light-cone vectors but is instead Lorentz covariant; and (2) it is an expansion in a basis of *local* operators. Since the matrix elements of local operators are the same in Euclidean and Minkowski space—recall the discussion in Sections 3.2 and 4.2—we easily use the OPE to interpret our lattice results.

We have already seen an example of a short-distance OPE in Section 2.2.2, where the forward Compton amplitude was shown to be a power series in ω with PDF moments as the coefficients. Similarly, we find that the OPE of the OFCA is a power series in $\bar{\omega}$ with GPD moments as coefficients. There exist in the literature several OPEs of the OFCA [204–207]. However, as these largely focus on the spin-zero case and/or significantly pre-date GPDs, in this section we give our own OPE. We have used these previous studies, as well as expansions using the related light-ray operator formalism [20,201,208], as a guide.

[§]This means that, unlike Tarrach, we will not have a tensor decomposition free of kinematic zeroes and singularities. While this limits the generality of our results to all possible kinematics, it is completely adequate for our purpose.

Coordinate space matrix element

We start by recalling the OPE of the coordinate space current product, Eqs. (2.44) and (2.56), which gave us the ‘handbag’ contribution** [47, 51]:

$$\begin{aligned} \mathcal{T}\{j_\mu(z/2)j_\nu(-z/2)\} = & -2\frac{i}{2\pi^2}\frac{z^\mu}{(z^2-i\epsilon)^2}\left[\mathcal{S}_{\mu\rho\nu\kappa}\sum_{n=1,3,5}^{\infty}\frac{(-i)^n}{n!}z_{\mu_1}\dots z_{\mu_n}\mathcal{O}_f^{(n+1)\kappa\mu_1\dots\mu_n}(0)\right. \\ & \left.+i\varepsilon_{\mu\nu\rho\kappa}\sum_{n=0,2,4}^{\infty}\frac{(-i)^n}{n!}z_{\mu_1}\dots z_{\mu_n}\tilde{\mathcal{O}}_f^{(n+1)\kappa\mu_1\dots\mu_n}(0)\right], \end{aligned} \quad (5.3)$$

where $\mathcal{S}_{\mu\rho\nu\kappa} = g_{\mu\rho}g_{\nu\kappa} + g_{\mu\kappa}g_{\nu\rho} - g_{\mu\nu}g_{\rho\kappa}$, and the operators are defined in Eqs. (2.40) and (2.41).

In the forward case, the leading-order handbag term (see Fig. 2.5) is the dominant contribution to the Compton amplitude as long as $Q^2 \gg \Lambda_{\text{QCD}}^2$, and it is the only contribution in the asymptotic Bjorken limit, $Q^2 \rightarrow \infty$. Similarly, in the off-forward case the handbag contribution dominates as long as either $|q^2|$ or $|q'^2|$ are large [200]; in our case it is more convenient to express this as $\bar{Q}^2 \gg \Lambda_{\text{QCD}}^2$. However, additionally we need to keep our hard momentum transfer much greater than our soft momentum transfer [209]: $\bar{Q}^2 \gg |t|$.

To go from Eq. (5.3) to the OFCA, we simply need to: (1) take the matrix element between off-forward states, $\langle P'|\dots|P\rangle$; and (2) Fourier transform. Although formally simple, these steps can become quite involved. Hence we have kept most of the details in Appendix E, and below only sketch the process.

For convenience, we define the Dirac bilinears

$$\begin{aligned} h^\mu &= \bar{u}(P')\gamma^\mu u(P), & e^\mu &= \bar{u}(P')\frac{i\sigma^{\mu\alpha}\Delta_\alpha}{2m_N}u(P), \\ \tilde{h}^\mu &= \bar{u}(P')\gamma^\mu\gamma_5 u(P), & \tilde{e}^\mu &= \frac{\Delta^\mu}{2m_N}\bar{u}(P')\gamma_5 u(P). \end{aligned} \quad (5.4)$$

To take the off-forward matrix element of the current product OPE, Eq. (5.3), we simply substitute the off-forward matrix elements from Eqs. (2.78) and (D.6) into this expression. For instance, the $\mu \leftrightarrow \nu$ symmetric component is

$$\begin{aligned} \langle N(P')|\mathcal{T}\{j_{\{\mu}(z/2)j_{\nu\}}(-z/2)\}|N(P)\rangle = & -2\frac{i}{2\pi^2}\frac{z^\mu}{(z^2-i\epsilon)^2}\mathcal{S}_{\mu\rho\nu\kappa} \\ & \times \sum_{n=1,3,5}^{\infty}\frac{(-i)^n}{n!}\sum_{j=0,2,4}^n\left\{\frac{1}{n+1}(\Delta\cdot z)^j(\bar{P}\cdot z)^{n-j}[h^\kappa A_{n+1,j}(t) + e^\kappa B_{n+1,j}(t)]\right. \\ & + \frac{n-j}{n+1}(\Delta\cdot z)^j(\bar{P}\cdot z)^{n-j-1}\bar{P}^\kappa[A_{n+1,j}(t)h\cdot z + B_{n+1,j}(t)e\cdot z] \\ & + \frac{j}{n+1}(\Delta\cdot z)^{j-1}(\bar{P}\cdot z)^{n-j}\Delta^\kappa[A_{n+1,j}(t)h\cdot z + B_{n+1,j}(t)e\cdot z] \\ & \left.+ \delta_{j,0}\Delta^\kappa(\Delta\cdot z)^n C_{n+1}(t)\frac{1}{m_N}\bar{u}(P')u(P)\right\}. \end{aligned} \quad (5.5)$$

**Here, we drop the factor of the quark charge squared, e_f^2 , and the sum over flavours, both of which are simple to reintroduce.

The anti-symmetric component is given in Eq. (E.1).

Fourier transform

Then, to Fourier transform these matrix elements the general recipe is

1. Introduce Fourier conjugates,

$$\begin{aligned} (\bar{P} \cdot z)^n &= i^n \int_{-\infty}^{\infty} d\chi e^{i\chi \bar{P} \cdot z} \frac{\partial^n}{\partial \chi^n} \delta(\chi), \\ (\Delta \cdot z)^n &= i^n \int_{-\infty}^{\infty} d\eta e^{i\eta \Delta \cdot z} \frac{\partial^n}{\partial \eta^n} \delta(\eta), \\ h \cdot z &= i \int_{-\infty}^{\infty} d\tilde{\chi}_1 e^{i\tilde{\chi}_1 h \cdot z} \frac{\partial}{\partial \tilde{\chi}_1} \delta(\tilde{\chi}_1), \\ e \cdot z &= i \int_{-\infty}^{\infty} d\tilde{\chi}_2 e^{i\tilde{\chi}_2 e \cdot z} \frac{\partial}{\partial \tilde{\chi}_2} \delta(\tilde{\chi}_2). \end{aligned}$$

For the polarised component $h(e) \rightarrow \tilde{h}(\tilde{e})$, but otherwise the process is the same.

2. Use the identity

$$\int d^4 z e^{il \cdot z} \frac{z^\mu}{2\pi^2(z^2 - i\epsilon)^2} = \frac{l^\mu}{l^2 + i\epsilon}$$

to integrate out the z -dependence.

3. Use the identity

$$\int_a^b dx f(x) \frac{\partial^n}{\partial x^n} \delta(x - y) = (-1)^n \frac{\partial^n}{\partial x^n} f(x) \Big|_{x=y},$$

to evaluate the integrals over the Fourier conjugates.

The final result for the component symmetric in $\mu \leftrightarrow \nu$ is

$$\begin{aligned} T^{\{\mu\nu\}}(\bar{\omega}, \vartheta, t) &= \frac{2}{Q^2} \sum_{n=2,4,6}^{\infty} \sum_{j=0,2,4}^{n-1} \left\{ \frac{2}{n} \bar{\omega}^{n-2} (-2\xi)^j [h^{\{\mu} A_{n,j}(t) + e^{\{\mu} B_{n,j}(t)] (\bar{\omega} \bar{q}^{\nu\}} + 2\bar{P}^{\nu\})} \right. \\ &+ \frac{4}{Q^2} \frac{1}{n} \bar{\omega}^{n-3} (-2\xi)^j [A_{n,j}(t) h \cdot \bar{q} + B_{n,j}(t) e \cdot \bar{q}] \left((n-1) \bar{\omega} \bar{P}^{\{\mu} \bar{q}^{\nu\}} + (n-2) \bar{P}^\mu \bar{P}^\nu \right) \\ &+ \frac{4}{Q^2} \delta_{j,0} \bar{\omega}^{n-3} (-2\xi)^n C_n(t) (h \cdot \bar{q} - e \cdot \bar{q}) (\bar{\omega} \bar{P}^{\{\mu} \bar{q}^{\nu\}} + \bar{P}^\mu \bar{P}^\nu) \\ &\left. - g^{\mu\nu} \bar{\omega}^{n-1} \left((-2\xi)^j [A_{n,j}(t) h \cdot \bar{q} + B_{n,j}(t) e \cdot \bar{q}] + \delta_{j,0} (-2\xi)^n C_n(t) (h \cdot \bar{q} - e \cdot \bar{q}) \right) \right\}, \end{aligned} \tag{5.6}$$

where we have used $\xi = \vartheta/\bar{\omega}$ to simplify. While for the anti-symmetric contribution, we have

$$T^{[\mu\nu]}(\bar{\omega}, \vartheta, t) = \frac{2}{\bar{Q}^2} i\varepsilon^{\mu\nu\rho\kappa} \sum_{n=1,3,5}^{\infty} \sum_{j=0,2,4}^{n-1} \bar{\omega}^{n-2} (-2\xi)^j \left\{ \frac{1}{n} \left[\tilde{h}_\kappa \tilde{A}_{n,j}(t) + \tilde{e}_\kappa \tilde{B}_{n+1,j}(t) \right] \bar{\omega} \bar{q}_\rho \right. \\ \left. + \frac{2}{\bar{Q}^2} \frac{n-1}{n} \bar{P}_\kappa \bar{q}_\rho \left[\tilde{A}_{n,j}(t) \tilde{h} \cdot \bar{q} + \tilde{B}_{n+1,j}(t) \tilde{e} \cdot \bar{q} \right] \right\}, \quad (5.7)$$

where we have used the bilinear definitions given in Eq. (5.4).

Comparison to canonical results

It is useful to compare our results to existing perturbative expansions using the light-like kinematics, as in Eq. (2.77). This serves two purposes: (1) it is a cross-check of our results, and (2) it demonstrates how the light-cone kinematics simplify the expression massively but also lead us to lose information.

To start, we note that the Sudakov decomposition (see Appendix D) is

$$\bar{P}^\mu \simeq \bar{n}^\mu, \quad \bar{q}^\mu \simeq \frac{\bar{Q}^2}{2\xi} n^\mu, \quad h^\mu \simeq (n \cdot h) \bar{n}^\mu, \quad e^\mu \simeq (n \cdot e) \bar{n}^\mu \\ \tilde{h}^\mu \simeq (n \cdot \tilde{h}) \bar{n}^\mu, \quad \tilde{e}^\mu \simeq (n \cdot \tilde{e}) \bar{n}^\mu.$$

Therefore, with DVCS kinematics ($\xi \simeq \bar{\omega}^{-1}$ and $\vartheta \simeq 1$), Eq. 5.6 becomes

$$T^{\{\mu\nu\}} = (n^\mu \bar{n}^\nu + n^\nu \bar{n}^\mu - g^{\mu\nu}) \sum_{n=2,4,6}^{\infty} \xi^{-n} \left[\left(\sum_{j=0,2,4}^{n-1} (2\xi)^j A_{n,j}(t) + (2\xi)^n C_{n+1}(t) \right) h \cdot n \right. \\ \left. + \left(\sum_{j=0,2,4}^{n-1} (2\xi)^j B_{n,j}(t) - (2\xi)^n C_{n+1}(t) \right) e \cdot n \right]. \quad (5.8)$$

Then, using the polynomiality relations, Eq. (2.79), this becomes^{††}

$$T^{\{\mu\nu\}} = (n^\mu \bar{n}^\nu + n^\nu \bar{n}^\mu - g^{\mu\nu}) \sum_{n=2,4,6}^{\infty} \xi^{-n} \int_{-1}^1 dx x^{n-1} [H(x, \xi, t) h \cdot n + E(x, \xi, t) e \cdot n] \\ = \frac{1}{2} (g^{\mu\nu} - n^\mu \bar{n}^\nu - n^\nu \bar{n}^\mu) \int_{-1}^1 dx \left(\frac{1}{x - \xi + i\varepsilon} + \frac{1}{x + \xi + i\varepsilon} \right) \\ \times [H(x, \xi, t) h \cdot n + E(x, \xi, t) e \cdot n], \quad (5.9)$$

and hence we recover the standard perturbative expansion of the DVCS amplitude, Eq. (2.77). The same process can be applied to the anti-symmetric component—see Appendix E. Comparing Eqs. (5.6) and (5.9), we can see just how much information is lost by using collinear light-like kinematics.

^{††}Note that, since definitions of ξ often differ by a factor of two between different works, polynomiality expressions may be expressed in powers of 2ξ or just ξ .

Electromagnetic gauge invariance

Further, notice that Eqs. (5.6) and (5.7) violate electromagnetic (EM) gauge invariance (their Ward identities) by terms linear in $\Delta_{\perp}^{\mu} = \Delta^{\mu} + (2\partial/\bar{\omega})\bar{P}^{\mu}$. Specifically, Eqs. (5.6) and (5.7) are transverse with respect to \bar{q}_{μ} but not Δ_{μ} . Since the Ward identities for off-forward scattering can be expressed as

$$(\bar{q} + \Delta/2)_{\mu} T^{\mu\nu} = 0 = (\bar{q} - \Delta/2)_{\nu} T^{\mu\nu},$$

this means that these expressions do not completely satisfy their Ward identities. This property is found in all leading-twist expansions of the off-forward Compton amplitude [20, 208, 210].

We can understand this by noting that our coordinate space OPE, Eq. (5.3), has current conservation with respect to the displacement z_{μ} :

$$\partial_z^{\mu} \mathcal{T} \{j_{\mu}(X + z/2) j_{\nu}(X - z/2)\} = 0.$$

However, with respect to the central coordinate, X_{μ} ,

$$\partial_X^{\mu} \mathcal{T} \{j_{\mu}(X + z/2) j_{\nu}(X - z/2)\} \neq 0.$$

The EM gauge invariance of this leading-twist OFCA has been studied in detail elsewhere [20, 207, 208, 210], where it has been found that gauge invariance can be restored by considering ‘total derivative’ operators—operators that contain ∂_X^{μ} derivatives^{‡‡}—which are typically left out of the OPE since (1) they vanish between forward matrix elements; and (2) they are in-principle twist-three.

Fortunately for us, the process of including the total derivative operators is equivalent to the *ad hoc* inclusion of tensor structures that restore the gauge invariance: $\bar{P}^{\mu}\Delta^{\nu}$, $h^{\mu}\Delta^{\nu}$, $e^{\mu}\Delta^{\nu}$, $\Delta^{\mu}\Delta^{\nu}$, etc. Therefore, our work for the perturbative expansion is complete: we can match, for instance, the $g_{\mu\nu}$ contribution in Eq. (5.6) to a gauge invariant tensor decomposition, without worrying about extra gauge dependent terms.

5.1.3 Tensor decomposition

From Feynman-Hellmann techniques, we compute the full, non-perturbative Compton amplitude, not just the leading-twist contribution. Therefore, our ultimate aim in this section is to derive a non-perturbative tensor decomposition, as we saw in the forward case, Eq. (2.20), that can be matched to the OPE result. This has already been accomplished by Tarrach [197], building on the works of Bardeen and Tung [211] and Perrottet [196]. Tarrach’s basis of tensor structures is chosen to minimise the number of kinematic poles and singularities; this basis, however, is extremely difficult to match onto the leading-twist GPDs (and PDFs). Hence, starting with Tarrach’s decomposition, we rework it into a basis that resembles the OPE results, Eqs. (5.6) and (5.7).

^{‡‡}Since ∂_X^{μ} produces factors of $-i\Delta^{\mu}$ between two off-forward states, these total derivatives produce vanishing contribution in the forward limit, but non-vanishing contributions in the off-forward case.

As previously discussed, the OFCA, Eq. (2.72), can be decomposed into 18 linearly independent tensor structures [196–199, 212]:

$$T^{\mu\nu}(\bar{\omega}, \vartheta, t, \bar{Q}^2) = \sum_{i=1}^{18} \mathcal{A}_i(\bar{\omega}, \vartheta, t, \bar{Q}^2) L_i^{\mu\nu},$$

where \mathcal{A}_i are invariant amplitudes and $L_i^{\mu\nu}$ are Lorentz tensors and Dirac bilinears.

As a result of the Ward identities, $q_\mu T^{\mu\nu} = 0 = q'_\nu T^{\mu\nu}$, contributions to the Compton amplitude that are proportional to q_ν or q'_μ are not linearly independent. Hence we can write the OFCA as

$$T^{\mu\nu} = \bar{T}_{\rho\sigma} \mathcal{P}^{\mu\rho} \mathcal{P}^{\sigma\nu},$$

where the gauge projector is

$$\mathcal{P}^{\mu\nu} = g^{\mu\nu} - \frac{q'^\mu q^\nu}{q \cdot q'}, \quad (5.10)$$

and $\bar{T}_{\mu\nu}$ is the OFCA without q_ν or q'_μ terms.

Therefore, the tensor decomposition basis of the full OFCA is determined by that of $\bar{T}_{\mu\nu}$, since all other terms are entirely determined by the Ward identities. To arrive at a suitable basis, we take Tarrach's basis and apply various Gordon(-type) identities, to arrive at an expression that can be easily matched to the OPE. The details of this process are outlined in Appendix E. The final result is

$$\begin{aligned} \bar{T}_{\mu\nu} = & \frac{1}{2\bar{P} \cdot \bar{q}} \left\{ - \left(h \cdot \bar{q} \mathcal{H}_1 + e \cdot \bar{q} \mathcal{E}_1 \right) g_{\mu\nu} + \frac{1}{\bar{P} \cdot \bar{q}} \left(h \cdot \bar{q} \mathcal{H}_2 + e \cdot \bar{q} \mathcal{E}_2 \right) \bar{P}_\mu \bar{P}_\nu \right. \\ & \left. + \mathcal{H}_3 h_{\{\mu} \bar{P}_{\nu\}} \right\} + \frac{i}{2\bar{P} \cdot \bar{q}} \epsilon_{\mu\nu\rho\kappa} \bar{q}^\rho \left\{ \tilde{h}^\kappa \tilde{\mathcal{H}}_1 + \tilde{e}^\kappa \tilde{\mathcal{E}}_1 + \frac{1}{\bar{P} \cdot \bar{q}} \left[(\bar{P} \cdot \bar{q} \tilde{h}^\kappa - \tilde{h} \cdot \bar{q} \bar{P}^\kappa) \tilde{\mathcal{H}}_2 \right. \right. \\ & \left. \left. + (\bar{P} \cdot \bar{q} \tilde{e}^\kappa - \tilde{e} \cdot \bar{q} \bar{P}^\kappa) \tilde{\mathcal{E}}_2 \right] \right\} + \left(\bar{P}_\mu q'_\nu + \bar{P}_\nu q_\mu \right) \left(h \cdot \bar{q} \mathcal{K}_1 + e \cdot \bar{q} \mathcal{K}_2 \right) \\ & + \left(\bar{P}_\mu q'_\nu - \bar{P}_\nu q_\mu \right) \left(h \cdot \bar{q} \mathcal{K}_3 + e \cdot \bar{q} \mathcal{K}_4 \right) + q_\mu q'_\nu \left(h \cdot \bar{q} - e \cdot \bar{q} \right) \mathcal{K}_5 \\ & + h_{[\mu} \bar{P}_{\nu]} \mathcal{K}_6 + \left(h_\mu q'_\nu + h_\nu q_\mu \right) \mathcal{K}_7 + \left(h_\mu q'_\nu - h_\nu q_\mu \right) \mathcal{K}_8 + \bar{P}_{\{\mu} \bar{u}(P') i \sigma_{\nu\}} u(P) \bar{q}^\alpha \mathcal{K}_9, \end{aligned} \quad (5.11)$$

using the Dirac bilinears from Eq. (5.4). In Eq. (5.11), there are nine \mathcal{K} , five unpolarised (\mathcal{H} and \mathcal{E}) and four polarised ($\tilde{\mathcal{H}}$ and $\tilde{\mathcal{E}}$) amplitudes, which gives 18 in total.

The basis in Eq. (5.11) is chosen to match onto the high-energy limit, from the OPE expression, Eqs. (5.6) and (5.7). While this does introduce kinematic singularities into our basis, these are not relevant to the leading-twist contribution or our numerical calculation.

The amplitudes of Eq. (5.11) also reduce in the forward ($t \rightarrow 0$) limit to the more well-known functions of the forward Compton amplitude:

$$\begin{aligned} \mathcal{H}_1 & \xrightarrow{t \rightarrow 0} \mathcal{F}_1, & \mathcal{H}_2 + \mathcal{H}_3 & \xrightarrow{t \rightarrow 0} \mathcal{F}_2, \\ \tilde{\mathcal{H}}_1 & \xrightarrow{t \rightarrow 0} \tilde{g}_1, & \tilde{\mathcal{H}}_2 & \xrightarrow{t \rightarrow 0} \tilde{g}_2, \end{aligned}$$

where $\mathcal{F}_{1,2}$ are the Compton structure functions [37] and $\text{Im} \tilde{g}_{1,2} = 2\pi g_{1,2}$, for $g_{1,2}$ the spin-dependent, deep-inelastic structure functions [57], which we will study in Chapter 7. On the other hand, the \mathcal{K} amplitudes vanish in the forward limit.

To be consistent with the rest of the off-forward literature, we refer to the amplitudes in Eq. (5.11) as *Compton form factors* (CFFs). Therefore, when we are at $t \neq 0$ these amplitudes are CFFs, but when we are at $t = 0$ they become Compton structure functions.

Comparison to OPE

Comparing the OPE results, Eqs. (5.6) and (5.7), to interpret the high energy limit of each of the scalar amplitudes in the tensor decomposition, we have:

- A complete list of the leading-twist contribution to all the amplitudes is given in Eq. (E.17). All of the \mathcal{K} amplitudes vanish. For the remaining nine amplitudes, these are expressed in terms of a sum of GPDs moments:

$$\mathcal{H}_1(\bar{\omega}, \vartheta, t) = 2 \sum_{n=1}^{\infty} \bar{\omega}^{2n} \int_{-1}^1 dx x^{2n-1} H(x, \vartheta/\bar{\omega}, t).$$

- We find off-forward equivalents of the Callan-Gross relation, Eq. (2.37):

$$\mathcal{H}_1 = \frac{\bar{\omega}}{2} (\mathcal{H}_2 + \mathcal{H}_3), \quad \mathcal{E}_1 = \frac{\bar{\omega}}{2} \mathcal{E}_2. \quad (5.12)$$

For the forward Compton amplitude, Feynman-Hellmann methods have been used to determine power-suppressed Callan-Gross breaking [38].

- At leading-twist, the polarised scalar amplitudes have an off-forward analogue of the Wandzura-Wilczek relation, Eq. (2.68):

$$\int_0^1 dx x^n \text{Im} \tilde{\mathcal{H}}_1(1/x, \vartheta/\bar{\omega}, t) = -\frac{n+1}{n} \int_0^1 dx x^n \text{Im} \tilde{\mathcal{H}}_2(1/x, \vartheta/\bar{\omega}, t), \quad (5.13)$$

and similarly for the replacement $\tilde{\mathcal{H}} \rightarrow \tilde{\mathcal{E}}$. In the $t \rightarrow 0$ limit, this reduces to the Wandzura-Wilczek relation [68, 75], Eq. (2.68).

- The leading-twist contribution to the subtraction function, Eq. (5.18), is

$$S_1(\vartheta, t) = 2 \sum_{n=1}^{\infty} (2\vartheta)^{2n} C_{2n}(t), \quad (5.14)$$

a result that has been found in previous studies using different formalisms [84–87]. Therefore, a lattice calculation of S_1 for $\vartheta \neq 0$ could be used to extract the D -term.

Dispersion relation

Recall from the Section 4.2 that dispersion relations are important for our method, as they allow us to relate the Compton amplitude in the unphysical region $|\bar{\omega}| < 1$, where our lattice calculation is possible, to the physical Compton amplitude with $|\bar{\omega}| > 1$. Therefore, here we present equations of the form in Eq. (4.79) for the off-forward amplitudes in Eq. (5.11). To do this we quote some results derived in Regge theory [213–215]—more details on the analytic features of the amplitudes can be found in Appendix B.

We start by defining the variable

$$\nu = \frac{\bar{P} \cdot \bar{q}}{m_N}. \quad (5.15)$$

Then, from Refs. [213–215], in the Regge limit $\nu \rightarrow \infty$ with fixed t and \bar{Q}^2 , our amplitudes have the following behaviour:

$$\mathcal{H}_1, \mathcal{E}_1, \mathcal{K}_6 \sim \nu^{\alpha_M(t)}, \quad \text{all other amplitudes} \sim \nu^{\alpha_M(t)-1}, \nu^{\alpha_M(t)-2}, \text{ or } \nu^{\alpha_M(t)-3}, \quad (5.16)$$

where $\alpha_M(t) \lesssim 0.5$. Since $\bar{\omega} = m_N \nu / \bar{Q}^2$, at fixed \bar{Q}^2 the amplitudes will go like

$$\lim_{\bar{\omega} \rightarrow \infty} \mathcal{H}_1, \mathcal{E}_1, \mathcal{K}_6 \rightarrow \infty, \quad \text{while} \quad \lim_{\bar{\omega} \rightarrow \infty} \mathcal{A} \rightarrow 0, \quad (5.17)$$

for all other amplitudes.

As can be seen in Appendix B, this means that the amplitudes \mathcal{H}_1 , \mathcal{E}_1 and \mathcal{K}_6 satisfy subtracted dispersion relations:

$$\begin{aligned} \mathcal{H}_1(\bar{\omega}, \vartheta, t, \bar{Q}^2) &= S_1(\vartheta, t, \bar{Q}^2) + \frac{2\bar{\omega}^2}{\pi} \int_0^1 dx \frac{x \text{Im} \mathcal{H}_1(x, \vartheta, t, \bar{Q}^2)}{1 - x^2 \bar{\omega}^2 - i\epsilon}, \\ \mathcal{E}_1(\bar{\omega}, \vartheta, t, \bar{Q}^2) &= -S_1(\vartheta, t, \bar{Q}^2) + \frac{2\bar{\omega}^2}{\pi} \int_0^1 dx \frac{x \text{Im} \mathcal{E}_1(x, \vartheta, t, \bar{Q}^2)}{1 - x^2 \bar{\omega}^2 - i\epsilon} \\ \mathcal{K}_6(\bar{\omega}, \vartheta, t, \bar{Q}^2) &= S_2(\vartheta, t, \bar{Q}^2) + \frac{2\bar{\omega}^2}{\pi} \int_0^1 dx \frac{x \text{Im} \mathcal{K}_6(x, \vartheta, t, \bar{Q}^2)}{1 - x^2 \bar{\omega}^2 - i\epsilon}. \end{aligned} \quad (5.18)$$

Since the amplitude \mathcal{K}_6 vanishes for zero-skewness kinematics and all our lattice calculations are at zero-skewness, this amplitude does not concern us.

From Eq. (5.18), we define

$$\begin{aligned} \bar{\mathcal{H}}_1(\bar{\omega}, \vartheta, t, \bar{Q}^2) &\equiv \mathcal{H}_1(\bar{\omega}, \vartheta, t, \bar{Q}^2) - S_1(\vartheta, t, \bar{Q}^2), \\ \bar{\mathcal{E}}_1(\bar{\omega}, \vartheta, t, \bar{Q}^2) &\equiv \mathcal{E}_1(\bar{\omega}, \vartheta, t, \bar{Q}^2) + S_1(\vartheta, t, \bar{Q}^2). \end{aligned} \quad (5.19)$$

Note that S_1 defined in Eq. (5.18) is a generalisation of the forward Compton amplitude subtraction function in Eq. (2.26): $S_1(\vartheta, t, \bar{Q}^2) \xrightarrow{t \rightarrow 0} S_1(Q^2)$. The forward subtraction function, $S_1(Q^2)$, was briefly discussed in Section 2.2.2 and will be the focus of Chapter 8. The off-forward subtraction function is physically interesting as a test of the ‘fixed pole’ hypothesis in Regge phenomenology [216, 217], and moreover because it is a background for experimental determinations of the proton pressure distribution [89].

The other amplitudes satisfy an *unsubtracted* dispersion relation, such as for the polarised Compton structure functions^{§§}, Eq. (2.54). These dispersion relations are examples of a Fredholm integral equation as in Eq. (4.79). Again, the inverse problem arises from the difficulty associated with inverting these integral equations to solve for the amplitude in the physical region.

^{§§}The form of the unsubtracted dispersion relation depends on whether or not a factor of $1/\bar{P} \cdot \bar{q}$ has been taken out of the amplitude, thereby making it odd under $\bar{\omega} \rightarrow -\bar{\omega}$. See Appendix B for more details.

In the $t \rightarrow 0$ limit, the dispersion relation for $\bar{\mathcal{H}}_1$ recovers Eq. (2.26):

$$\bar{\mathcal{H}}_1(\bar{\omega}, \vartheta, t, \bar{Q}^2) \xrightarrow{t \rightarrow 0} 4\omega^2 \int_0^1 dx \frac{x F_1(x, Q^2)}{1 - x^2 \omega^2 - i\epsilon},$$

where F_1 is the deep-inelastic scattering structure function. However, unlike the forward case, there is no optical theorem to relate $\text{Im}\mathcal{H}_{1,2}$ to an inclusive cross section. Instead, we can compare the Minkowski amplitudes, $\text{Im}\mathcal{A}$, to those extracted from experiment in DVCS or a related process. Moreover, at large values of the hard scale, $\bar{Q}^2 \gg \Lambda_{\text{QCD}}^2$, we can interpret the Mellin moments of the CFFs as GPD moments, using the OPE result.

5.1.4 Parameterisation for the lattice

In Chapter 4, we derived the Feynman-Hellmann relation, Eq. (4.50), that allowed us to calculate the OFCA. In particular, we calculate the quantity

$$\mathcal{R}_{\mu\nu}(\bar{\omega}, t, \bar{Q}^2) = \frac{\sum_{s,s'} \text{tr}[\Gamma u(P', s') T_{\mu\nu} \bar{u}(P, s)]}{\sum_s \text{tr}[\Gamma_{\text{unpol}} u(P', s) \bar{u}(P', s)]},$$

where Γ is a spin-parity projector.

Using the results of the tensor decomposition and OPE, Eqs. (5.11) and (E.17), we want to parameterise $\mathcal{R}_{\mu\nu}$ in terms of leading-twist GPDs. To do so, we note that for our lattice calculation we have the following restrictions:

- We choose the $\mu = \nu = 3$ component of the Compton amplitude.
- The Feynman-Hellmann relation requires $\bar{q}^0 = \Delta^0 = 0$.
- We choose zero-skewness ($\xi = 0 = \vartheta$) kinematics by choosing $\mathbf{q}_1^2 = \mathbf{q}_2^2$.
- We choose the spin-parity projector $\Gamma = (\mathbb{I} + \gamma_0)/2$.

Although it cannot be accessed experimentally, the zero-skewness region is physically interesting as at zero-skewness GPDs can be Fourier transformed to spatial probability distributions [23]. Moreover, the GFFs that parameterise the zero-skewness GPD moments are those relevant to the spin decomposition and mechanical properties of hadrons.

This zero-skewness condition also removes the tensor structures with scalar amplitudes $\mathcal{K}_{3,4,6,8,9}$ and $\tilde{\mathcal{E}}_2$ (see Appendix E). Further, by calculating the $\mu = \nu = 3$ component and taking a spin trace, we remove tensor structures associated with $\tilde{\mathcal{H}}_1$ and $\tilde{\mathcal{E}}_1$. While there is a contribution from the tensor structure with amplitude $\tilde{\mathcal{H}}_2$, it is suppressed by a factor of $1/\bar{Q}^4$. Hence it is very small compared to the \mathcal{H} and \mathcal{E} terms. See Appendix F for the results of the spin-parity traces.

Finally, our lattice calculation will have a hard scale of $\bar{Q}^2 \sim 7 \text{ GeV}^2$. As such, we can approximately treat the remaining amplitudes, $\mathcal{K}_{1,2,5,7}$, as suppressed since they have no leading-twist contribution. This leaves only the $\mathcal{H}_{1,2,3}$ and $\mathcal{E}_{1,2}$ amplitudes.

Applying these conditions, Eq. (4.55) becomes

$$\begin{aligned} \mathcal{R}_{\mu\nu}(\bar{\omega}, \vartheta, t, \bar{Q}^2) = & \frac{1}{E_N + m_N} \left\{ -g^{\rho\sigma} [(E_N + m_N)\mathcal{H}_1 + \frac{t}{4m_N}\mathcal{E}_1] \right. \\ & \left. + \frac{\bar{P}^\rho \bar{P}^\sigma}{\bar{P} \cdot \bar{q}} [(E_N + m_N)(\mathcal{H}_2 + \mathcal{H}_3) + \frac{t}{4m_N}\mathcal{E}_2] \right\} \mathcal{P}_{\mu\rho} \mathcal{P}_{\sigma\nu}, \end{aligned} \quad (5.20)$$

with $\mathcal{P}^{\mu\nu}$ as defined in Eq. (5.10).

Next, we note that at $\bar{\omega} = 0$

$$\mathcal{R}_{\mu\nu}(\bar{\omega} = 0, t, \bar{Q}^2) = \left(1 - \frac{t}{4m_N(E_N + m_N)}\right) \left(-g_{\mu\nu} + \frac{q'_\mu q'_\nu}{q \cdot q'}\right) S_1(t, \bar{Q}^2), \quad (5.21)$$

using the subtraction function definition in Eq. (5.18).

Therefore, subtracting off the $\bar{\omega} = 0$ contribution,

$$\bar{\mathcal{R}}_{\mu\nu}(\bar{\omega}, t, \bar{Q}^2) = \mathcal{R}_{\mu\nu}(\bar{\omega}, t, \bar{Q}^2) - \mathcal{R}_{\mu\nu}(\bar{\omega} = 0, t, \bar{Q}^2), \quad (5.22)$$

is equivalent to replacing $\mathcal{H}_1 \rightarrow \bar{\mathcal{H}}_1$ and $\mathcal{E}_1 \rightarrow \bar{\mathcal{E}}_1$ in Eq. (5.20), where we have used the definition Eq. (5.19).

As we discuss in Section 5.2 and in more depth in Chapter 8, our calculation of S_1 has asymptotic behaviour at odds with the prediction from the OPE. Since this will be our primary focus in Chapter 8, we do not discuss the subtraction in great depth in this chapter.

Next we substitute the OPE results from Eq. (E.17) into Eq. (5.21):

$$\bar{\mathcal{R}}_{\mu\nu}(\bar{\omega}, t) = 2K_{\mu\nu} \sum_{n=1}^{\infty} \bar{\omega}^{2n} \left[A_{2n,0}(t) + \frac{t}{4m_N(E_N + m_N)} B_{2n,0}(t) \right], \quad (5.23)$$

where we have defined the kinematic factor

$$K_{\mu\nu} = \frac{\bar{P}_\mu \bar{q}_\nu + \bar{P}_\nu \bar{q}_\mu + \Delta_{[\mu} \bar{P}_{\nu]}}{\bar{P} \cdot \bar{q}} + \frac{\bar{Q}^2}{(\bar{P} \cdot \bar{q})^2} \bar{P}_\mu \bar{P}_\nu + \delta_{\mu\nu}, \quad (5.24)$$

which neglects suppressed $\Delta_\mu \Delta_\nu / \bar{P} \cdot \bar{q}$ terms.

For a first approximation of extracting the GPD moments, we will calculate

$$\bar{\mathcal{R}}_{kk}(\bar{\omega}, t, \bar{Q}^2) / K_{kk}(\bar{P}_3, \bar{q}_3, \bar{P} \cdot \bar{q}, \bar{Q}^2).$$

Since our lattice calculations are in frames that are roughly near the rest frame (i.e. $E_N \approx m_N$), we can approximate combination of GFFs in Eq. (5.23) as a Lorentz scalar:

$$M_n^f(t) \equiv A_{n,0}^f(t) + \frac{t}{8m_N^2} B_{n,0}^f(t). \quad (5.25)$$

Therefore,

$$\bar{\mathcal{R}}_{kk}(\bar{\omega}, t) / K_{kk} = 2 \sum_{n=1}^{\infty} \bar{\omega}^{2n} M_{2n}^f(t), \quad (5.26)$$

allowing a fit in $\bar{\omega}$ to extract the moments, $M_n^f(t)$.

Limitations

We highlight that this parameterisation is limited for a two main reasons

1. It is desirable to determine the helicity-conserving (A GFFs or equivalently \mathcal{H} CFFs) and helicity-flipping structures (B GFFs or equivalently \mathcal{E} CFFs) independently. By contrast, we only extract the linear combination in Eq. (5.23).

Table 5.1: Details of the gauge ensemble used in this chapter [218].

N_f	c_{SW}	β	κ_l, κ_s	$N_L^3 \times N_T$	a [fm]	m_π [MeV]	Z_V	N_{cfg}
2 + 1	2.65	5.50	0.1209	$32^3 \times 64$	0.074	468	0.861	1764

2. We are ultimately interested in looking at the \bar{Q}^2 dependence of the CFFs and the difference between, for instance \mathcal{H}_1 and $\mathcal{H}_2 + \mathcal{H}_3$, which would provide highly interesting and useful phenomenological information. However, in the above parameterisation we have lost this information, by approximating the CFFs with their leading-twist contributions.

We will address both these issues in Chapter 6. However, the lattice calculation presented in this chapter is highly exploratory, and our main goal is to show that we are capable of calculating the OFCA with this method.

5.2 Lattice Results

We are now ready to apply the Feynman-Hellmann formalism of Chapter 4 and the parameterisation presented above for an exploratory lattice calculation of the OFCA.

5.2.1 Simulation details

To perform this calculation, we use gauge ensembles generated by the CSSM/QCDSF/UKQCD collaboration [218]. These configurations are at the SU(3) flavour symmetric point, $\kappa_l = \kappa_s$, with a non-physical pion mass, $m_\pi = 468$ MeV, approximately three times the physical mass. Details of these gauge ensembles are given in Table 5.1.

Feynman-Hellmann implementation

As discussed in Section 4.2, we implement Feynman-Hellmann on the level of perturbed quark propagators:

$$S_\lambda(z_n, z_m) = [M - \lambda_1 \mathcal{O}_1 - \lambda_2 \mathcal{O}_2]_{n,m}^{-1}, \quad (5.27)$$

where M is the usual fermion matrix. To get the $\mu = \nu = 3$ component of the OFCA we choose the perturbing matrices to be

$$[\mathcal{O}_1]_{n,m} = \delta_{n,m} (e^{i\mathbf{q}_1 \cdot \mathbf{z}_n} + e^{-i\mathbf{q}_1 \cdot \mathbf{z}_n}) \gamma_3, \quad [\mathcal{O}_2]_{n,m} = \delta_{n,m} (e^{i\mathbf{q}_2 \cdot \mathbf{z}_n} + e^{-i\mathbf{q}_2 \cdot \mathbf{z}_n}) \gamma_3. \quad (5.28)$$

As discussed in Section 4.2, this means that our results do not include disconnected contributions to the OFCA. These contributions could be calculated with an extension of the FH method that would incur significantly greater computational costs.

Recall the Feynman-Hellmann relation, Eq. (4.50):

$$\left. \frac{\partial^2}{\partial \lambda_1 \partial \lambda_2} \frac{\mathcal{G}_\lambda(\tau)}{\mathcal{G}_0(\tau)} \right|_{\lambda=0} \stackrel{\tau \gg a}{\simeq} B_{\text{int}} + \frac{\tau}{2E_N(\mathbf{p}')} T_{kk}(\mathbf{p}, \mathbf{p}'; \mathbf{q}_1, \mathbf{q}_2).$$

Table 5.2: Current insertion momenta, $\mathbf{q}_{1,2}$, and derived kinematics for two sets of correlators. All data on configurations with $N_L^3 \times N_T = 32^3 \times 64$, $\kappa_{l,s} = 0.1209$, $\beta = 5.5$.

\bar{Q}^2 [GeV ²]	t [GeV ²]	\mathbf{q}_1 $2\pi/L$	\mathbf{q}_2 $2\pi/L$	Δ $2\pi/L$	λ	N_{meas}
7.13	0	(5, 1, 0)	—	—	(0.0125, 0.025)	7036
7.13	-1.10	(1, 5, 1)	(-1, 5, 1)	(2, 0, 0)	(0.0125, 0.025)	996
6.03	-2.20	(4, 2, 2)	(2, 4, 2)	(2, -2, 0)	(0.0125, 0.025)	996

In practice, we approximate the mixed second-order derivative by Eq. (4.53):

$$R_\lambda \equiv \frac{\mathcal{G}_{(\lambda,\lambda)} + \mathcal{G}_{(-\lambda,-\lambda)} - \mathcal{G}_{(\lambda,-\lambda)} - \mathcal{G}_{(-\lambda,\lambda)}}{\mathcal{G}_{(0,0)}}.$$

Therefore, to evaluate R_λ we need to calculate the perturbed propagators for four combinations: $(\lambda_1, \lambda_2) = (\lambda, \lambda), (-\lambda, -\lambda), (-\lambda, \lambda)$, and $(\lambda, -\lambda)$. Moreover, because we want to ensure that we are extracting the λ^2 contribution of R_λ , we calculate two magnitudes of $\lambda = 0.0125, 0.025$, chosen based on λ -tuning tests carried out in the forward case [37, 178].

Kinematics

The momenta $\mathbf{q}_{1,2}$ we choose in our perturbing matrices, Eq. (5.28), determine the hard and soft momentum transfers from Eq. (2.74):

$$\bar{Q}^2 = \frac{1}{4}(\mathbf{q}_1 + \mathbf{q}_2)^2 = \bar{\mathbf{q}}^2, \quad t = -(\mathbf{q}_1 - \mathbf{q}_2)^2 = -\Delta^2. \quad (5.29)$$

Moreover, as we discussed previously, the zero-skewness case is set by

$$\vartheta = -\frac{\Delta \cdot \bar{\mathbf{q}}}{\bar{Q}^2} = \frac{q^2 - q'^2}{2\bar{Q}^2} = 0,$$

and hence we ensure zero-skewness by choosing $|\mathbf{q}_1| = |\mathbf{q}_2|$.

Therefore, in choosing our momenta $\mathbf{q}_{1,2}$, we want $|\mathbf{q}_1| = |\mathbf{q}_2|$; see Fig. 5.2.1. Moreover, for our initial studies, we are mostly interested in varying the soft momentum transfer, t , at fixed \bar{Q}^2 . Hence we calculate two sets of correlators, with different $\mathbf{q}_{1,2}$ —see Table 5.2. This gives us two different values of the soft momentum transfer, $t = -1.10, -2.20$ GeV², with $\bar{Q}^2 \approx 7, 6$ GeV², respectively. While these two \bar{Q}^2 values are quite different, for \bar{Q}^2 sufficiently large, we expect this difference in \bar{Q}^2 to be minimal compared to the change in t . However, this is the sort of claim we can investigate in future studies.

Then, the $\bar{\omega}$ values are determined by the sink momentum \mathbf{p}' :

$$\bar{\omega} = \frac{4\mathbf{p}' \cdot (\mathbf{q}_1 + \mathbf{q}_2)}{(\mathbf{q}_1 + \mathbf{q}_2)^2}. \quad (5.30)$$

Looking at our parameterisation, Eq. (5.23), we can see that multiple $\bar{\omega}$ values are required to extract the GPD moments.

Recall the constraints on our sink momenta, Eq. (4.38):

- We must keep $|\mathbf{p}'| = |\mathbf{p}' - \mathbf{q}_1 + \mathbf{q}_2|$.

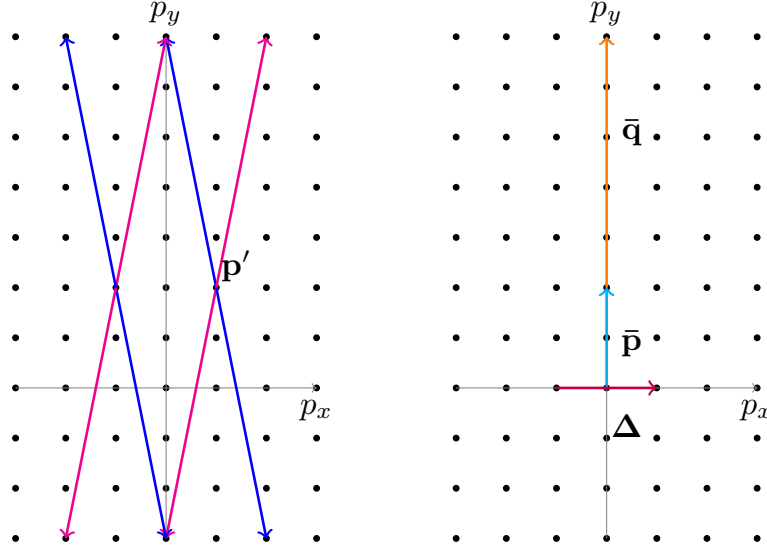


Figure 5.2: Example of kinematic set up for lattice off-forward scattering. Left: the magenta vectors are $\pm\mathbf{q}_1$ and the blue vectors are $\pm\mathbf{q}_2$. Right: derived kinematics, $\bar{\mathbf{p}}$, $\bar{\mathbf{q}}$, and Δ (Eq. (5.25)) of the left diagram.

- And we need that $|\mathbf{p}'| < |\mathbf{p}' + n\mathbf{q}_1 + m\mathbf{q}_2|$ for all other integers n, m .

For simplicity, we define the dimensionless sink momentum as \mathbf{n}' :

$$\mathbf{p}' = \frac{2\pi}{L}\mathbf{n}', \text{ for } \mathbf{n}'_i \in \mathbb{N}. \quad (5.31)$$

Recall from Chapter 3 that large sink momenta, $|\mathbf{p}'|$, decreases the quality of the signal. Therefore, we keep $\mathbf{n}'^2 \leq 5$, which corresponds to $\mathbf{p}'^2 \leq 1.37 \text{ GeV}^2$. Finally, by the arguments in Section 4.2, we note that we must exclude values of \mathbf{p}' that give $|\bar{\omega}| > 1$.

The explicit values of $\bar{\omega}$ for our kinematics are shown in Table 5.3. Since our amplitude is invariant under the exchanges $\Delta^\mu \rightarrow -\Delta^\mu$, $\bar{\omega} \rightarrow -\bar{\omega}$, we average over $\pm\mathbf{p}'$, $\pm(\mathbf{p}' - \mathbf{q}_1 + \mathbf{q}_2)$ to increase our statistics. We do not report these sink momenta in Table 5.3.

Table 5.3: Left: $t = -1.10 \text{ GeV}^2$. Right: $t = -2.20 \text{ GeV}^2$. Corresponding $\mathbf{q}_{1,2}$ values are given in Table 5.2.

\mathbf{n}'	$\bar{\omega}$	\mathbf{n}'^2	\mathbf{n}'	$\bar{\omega}$	\mathbf{n}'^2
(1, 0, 0)	0	1	(1, -1, 0)	0	2
(1, 0, 1)	0.08	2	(1, -1, 1)	0.18	3
(1, 0, 2)	0.15	5	(2, 0, -1)	0.36	4
(1, 1, -1)	0.31	3	(2, 0, 0)	0.55	4
(1, 1, 0)	0.38	2	(2, 0, 1)	0.73	5
(1, 1, 1)	0.46	3			
(1, 2, 0)	0.77	5			

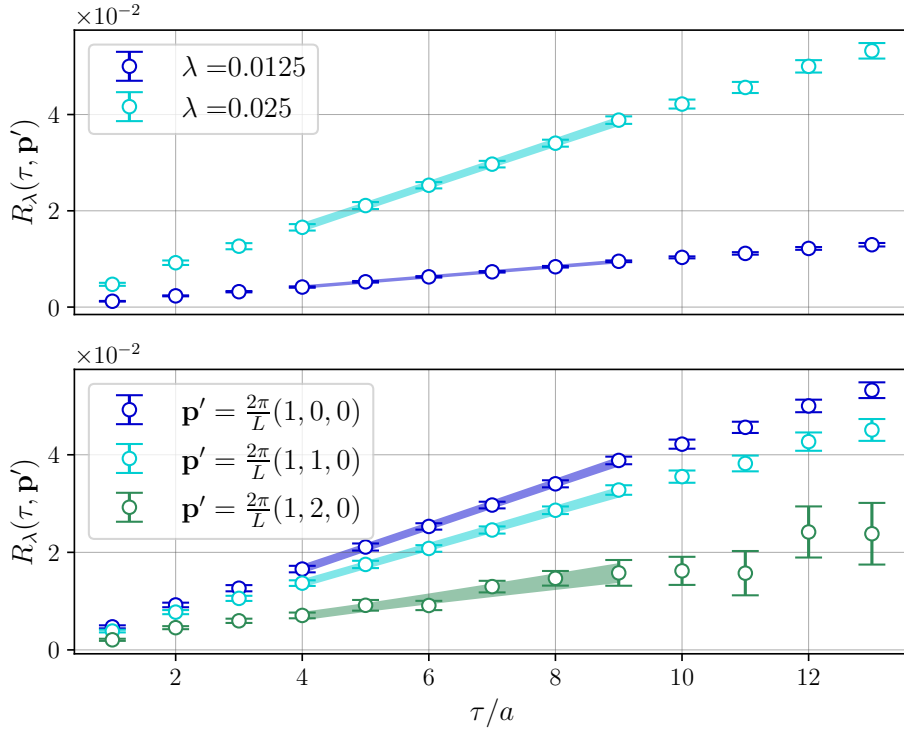


Figure 5.3: Plot of τ fits for R_λ , as defined in Eq. (4.53), for up quarks and $t = -1.10 \text{ GeV}^2$. Top: R_λ for $\mathbf{p}' = (2\pi/L)(1, 0, 0)$ for the two different λ values. Bottom: R_λ with $\lambda = 0.025$ for a range of momenta.

5.2.2 Determining the Compton amplitude

Now we present the results of this lattice calculation, starting with the fits in Euclidean time and the Feynman-Hellmann parameter, λ , to extract the off-forward Compton amplitude.

Euclidean time fits

Recall that we constructed the combination of correlators, $R_\lambda(\tau, \mathbf{p}')$ in Eq. (4.53) to extract the OFCA. From our Feynman-Hellmann relation, Eq. (4.50), $R_\lambda(\tau)$ will have the functional form $f(\tau) = a\tau + b$, where τ is Euclidean time. Then, from the Feynman-Hellmann relation in Eq. (4.50), the slope a is proportional to the OFCA, while b is a superfluous parameter.

For the fitting in Euclidean time we use the same fit window for all sink momenta: $\tau_{\min} = 4a$, $\tau_{\max} = 9a$. This fit window is chosen based on (1) where the signal is roughly linear, and (2) where we have $\chi^2/\text{dof} \sim 1$ for all sink momenta. We present a significantly improved procedure to choose the fit windows in Chapters 6 and 7. However, since this chapter's calculation is more proof-of-principle, we use this simple procedure.

We calculate the χ^2/dof of the Euclidean time fits using the full covariance matrix and report these values in Table 5.4, where we show that $\chi^2/\text{dof} \sim 1$ for all the momenta, demonstrating that the data is largely well described by a linear fit. An example of the Euclidean time fits for the $t = -1.10 \text{ GeV}^2$ results is given in Figure 5.3.

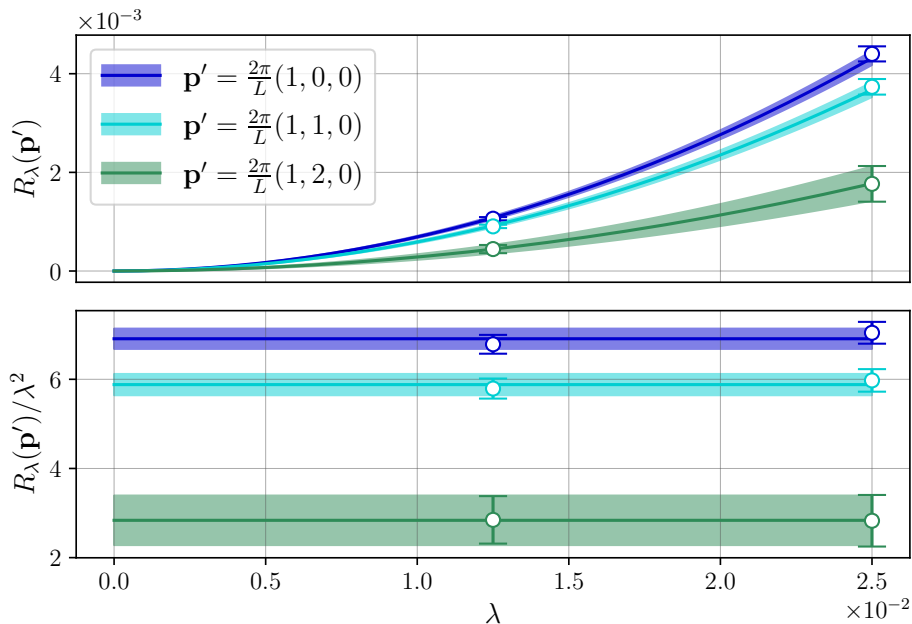


Figure 5.4: Plot of λ -dependence of R_λ after fitting in Euclidean time, for the same data as Fig. 5.3. Top: R_λ appears very well-described by $f(\lambda) = c\lambda^2$. Bottom: comparing the extracted c and R_λ/λ^2 , we see small tensions between the fit and the data.

Recall in Chapter 4 that we showed there are Feynman-Hellmann excited states induced by the kinematics \bar{Q}^2 or $|t| \ll m_N^2$, and $|\bar{\omega}| \rightarrow 1$. Since we are not particularly near these kinematic limits for this calculation, we need not consider excited states in too much detail—attested to by the good quality of our linear fits. However, in Chapter 6, we will consider these contributions in greater detail.

Feynman-Hellmann parameter fits

Once we have fit $R_\lambda(\mathbf{p}')$ as a function of the Euclidean time, we next investigate its behaviour as a function of the Feynman-Hellmann coupling, λ . From the Feynman-Hellmann relation, Eq. (4.50), and Eq. (4.52), the coefficient of the λ^2 contribution is proportional to the OFCA, and the next-to-leading order term is $\mathcal{O}(\lambda^4)$, which is suppressed by $\sim 10^{-2}$ for our chosen λ .

For goodness-of-fit, we find that the calculation of a χ^2/dof using the covariance matrix is not suitable for this highly-correlated data with two values—see Appendix G. Instead, we examine the effect of $\mathcal{O}(\lambda^4)$ contaminations by calculating the quotient $\lambda_1^2 R_{\lambda_2} / (\lambda_2^2 R_{\lambda_1})$, which is 1 for perfectly quadratic results. In Table 5.4, we can see that, although the central value of this quotient is close to 1 for all momenta, not all are within errors of 1. This indicates a 2 – 4% contamination from higher order terms, which is negligible compared to our overall errors. Controlling such suppressed, higher order contributions is a current area of investigation [219].

Hence for this study, we find it sufficient to use the purely quadratic fit function, $f(\lambda) = c\lambda^2$. In Figure 5.4, we plot the normalised ratio, R_λ/λ^2 , as a function of λ ,

Table 5.4: Parameters demonstrating the quality of fits in Euclidean time and the Feynman-Hellmann parameter, λ , for the up quark results with $t = -1.10 \text{ GeV}^2$.

\mathbf{n}'	χ^2/dof (τ fits)	$\lambda_1^2 R_{\lambda_2}/(\lambda_2^2 R_{\lambda_1})$
(1,0,0)	0.87	1.039(4)
(1,0,1)	1.1	1.033(5)
(1,0,2)	0.75	1.01(2)
(1,1,-1)	0.49	1.019(6)
(1,1,0)	1.0	1.032(4)
(1,1,1)	0.57	1.022(6)
(1,2,0)	1.6	0.99(3)

and compare this to the quadratic coefficient from the fit. We observe that the data is reasonably well described by a purely quadratic fit.

Using the Feynman-Hellmann relation, Eq. (4.50), we can now interpret the quadratic coefficient as proportional to the off-forward Compton amplitude. Then, by varying the sink momentum, we can calculate the amplitude at multiple values of the scaling variable, $\bar{\omega}$. The results are shown in Figure 5.5.

The forward $t = 0$ curve in this plot is a fit to the $Q^2 = 7.13 \text{ GeV}^2$ results from Ref. [37]. As that study also used the Feynman-Hellmann method and the same gauge configurations as the present calculation, we can compare it to our off-forward, $t \neq 0$, results to determine the t -dependence of the OFCA.

5.2.3 Moment fitting

As discussed in Section 4.2, the Euclidean Compton amplitude is itself unphysical, and it can only be related to the physical Compton amplitude through an integral equation, Eq. (4.79). Moreover, in Sections 3.2 and 4.2 we outlined some methods to overcome this problem. In this section we apply the moment fitting method and determine the two leading even moments.

Using the results of our OPE, Eq. (5.23), we can interpret the moments of the OFCA as GPD moments, defined in Eq. (5.25). Hence, using Eq. (5.23), a fit in $\bar{\omega}$ to the function

$$f_{N_{\max}}(\bar{\omega}, t) = 2 \sum_{n=1}^{N_{\max}} \bar{\omega}^{2n} M_{2n}(t) \quad (5.32)$$

yields the first N_{\max} even moments of the OFCA at fixed t and \bar{Q}^2 values. Since $|\bar{\omega}| < 1$ a truncation in this series is justified. At leading-twist, these moments are approximately the following linear combination of generalised form factors:

$$M_n(t) = A_{n,0}(t) + \frac{t}{8m_N^2} B_{n,0}(t).$$

To fit the moments, we use Bayesian Markov chain Monte Carlo (MCMC) implemented with the PyMC3 library [220, 221]. This takes prior distributions as inputs, and outputs

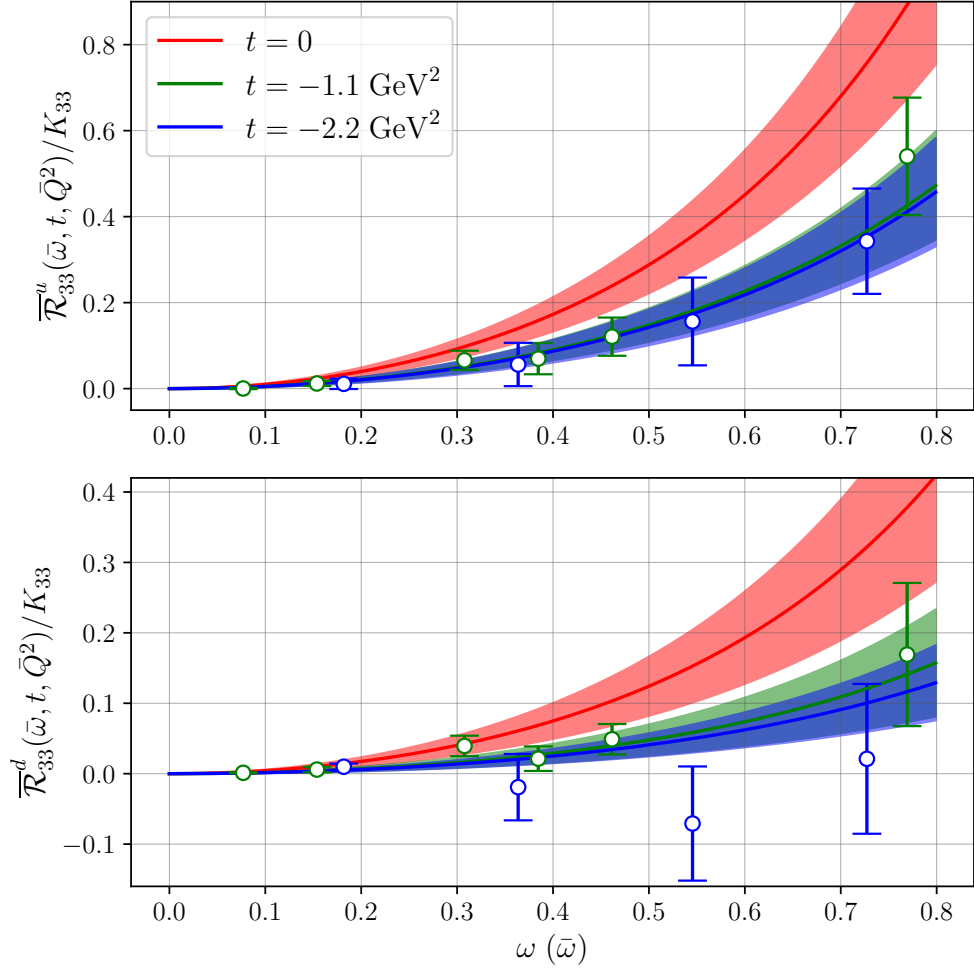


Figure 5.5: Plot of $\bar{\mathcal{R}}$, as defined in Eq. (5.23), divided by the kinematic factor, K_{33} , from Eq. (5.24). The top plot is for up quarks, while the bottom is for down quarks. The red curve is a parameterisation of results from Ref. [37]. The blue and green curves are from the moment fits.

a posterior distribution based on minimising $\exp(-\chi^2/2)$. The χ^2 is given by

$$\chi^2 = \sum_i \frac{[f^{\text{model}}(\omega_i) - f^{\text{lattice}}(\omega_i)]^2}{\sigma^2}, \quad (5.33)$$

where σ^2 is the sum of the variances—i.e. the trace of the covariance matrix. By sampling prior distributions, we can apply physically-motivated constraints on our parameters and regularise parameter space, which helps prevent over-fitting [37].

For this chapter and Chapters 6 and 7, we use uniform prior distributions. However, we need to be careful that our priors are not too severe for the data (indicated by a skewed posterior distribution) or that our parameters are unconstrained (indicated by a flat posterior distribution—i.e. the posterior is the same as the prior distribution up to statistical fluctuations). Ideally, given normally distributed lattice data, the posterior distribution will also be normally distributed.

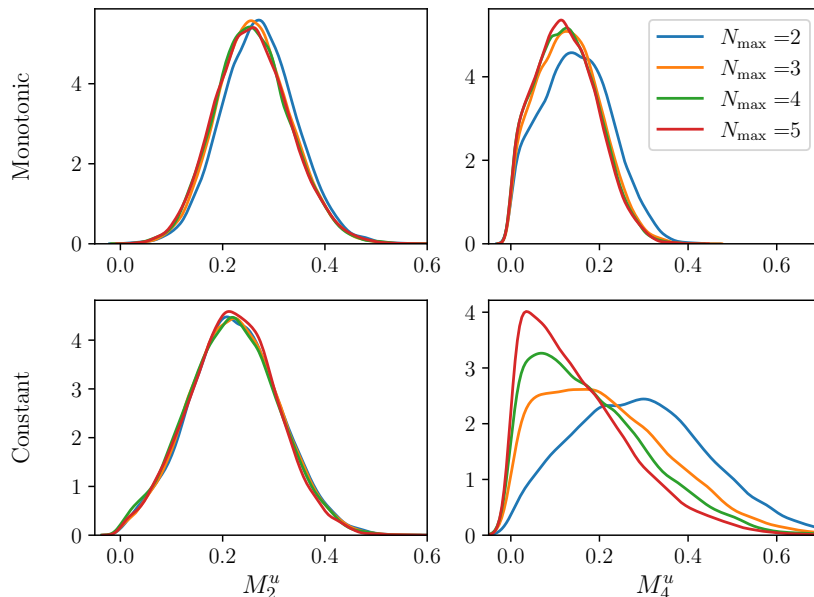


Figure 5.6: Density distributions for the first two up quark moments at $t = -1.10 \text{ GeV}^2$. The upper two plots use monotonic in n priors distributions, Eq. (5.34), while the lower two plots use constant in n positive distributions, Eq. (5.35). N_{\max} is the number of moments fit in the parameterisation, Eq. (5.32).

In the case of the *forward* Compton amplitude, we can use the monotonically decreasing condition on the moments, Eq. (2.31). However, for the off-forward amplitude, there is no optical theorem connecting the OFCA to a scattering cross section, and hence no requirement for the off-forward scalar amplitudes to be positive definite. However, our moments, defined in Eq. (5.25), are dominated by $A_{n,0}(t)$, the moments of the zero-skewness GPD $H(x,t)$, which is typically treated as positive in model-dependent parameterisations [222–225]. Therefore, it is reasonable for the proof-of concept calculation in this chapter to treat the underlying distribution as strictly positive on the domain $x \in [-1, 1]$, and thus its moments as monotonically decreasing for fixed t :

$$0 \leq M_{n+1}(t) \leq M_n(t), \quad \text{for } n \in \mathbb{N}. \quad (5.34)$$

In Chapter 6, we will use physically motivated GPD constraints to provide better prior distributions for our sampling [226–228].

Another model-dependency is the order of truncation in the $\bar{\omega}$ polynomial: N_{\max} in Eq. (5.32). Although the Bayesian MCMC is capable of taking more fit parameters than the number of $\bar{\omega}$ points, it is unlikely that all these parameters will be constrained. Therefore, as a rule of thumb we use N_{\max} to at most equal to the number of $\bar{\omega}$ values.

In Figure 5.6, we present the posterior densities for the up quark, $t = -1.10 \text{ GeV}^2$ moments. To examine the model-dependence, we compare the moments fit using monotonically decreasing in n priors, Eq. (5.34), to those fit with constant in n ; that is, where the same prior is used for each moment:

$$0 \leq M_n \leq 100, \quad \text{for all } n \in \mathbb{N}. \quad (5.35)$$

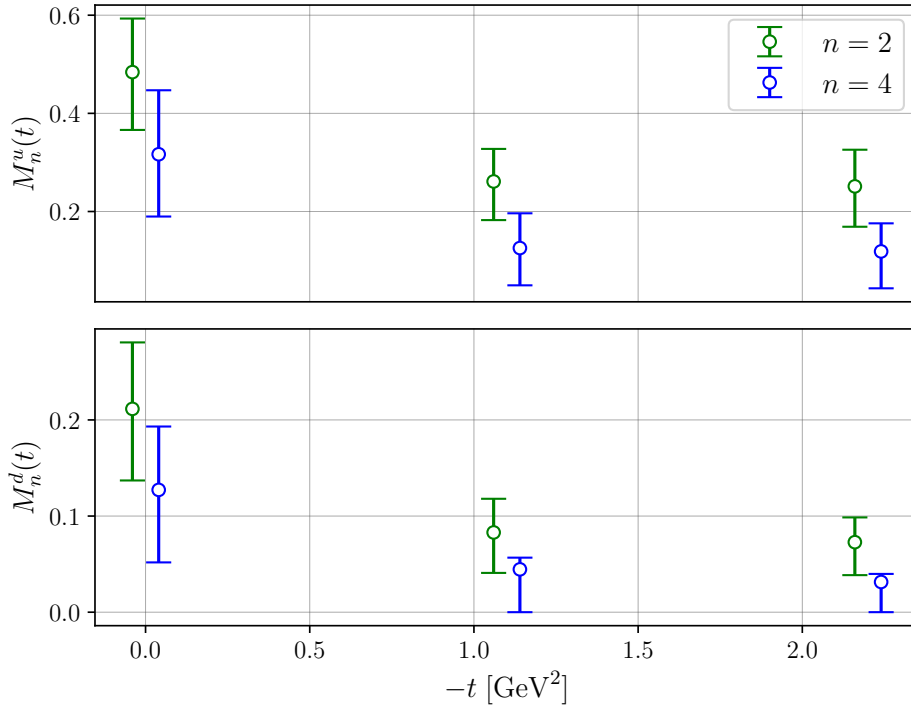


Figure 5.7: The t -dependence of the first two even moments, $M_n^f(t)$, defined in Eq. (5.25). The top plot is for up and the bottom is for down quarks. The $t = 0$ points are from a fit to results in Ref. [37].

Moreover, we vary N_{\max} between two and five.

We observe that the leading moment, M_2 , is stable as N_{\max} is varied. Moreover, the values of M_2 , as extracted with the monotonic and constant moments, are highly consistent. On the other hand, the value of M_4 differs significantly depending on whether monotonic or constant priors are used. For the constant in n moments, the M_4 distributions are heavily skewed towards zero, and do not converge with N_{\max} . By contrast, the monotonically sampled moments, M_4 , does not depend greatly on the order of truncation for $N_{\max} > 2$, and the distributions appear only slightly skewed towards zero.

Since we are limited to $|\bar{\omega}| < 1$, the higher moments will be suppressed by a factor of $\bar{\omega}^{2N}$ for some N with respect to the lower moments. Moreover, large sink momentum is required to access high $\bar{\omega}$, Eq. (5.30). Recall from Chapter 3 that large sink momentum makes a clean signal harder to obtain. As such, the lower moments are generally easier to obtain. For this preliminary study, we choose to fit the first four even moments, $n = 2, 4, 6, 8$, using monotonic conditions, and report the first two even moments. For consistency, we only fit the first four moments of the forward results as well.

We present results for the t -dependence of the leading moments in Figure 5.7. The values of the $n = 2$ GPD moments are statistically consistent with moments from three-point lattice calculations at a comparable pion mass [127]. The decay in the moments with increasing $-t$ is as expected from other lattice studies [122–127]. However, the $n = 4$ moments have never been determined from three-point methods, and therefore there are no analogous lattice studies to compare to.

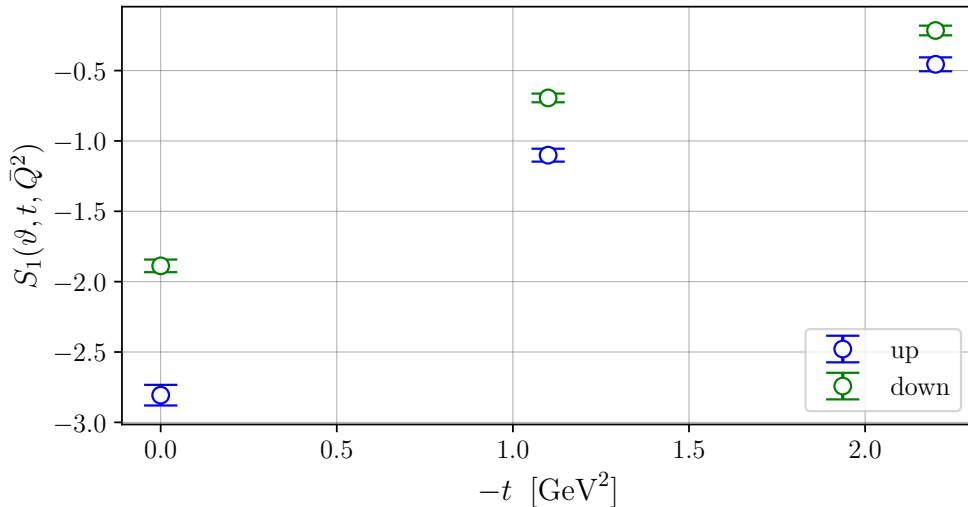


Figure 5.8: The off-forward subtraction function, defined in Eq. (5.18), with respect to the soft momentum transfer, t , with the other Lorentz scalars fixed: $\vartheta = 0$ and $\bar{Q}^2 \approx 7 \text{ GeV}^2$. Plotted are the results for up and down quarks.

Experimental determinations of GPDs have not advanced to the stage of model-independent moment determinations, and hence there are no comparable experimental results for $t \neq 0$. By contrast, the forward ($t = 0$) moments have been determined from deep-inelastic scattering over a range of Q^2 . We find that at $t = 0$ our $n = 2$ moment is consistent with experiment; however, the $n = 4$ moment is larger than the experimental moments by approximately a factor of two at a similar Q^2 [44]. Therefore, it is likely that the $n = 4$ moments for the off-forward ($t \neq 0$) results are also anomalously large. We discuss this issue further in Chapter 6.

Off-forward subtraction function

Finally, we present our results for the off-forward subtraction function, $S_1(\vartheta, t, \bar{Q}^2)$, as defined in Eq. (5.18). From Eq. 5.21, we see that the subtraction function is proportional to the OFCA at $\bar{\omega} = 0$, and hence we can extract this quantity directly from our lattice calculation.

From our OPE, Eq. (5.14), we expect that this quantity behaves like

$$S_1(\vartheta, t, \bar{Q}^2) = 2 \sum_{n=1}^{\infty} (2\vartheta)^{2n} C_{2n}(t),$$

for $\bar{Q}^2 \gg \Lambda_{\text{QCD}}^2$. Hence for our results, where $\vartheta = 0$, we should have $S_1(\vartheta = 0, t, \bar{Q}^2) \approx 0$, with additional terms suppressed by $1/\bar{Q}^2$. As such, we expect the subtraction function contribution to be suppressed compared to the leading moments.

By contrast, our results, Fig. 5.8, show that S_1 is significantly larger than all the leading moments. This is an intriguing result, as the off-forward subtraction function is of interest to Regge phenomenologists [216, 217] and for determinations of the proton pressure distribution [89].

In Chapter 8, we will investigate this anomalous behaviour of the subtraction function more thoroughly in the case of forward kinematics, and attempt to determine if it is an artefact of our calculation or a gap in our understanding of high-energy physics.

5.3 Conclusion and Outlook

In this chapter, we presented the first calculation of the off-forward Compton amplitude in lattice QCD using the Feynman-Hellmann method. The first step was to derive a non-perturbative parameterisation of the off-forward Compton amplitude that was comparable to Euclidean calculations, and moreover that could be interpreted in terms of GPDs at large \bar{Q}^2 . We achieved this by matching a short-distance OPE to a tensor decomposition.

In terms of the numerical calculation, the signal determined from the perturbed propagators is consistent with ground-state dominance (linear in Euclidean time), and moreover the signal is quadratic as a function of the Feynman-Hellmann coupling, as expected. This demonstrates that, within systematics, this method is capable of isolating the off-forward Compton amplitude.

Moreover, we fit the moments of GPDs to this Compton amplitude; the leading $n = 2$ moments are consistent with other lattice QCD calculations, while the $n = 4$ moments showed tension with experimental values at a similar Q^2 . However, since we have not performed an investigation of the lattice systematics such as the spacing, volume, pion mass as well as any Feynman-Hellmann specific systematics, this sort of tension is unsurprising—we will discuss this more in Chapter 6. We also saw that the off-forward subtraction function was at odds with the prediction from the OPE. This behaviour is investigated in detail in Chapter 8.

Finally, we note that a major drawback of this chapter's calculation is that we were forced to make leading-twist approximations and moreover only extracted a linear combination of the helicity-conserving and -flipping amplitudes. In the next chapter we show how to determine the Compton form factors \mathcal{H}_1 and \mathcal{E}_1 separately, without a leading-twist approximation.

The Off-Forward Compton Amplitude: Part II

In this chapter we present an improved calculation of the off-forward Compton amplitude. In particular, we separately determine the helicity-conserving and -flipping Compton form factors (CFFs), \mathcal{H}_1 and \mathcal{E}_1 , respectively, and show how to extract the OFCA without recourse to leading-twist approximations. This calculation uses one value of the hard momentum transfer, $\bar{Q}^2 \approx 5 \text{ GeV}^2$, and four values of the soft momentum transfer, $t \approx 0, -0.29, -0.57, -1.14 \text{ GeV}^2$, with zero-skewness kinematics at an unphysical pion mass of $m_\pi \approx 412 \text{ MeV}$.

The separate extraction of \mathcal{H}_1 and \mathcal{E}_1 is important for two reasons. Firstly, at leading-twist these CFFs are related by a convolution (recall Section 4.2) to the generalised parton distributions (GPDs) H and E , respectively. Therefore, the separate determination of \mathcal{H}_1 and \mathcal{E}_1 allows us to calculate the moments $A_{n,0}$ and $B_{n,0}$ separately, and furthermore attempt a determination of the GPDs directly. This is in contrast to the results in Chapter 5, which were a linear combination of $\mathcal{H}_{1,2,3}$ and $\mathcal{E}_{1,2}$, and hence were more difficult to directly relate to the GPDs.

Secondly, by determining \mathcal{H}_1 and \mathcal{E}_1 without leading-twist approximations, we open up the possibility of studying their \bar{Q}^2 dependence, as has already been achieved in the forward case [38]. Since most measurements of deeply virtual Compton scattering (DVCS) are in the region $Q^2 \approx 1 - 12 \text{ GeV}^2$ and contain additional $|t|/Q^2$ corrections [229,230], the \bar{Q}^2 dependence of the OFCA is highly interesting phenomenological information. At the moment, experimental studies of the hard scale dependence of DVCS are limited [231,232], but show non-trivial Q^2 dependence [233,234]. While the isolation of \mathcal{H}_1 and \mathcal{E}_1 in this chapter lays the groundwork for studying their \bar{Q}^2 dependence, for this work our results are at a single \bar{Q}^2 value.

By contrast, for quasi- and pseudo-GPD studies such additional higher-twist corrections are a systematic error that needs to be removed. In particular, a model calculation of quasi- and pseudo-GPDs suggested that these methods cannot sufficiently control higher-twist corrections for $|t| \gtrsim 0.5 \text{ GeV}^2$ [235]. Therefore, while higher-twist corrections are a significant systematic error for the quasi- and pseudo-GPDs, for calculations of the off-forward Compton amplitude they can provide useful physical information.

We also present more modest improvements to the method of Chapter 5: To improve the quality and efficiency of Euclidean time fitting, we implement a weighted averaging method for these fits. Further, in contrast to the simple monotonic condition on the Mellin

moments used in Chapter 5.34, we derive model-independent constraints on the moments, which allow us to determine moments that violate monotonicity.

The structure of this chapter follows: in Section 6.1 we derive the kinematics that allow us to isolate \mathcal{H}_1 and \mathcal{E}_1 . Then, in Section 6.2 we perform the lattice calculation, determining the moments in a similar way to Chapter 5, and then perform a model-dependent fit to determine the $H(x, t)$ GPD.

6.1 Set-up and Parameterisation

In the previous chapter, we isolated a complicated linear combination of the CFFs $\mathcal{H}_{1,2,3}$ and $\mathcal{E}_{1,2}$:

$$\begin{aligned} \mathcal{R}_{\mu\nu}(\bar{\omega}, t, \bar{Q}^2) = & \frac{1}{E_N + m_N} \left\{ -g_{\rho\sigma} [(E_N + m_N)\mathcal{H}_1 + \frac{t}{4m_N}\mathcal{E}_1] \right. \\ & \left. + \frac{\bar{P}_\rho \bar{P}_\sigma}{\bar{P} \cdot \bar{q}} [(E_N + m_N)(\mathcal{H}_2 + \mathcal{H}_3) + \frac{t}{4m_N}\mathcal{E}_2] \right\} \mathcal{P}_{\mu\rho} \mathcal{P}_{\sigma\nu}. \end{aligned}$$

After dropping all but the leading-twist contributions, this allowed us to calculate moments that were a linear combination of GPD moments,

$$M_n(t) = A_{2,0}(t) + \frac{t}{8m_N^2} B_{2,0}(t),$$

after further assuming that $E_N \approx m_N$.

Here, we improve on this parameterisation significantly: (1) we isolate a linear combination of \mathcal{H}_1 and \mathcal{E}_1 with only highly suppressed \bar{Q}^{-3} corrections; and (2) we then use spin-parity projectors to separately determine \mathcal{H}_1 and \mathcal{E}_1 .

We begin with the tensor decomposition from the previous chapter, Eq. (5.11). Since we perform the lattice calculation of this chapter at $\xi = 0 = \vartheta$, we can eliminate the structures in Eq. (5.11) that vanish in this kinematic region [197]:

$$\begin{aligned} \bar{T}_{\mu\nu} = & \frac{1}{2\bar{P} \cdot \bar{q}} \left\{ - \left(h \cdot \bar{q} \mathcal{H}_1 + e \cdot \bar{q} \mathcal{E}_1 \right) g_{\mu\nu} + \frac{1}{\bar{P} \cdot \bar{q}} \left(h \cdot \bar{q} \mathcal{H}_2 + e \cdot \bar{q} \mathcal{E}_2 \right) \bar{P}_\mu \bar{P}_\nu \right. \\ & \left. + \mathcal{H}_3 h_{\{\mu} \bar{P}_{\nu\}} \right\} + \frac{i}{2\bar{P} \cdot \bar{q}} \epsilon_{\mu\nu\rho\kappa} \bar{q}^\rho \left\{ \tilde{h}^\kappa \tilde{\mathcal{H}}_1 + \tilde{e}^\kappa \tilde{\mathcal{E}}_1 + \frac{1}{\bar{P} \cdot \bar{q}} \left[(\bar{P} \cdot \bar{q} \tilde{h}^\kappa - \tilde{h} \cdot \bar{q} \bar{P}^\kappa) \tilde{\mathcal{H}}_2 \right] \right\} \quad (6.1) \\ & + \left(\bar{P}_\mu q'_\nu + \bar{P}_\nu q'_\mu \right) \left(h \cdot \bar{q} \mathcal{K}_1 + e \cdot \bar{q} \mathcal{K}_2 \right) + q'_\mu q'_\nu (h \cdot \bar{q} - e \cdot \bar{q}) \mathcal{K}_5 \\ & + \left(h_\mu q'_\nu + h_\nu q'_\mu \right) \mathcal{K}_7. \end{aligned}$$

The key kinematic choice for this chapter is that we always take the soft momentum transfer, Δ , to be parallel to the direction of current, $\hat{\mathbf{e}}_k$:

$$\Delta \propto \hat{\mathbf{e}}_k. \quad (6.2)$$

Since both $\bar{\mathbf{q}}$ and $\bar{\mathbf{p}}$ are orthogonal to Δ^* , this kinematic choice means that any terms in our tensor decomposition with an uncontracted \bar{q}_μ or \bar{P}_μ vanish.

Therefore, the only terms that survive are

*We can see this by noting that, from the zero-skewness condition, $\bar{q} \cdot \Delta = 0$; and $\bar{P} \cdot \Delta = (P'^2 - P^2)/2 = 0$.

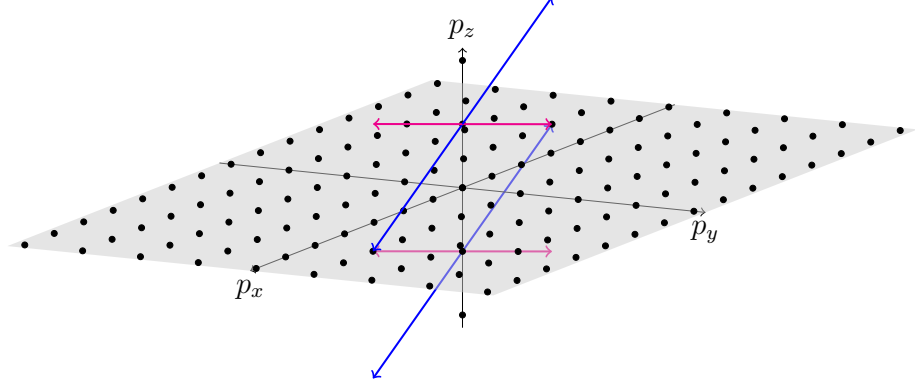


Figure 6.1: Diagram of momentum insertions for $\mathbf{q}_1 = (5, 3, 1)$ (magenta arrows) and $\mathbf{q}_2 = (5, 3, -1)$ (blue arrows). Therefore, the momentum transfer Δ is completely in the z direction, while the $\bar{\mathbf{p}}$ and $\bar{\mathbf{q}}$ vectors are in the $x - y$ plane.

- $g_{\mu\nu}$ terms that give us the desired \mathcal{H}_1 and \mathcal{E}_1 amplitudes.
- $\Delta_\mu \Delta_\nu$ terms that are generally suppressed.

As such, this kinematic choice minimises the effects of EM gauge dependent terms and hence discretisation artefacts, as our local current does not satisfy the continuum Ward identities [236, 237]. Moreover, it helps us isolate \mathcal{H}_1 and \mathcal{E}_1 instead of a linear combination of other Compton form factors.

Below we sketch how the polarised tensor structures vanish with this kinematic choice, and moreover give the order to which the $\mathcal{K}_{1,2,5,7}$ amplitudes are suppressed.

Vanishing polarised terms

After gauge projection with Eq. (5.10), the polarised CFFS, $\tilde{\mathcal{H}}_{1,2}$ and $\tilde{\mathcal{E}}_{1,2}$, will be attached to the tensor structure[†]

$$\Delta_{\{\mu\epsilon_\nu\}\sigma\rho\kappa}\Delta^\sigma\bar{q}^\rho\tilde{h}^\kappa.$$

Now if we choose the condition in Eq. (6.2), we have $\nu = \sigma$, and hence the above equation must vanish. This removes $\tilde{\mathcal{H}}_2$ completely, whereas in the kinematics of the previous chapter it was only suppressed.

Suppressed contributions

Further, the $\mathcal{K}_{1,2,5,7}$ amplitudes have no $g_{\mu\nu}$ tensor structure. Therefore, after gauge projection, the only contribution that survives is

$$\frac{\Delta_k \Delta_k}{q \cdot q'} \mathcal{K}_{1,2,5,7} \sim \frac{-t}{\bar{Q}^2} \mathcal{K}_{1,2,5,7}.$$

Hence these tensor structures, which are already \bar{Q}^{-1} suppressed, are further suppressed by $|t|/\bar{Q}^2$, making them \bar{Q}^{-3} .

[†]Unlike the forward case, it is not true that the polarised terms vanish by taking $\mu = \nu$. This is a consequence of the off-forward Ward identities, $q_\mu T^{\mu\nu} = 0 = T^{\mu\nu} q'_\nu$, which gives the gauge projector $\mathcal{P}^{\mu\nu}$ in Eq. (5.10) anti-symmetric contributions. Hence $\epsilon_{\mu'\nu'\rho\kappa} \mathcal{P}^{\mu\mu'} \mathcal{P}^{\nu'\nu}$ has both symmetric and anti-symmetric components.

Final decomposition

Therefore, up to \bar{Q}^{-3} corrections, the gauge-projected Compton amplitude is

$$\begin{aligned}
T_{kk} = & \frac{1}{2\bar{P} \cdot \bar{q}} \left[\left(h \cdot \bar{q} \mathcal{H}_1 + e \cdot \bar{q} \mathcal{E}_1 \right) \left(1 + \frac{q'_k q_k}{q \cdot q'} \right) \right. \\
& + \frac{1}{\bar{P} \cdot \bar{q}} \left(h \cdot \bar{q} \mathcal{H}_2 + e \cdot \bar{q} \mathcal{E}_2 \right) \left(\bar{P}_k \bar{P}_k - \frac{\bar{P} \cdot \bar{q}}{q \cdot q'} (q'_k \bar{P}_k + \bar{P}_k q_k) + \left(\frac{\bar{P} \cdot \bar{q}}{q \cdot q'} \right)^2 q'_k q_k \right) \\
& \left. + \mathcal{H}_3 \left(\bar{P}_k h_k - \frac{\bar{P} \cdot \bar{q}}{q \cdot q'} (q'_k h_k + h_k q_k) + \frac{\bar{P} \cdot \bar{q} h \cdot \bar{q}}{(q \cdot q')^2} q'_k q_k \right) \right]. \quad (6.3)
\end{aligned}$$

The Dirac bilinear $h_\mu = \bar{u}(P') \gamma_\mu u(P)$ is orthogonal to Δ_μ , so that the h_k terms, which are proportional to $h \cdot \Delta$, must vanish. Moreover, as previously explained, $\bar{P}_k = 0 = \bar{q}_k$. Therefore, Eq. (6.3) becomes

$$T_{kk} = \frac{1}{2\bar{P} \cdot \bar{q}} \left[\left(h \cdot \bar{q} \mathcal{H}_1 + e \cdot \bar{q} \mathcal{E}_1 \right) \left(1 - \frac{\Delta_k \Delta_k}{4q \cdot q'} \right) - \frac{\bar{P} \cdot \bar{q}}{4(q \cdot q')^2} \left(h \cdot \bar{q} (\mathcal{H}_2 + \mathcal{H}_3) + e \cdot \bar{q} \mathcal{E}_2 \right) \Delta_k \Delta_k \right]. \quad (6.4)$$

Recall the off-forward Callan-Gross relations derived in the previous chapter, Eq. (5.12). Therefore, if we are not completely at $\bar{Q}^2 \rightarrow \infty$, there remain small Callan-Gross violating terms, $\Delta \mathcal{H}_{CG}$ and $\Delta \mathcal{E}_{CG}$, which are $\mathcal{O}(\alpha_S)$ and therefore suppressed:

$$\frac{\bar{\omega}}{2} (\mathcal{H}_2 + \mathcal{H}_3) = \mathcal{H}_1 + \Delta \mathcal{H}_{CG}, \quad \frac{\bar{\omega}}{2} \mathcal{E}_2 = \mathcal{E}_1 + \Delta \mathcal{E}_{CG}.$$

Further, note that $q \cdot q' = -\bar{Q}^2 + t/4$. Hence Eq. (6.4) becomes

$$\begin{aligned}
T_{kk} = & \frac{1}{2\bar{P} \cdot \bar{q}} \left\{ \left(h \cdot \bar{q} \mathcal{H}_1 + e \cdot \bar{q} \mathcal{E}_1 \right) \left(1 - \frac{\Delta_k \Delta_k}{4(\bar{Q}^2 - t/4)} \frac{t}{4(\bar{Q}^2 - t/4)} \right) \right. \\
& \left. - \left(h \cdot \bar{q} \Delta \mathcal{H}_{CG} + e \cdot \bar{q} \Delta \mathcal{E}_{CG} \right) \frac{\Delta_k \Delta_k}{4(\bar{Q}^2 - t/4)} \frac{\bar{Q}^2}{\bar{Q}^2 - t/4} \right\}. \quad (6.5)
\end{aligned}$$

Given that $\Delta \mathcal{H}_{CG}$ and $\Delta \mathcal{E}_{CG}$ are $\mathcal{O}(\alpha_S)$, with the extra $|t|/\bar{Q}^2$ suppression, they are at best \bar{Q}^{-3} . Therefore, up to \bar{Q}^{-3} corrections, the OFCA is

$$T_{kk} = \frac{1}{2\bar{P} \cdot \bar{q}} \left(h \cdot \bar{q} \mathcal{H}_1 + e \cdot \bar{q} \mathcal{E}_1 \right). \quad (6.6)$$

This is a drastic improvement on the previous chapter, where we truncated all terms that were not leading-order (\bar{Q}^{-1} and higher), and only isolated a linear combination of $\mathcal{H}_{1,2,3}$ and $\mathcal{E}_{1,2}$. Here, we have either eliminated completely unwanted tensor structures, or suppressed them by a further $|t|/\bar{Q}^2$, with only a simple linear combination of \mathcal{H}_1 and \mathcal{E}_1 remaining.

Recall leading-twist contributions to these amplitudes, Eq. (E.17):

$$\begin{aligned}\lim_{\bar{Q}^2 \rightarrow \infty} \mathcal{H}_1(\omega, t, \bar{Q}^2) &= 2 \sum_{n=1}^{\infty} \bar{\omega}^{2n} A_{2n,0}(t), \\ \lim_{\bar{Q}^2 \rightarrow \infty} \mathcal{E}_1(\omega, t, \bar{Q}^2) &= 2 \sum_{n=1}^{\infty} \bar{\omega}^{2n} B_{2n,0}(t).\end{aligned}\tag{6.7}$$

Moreover, as $t \rightarrow 0$, we have $\mathcal{H}_1 \rightarrow \mathcal{F}_1$, the forward Compton structure function.

Finally, note that it is possible to calculate T_{44} to get a further linear combination that includes $\mathcal{H}_{2,3}$ and \mathcal{E}_2 , as has been done in the forward case [38]. By doing so one could explicitly calculate the power-suppressed off-forward Callan-Gross violations, as has been done for the forward Compton amplitude using Feynman-Hellmann [38].

6.1.1 Spin-parity projectors

Recall from our Feynman-Hellmann relation, Eq. (4.54), that we calculate the quantity

$$\mathcal{R}_{\mu\nu}^{\Gamma} = \frac{\sum_{s,s'} \text{tr}[\Gamma u(P', s') T_{\mu\nu} \bar{u}(P, s)]}{\sum_s \text{tr}[\Gamma_{\text{unpol}} u(P', s) \bar{u}(P', s)]},\tag{6.8}$$

where Γ is a spin-parity projector. We fix the denominator to have an unpolarised spin-parity projector, and vary the numerator's projector.

Therefore, by using two different spin-parity projectors we can construct a pair of linear equations and solve for \mathcal{H}_1 and \mathcal{E}_1 . The spin-parity projectors we use are the polarised and unpolarised:

$$\Gamma_{\text{unpol}} = \frac{1}{2}(\mathbb{I} + \gamma_0), \quad \Gamma_{\text{pol}} = \frac{1}{2}(\mathbb{I} + \gamma_0)\boldsymbol{\gamma} \cdot \hat{\mathbf{e}}_{\text{pol}}\gamma^5,\tag{6.9}$$

where $\hat{\mathbf{e}}_{\text{pol}}$ is the direction of the polarisation vector we choose, not to be confused with the unit vector from Eq. (6.2).

Applying the result in Eq. (6.6), we get the linear system of equations

$$\begin{pmatrix} \mathcal{R}_{kk}^{\text{unpol}} \\ \mathcal{R}_{kk}^{\text{pol}} \end{pmatrix} = \begin{pmatrix} N_{\text{unpol}}^{\mathcal{H}} & N_{\text{unpol}}^{\mathcal{E}} \\ N_{\text{pol}}^{\mathcal{H}} & N_{\text{pol}}^{\mathcal{E}} \end{pmatrix} \begin{pmatrix} \mathcal{H}_1 \\ \mathcal{E}_1 \end{pmatrix}.\tag{6.10}$$

Then, as long as the matrix of N factors is invertible, we can isolate \mathcal{H}_1 and \mathcal{E}_1 separately. Note that this process would have been very difficult to do for the results of Chapter 5, as we were dealing with a complicated linear combination of tensor structures, including $h^\mu \bar{P}^\nu$. Therefore, the kinematic choice in Eq. (6.2) also makes this separation of helicity-conserving and -flipping amplitudes possible.

As shown in Appendix F, the N factors for the unpolarised projector are

$$N_{\text{unpol}}^{\mathcal{H}} = 1, \quad N_{\text{unpol}}^{\mathcal{E}} = \frac{t}{4m_N(E_N + m_N)},\tag{6.11}$$

while for the polarised projector they are slightly more cumbersome:

$$\begin{aligned}
N_{\text{pol}}^{\mathcal{H}} &= \frac{i(\boldsymbol{\Delta} \times \hat{\mathbf{e}}_{\text{pol}}) \cdot \bar{\mathbf{q}}}{2\bar{P} \cdot \bar{\mathbf{q}}}, \\
N_{\text{pol}}^{\mathcal{E}} &= i \left\{ ((E_N + m_N)^2 + t/4)(\boldsymbol{\Delta} \times \hat{\mathbf{e}}_{\text{pol}}) \cdot \bar{\mathbf{q}} - (\bar{\mathbf{P}} \cdot \hat{\mathbf{e}}_{\text{pol}} + \boldsymbol{\Delta} \cdot \hat{\mathbf{e}}_{\text{pol}}/2)(\boldsymbol{\Delta} \times \hat{\mathbf{P}}) \cdot \bar{\mathbf{q}} \right. \\
&\quad \left. + \bar{P} \cdot \bar{\mathbf{q}}(\boldsymbol{\Delta} \times \hat{\mathbf{e}}_{\text{pol}}) \cdot \bar{\mathbf{P}} - t/2(\bar{\mathbf{P}} \times \hat{\mathbf{e}}_{\text{pol}}) \cdot \bar{\mathbf{q}} \right\} \left(4\bar{P} \cdot \bar{\mathbf{q}} m_N (E_N + m_N) \right)^{-1}.
\end{aligned} \tag{6.12}$$

The N_{pol} factors depend on the choice of $\hat{\mathbf{e}}_{\text{pol}}$, which in principle gives us four total simultaneous equations. However, in practice there is only one choice of polarisation for which

$$\frac{i(\boldsymbol{\Delta} \times \hat{\mathbf{e}}_{\text{pol}}) \cdot \bar{\mathbf{q}}}{2\bar{P} \cdot \bar{\mathbf{q}}} \sim 1,$$

while for the other choices, this is suppressed. Hence there is only one choice of polarisation that gives a reasonable signal.

As in the previous chapter, we can also use these results to determine the off-forward subtraction function, Eq. (5.18). Since \mathcal{H}_1 and \mathcal{E}_1 are the only structures in the zero-skewness Compton amplitude that have subtraction terms—i.e. non-zero $\bar{\omega} = 0$ contributions—we can determine them without needing to truncate non-leading-twist contributions.

Using the Gordon identity, we have that

$$\frac{h \cdot \bar{\mathbf{q}}}{2\bar{P} \cdot \bar{\mathbf{q}}} = \frac{e \cdot \bar{\mathbf{q}}}{2\bar{P} \cdot \bar{\mathbf{q}}} + \frac{\bar{u}(P')u(P)}{2m_N}.$$

Hence, substituting this into Eq. (6.4) and noting that $\mathcal{H}_1(\bar{\omega} = 0) = S_1 = -\mathcal{E}_1(\bar{\omega} = 0)$, we have

$$T_{kk}(\bar{\omega} = 0, t, \bar{Q}^2) = \frac{\bar{u}(P')u(P)}{2m_N} \left(1 + \frac{\Delta_k \Delta_k}{4(\bar{Q}^2 - t/4)} \right) S_1(t, \bar{Q}^2). \tag{6.13}$$

After performing the spin-parity traces, this becomes

$$\mathcal{R}_{kk}^{\text{unpol}}(\bar{\omega} = 0, t, \bar{Q}^2) = \left(1 - \frac{t}{4m_N(E_N + m_N)} \right) \left(1 + \frac{\Delta_k \Delta_k}{4(\bar{Q}^2 - t/4)} \right) S_1(t, \bar{Q}^2), \tag{6.14}$$

$$\mathcal{R}_{kk}^{\text{pol}}(\bar{\omega} = 0, t, \bar{Q}^2) = 0. \tag{6.15}$$

GPD fitting priors

In Chapter 5, we fit the moments of the GPDs using the monotonic decreasing condition for fixed t Eq. (5.34):

$$0 \leq M_{n+1}(t) \leq M_n(t), \quad \text{for } n \in \mathbb{N}.$$

This condition is completely justified in the forward ($t = 0$) case, since the F_1 structure function is proportional to the deep-inelastic scattering cross section—recall Eq. (2.31). However, there is no model-independent justification for such a condition in the case of the \mathcal{H}_1 Compton form factor. Moreover, there are good reasons to believe monotonicity is completely invalid for the down quark contribution to the \mathcal{E}_1 CFF: lattice studies of the $B_{n,0}^d$, $n = 1, 2, 3$ moments are negative [122–127].

As such, we derive model-independent constraints on GPD moments that can be used as Bayesian fitting priors. We start with the model-independent constraints on the twist-two unpolarised GPDs given in Refs. [226–228]. At $\xi = 0$ these are

$$|H(x, t)| \leq |q(x)|, \quad |E(x, t)| \leq \frac{2m_N}{\sqrt{-t}} |q(x)|, \quad (6.16)$$

where $q(x)$ is the corresponding parton distribution function.

Focusing on the helicity-conserving GPD, $H(x, t)$, for $x > 0$, we multiply by x^n to get

$$x^n |H(x, t)| \leq x^n |q(x)| = x^n q(x), \quad (6.17)$$

where we have used that $q(x)$ is positive in the domain $x \in (0, 1)$.

Again, keeping $x > 0$,

$$x^n |H(-x, t)| \leq x^n |q(-x)| = x^n |-\bar{q}(x)| = x^n \bar{q}(x). \quad (6.18)$$

We have used the fact that $q(-x) = -\bar{q}(x)$, and $\bar{q}(x) \geq 0$ for $x \in (0, 1)$.

From the triangle inequality, we have that

$$x^n |H(x, t) - H(-x, t)| \leq x^n (|H(-x, t)| + |-H(-x, t)|) \leq x^n (q(x) + \bar{q}(x)). \quad (6.19)$$

Therefore, for n odd,

$$\left| \int_{-1}^1 dx x^n H(x, t) \right| \leq \int_0^1 dx x^n |H(x, t) - H(-x, t)| \leq \int_0^1 dx x^n q^{(+)}(x), \quad (6.20)$$

where we have defined $q^{(+)}(x) = q(x) + \bar{q}(x)$.

Similarly, for the E GPD, we can repeat the above steps since the factor of $2m_N/\sqrt{-t}$ is positive and independent of x :

$$\left| \int_{-1}^1 dx x^n E(x, t) \right| \leq \int_0^1 dx x^n |E(x, t) - E(-x, t)| \leq \frac{2m_N}{\sqrt{-t}} \int_0^1 dx x^n q^{(+)}(x). \quad (6.21)$$

Therefore, we have our constraints:

$$|A_{n,0}(t)| \leq a_n, \quad |B_{n,0}(t)| \leq \frac{2m_N}{\sqrt{-t}} a_n, \quad \text{for } n \text{ even.} \quad (6.22)$$

Clearly, this means that the constraints on the B GFFs become looser as $t \rightarrow 0$.

Strictly speaking, these constraints only apply to leading-twist GPDs, and therefore they are only true for GPD moments and not the moments of the CFFs[‡]. Therefore, there are finite $\Lambda_{\text{QCD}}^2/\bar{Q}^2$ corrections to these inequalities for our Compton form factors. However, since we are at $\bar{Q}^2 \approx 5 \text{ GeV}^2$, these corrections will be suppressed.

[‡]We note that some model independent constraints on the off-forward amplitude itself exists [238].

Table 6.1: Details of the gauge ensemble used in this chapter [239].

N_f	c_{SW}	β	κ_l, κ_s	$N_L^3 \times N_T$	a [fm]	m_π [MeV]	Z_V	N_{cfg}
2 + 1	2.48	5.65	0.122005	$48^3 \times 96$	0.068	412	0.871	537

6.2 Lattice Results and Phenomenology

In this section, we present the results of our lattice calculation, using the Feynman-Hellmann relation derived in Chapter 4, and the analytic results given in the previous section.

6.2.1 Simulation details

We use a gauge ensemble from the CSSM/QCDSF/UKQCD collaboration [239]. As with the previous chapter, our gauge configurations are at the SU(3) flavour symmetric point, $\kappa_l = \kappa_s$, and we are at a similarly larger-than-physical pion mass— $m_\pi \approx 412$ MeV in this chapter compared to $m_\pi \approx 470$ MeV in the previous chapter. In contrast to the calculation in Chapter 5, our lattice has many more lattice sites: $48^3 \times 96$ compared to $32^3 \times 64$. This larger lattice size is the most important difference between the two gauge ensembles: it allows us to span a much wider range of $\bar{\omega}$ values and t values. The details of our gauge ensemble are given in Table 6.1.

Feynman-Hellmann implementation

The basic implementation of Feynman-Hellmann is no different to what is outlined in Chapters 4 and 5. We calculate perturbed quark propagators,

$$S_\lambda(z_n, z_m) = [M - \lambda_1 \mathcal{O}_1 - \lambda_2 \mathcal{O}_2]_{n,m}^{-1},$$

where $\mathcal{O}_{1,2}$ are our perturbing matrices.

As discussed in the previous section, we choose the direction of our current to be parallel with that of the soft momentum transfer, $\mathbf{\Delta}$, Eq. (6.2). For some of our kinematics—see Table 6.2—we have for instance $\mathbf{\Delta} \propto (1, -1, 0)$, which means our currents must be in this direction. This is easily achieved by taking the perturbing matrices

$$[\mathcal{O}_1]_{n,m} = \delta_{n,m} (e^{i\mathbf{q}_1 \cdot \mathbf{z}_n} + e^{-i\mathbf{q}_1 \cdot \mathbf{z}_n}) \boldsymbol{\gamma} \cdot \hat{\mathbf{e}}_k, \quad [\mathcal{O}_2]_{n,m} = \delta_{n,m} (e^{i\mathbf{q}_2 \cdot \mathbf{z}_n} + e^{-i\mathbf{q}_2 \cdot \mathbf{z}_n}) \boldsymbol{\gamma} \cdot \hat{\mathbf{e}}_k. \quad (6.23)$$

So, for example, with $\mathbf{\Delta} \propto (1, -1, 0)$,

$$\boldsymbol{\gamma} \cdot \hat{\mathbf{e}}_k = \frac{1}{\sqrt{2}} (\gamma_1 - \gamma_2),$$

which is simple to implement.

We use the same Feynman-Hellmann relation as the previous chapter, Eq. (4.50), and we approximate the mixed second-order derivative by Eq. (4.53).

Table 6.2: Current insertion momenta, $\mathbf{q}_{1,2}$, and derived kinematics for two sets of correlators. All data on configurations with $N_L^3 \times N_T = 48^3 \times 96$, $\kappa_{l,s} = 0.122005$, $\beta = 5.65$.

\bar{Q}^2 [GeV ²]	t [GeV ²]	\mathbf{q}_1 $2\pi/L$	\mathbf{q}_2 $2\pi/L$	Δ $2\pi/L$	λ	N_{meas}
4.86	0	(5, 3, 0)	—	—	(0.0125, 0.025)	1605
4.79	-0.29	(4, 3, 3)	(3, 4, 3)	(1, -1, 0)	(0.0125, 0.025)	1031
4.86	-0.57	(5, 3, 1)	(5, 3, -1)	(0, 0, 2)	(0.0625, 0.0125)	1072
4.86	-1.14	(4, 2, 4)	(2, 4, 4)	(2, -2, 0)	(0.0625, 0.0125)	1031

Kinematics

As in the previous chapter, we choose zero-skewness kinematics by setting $|\mathbf{q}_1| = |\mathbf{q}_2|$. We calculate three separate sets of propagators, with three non-zero values of the soft momentum transfer: $t = -0.29, -0.57, -1.14$ GeV². Since these results have a larger lattice size than the previous chapter's, we are able to access lower t values more easily, as $t \propto 1/L^2$. Moreover, we are interested in keeping the hard momentum transfer, \bar{Q}^2 , as fixed as possible between the data sets with different t values. This allows us to isolate the t dependence from the \bar{Q}^2 dependence. For $t = 0, -0.57, -1.14$ GeV², we have the exact same hard scale: $\bar{Q}^2 = 4.86$ GeV². For $t = -0.29$ GeV² it is slightly smaller at $\bar{Q}^2 = 4.79$ GeV². However, we do not expect this slight change in \bar{Q}^2 to have much of an effect. The momentum transfers and Feynman-Hellmann parameters of our different data sets are summarised in Table 6.2.

Furthermore, the larger value of L allows for a greater spread of $\bar{\omega}$ values. This is because our sink momentum squared is

$$\mathbf{p}'^2 = \left(\frac{2\pi}{L}\right)^2 \mathbf{n}'^2, \text{ for } \mathbf{n}'_i \in \mathbb{N},$$

where \mathbf{n}' is the dimensionless sink momentum defined in Eq. (5.31). Hence with larger L we can go to larger \mathbf{n}'^2 compared to the smaller lattice in the previous chapter. In Chapter 5, we limited ourselves to $\mathbf{n}'^2 \leq 5$, which corresponds to $\mathbf{p}' \leq 1.17$ GeV. In this chapter, we limit ourselves to $\mathbf{n}'^2 \leq 10$, which corresponds to $\mathbf{p}' \leq 1.19$ GeV. Hence the maximum sink momentum of the two chapters are approximately equal.

Again, as in the previous chapter, we keep our sink momentum such that the kinematic conditions of our FH relation are met: Eq. (4.38). The sink momenta that meet all these conditions and their corresponding $\bar{\omega}$ values are given in Table 6.3. We can see the much wider spread of $\bar{\omega}$ values compared to the $\bar{\omega}$ values from Chapter 5 given in Table 5.3. Also, note that the $t = -0.29$ GeV² results have no $\bar{\omega} = 0$ term, and hence we will need to fit the subtraction function in these results, rather than determine it directly.

Note that the unpolarised amplitude is invariant under $\Delta^\mu \rightarrow -\Delta^\mu$ and $\bar{\omega} \rightarrow -\bar{\omega}$, while the polarised changes sign under these exchanges. Therefore, we average our unpolarised results over these exchanges:

$$\bar{\mathcal{R}}_{kk}^{\text{unpol}} = \frac{\mathcal{R}_{kk}^{\text{unpol}}(\mathbf{p}') + \mathcal{R}_{kk}^{\text{unpol}}(-\mathbf{p}') + \mathcal{R}_{kk}^{\text{unpol}}(\mathbf{p}' - \mathbf{q}_1 + \mathbf{q}_2) + \mathcal{R}_{kk}^{\text{unpol}}(-(\mathbf{p}' - \mathbf{q}_1 + \mathbf{q}_2))}{4},$$

Table 6.3: Dimensionless sink momenta, \mathbf{n}' , and corresponding $\bar{\omega}$ values for the three different sets of off-forward data. Left: $t = -0.29 \text{ GeV}^2$. Center: $t = -0.57 \text{ GeV}^2$. Right: $t = -1.14 \text{ GeV}^2$.

\mathbf{n}'	$\bar{\omega}$	\mathbf{n}'^2	\mathbf{n}'	$\bar{\omega}$	\mathbf{n}'^2	\mathbf{n}'	$\bar{\omega}$	\mathbf{n}'^2
(1, 0, -1)	0.03	2	(0, 0, 1)	0.0	1	(1, -1, 0)	0.0	2
(0, -1, 2)	0.15	5	(-1, 2, 1)	0.06	6	(2, 0, -1)	0.12	5
(1, 0, 0)	0.21	1	(1, -1, 1)	0.12	3	(1, -1, 1)	0.24	3
(2, 1, -2)	0.27	9	(0, 1, 1)	0.18	2	(2, 0, 0)	0.35	4
(0, -1, 3)	0.33	10	(2, -2, 1)	0.24	9	(1, -1, 2)	0.47	6
(1, 0, 1)	0.39	2	(1, 0, 1)	0.29	2	(2, 0, 1)	0.59	5
(2, 1, -1)	0.45	6	(0, 2, 1)	0.35	5	(3, 1, 0)	0.71	10
(1, 0, 2)	0.57	5	(2, -1, 1)	0.41	6	(2, 0, 2)	0.82	8
(2, 1, 0)	0.63	5	(1, 1, 1)	0.47	3			
(1, 0, 3)	0.75	10	(0, 3, 1)	0.53	10			
(2, 1, 1)	0.81	6	(2, 0, 1)	0.59	5			
			(1, 2, 1)	0.65	6			
			(2, 1, 1)	0.76	6			
			(3, 0, 1)	0.88	10			
			(2, 2, 1)	0.94	9			

and for the polarised results we have

$$\bar{\mathcal{R}}_{kk}^{\text{pol}} = \frac{\mathcal{R}_{kk}^{\text{pol}}(\mathbf{p}') - \mathcal{R}_{kk}^{\text{pol}}(-\mathbf{p}') - \mathcal{R}_{kk}^{\text{pol}}(\mathbf{p}' - \mathbf{q}_1 + \mathbf{q}_2) + \mathcal{R}_{kk}^{\text{pol}}(-(\mathbf{p}' - \mathbf{q}_1 + \mathbf{q}_2))}{4}.$$

6.2.2 Determining the Compton amplitude

Euclidean time fits: weighted averages

As in Chapter 5, we use a simple linear function, $f(\tau) = a\tau + b$, to fit the combination of correlators, $R_\lambda(\tau)$, as defined in Eq. (4.53). However, whereas in the previous chapter, our Euclidean time fit windows were chosen by eye and checking where $\chi^2/\text{dof} \sim 1$, in this chapter we use a weighted averaging method. Weighted averaging allows us to automate this fitting process, which is important given that we have many more $\bar{\omega}$ values and one more t value compared with the previous chapter; similarly, we also calculate the polarised spin-parity projector, thereby doubling our number of results. Moreover, weighted averaging allows us to preference fits based on quantitative measures, removing biases and selecting the best possible fit window.

We start by choosing an absolute upper and lower bound on our fit windows: $[T_{\min}, T_{\max}]$. Within this range, we fit all the time windows $[\tau_{\min}, \tau_{\max}]$, such that $\tau_{\max} - \tau_{\min} \geq 3$, which keeps the number of degrees of freedom greater than zero.

To choose $[T_{\min}, T_{\max}]$, we define the quantity

$$\Delta_\tau R_\lambda(\tau) = \frac{R_\lambda(\tau + \delta\tau) - R_\lambda(\tau)}{\delta\tau}, \quad (6.24)$$

where we choose $\delta\tau = 2$.

This quantity allows us to better see by eye where $R_\lambda(\tau)$ deviates from a linear function, in a similar fashion to how the effective mass, Eq. (3.33), allows us to see the deviation of the unperturbed correlator from an exponential.

Below we give an outline of the weighted averaging process

1. In the interest of saving time, we do not individually choose $[T_{\min}, T_{\max}]$ for each data set. Instead, we choose by eye $[T_{\min}, T_{\max}]$ for the largest sink momentum, i.e. the correlators for which $|\mathbf{p}'|$ is greatest. These will be the noisiest results, and so it will be easiest to see the value of T_{\max} at which the signal decays.
2. While the T_{\min} from the previous step is used for all momenta, T_{\max} varies between momenta. To automate finding T_{\max} for other momenta, we start by looking at the *unperturbed* two-point function for the maximum momentum, $\mathcal{G}_{(0,0)}(\mathbf{p}_{\max}, \tau)$. At our chosen T_{\max} , the mean of this two-point function will be a certain number of standard deviations, N_σ , from zero:

$$|\overline{\mathcal{G}}(T_{\max})| - N_\sigma \delta \mathcal{G}(T_{\max}) \leq 0. \quad (6.25)$$

3. Then, to find T_{\max} for the other momenta, we take this N_σ as an input, and choose T_{\max} as the earliest time for which Eq. (6.25) is satisfied.
4. Now that we have $[T_{\min}, T_{\max}]$ for all momenta, we fit every allowed fit window, labelled i , and assign to it a weight [240, 241]:

$$\tilde{w}^i = \frac{p(\delta a^i)^{-2}}{\sum_{i'} p(\delta a^{i'})^{-2}}, \quad (6.26)$$

where a^i is the slope parameter from the i^{th} fit, δa^i is the statistical error and $p(a^i)$ is the p -value determined by

$$p(a^i) = \tilde{\Gamma}(N_{\text{dof}}/2, \chi^2/2) / \tilde{\Gamma}(N_{\text{dof}}/2),$$

with $\tilde{\Gamma}$ the regularised upper incomplete gamma function:

$$\tilde{\Gamma}(s, x) = \int_x^\infty dt t^{s-1} e^{-t}, \quad \tilde{\Gamma}(s) = \int_0^\infty dt t^{s-1} e^{-t}.$$

The weight in Eq. (6.26) is designed to penalise poor fits (those with large χ^2/N_{dof}), as well as unconstrained fits (those with large δa^i).

5. Finally, we calculate the weighted average of the slope parameter:

$$a_{\text{wavg}} = \sum_i \tilde{w}^i a^i,$$

which we treat as proportional to the Compton amplitude from our FH relation, Eq. (4.50).

Hence this method allows us to fit a very large amount of data by only choosing $[T_{\min}, T_{\max}]$ for the noisiest momentum.

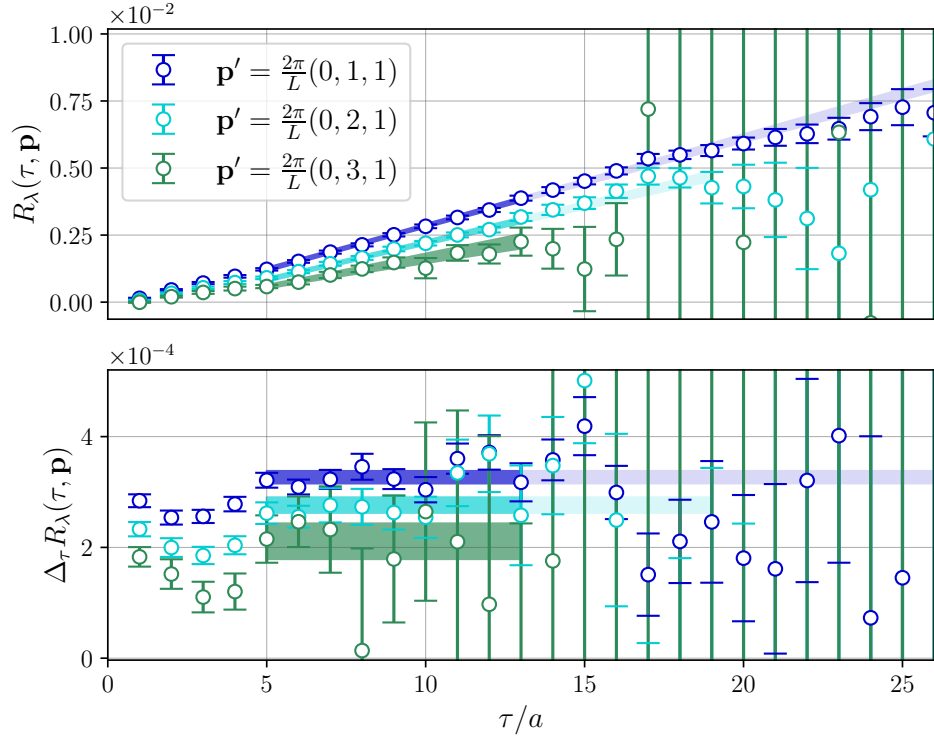


Figure 6.2: Plot of τ fits for R_λ , as defined in Eq. (4.53) and the ‘effective mass’, $\Delta_\tau R_\lambda$, defined in Eq. (6.24), for the up quarks, unpolarised, and $\lambda = 0.0125$. The shaded bands are fits to the function $f(\tau) = a\tau + b$ using weighted averages; the lighter shade is the whole range considered, and the darker shade is the fit window with the highest weight.

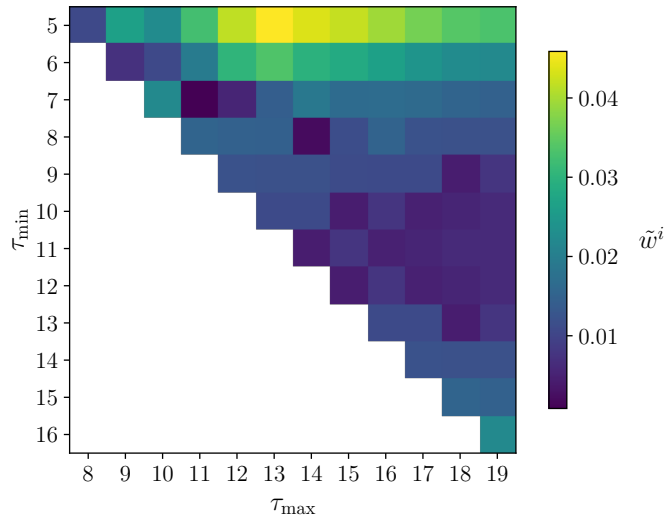


Figure 6.3: Heat map showing the weight assigned to each fit window, for up quarks, unpolarised, $\mathbf{p} = \frac{2\pi}{L}(0, 2, 1)$, $\lambda = 0.0125$ results. This corresponds to the light blue points in Fig. 6.2. The weight, \tilde{w}^i , is defined in Eq. (6.26).

As an example we plot the $t = -0.57 \text{ GeV}^2$ fits for $\lambda = 0.0125$, up quarks and the unpolarised projector in Fig. 6.2. The range of fits $T_{\min}, T_{\max} = 5, 13$ has been chosen by eye for the largest momentum in this data set, $\mathbf{p}' = \frac{2\pi}{L}(0, 3, 1)$, which is then used to find T_{\max} for all other momenta. In Fig. 6.3, we present a heatmap of the weights, Eq. (6.26).

Feynman-Hellmann excited states

As discussed in our Feynman-Hellmann chapter, there are a number of kinematic limits in which Feynman-Hellmann excited states are weakly suppressed—see Eq. (4.40). For instance, when $|t| \ll m_N^2$, the excited states behave like

$$\frac{e^{-(E_N(\mathbf{p}'+\mathbf{\Delta})-E_N(\mathbf{p}'))\tau}}{E_N(\mathbf{p}'+\mathbf{\Delta})-E_N(\mathbf{p}')} \sim \tau,$$

which contaminates the linear in τ term that we wish to extract.

While the Euclidean time fits for the $t = -0.57, -1.14 \text{ GeV}^2$ are quite reasonable, for the $t = -0.29 \text{ GeV}^2$ data set there appear to be greater contaminations in the early time slices (see Fig. H.2 of Appendix H). Hence this difficulty probably derives from weakly suppressed FH excited states, since $t = -0.29 \text{ GeV}^2$ is the smallest soft momentum transfer we have yet computed. Here, we only use this insight diagnostically to explain why the signal for the lowest t value is poor. Controlling this systematic is a goal of future work.

Similarly, we have weakly suppressed FH excited states for $|\bar{\omega}| \approx 1$. Since we have much larger $\bar{\omega}$ values in this chapter (Table 6.3), we are more prone to similar weakly suppressed excited states—we discuss this further later in this section.

Feynman-Hellmann parameter fits

For fits in the Feynman-Hellmann parameter λ , we use the same fit function as Chapter 5: $f(\lambda) = c\lambda^2$. The results are presented in Fig. 6.4. We note that, compared to the previous chapter's results, Fig. 5.4, there appears to be less $\mathcal{O}(\lambda^4)$ contamination. This could be because our λ values are slightly smaller for some of the data sets in this chapter. Alternatively, since we use different weights for each λ , it could be that the weighted averaging is better at isolating the respective ground state of each λ value. Further, we note that the difficulty discussed in Appendix G remains, since we again only have two λ values that are highly correlated.

Separating \mathcal{H} and \mathcal{E}

Now that we have our lattice results for the ratio \mathcal{R}^Γ , we take two spin projectors, $\Gamma_{\text{unpol}}, \Gamma_{\text{pol}-\hat{e}}$, and from these solve for the helicity-conserving and -flipping amplitudes, \mathcal{H}_1 and \mathcal{E}_1 , respectively. Recall Eq. (6.10):

$$\begin{pmatrix} \mathcal{R}_{kk}^{\text{unpol}} \\ \mathcal{R}_{kk}^{\text{pol}} \end{pmatrix} = \begin{pmatrix} N_{\text{unpol}}^{\mathcal{H}} & N_{\text{unpol}}^{\mathcal{E}} \\ N_{\text{pol}}^{\mathcal{H}} & N_{\text{pol}}^{\mathcal{E}} \end{pmatrix} \begin{pmatrix} \mathcal{H}_1 \\ \mathcal{E}_1 \end{pmatrix}.$$

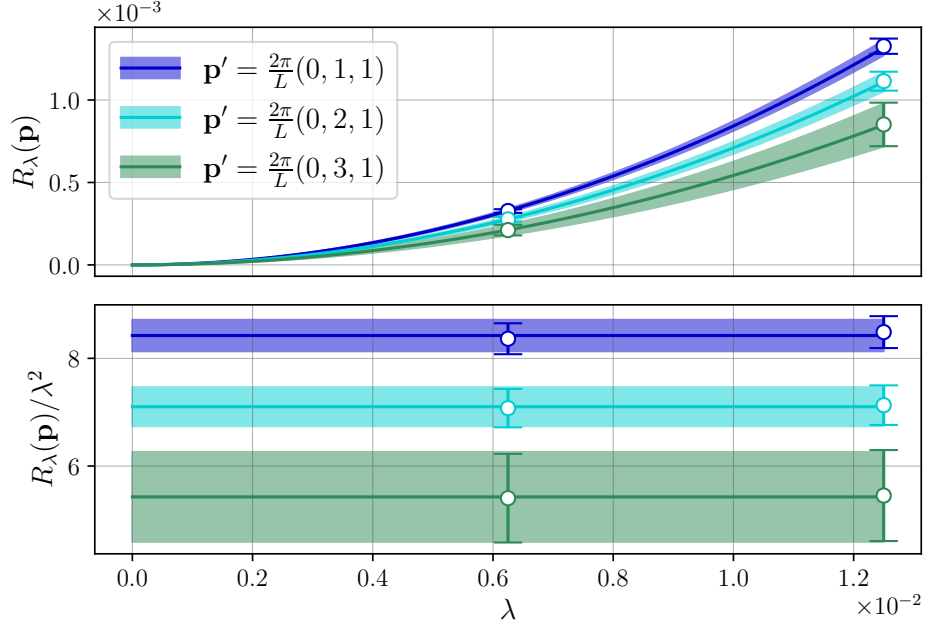


Figure 6.4: Plot of λ -dependence of R_λ after fitting in Euclidean time, for the same data as Fig. 6.2. Top: R_λ appears very well-described by $f(\lambda) = c\lambda^2$. Bottom: comparing the extracted b and R_λ/λ^2 , there appears to be less $\mathcal{O}(\lambda^4)$ contamination than, for instance, Fig. 5.4.

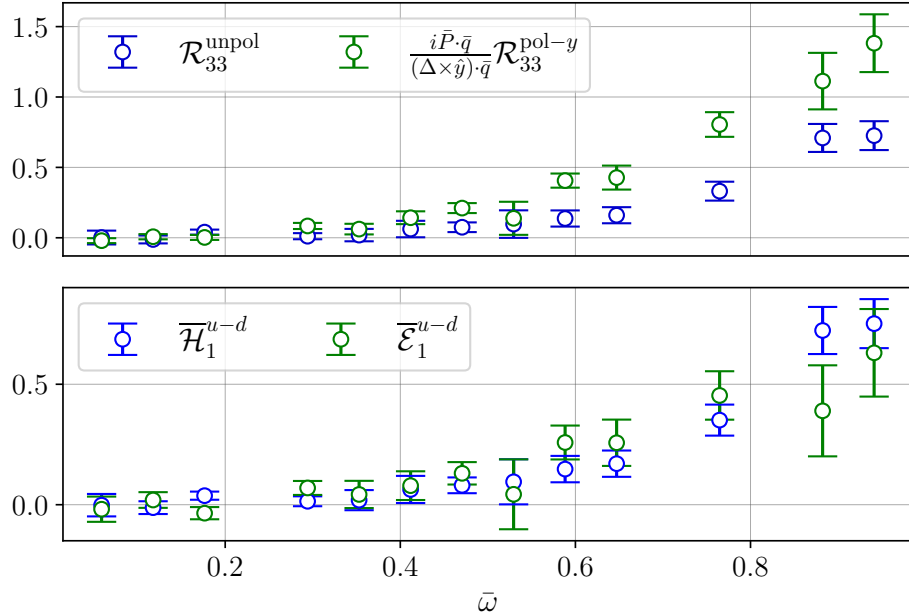


Figure 6.5: Top: the quantity \mathcal{R}_{kk}^Γ , as defined in Eq. (4.55), for $t = -0.57 \text{ GeV}^2$, $u - d$ quarks; note the polarised is normalised to keep the pre-factor of \mathcal{H}_1 unity. Bottom: the extracted Compton form factors.

Since $N_{\text{unpol}}^{\mathcal{H}} = 1$, we normalise our polarised results by $N_{\text{pol}}^{\mathcal{H}}$ so that they are on the same order as the unpolarised:

$$\begin{pmatrix} \mathcal{R}_{kk}^{\text{unpol}} \\ \mathcal{R}_{kk}^{\text{pol}}/N_{\text{pol}}^{\mathcal{H}} \end{pmatrix} = \begin{pmatrix} 1 & N_{\text{unpol}}^{\mathcal{E}} \\ 1 & N_{\text{pol}}^{\mathcal{E}}/N_{\text{pol}}^{\mathcal{H}} \end{pmatrix} \begin{pmatrix} \mathcal{H}_1 \\ \mathcal{E}_1 \end{pmatrix}. \quad (6.27)$$

Note that for most of our kinematics, we have

$$|N_{\text{unpol}}^{\mathcal{E}}| \ll 1, \quad N_{\text{pol}}^{\mathcal{H}}/N_{\text{pol}}^{\mathcal{E}} \approx 1, \quad \mathcal{R}_{kk}^{\text{unpol}} \sim \mathcal{R}_{kk}^{\text{pol}}/N_{\text{pol}}^{\mathcal{H}}. \quad (6.28)$$

Hence if we set $N_{\text{pol}}^{\mathcal{H}}/N_{\text{pol}}^{\mathcal{E}} = 1$, which is generally a very good approximation, then we have

$$\begin{pmatrix} \mathcal{H}_1 \\ \mathcal{E}_1 \end{pmatrix} = \frac{1}{1 - N_{\text{unpol}}^{\mathcal{E}}} \begin{pmatrix} 1 & -N_{\text{unpol}}^{\mathcal{E}} \\ -1 & 1 \end{pmatrix} \begin{pmatrix} \mathcal{R}_{kk}^{\text{unpol}} \\ \mathcal{R}_{kk}^{\text{pol}}/N_{\text{pol}}^{\mathcal{H}} \end{pmatrix}. \quad (6.29)$$

Therefore, since $N_{\text{unpol}}^{\mathcal{E}}$ is small for our kinematics, $\mathcal{H}_1 \approx \mathcal{R}_{kk}^{\text{unpol}}$, and is hence well-constrained. On the other hand, $\mathcal{E}_1 \approx \mathcal{R}_{kk}^{\text{pol}}/N_{\text{pol}}^{\mathcal{H}} - \mathcal{R}_{kk}^{\text{unpol}}$, the difference of two large signals, which means the results for the helicity-flipping amplitude tend to be somewhat noisier.

For our polarised Compton amplitude, the N factors are dominated by

$$N_{\text{pol}}^{\mathcal{H}}, N_{\text{pol}}^{\mathcal{E}} \sim \frac{(\boldsymbol{\Delta} \times \hat{\mathbf{e}}_{\text{pol}}) \cdot \bar{\mathbf{q}}}{2\bar{P} \cdot \bar{\mathbf{q}}}, \quad (6.30)$$

and hence we choose the spin polarisation direction, $\hat{\mathbf{e}}_{\text{pol}}$, such that this vector triple product is maximised. For $t = -0.57 \text{ GeV}^2$, this means $\hat{\mathbf{e}} = \hat{\mathbf{y}}$, while for the other two sets ($t = -0.29, -1.1 \text{ GeV}^2$), we choose $\hat{\mathbf{e}} = \hat{\mathbf{z}}$.

In general, we find a good signal for both polarised and unpolarised results. However, since \mathcal{H}_1 is dominant in the signal, Eq. (6.28), we observe that the signal of the \mathcal{E}_1 CFF is slightly worse. See Fig. 6.5, where we plot the ratios \mathcal{R} and the Compton form factors for $t = -0.57 \text{ GeV}^2$ and the $u - d$ combinations.

Furthermore, since the polarised pre-factors go like $N \sim |\boldsymbol{\Delta}|$ (Eq. (6.30)), at smaller values of $|t|$, we expect the polarised signal to be worse. This is what we observe in the $t = -0.29 \text{ GeV}^2$ results—see Fig. H.4 of Appendix H.

Off-forward subtraction function

As in the previous chapter, we can extract the off-forward subtraction function, S_1 , as defined in Eq. (5.18), from the $\bar{\omega} = 0$ results of the unpolarised results—see Eq. (6.14). We note that our results in Fig. 6.6 are similar to those from Chapter 5—see Fig. 5.8. As discussed in Chapter 5, our results for the subtraction function appear to violate the OPE prediction for this quantity. We discuss the forward subtraction function in detail in Chapter 8.

Note there is no $\bar{\omega} = 0$ result for the $t = -0.29 \text{ GeV}^2$ data, and hence these points are from the fit to that data that we perform in the next section.

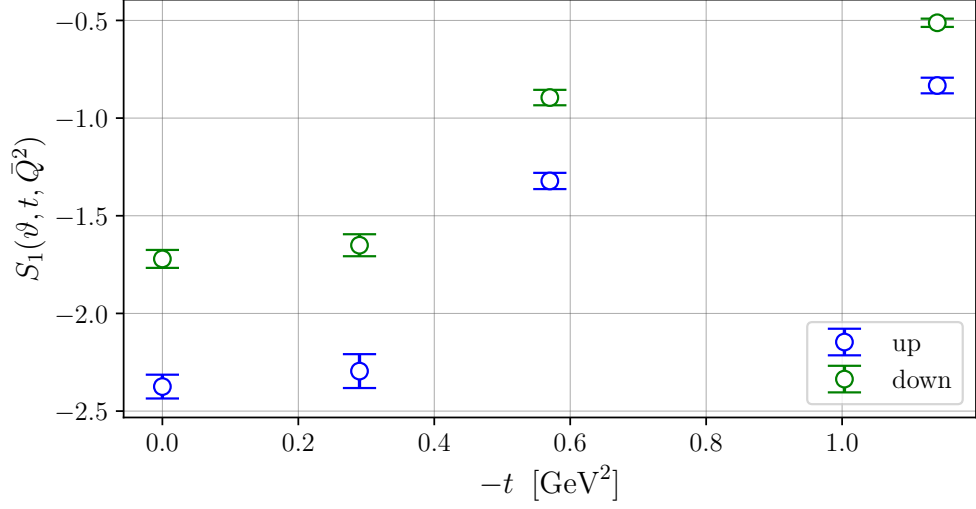


Figure 6.6: The off-forward subtraction function, defined in Eq. (5.18) for our range of t values and with $\bar{Q}^2 \approx 5 \text{ GeV}^2$ and $\vartheta = 0$. Shown are results for up and down quarks,

6.2.3 Moment fits

Now that we have the two Compton form factors, \mathcal{H}_1 and \mathcal{E}_1 , as functions of $\bar{\omega}$ for a range of t values, we can fit the moments of these using Bayesian Markov chain Monte Carlo (MCMC) as in Chapter 5. However, in contrast to that chapter, we use the model-independent GPD priors in Eq. (6.22). For the $t = 0, -0.57, -1.14 \text{ GeV}^2$ results, we use the following parameterisation for both of the *subtracted* CFFs:

$$f_{N_{\max}}(\bar{\omega}, t) = 2 \sum_{n=1}^{N_{\max}} \bar{\omega}^{2n} M_{2n}(t).$$

Since $|\bar{\omega}| < 1$, we can truncate this power series at a reasonable N_{\max} .

For the $t = -0.29 \text{ GeV}^2$ results, we must fit the subtraction function:

$$f_{N_{\max}}^{\text{unsub}}(\bar{\omega}, t) = S(t) + 2 \sum_{n=1}^{N_{\max}} \bar{\omega}^{2n} M_{2n}(t), \quad (6.31)$$

where $S(t)$ is constant in $\bar{\omega}$.

From our OPE results, Eq. (E.17), we can interpret the leading twist contributions to each of the amplitudes at zero-skewness ($\vartheta = 0 = \xi$) as towers of GPD moments, Eq. (6.7). Therefore, unlike the previous chapter, we are now able to separately calculate the helicity-conserving and -flipping GPD moments, $A_{n,0}$ and $B_{n,0}$, respectively. From here on we generally ignore the power corrections that arise from the fact that we have not extrapolated to $\bar{Q}^2 \rightarrow \infty$, and we treat our moments of the Compton form factors as GPD moments.

To use the GPD based prior distributions, Eq. (6.22), we need the forward moments a_n as an input. We determine these forward moments from the forward ($t = 0$) Compton amplitude calculated with Feynman-Hellmann at the same Q^2 value. Since the forward

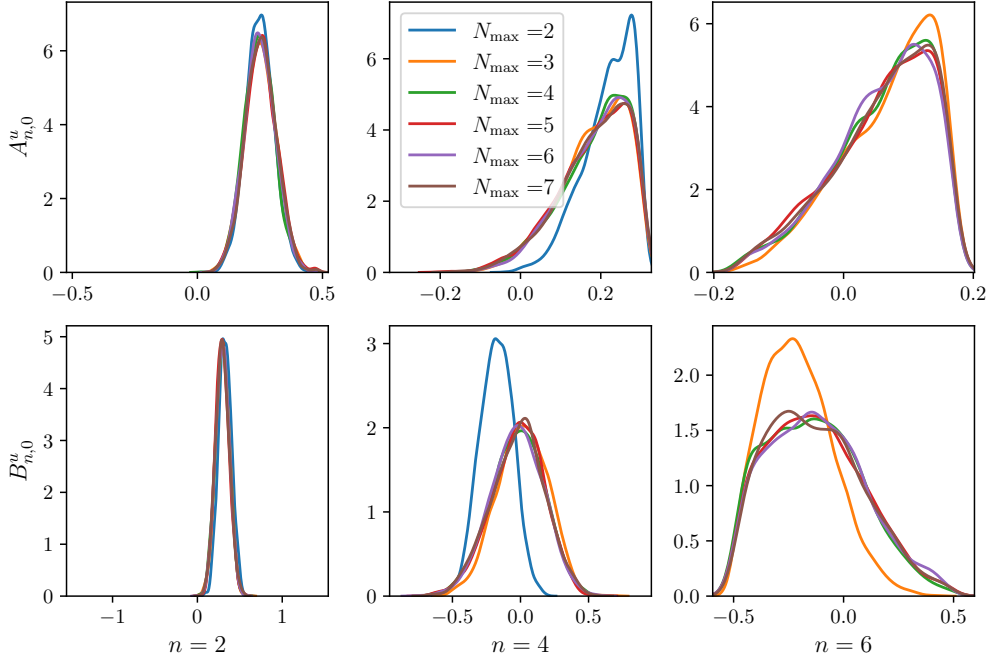


Figure 6.7: Density distributions for the n^{th} moment of the \mathcal{H}_1 CFF (top), and the \mathcal{E}_1 CFF (bottom) for the up quark and $t = -0.57 \text{ GeV}^2$ results. The bounds of the x -axis indicate the range of our prior distributions. N_{max} is the order of truncation in the $\bar{\omega}$ polynomial.

moments do satisfy the monotonically decreasing condition, we determine a_n with monotonic priors as in Refs. [37, 38]

Taking these forward moments, we use the following priors to fit our GPD moments:

$$|A_{n,0}(t)| \leq \bar{a}_n + \delta a_n, \quad |B_{n,0}(t)| \leq \frac{2m_N}{\sqrt{-t}}(\bar{a}_n + \delta a_n). \quad (6.32)$$

As in the previous chapter, the prior is uniformly distributed in this range. To fit the subtraction function for the $t = -0.29 \text{ GeV}^2$ results, we use the $\bar{\omega} = 0.03$ results, which should be very close to the subtraction function, and take a uniform prior distribution in the range

$$0.5\mathcal{H}_1(\bar{\omega} = 0.03) \leq S_1 \leq 1.5\mathcal{H}_1(\bar{\omega} = 0.03). \quad (6.33)$$

Although this seems somewhat arbitrary, using these priors the posterior for the subtraction function is a well-defined normal distribution—see Fig. H.6.

Results

In Fig. 6.7, we plot the posterior density distributions for the up quark moments of the two CFFs at $t = -0.57 \text{ GeV}^2$. We show the lowest three moments, and vary N_{max} , the order of truncation in the $\bar{\omega}$ polynomial; that is, the highest moment is $M_{2N_{\text{max}}}$. For the first two moments, we find good agreement among all N_{max} except $N_{\text{max}} = 2$. This likely reflects the larger number of $\bar{\omega}$ values in this chapter, which reduces the dependence on truncation order.

As we expect, the leading $n = 2$ moment is well-determined for both A and B moments, as it is constrained by the small $\bar{\omega}$ data, which is cleaner and has more $\bar{\omega}$ points. For $n = 4$ the B GFF is approximately normally distributed, although its errors are quite large. For the higher n A GFFs, the distributions skew rightwards. This shows that for the higher n A GFFs the fit prefers a higher value than what is allowed by the prior. This is concerning, since our GPD priors in Eq. (6.22) are model-independent. We will return to the unusually large values of A GFF moments for $n > 2$ in our section on systematics.

As can be seen in Fig. 6.8, the data is generally well described by the fit. The clear exception is the $t = -0.29 \text{ GeV}^2$ data, which is much worse both in terms of the Compton form factors (Fig. 6.8), and the determined moments (Fig. 6.10); see also Fig. H.4. We discuss difficulties associated with the $t = -0.29 \text{ GeV}^2$ and \mathcal{E}_1 results in our section on systematic errors.

In Fig. 6.9, we plot the moments of \mathcal{H}_1 , and in Fig. 6.10 those of \mathcal{E}_1 , both of which we interpret as their leading twist GPD moment contributions, $A_{2,0}$ and $B_{2,0}$, respectively. Further, in Fig. 6.11, we plot the isovector combination of these moments compared to the moments extracted from lattice three-point calculations at a similar pion mass [127].

For these moment plots, we also perform a simple dipole fit to the moments as a function of t :

$$G(t) = \frac{G(0)}{1 - t/m_{\text{dip}}^2}. \quad (6.34)$$

There are theoretical motivations to use this parameterisation for $|t| < 1 \text{ GeV}^2$ [242], and moreover it has been used in numerous previous lattice studies of GPD moments. There are other parameterisations that are commonly used, including the tripole [243] and z -fit [244]. However, since our error bars are large and we have a small sample of t values, we restrict ourselves to this simple dipole fit. The results of the parameters for these fits are presented in Table 6.4.

Looking at Fig. 6.9, we note that the $A_{2,0}$ and $A_{4,0}$ moment are generally well-determined. This is a result of the fact that the \mathcal{H}_1 CFF is dominant in our data. The $A_{2,0}$ moments are generally in good agreement with other determinations of this GFF using three-point function methods [122–127]. They are also in agreement with the previous chapter's set of results, Fig. 5.7, which are dominated by the $A_{n,0}$ GFFs, and hence we expect the data sets to largely agree.

As discussed in Chapter 5, the $A_{4,0}$ at $t = 0$ is approximately a factor of two larger than this moment measured experimentally at a similar hard scale [44]. Moreover, recall from Fig. 6.7 that the $A_{4,0}$ distribution at $t = -0.57 \text{ GeV}^2$ skewed rightwards, indicating that the upper bound from the priors is too severe and that a less constrained fit would return an *even higher value*. We discuss possible sources of this anomalous behaviour in our section on systematic errors.

In Fig. 6.10, by contrast, we see that our $B_{2,0}$ is less well-determined, especially for smaller $|t|$, and the $B_{4,0}$ results are quite unconstrained. In its very general features, $B_{2,0}$ agrees with previous three-point lattice results: the up quark contribution is positive, while the down quark contribution is largely negative [122–127]. Encouragingly the $B_{2,0}^{u-d}$ contribution (see Fig. 6.11) agrees well with previous lattice studies at a similar pion mass [127]. On the other hand, there is tension between our $B_{2,0}^{u+d}$ results, and those of other lattice calculations. Moreover, we note that the dipole parameters are generally

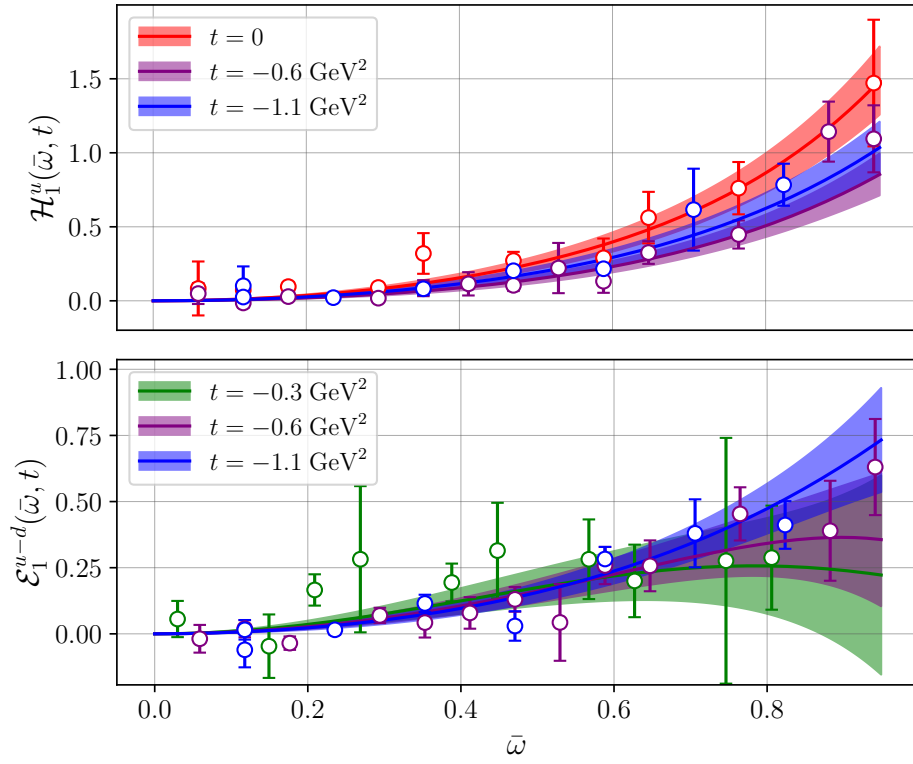


Figure 6.8: The Compton form factor for three different t values, and the fit to these points using the parameterisation in Eq. (5.32) and the prior distributions in Eq. (6.32). Top: the \mathcal{H}_1 CFF for up quarks with the data points for the forward results omitted. Bottom: the \mathcal{E}_1 CFF for the isovector combination.

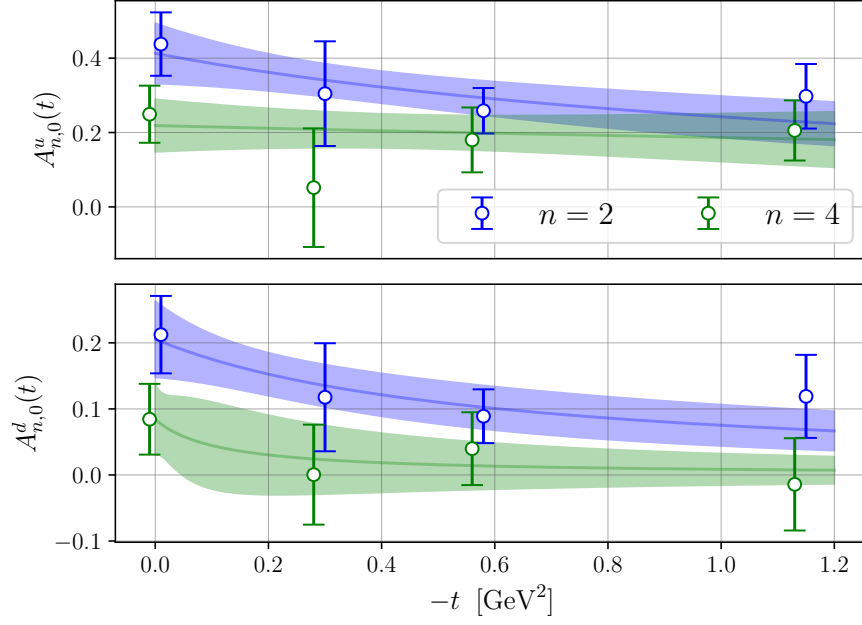


Figure 6.9: The first two even moments of the \mathcal{H}_1 Compton form factor as a function of t . The shaded band is a plot to the parameterisation in Eq. (6.34). Top: up quarks; bottom: down quarks.

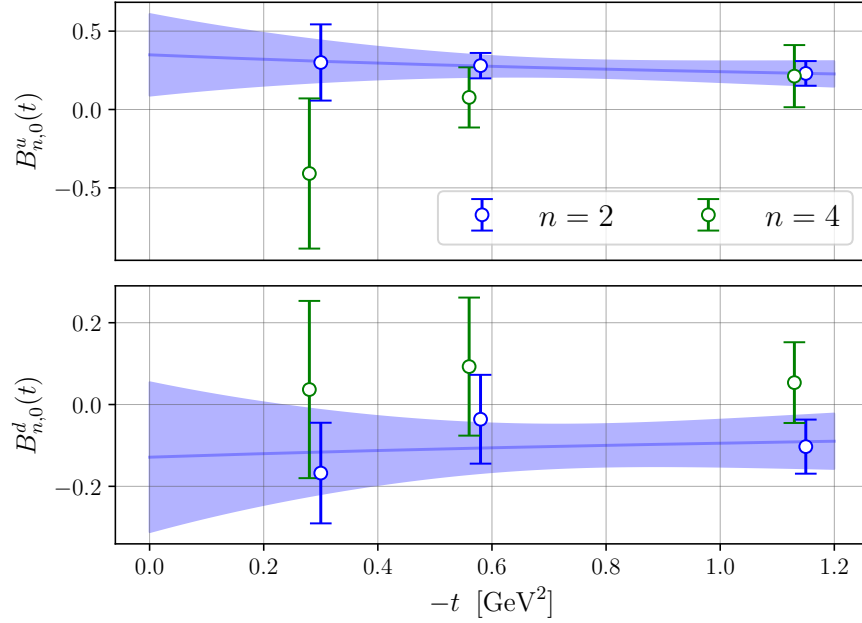


Figure 6.10: The first two even moments of the \mathcal{E}_1 Compton form factor as a function of t . The shaded band is a plot to the parameterisation in Eq. (6.34). Top: up quarks; bottom: down quarks.

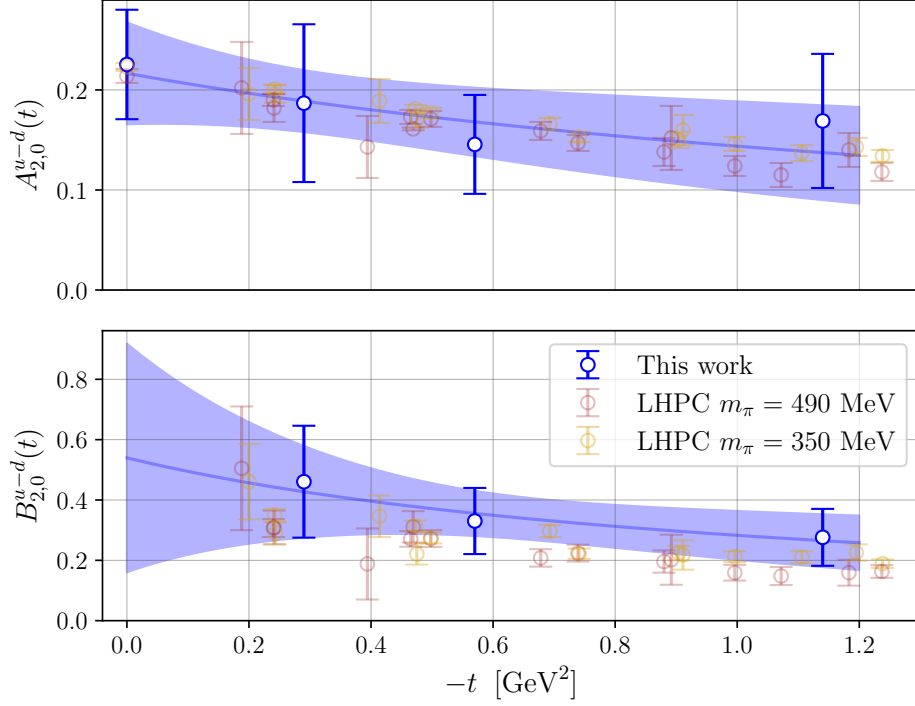


Figure 6.11: The $n = 2$ isovector moments compared to moments from a lattice three-point calculation of GPDs with comparable pion masses [127].

much more poorly determined for the B form factors. This is likely due to the larger error bars, especially for $t = 0.29$ GeV², and the fact that there is no $t = 0$ result for this GFF.

Finally, we compare our $u - d$, $n = 2$ results to three-point results from Ref. [127]: one set with $m_\pi = 350$ MeV, and another with $m_\pi = 500$ MeV. Both these pion masses are close to our pion mass of $m_\pi = 412$ MeV. Similarly, our lattice volume is $L \sim 3$ fm, which is close to the lattice sizes used for the three-point calculations. However, our lattice had many more sites: $N_L^3 \times N_T = 48^3 \times 96$, compared to $N_L^3 \times N_T = 28^3 \times 32$ and $N_L^3 \times N_T = 20^3 \times 32$ for the three-point function studies. We find strong agreement between our results and the three-point calculations. While our error bars are significantly larger than many of those for the three-point functions, our method is still exploratory and there are many possible avenues to improve the quality of our signal—in particular, see Chapter 8. Nonetheless the agreement between our method and the three-point study is encouraging.

There are also higher-twist— m_N^2/\bar{Q}^2 , $|t|/\bar{Q}^2$ and $\Lambda_{\text{QCD}}^2/\bar{Q}^2$ —corrections to our moments that should, even in the continuum limit, distinguish our moments from the three-point moments. Although it is difficult to comment on these effects here, we note that the $|t|/\bar{Q}^2$ effects will increase with $|t|$, which could possibly account for the slight increase in the $t = -1.1$ GeV² for $A_{2,0}$ shown in Fig. 6.11.

Similarly, we see a reasonable agreement between the parameters from the dipole fit and those of lattice three-point studies at a similar pion mass for the isovector $n = 2$ moment [127]. Theoretically it is expected that dipole mass increases with n , which in

Table 6.4: Summary of parameters from our dipole fit. The dipole mass for some GFF, G , is labelled m_G .

	u	d	$u - d$
$A_{2,0}(0)$	0.413(81)	0.205(58)	0.217(51)
$B_{2,0}(0)$	0.35(26)	-0.13(18)	0.54(38)
$A_{4,0}(0)$	0.219(70)	0.084(54)	0.174(63)
$m_{A_{2,0}}$	1.19(48)	0.76(33)	1.40(91)
$m_{B_{2,0}}$	1.5(2.1)	1.7(5.1)	1.05(96)
$m_{A_{4,0}}$	2.4(4.0)	0.34(54)	$1\text{e}+04 \pm 2.7\text{e}+11$

Table 6.4 we can see is largely the case, comparing $m_{A_{2,0}}$ and $m_{A_{4,0}}$. However, as we will discuss, the higher moments of \mathcal{H}_1 may be affected by lattice artefacts.

Finally, as a point of comparison, we note that we can use the Ji sum rule, Eq. (2.82), to determine the contribution to the total proton spin from quark spin and orbital angular momentum:

$$\langle J_{u-d}^3 \rangle = \frac{1}{2} [A_{2,0}^{u-d}(0) + B_{2,0}^{u-d}(0)] = 0.39(22),$$

which agrees with lattice three-point studies at a similar pion mass [127]. However, due to the large size of the error bars on $B_{2,0}(0)$, the errors are significantly larger than those for the three-point studies.

6.2.4 Generalised parton distribution fit

Finally, we attempt a fit to our data using a GPD model. As discussed in Sections 3.2 and 4.2, extracting a parton distribution from the Compton amplitude in the $|\bar{\omega}| < 1$ region is an ill-conditioned inverse problem: the resulting parton distribution will be very sensitive to fluctuations in our data [161]. Therefore, a direct inversion method such as singular value decomposition would require much more precise data and a greater spread of $\bar{\omega}$ values than is currently available.

Instead, one can use a simplified parton distribution ansatz with a finite number of parameters and our Bayesian MCMC fitting procedure. Although this means sacrificing model-independence, it also gives us far more traction in solving for the GPD. This approach has already been applied to Ioffe time distributions of forward parton distributions [139] and the forward Compton amplitude from Feynman-Hellmann [161]. Here, we simultaneously fit the forward ($t = 0$) and off-forward data to our parameterisation. A similar global fit to lattice three-point moments and quasi-GPDs has also been carried out [245].

For our GPD model we use a simple Regge-inspired parameterisation [222–225],

$$H(x, t) = \frac{\Gamma(3 - \alpha_0 + \beta)}{\Gamma(2 - \alpha_0)\Gamma(\beta + 1)} A x^{-\alpha(t)} (1 - x)^\beta, \quad (6.35)$$

where $\alpha(t) = \alpha_0 + \alpha' t$. This gives us a total of four parameters: A, α_0, α' and β . The above parameterisation is normalised so that $A = A_{2,0}(t = 0)$, the leading PDF moment. Note that Γ here is the complete gamma function, not to be confused with the regularised

gamma function, $\tilde{\Gamma}$, in Eq. (6.26) or the spin-parity projector. We also note that this model is best justified for valence quarks, though our results include sea quark contributions.

From our OPE results, Eq. (E.17), we know that at leading-twist

$$\mathcal{H}_1(\bar{\omega}, t) = 2 \sum_{n=1} \bar{\omega}^n \int_{-1}^1 dx x^{2n-1} H(x, t) = 2 \sum_{n=1} \bar{\omega}^n \int_0^1 dx x^{2n-1} H^{(+)}(x, t), \quad (6.36)$$

where we have defined $H^{(+)}(x, t) = H(x, t) - H(-x, t)$. Inserting our model GPD for $H^{(+)}(x, t)$, we find our final parameterisation:

$$\mathcal{H}_1(\bar{\omega}, t) = 2A \sum_{n=1}^{\infty} \bar{\omega}^{2n} \frac{\Gamma(2n - \alpha(t))\Gamma(3 - \alpha_0 + \beta)}{\Gamma(2 - \alpha_0)\Gamma(1 + 2n - \alpha(t) + \beta)}, \quad (6.37)$$

So the n^{th} moment is

$$A_{n,0}(t) = A \frac{\Gamma(n - \alpha(t))\Gamma(3 - \alpha_0 + \beta)}{\Gamma(2 - \alpha_0)\Gamma(1 + n - \alpha(t) + \beta)}. \quad (6.38)$$

Unlike the previous section, there is no reason to truncate the power series in $\bar{\omega}$, since each moment does not add another parameter, but on the contrary allows us to better constrain our given four parameters. Recall that, due to the ill-conditioned inverse problem, small changes in our $\bar{\omega}$ space fit can result in much larger changes in our parton distributions. As such, we choose a very large order of truncation, $n = 100$, in our fit.

Note that the above series can be resummed as

$$\begin{aligned} \mathcal{H}_1(\bar{\omega}, t) &= 2A\bar{\omega}^2 \frac{\Gamma(3 + \beta - \alpha_0)\Gamma(2 - \alpha(t))}{\Gamma(3 + \beta - \alpha(t))\Gamma(2 - \alpha_0)} \\ &\times {}_3F_2 \left[\begin{matrix} 1, (2 - \alpha(t))/2, (3 - \alpha(t))/2 \\ (3 + \beta - \alpha(t))/2, (4 + \beta - \alpha(t))/2 \end{matrix}; \bar{\omega}^2 \right], \end{aligned} \quad (6.39)$$

where ${}_3F_2$ is a generalised hypergeometric function.

While the GPD ansatz in Eq. (6.35) is useful, it is known that for $|t| \gtrsim 0.8 \text{ GeV}^2$ this parameterisation does not reproduce the behaviour of the Dirac form factor F_1 , which is the $n = 1$ GPD moment [246, 247]. As a result, we use only the $t = 0, -0.29, -0.57 \text{ GeV}^2$ data, dropping the $t = -1.1 \text{ GeV}^2$ results from our fit. Other, more involved GPD models exist [222–225, 246–249]; however, for a first attempt we stick to this simplest model.

Due to monotonicity of the forward moments (Eq. (5.34)), we can constrain A . Further, from integrability of Eq. (6.35), we can constrain $\alpha(t)$ and β :

$$0 \leq A \leq 1, \quad \alpha(t) < 2, \quad \beta > -1. \quad (6.40)$$

To ensure that our Compton amplitude shrinks in size with increasing $-t$, we choose $\alpha' > 0$. Phenomenologically and from Regge theory, we expect $\alpha' \approx 0.9 \text{ GeV}^{-2}$ for valence quarks [250], and $\alpha' \approx 0.2 \text{ GeV}^{-2}$ for sea quarks [251]. Since we only look at the $u - d$ contribution that has no sea quarks, we centre our priors around the former value. In practice, since we always choose $\alpha' > 0$ and we have $t < 0$, the bound $\alpha(t) = \alpha_0 + \alpha't < 2$ means that we only need to keep $\alpha_0 < 2$, since $\alpha't < 0$.

Therefore, to test the model-dependence of our fit to changes in the prior distributions, we use three ranges of uniform priors given in the table below. They are chosen to conform

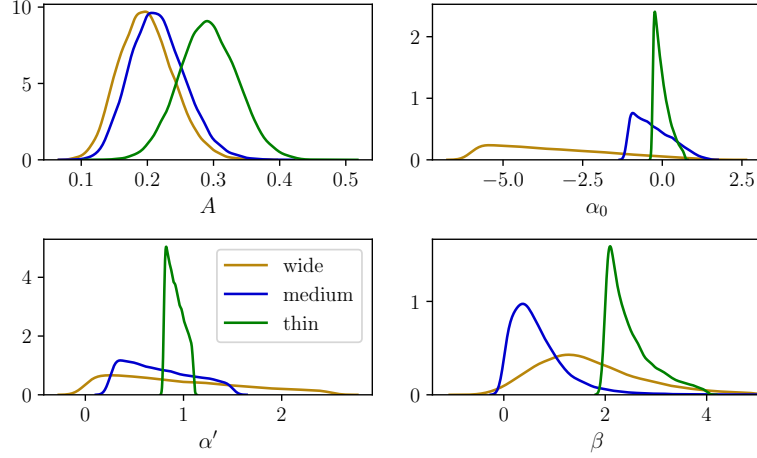


Figure 6.12: Density distributions for the fit parameters of the GPD ansatz, Eq. (6.35). The different colours are the three different prior distribution widths: ‘wide’, ‘medium’ and ‘thin’.

to the aforementioned conditions, and to be roughly centered around the phenomenologically expected values: $\alpha_0 = 0.2$, $\alpha' = 0.9 \text{ GeV}^{-2}$ and $\beta = 3$.

	A	α_0	$\alpha' [\text{GeV}^{-2}]$	β
thin	[0, 1]	[-0.3, 0.7]	[0.8, 1.1]	[2, 4]
medium	[0, 1]	[-1.1, 1.5]	[0.25, 1.5]	[0, 6]
wide	[0, 1]	[-6, 1.9]	[0.0, 2.5]	[-0.9, 8]

As can be seen in Fig. 6.12, the posterior distributions are highly sensitive to the choice of prior distribution, and typically do not favour the phenomenological values, except for A . For β with ‘wide’ and ‘medium’ priors, the posterior is reasonably well-constrained, although the peak differs significantly from the phenomenologically expected value of $\beta \approx 3$. For α_0 and α' , the distributions are skewed but otherwise poorly defined, reflecting that the data does not constrain these parameters well.

In the top panel of Fig. 6.13, we show the CFF \mathcal{H}_1 at $t = -0.57 \text{ GeV}^2$ compared to the parameterisation fits. We note that the ‘wide’ and ‘medium’ prior limits are a reasonably good fit to this data. On the other hand, the ‘thin’ fit, which is chosen based on phenomenologically reasonable prior distributions, is a poor match for the higher $\bar{\omega}$ values.

In the lower panel of Fig. 6.13, we plot the resulting parton distribution weighted by x , $x p(x)$. This is simply the fit to Eq. (6.35) at $t = 0$ weighted by x . Phenomenologically, we expect it to peak between $x \approx 0.2$ – 0.3 . Instead, the ‘medium’ and ‘wide’ distributions peak at a much larger x value. We saw in Fig. 6.12 that the data favoured β smaller than the phenomenological expectation. Since the $x \rightarrow 1$ behaviour is dominated by $(1-x)^\beta$, the fact that the data prefers small β is borne out in x space by a distribution that does not drop sufficiently quickly for $x \rightarrow 1$.

It is also noteworthy that, while the ‘wide’ and ‘medium’ parameter fits are almost identical in $\bar{\omega}$ space, they produce quite different parton distributions. This is a result of the ill-conditioned inverse problem: small changes in our Compton amplitude lead to much larger changes in the parton distribution.

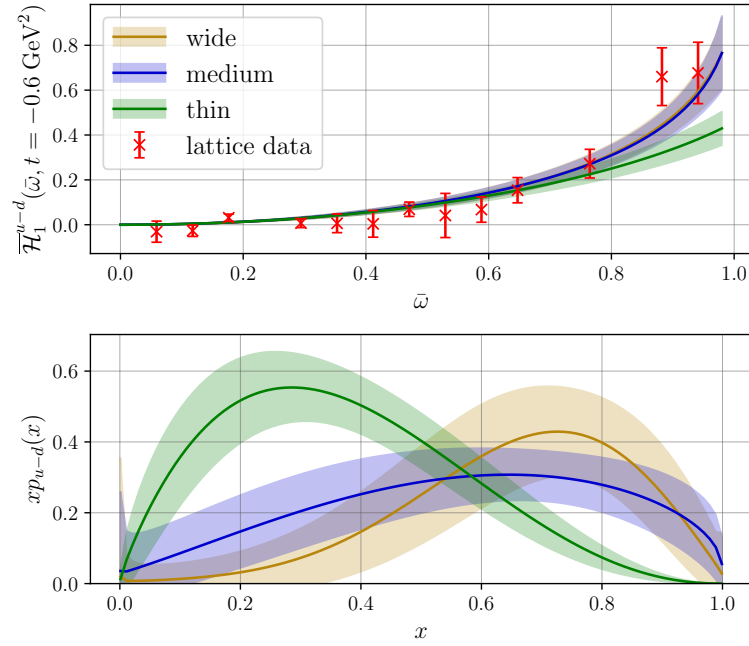


Figure 6.13: Top: the \mathcal{H}_1 Compton form factor and fits to it for the three prior distribution widths. Bottom: the corresponding forward PDFs weighted by x .

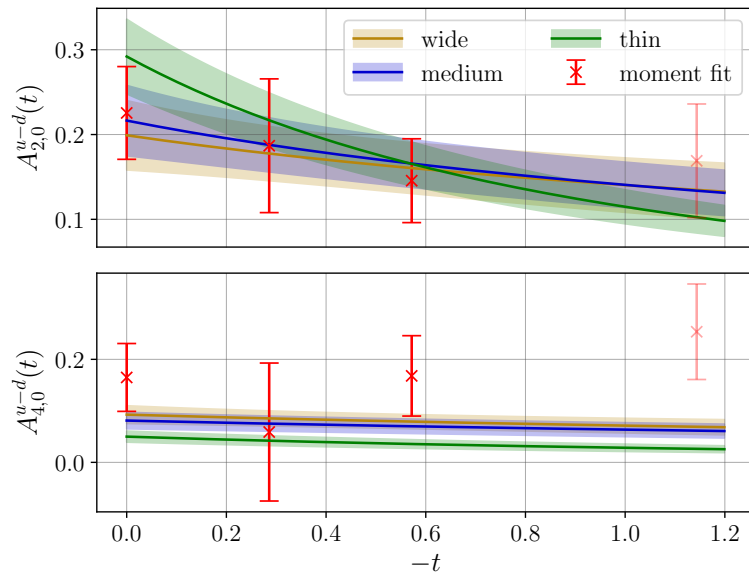


Figure 6.14: A comparison of the first two moments from the model fits and the direct moment fits. Recall that the $t = -1.1 \text{ GeV}^2$ data was not used in our model fits.

Finally, in Fig. 6.14 we compare the moments from this GPD model fit to the largely model-independent moment fits we presented previously. While the $A_{2,0}$ moments agree across t values for all the fits[§], there is less agreement among the $A_{4,0}$ results. In particular, the ‘wide’ and ‘medium’ results are just consistent with the moment fit, while the ‘thin’ results are consistent with only one of the t values from the moment fit. As discussed previously, the $A_{4,0}$ at $t = 0$ from our moment fit is approximately a factor of two larger than that measured experimentally [44].

Therefore, this demonstrates that for our large $\bar{\omega}$ results, our \mathcal{H}_1 is anomalously large, which leads to unphysically small values of β and hence a parton distribution that peaks at a later value of x than expected. This is the same effect we saw for the moment fit: the $A_{n,0}$ moments for $n > 2$ are unphysically large, and these moments are similarly constrained by large $\bar{\omega}$.

6.2.5 Systematic errors

Here, we address some of the anomalous results presented in this chapter: (1) the poor quality of the $t = -0.29 \text{ GeV}^2$ results; (2) the \mathcal{E}_1 Compton form factor and its moments, $B_{n,0}$, especially for isoscalar combination; and (3) the magnitude of the $A_{n,0}$ moments for $n > 2$.

As discussed previously in this chapter, there are a number of reasons why the \mathcal{E}_1 and $t = -0.29 \text{ GeV}^2$ results will be poorer both independently, as well as the \mathcal{E}_1 results at $t = -0.29 \text{ GeV}^2$. We recapitulate these below:

- The contamination from FH excited states is worse from small $|t|$, Eq. (4.39).
- There is no $\bar{\omega} = 0$ term for the $t = -0.29 \text{ GeV}^2$ results, so the subtraction term must also be fit.
- In the combined polarised and unpolarised signals, \mathcal{E}_1 is suppressed with respect to \mathcal{H}_1 , Eq. (6.28).
- Similarly, the \mathcal{R}^{pol} data goes like $|\Delta|$, leading to poorer signal for \mathcal{E}_1 at low $|t|$.
- The prior distributions, Eq. (6.22), for the moments of \mathcal{E}_1 have an upper bound of $2m_N/\sqrt{-t}$, and hence the priors are much looser for small $|t|$.

As such, we expect the $t = -0.29 \text{ GeV}^2$ results, particularly for \mathcal{E}_1 , to be the lowest quality. From the Compton amplitude (Fig. 6.8) and the moments (Fig. (6.10)) this appears to be the case—supplementary results are given in Appendix H.

We also saw in both the moment fit and the GPD model fit that the large $\bar{\omega}$ values lead to unphysical results. Since the large $\bar{\omega}$ values are determined by large sink momenta, \mathbf{p}' , there are two likely systematic errors associated with high momentum:

- **Euclidean time fits:** at large \mathbf{p}' it is more difficult to isolate the ground state at the sink, as discussed in Chapter 3. Similarly, as we showed in Chapter 4, in the limit $|\bar{\omega}| \rightarrow 1$, FH excited states are less suppressed—Eq. (4.40). Both of these contributions could prevent a clean isolation of the off-forward Compton amplitude for large $\bar{\omega}$.

[§]Recall that we have dropped the $t = -1.1 \text{ GeV}^2$ results from our fit.

- **Discretisation artefacts:** it is possible that $\mathcal{O}(a|\mathbf{p}'|)$ and $\mathcal{O}(a|\mathbf{q}_{1,2}|)$ discretisation errors in our lattice Compton amplitude are worse for large $\bar{\omega}$. This is because for large $\bar{\omega}$ we need larger $|\mathbf{p}'|$ and project out the largest contribution from the $\mathbf{q}_{1,2}$ vectors—see Eq. (5.30).

There are methods such as distillation [144] and momentum smearing [252, 253] to improve extraction of matrix elements for momenta as high as $|\mathbf{p}'| \simeq 3$ GeV, more than double the value of $|\mathbf{p}'| \simeq 1$ GeV used here. Similarly, lattice Feynman-Hellmann calculations have previously performed multi-state fits to account for FH induced excited states [173]. In Chapter 8, we will discuss discretisation effects in greater detail; however, a full investigation of discretisation effects is beyond the scope of this thesis.

Of course, there are many other lattice systematics to investigate, both those that are unique to our method and general artefacts. Here, we only listed the systematics that may explain some of our anomalous results.

6.3 Conclusion and Outlook

In this chapter, we have implemented a range of improvements to the lattice calculation in Chapter 5, both conceptual and numerical. We isolated the Compton form factors \mathcal{H}_1 and \mathcal{E}_1 , with much greater range of $\bar{\omega}$ values, and with one more t value than the previous chapter. The leading moments for these Compton form factors were found to be consistent with lattice calculations at a similar pion mass, which is a promising sign for future calculations.

Moreover, the isolation of these two CFFs opens up the possibility of studying higher-twist contributions, as has been done in the forward case with Feynman-Hellmann [38]. Similarly, by isolating these two form factors, it is possible to perform fits using GPD models. A successful implementation of model fits and the determination of higher-twist contributions would both be very exciting from a phenomenological perspective.

Finally, we also made more incremental improvements to our method, implementing weighted averaging for the Euclidean time fits, and deriving prior distributions for our moments that reflect positivity constraints on GPDs, allowing us to fit non-positive definite CFFs such as \mathcal{E}_1^d . As such, the numerical recipe outlined in this chapter lays the groundwork for future studies.

However, in isolating the different CFFs and performing the model GPD fit we have pushed our method to its limits, and demonstrated the need for greater control of lattice systematics. The most salient of these are listed below.

- Improved signal at large sink momenta, for which a number of methods are available [144, 252, 253]. This would help us improve the determination of higher moments, and possibly address the anomalous large $\bar{\omega}$ behaviour.
- Apropos the large $\bar{\omega}$ behaviour and the anomalous behaviour of the subtraction function (Fig. 6.6), a thorough investigation of lattice discretisation artefacts is necessary. In Chapter 8, we apply a lattice perturbation theory (LPT) calculation of the Compton amplitude [254] to correct some of these artefacts. Such a calculation could in principle be extended to off-forward kinematics and used to correct the $\mathcal{O}(a|\mathbf{p}'|)$ and $\mathcal{O}(a|\mathbf{q}_{1,2}|)$ artefacts discussed above.

- As we discussed in our Euclidean time fitting section and Chapter 4, for certain kinematics our Feynman-Hellmann excited states may be difficult to suppress. Along these lines, multi-state fits to FH calculations have been very successful for the extraction of the axial charge [173], a method which can be extended to our type of calculation.
- Finally, it is ideal that lattice systematics which are not specific to our type of calculation—unphysical quark masses, lattice spacing and volume—are accounted for before contact is made with phenomenology.

However, all of these difficulties can in principle be overcome. A calculation of the off-forward Compton amplitude that accounted for these systematics would give us a wealth of phenomenological knowledge:

- The off-forward subtraction function, $S_1(\vartheta, t, \bar{Q}^2)$, is of interest in relation to the question of the ‘fixed pole’ hypothesis in Regge phenomenology [216, 217]. Further, it is a background for experimental determinations of the proton pressure distribution [89]. Moreover by calculating this quantity for non-zero-skewness we could determine the D -term [87]. Our method is one of the few ways to calculate this quantity from first principles—we will discuss this further in Chapter 8.
- Higher-twist corrections and the scaling behaviour of the off-forward Compton amplitude is currently not well-studied from a theoretical or experimental perspective [231–234]. Our method allows us to determine the \bar{Q}^2 behaviour and isolate certain higher-twist contributions as was done in the forward case [38].
- Finally, we can also use this method to determine the x and t dependence of GPDs, which would complement efforts in the quasi- and pseudo-distribution approaches.

This work has been a starting point, showing the promise and also the limits of our present method.

Polarised Forward Compton Amplitude

In this chapter we take the tools developed in Chapters 4–6 and apply them to a calculation of the *polarised forward* Compton amplitude. We have already derived a Feynman-Hellmann relation for this quantity in Chapter 4. Moreover, we apply the method of separating \mathcal{H}_1 and \mathcal{E}_1 developed in Chapter 6 to extract the different spin-dependent Compton structure functions, \tilde{g}_1 and \tilde{g}_2 . Then, we determine Mellin moments of the two spin-dependent deep-inelastic scattering structure functions, g_1 and g_2 .

Recall in Chapter 2 we have already discussed in some detail the polarised forward Compton amplitude and its moments. For the purposes of our calculation, this polarised Compton amplitude is particularly interesting for two reasons: (1) the moments of the polarised structure functions are related to many physical quantities and sum rules; and (2) it is often the non-leading-twist contributions to these moments that are of the most interest—for instance, the higher-twist d_2 contribution or the effective strong coupling. Moreover, experimental determinations struggle to access small x kinematics which are necessary to measure these moments [255, 256]. Since our calculation is best suited to determine moments for a range of hard scale, Q^2 , values, we are uniquely positioned to determine physical quantities and test sum rules for the polarised structure functions.

The first moment of g_1 can be related by the Ellis-Jaffe sum rule, Eq. (2.65), to the axial coupling g_A , and in particular the axial decay constant g_A^{u-d} [71]. This first moment of g_1 can also be used to access the effective strong coupling, Eq. (2.66), which is particularly interesting as it extends the idea of the QCD coupling into the non-perturbative domain [72]. Lattice determinations of the axial coupling g_A through three-point functions have a long history, and have come under increased scrutiny recently as it has become clear that excited state contaminations are significant for such calculations [104]. This has motivated recent calculations of g_A through first-order Feynman-Hellmann, which may have better excited state control [173, 174, 181]. However, none of these three-point or first-order Feynman-Hellmann calculations are capable of accessing the hard scale dependence that is necessary to determine the effective coupling.

The first moment of g_2 is predicted to be zero by the Burkardt-Cottingham sum rule [74]; however, this prediction is not completely model-independent and therefore needs to be tested theoretically and experimentally. Experimental determinations of the first moment of g_2 are difficult due to the limited accessibility of low x data [255]. Although this sum rule has been investigated thoroughly in perturbative QCD [257–261], few lattice QCD methods exist to test it. Since we can access this moment with its higher-twist

corrections, ours is the first lattice calculation capable of testing the Burkardt-Cottingham sum rule to all orders.

Moreover, using the third moments of g_1 and g_2 , one can access the higher-twist but not power-suppressed matrix element d_2 [44, 70]. This observable contains interesting information about quark-gluon correlations within nucleons. There have been numerous experimental determinations of this quantity, but there is little agreement among these results due its small size and relatively large errors [262–268]. There have also been several lattice determinations of d_2 using three-point functions, starting with quenched [118] and later dynamical calculations [119–121]. Again, there is a great amount of variation in the lattice results, as there are among the experiments. This is in part due to the fact that d_2 is highly sensitive to changes in lattice spacing and pion mass [120], and in part due to the difficulty in resolving the small signal for d_2 .

Finally, there have been calculations of the twist-two parton distributions (the helicity or polarised PDFs) using the quasi-distribution [151–153] and pseudo-distribution [154] approaches. As $Q^2 \rightarrow \infty$, the structure function $g_1(x, Q^2)$ converges to this parton distribution function. However, these quasi- and pseudo-distribution studies in principle can only access the light-cone parton distributions, and not the higher-order contributions necessary to determine the effective strong coupling or test the Burkardt-Cottingham sum rule to all orders.

The structure of the chapter follows: In Section 7.1, we construct a parameterisation that separates the two spin-dependent Compton structure functions, $\tilde{g}_{1,2}$. Moreover, we derive prior distributions for the moments that we use for Bayesian Markov chain Monte Carlo fitting. Then in Section 7.2, we present our results for a single value of the hard scale, $Q^2 = 4.86 \text{ GeV}^2$. We also present our determinations of the aforementioned moments: g_A , d_2 as well as a test of the Burkardt-Cottingham sum rule. Further, we discuss some possible sources of lattice artefacts and methods to control them. Finally, in Section 7.3, we summarise these results and identify future areas of investigation. As such, this research lays the groundwork for further studies of the g_1 and g_2 structure functions using lattice Feynman-Hellmann methods.

7.1 Set-up and Parameterisation

We have already met the spin-dependent Compton structure functions, $\tilde{g}_{1,2}$, in Eq. (2.20):

$$T_{\mu\nu}(P, q) = \left(-g_{\mu\nu} + \frac{q_\mu q_\nu}{q^2}\right) \mathcal{F}_1(\omega, Q^2) + \left(P_\mu - \frac{P \cdot q}{q^2} q_\mu\right) \left(P_\nu - \frac{P \cdot q}{q^2} q_\nu\right) \frac{\mathcal{F}_2(\omega, Q^2)}{P \cdot q} + \frac{i}{P \cdot q} \epsilon_{\mu\nu\rho\kappa} q^\rho \left(s^\kappa \tilde{g}_1(\omega, Q^2) + \left(s^\kappa - \frac{s \cdot q}{P \cdot q} P^\kappa\right) \tilde{g}_2(\omega, Q^2)\right).$$

Recall the definition of the spin vector, Eq. (2.21):

$$s_\mu \equiv \frac{1}{2} \bar{u}(p, s) \gamma_\mu \gamma_5 u(p, s).$$

Similarly, we encountered these Compton structure functions in another form in Chapter 5, where we considered off-forward scattering. From Eq. (5.11), we note that $\tilde{g}_{1,2}$ are

the forward limit of $\tilde{\mathcal{H}}_{1,2}$:

$$\lim_{t \rightarrow 0} \tilde{\mathcal{H}}_{1,2}(\bar{\omega}, \vartheta, t, \bar{Q}^2) = \tilde{g}_{1,2}(\omega, Q^2).$$

These Compton structure functions can be related to the polarised structure functions of deep-inelastic scattering, $g_{1,2}$, by a dispersion relation, which was given in Eq. (2.54):

$$\tilde{g}_{1,2}(\omega, Q^2) = 4\omega \int_0^1 dx \frac{g_{1,2}(x, Q^2)}{1 - x^2\omega^2 - i\epsilon}.$$

As discussed in Section 4.2, for our lattice calculation we must stay in the region $|\omega| < 1$. Hence in the above equation it is very difficult to solve for $g_{1,2}$ directly.

Instead, as was given in Eq. (2.55), we can Taylor expand around $\omega = 0$,

$$\tilde{g}_{1,2}(\omega, Q^2) = 4 \sum_{n=1}^{\infty} \omega^{2n-1} \int_0^1 dx x^{2n-2} g_{1,2}(x, Q^2) = 4 \sum_{n=1}^{\infty} \omega^{2n-1} \tilde{M}_{2n-1}^{(1,2)}(Q^2),$$

and extract $\tilde{M}_n^{(1,2)}$, the Mellin moments of $g_{1,2}$. We discussed some of the properties of these moments in Section 2.2.3.

7.1.1 Parameterisation of the lattice calculation

Recall in Chapter 6 that we separated \mathcal{H}_1 and \mathcal{E}_1 using spin-parity projectors. In this chapter, we use a very similar procedure to separate out the Compton structure functions $\tilde{g}_{1,2}$.

First, recall that from our Feynman-Hellmann relation, Eq. (4.64), we determine the spin-parity traced forward Compton amplitude:

$$\mathcal{R}_{\mu\nu}^{\Gamma} = \frac{\sum_{s,s'} \text{tr}[\Gamma u(P, s') T_{\mu\nu} \bar{u}(P, s)]}{\sum_s \text{tr}[\Gamma_{\text{unpol}} u(P, s) \bar{u}(P, s)]}, \quad (7.1)$$

where Γ is a spin-parity projector such as

$$\Gamma_{\text{unpol}} = \frac{1}{2}(\mathbb{I} + \gamma_0), \quad \Gamma_{\text{pol}} = \frac{1}{2}(\mathbb{I} + \gamma_0) \boldsymbol{\gamma} \cdot \hat{\mathbf{e}}_{\text{pol}} \gamma^5,$$

where $\hat{\mathbf{e}}_{\text{pol}}$ is the direction of the polarisation vector.

Starting with the tensor decomposition of the forward Compton amplitude, Eq. (2.20), and choosing $\mu = 1$ and $\nu = 2$, we have

$$\begin{aligned} T_{12}(P, q) &= \frac{q_1 q_2}{q^2} \mathcal{F}_1(\omega, Q^2) + \left(P_1 - \frac{P \cdot q}{q^2} q_1 \right) \left(P_2 - \frac{P \cdot q}{q^2} q_2 \right) \frac{\mathcal{F}_2(\omega, Q^2)}{P \cdot q} \\ &\quad + \frac{i}{P \cdot q} \epsilon_{12\rho\kappa} q^\rho \left(s^\kappa \tilde{g}_1(\omega, Q^2) + \left(s^\kappa - \frac{s \cdot q}{P \cdot q} P^\kappa \right) \tilde{g}_2(\omega, Q^2) \right). \end{aligned}$$

Then, by choosing our kinematics such that $q_1 = 0 = P_1$, we can isolate the spin-dependent amplitudes:

$$\begin{aligned} T_{12} &= \frac{i}{P \cdot q} \epsilon_{1230} q_3 \left(\tilde{g}_1 s^0 + \left(s^0 - \frac{s \cdot q}{P \cdot q} p^0 \right) \tilde{g}_2 \right) \\ &= -\frac{i}{P \cdot q} q_3 \left(\tilde{g}_1 s^0 + \left(s^0 - \frac{s \cdot q}{P \cdot q} E_N \right) \tilde{g}_2 \right). \end{aligned} \quad (7.2)$$

Spin-parity projectors

Note that the spin-parity structure of all the tensor structures in Eq. (7.2) is carried by the spin vector, $2s_\mu = \bar{u} \gamma_\mu \gamma_5 u$, defined in Eq. (2.21).

If we choose the unpolarised spin parity projector, then*

$$\frac{\sum_{s,s'} \text{tr} [\Gamma_{\text{unpol}} u(p, s') s_\mu \bar{u}(p, s)]}{\sum_s \text{tr} [\Gamma_{\text{unpol}} u(p, s) \bar{u}(p, s)]} = 0,$$

which removes *all* the structures in Eq. (7.2). Therefore, we cannot use the unpolarised projector to construct a pair of equations as we did in Chapter 6.

Instead, we will use the polarised projector,

$$\Gamma_{\text{pol}} = \frac{1}{2} (\mathbb{I} + \gamma_0) \boldsymbol{\gamma} \cdot \hat{\mathbf{e}}_{\text{pol}} \gamma^5,$$

but with two different choices of the polarisation vector $\hat{\mathbf{e}}_{\text{pol}}$.

We denote $\mathcal{R}_{\mu\nu}^{\text{pol}-e_{\text{pol}}}$ as Eq. (7.1) with spin-parity projector Γ_{pol} and the polarisation vector chosen to be $\hat{\mathbf{e}}_{\text{pol}}$. Using this, we construct the linear system of equations,

$$\begin{pmatrix} \mathcal{R}_{12}^{\text{pol}-y} \\ \mathcal{R}_{12}^{\text{pol}-z} \end{pmatrix} = \begin{pmatrix} N_y^{(1)} & N_y^{(2)} \\ N_z^{(1)} & N_z^{(2)} \end{pmatrix} \begin{pmatrix} \tilde{g}_1 \\ \tilde{g}_2 \end{pmatrix}. \quad (7.3)$$

Hence, as long as this matrix of N factors is invertible, we can solve for $\tilde{g}_{1,2}$. When we discuss systematic errors, we will note that if the matrix of N factors is close to singular (i.e. the determinant is non-zero but very small), discretisation artefacts may be enhanced with respect to the structure functions we wish to isolate.

As shown in Appendix F,

$$N_{e_{\text{pol}}}^{(1)} = \frac{i \mathbf{p} \cdot \hat{\mathbf{e}}_{\text{pol}}}{\mathbf{p} \cdot \mathbf{q}} q_3, \quad N_{e_{\text{pol}}}^{(2)} = \frac{i m_N q_3}{\mathbf{p} \cdot \mathbf{q}} \left[\frac{\mathbf{p} \cdot \hat{\mathbf{e}}_{\text{pol}}}{E_N + m_N} - \frac{E_N \mathbf{q} \cdot \hat{\mathbf{e}}_{\text{pol}}}{\mathbf{p} \cdot \mathbf{q}} \right]. \quad (7.4)$$

Note that $\hat{\mathbf{e}}_{\text{pol}} = \hat{\mathbf{x}}$ will also remove all the structures in our chosen kinematics. Therefore, we only use the y and z directions.

7.1.2 Spin-dependent fitting priors

Here, as in Chapter 6, we derive some constraints on the moments of $g_{1,2}$ that we will use as prior distributions when we come to fit these moments using Bayesian Markov chain Monte Carlo (MCMC).

*See Appendix F for explicit results for the spin-parity traces.

The g_1 structure function

Unlike the moments of the unpolarised forward Compton amplitude, $g_{1,2}$ are not directly proportional to a scattering cross section, but to a *difference of cross sections*. As such, we cannot guarantee that $g_{1,2}$ are positive definite, and we instead have a weaker bound [44, 57, 269]:

$$\frac{|g_1 - \gamma^2 g_2|}{F_1} \leq 1, \quad (7.5)$$

where all the structure functions are understood to be at the same x and Q^2 values, and we have introduced the factor

$$\gamma \equiv \frac{2m_N x}{\sqrt{Q^2}}.$$

Since at our kinematics $Q^2 \gg m_N^2$, we can set $\gamma^2 \approx 0$ in Eq. (7.5) to get the following positivity bound on g_1 :

$$|g_1(x, Q^2)| \lesssim F_1(x, Q^2), \quad (7.6)$$

where F_1 is the spin-independent DIS structure function.

As such, following similar reasoning to the positivity bounds proof in Chapter 6, we can derive the relation between the moments of these two structure functions:

$$|\tilde{M}_n^{(1)}(Q^2)| = \left| \int_0^1 dx x^n g_1(x, Q^2) \right| \lesssim \int_0^1 dx x^n F_1(x, Q^2) = \frac{1}{2} M_n^{(1)}(Q^2), \quad (7.7)$$

where we need to be aware of the factor of two that was absorbed by the F_1 moments Eq. (2.29).

Note that the $n = 1$ moment of F_1 is difficult to determine. Even in the parton model, we have

$$M_1^{(1)} = \int_0^1 dx (q_f(x) + \bar{q}_f(x)),$$

which is hard to evaluate, since it cannot be related to a model independent sum rule.

Since the leading moment of g_1 will be well-determined in our calculation, it will be less sensitive to the prior, and hence we simply need a broad prior that does not over-constrain this parameter. Therefore, for the $n = 1$ moment, we use a reasonably loose prior that easily encompasses the expected values of $\tilde{M}_1^{(1)} \approx 0.5$ for up quarks and $\tilde{M}_1^{(1)} \approx -0.1$ for down quarks:

$$|\tilde{M}_1^{(1)}(Q^2)| \leq 2, \quad (7.8)$$

for both u and d quarks.

For higher moments, we can use the moments of F_1 as calculated from Feynman-Hellmann [37, 38]. Since we can only access the even in n moments of F_1 using this method, the bound is

$$|\tilde{M}_n^{(1)}(Q^2)| \lesssim \frac{1}{2} M_n^{(1)}(Q^2) \leq \frac{1}{2} M_{n-1}^{(1)}(Q^2), \quad \text{for } n = 3, 5, 7, \dots, \quad (7.9)$$

since the moments of F_1 are monotonically decreasing.

The g_2 structure function

Similarly, we have another positivity bound[†] [44, 57, 269]

$$\frac{\gamma|g_1 + g_2|}{F_1} \leq \sqrt{(1 + \gamma^2)\frac{F_2}{2xF_1} - 1}. \quad (7.10)$$

Since the upper bound is a non-linear combination of structure functions, it cannot be easily turned into a constraint on the moments. As such, we rearrange this inequality. We start by noting that the Callan-Gross relation, Eq. (2.37),

$$\frac{F_2}{2xF_1} = 1 + \mathcal{O}\left(\frac{m_N^2}{Q^2}, \frac{\Lambda_{\text{QCD}}^2}{Q^2}\right),$$

can be used to approximate Eq. 7.10 as

$$\frac{\gamma|g_1 + g_2|}{F_1} \lesssim \gamma \quad \Rightarrow \quad |g_1 + g_2| \lesssim F_1. \quad (7.11)$$

While this approximation is a bit crude, as we will see in the fitting process, it does not appear to over-constrain the parameters.

Using identical reasoning to the proofs for g_1 and in Chapter 6, we have

$$|\tilde{M}_n^{(2)}(Q^2)| \lesssim \frac{1}{2}M_n^{(1)}(Q^2) + |\tilde{M}_n^{(1)}(Q^2)|. \quad (7.12)$$

As with the g_1 moments, for $n = 1$ we use

$$|\tilde{M}_1^{(2)}(Q^2)| \leq 2, \quad (7.13)$$

and for $n = 3, 5, 7 \dots$

$$|\tilde{M}_n^{(2)}(Q^2)| \lesssim \frac{1}{2}M_n^{(1)}(Q^2) + |\tilde{M}_n^{(1)}(Q^2)| \leq \frac{1}{2}M_{n-1}^{(1)}(Q^2) + |\tilde{M}_n^{(1)}(Q^2)|, \quad (7.14)$$

since we have only calculated the n even moments of F_1 .

7.2 Lattice Results and Phenomenology

We are now ready to apply the Feynman-Hellmann relation in Chapter 4 to calculate the spin-dependent Compton structure functions, $\tilde{g}_{1,2}$ and interpret them. Since this calculation is exploratory, we use only one Q^2 value, and the intention here is simply to show the validity of this type of calculation. However, the initial results are promising.

7.2.1 Simulation details

This calculation uses the same gauge ensemble as Chapter 6; see table 6.1. In particular, we note that we are at the flavour symmetric point, $\kappa_l = \kappa_s$, with a larger than-physical

[†]Note that an improvement on the above bound is possible [270]. However, since this improved bound involves a non-linear combination of structure functions that is difficult to rearrange into a linear expression, for this exploratory study we stick to the simpler positivity bound derived here.

pion mass, $m_\pi = 412$ MeV, and a lattice volume of $N_L^3 \times N_T = 48^3 \times 96$. We use three sources, and hence $N_{\text{meas}} = 1600$.

Feynman-Hellmann implementation

As discussed in Section 4.2, we calculate perturbed quark propagators,

$$S_\lambda(z_n, z_m) = [M - \lambda_1 \mathcal{O}_1 - \lambda_2 \mathcal{O}_2]_{n,m}^{-1},$$

where M is the usual fermion matrix.

The component of the Compton amplitude that we want to determine, Eq. (7.2), is odd under $q \rightarrow -q$. Therefore, as discussed in Chapter 4, to isolate a signal that is odd in $\mathbf{q} \rightarrow -\mathbf{q}$, we choose one current carrying $\cos(\mathbf{q} \cdot \mathbf{z}_n)$ and the other $\sin(\mathbf{q} \cdot \mathbf{z}_n)$. Hence we use the perturbing matrices

$$[\mathcal{O}_1]_{n,m} = \delta_{n,m}(e^{i\mathbf{q} \cdot \mathbf{z}_n} + e^{-i\mathbf{q} \cdot \mathbf{z}_n})\gamma_1, \quad [\mathcal{O}_2]_{n,m} = i\delta_{n,m}(e^{i\mathbf{q} \cdot \mathbf{z}_n} - e^{-i\mathbf{q} \cdot \mathbf{z}_n})\gamma_2. \quad (7.15)$$

Again, as discussed in previous chapters, we only calculate the connected contributions to the Compton amplitude—i.e. only the diagrams where the photons are absorbed/emitted by valence quarks.

Recall our Feynman-Hellmann relation, Eq. (4.63):

$$\left. \frac{\partial^2}{\partial \lambda_1 \partial \lambda_2} \frac{\mathcal{G}_\lambda(\tau)}{\mathcal{G}_0(\tau)} \right|_{\lambda=0} \stackrel{\tau \gg a}{\simeq} B_{\text{int}} + \frac{i\tau}{2E_N(\mathbf{p})} T_{12}(\mathbf{p}, \mathbf{q}).$$

As in the previous chapters, we use the combination of correlators, R_λ , as defined in Eq. (4.53). And similarly, we use two λ magnitudes of $\lambda = 0.0125, 0.025$.

Kinematics

Our momentum scalars are determined by the FH insertion momentum, \mathbf{q} , and the sink momentum, \mathbf{p} :

$$Q^2 = \mathbf{q}^2, \quad \omega = \frac{2\mathbf{p} \cdot \mathbf{q}}{\mathbf{q}^2}. \quad (7.16)$$

We choose $\mathbf{q} = \frac{2\pi}{L}(0, 5, 3)$, which gives a hard scale of $Q^2 = 4.86$ GeV².

Recall from Chapter 4 that, for the FH relation to hold, we needed to satisfy the kinematic constraint, Eq. (4.57):

$$|\mathbf{p}| < |\mathbf{p} + n\mathbf{q}|, \quad n \in \mathbb{Z} \setminus \{0\}.$$

Moreover, to relate our Euclidean amplitude to the Minkowski, we need $|\omega| < 1$, and finally we choose our sink momentum such that $|\mathbf{p}| \leq 3\frac{2\pi}{L} = 1.13$ GeV. This is slightly less than the previous two chapters' upper bound on the sink momentum. In the case of forward kinematics, it is easier to access higher ω without large sink momentum—hence our slightly lower bound. Finally we note that at $\omega = 0$, since the lattice signal is by construction odd under $\omega \rightarrow -\omega$, our result is zero. With all these constraints, the explicit values of ω we use are given in Table 7.1.

Table 7.1: Sink momentum, \mathbf{p} , and corresponding ω values, for $\mathbf{q} = \frac{2\pi}{L}(0, 5, 3)$.

$\frac{L}{2\pi}\mathbf{p}$	ω	$(\frac{L}{2\pi}\mathbf{p})^2$
(0, -1, 2)	0.06	5
(0, 1, -1)	0.12	2
(0, 0, 1)	0.18	1
(0, 2, -2)	0.24	8
(0, 1, 0)	0.29	1
(0, 0, 2)	0.35	4
(0, 2, -1)	0.41	5
(0, 1, 1)	0.47	2
(0, 0, 3)	0.53	9
(0, 2, 0)	0.59	4
(0, 1, 2)	0.65	5
(0, 2, 1)	0.76	5
(0, 3, 0)	0.88	9
(0, 2, 2)	0.94	8

Finally, since our amplitude flips sign under $\mathbf{p} \rightarrow -\mathbf{p}$, we take

$$\overline{\mathcal{R}}_{12}^{\text{pol}} = \frac{\mathcal{R}_{12}^{\text{pol}}(\mathbf{p}) - \mathcal{R}_{12}^{\text{pol}}(-\mathbf{p})}{2}$$

to increase our statistics.

7.2.2 Determining the Compton amplitude

Euclidean time and Feynman-Hellmann parameter fits

We fit the same combination of correlators as the previous two chapters, R_λ , as defined in Eq. (4.53), using the fit function $f(\tau) = a\tau + b$ and interpret the slope, a , as proportional to a linear combination of Compton structure functions.

To perform the Euclidean time fits we use the weighted average procedure outlined in Section 6.2; a sample of the signal is present in Fig. 7.1. We note that this fit is significantly cleaner than most of the off-forward results in Chapter 6 (see for instance Fig. H.2). This likely reflects the fact that, due to our the forward kinematics of this chapter, we do not have FH excited states induced by $|t| \ll m_N^2$. Moreover, a heat map of the weights is shown in Fig. 7.2. We can see that the weight, Eq. (6.26), typically favours fitting at the earliest possible τ_{min} .

The analysis of the signal as a function of the FH parameter is no different to the previous to sections. We fit the single parameter function $f(\lambda) = c\lambda^2$, and observe that the signal is well-described by this function, with some suppressed $\mathcal{O}(\lambda^4)$ contaminations, which appear negligible compared to the overall error—see Fig. 7.3.

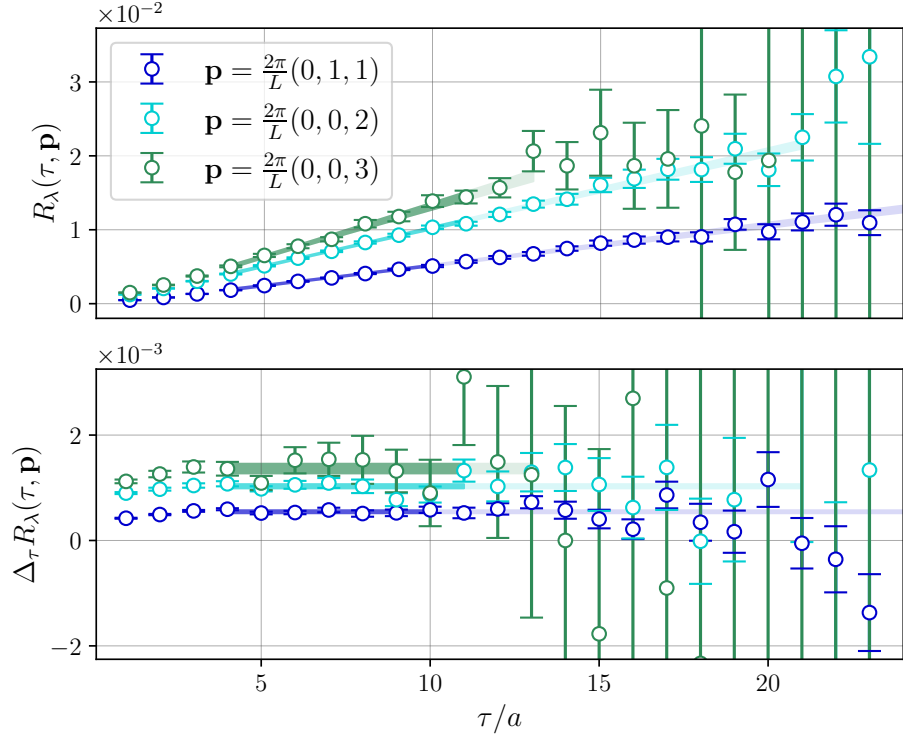


Figure 7.1: Plot of τ fits for R_λ , as defined in Eq. (4.53) and the ‘effective mass’, $\Delta_\tau R_\lambda$, defined in Eq. (6.24), for the up quarks, z polarised, and $\lambda = 0.0125$. The shaded bands are fits to the function $f(\tau) = a\tau + b$ using weighted averages; the lighter shade is the whole range considered, and the darker shade is the fit window with the highest weight.

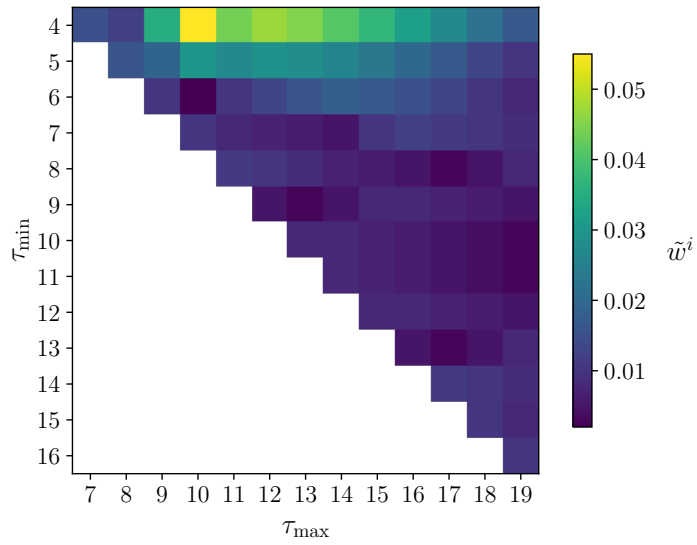


Figure 7.2: Heat map showing the weight assigned to each fit window, for up quarks, z polarised, $\mathbf{p} = \frac{2\pi}{L}(0, 2, 1)$, $\lambda = 0.0125$ results. The weight, \tilde{w}^i , is defined in Eq. (6.26).

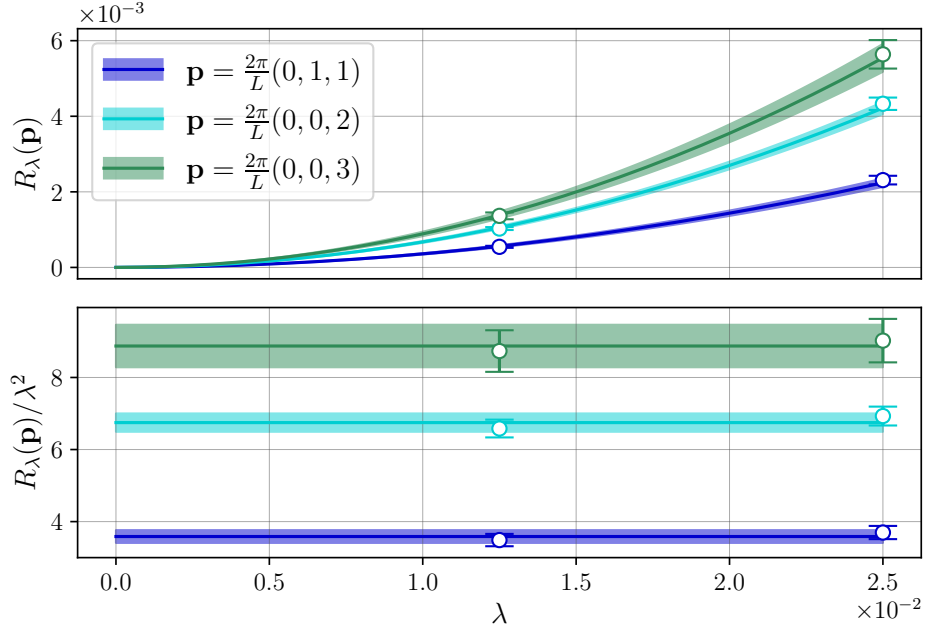


Figure 7.3: Plot of λ -dependence of R_λ after fitting in Euclidean time, for the same data as Fig. 7.1. Top: R_λ appears very well-described by $f(\lambda) = c\lambda^2$. Bottom: comparing the extracted b and R_λ/λ^2 , we can see some tensions between the fit and the data, indicating small $\mathcal{O}(\lambda^4)$ contaminations.

Separating g_1 and g_2

After extracting $\mathcal{R}_{12}^{\text{pol}}$ for the polarisation vector in the y and z directions, we then need to solve for the Compton structure functions, $\tilde{g}_{1,2}$. We do this using the linear equations in Eq. (7.3):

$$\begin{pmatrix} \mathcal{R}_{12}^{\text{pol}-y} \\ \mathcal{R}_{12}^{\text{pol}-z} \end{pmatrix} = \begin{pmatrix} N_y^{(1)} & N_y^{(2)} \\ N_z^{(1)} & N_z^{(2)} \end{pmatrix} \begin{pmatrix} \tilde{g}_1 \\ \tilde{g}_2 \end{pmatrix}.$$

The results for \mathcal{R} are shown in the top panel of Fig. 7.4, where we can see that the signal-to-noise of the data is somewhat better than comparable results for the off-forward—see Fig. 6.5. Note that, unlike the off-forward case, where the \mathcal{R} had the roughly the same ω behaviour as the extracted amplitudes, the polarised forward \mathcal{R} has no simple behaviour as a function of ω . This is because the N factors for the polarised case, Eq. (7.4), have significant dependence on the direction of the sink momentum, in contrast to the N factors for the off-forward case.

The extracted $\tilde{g}_{1,2}$ are shown in the bottom panel of Fig. 7.4. For the low to mid ω values, these structure functions are as we expect: \tilde{g}_1 is dominated by linear in ω behaviour, while \tilde{g}_2 is extremely small. However, we can see some erratic behaviour for the largest three ω values. This is interesting, as the corresponding data for the \mathcal{R} is very clean at these ω values. This behaviour is likely the result of a lattice artefact; we discuss this further in the section on systematic errors.

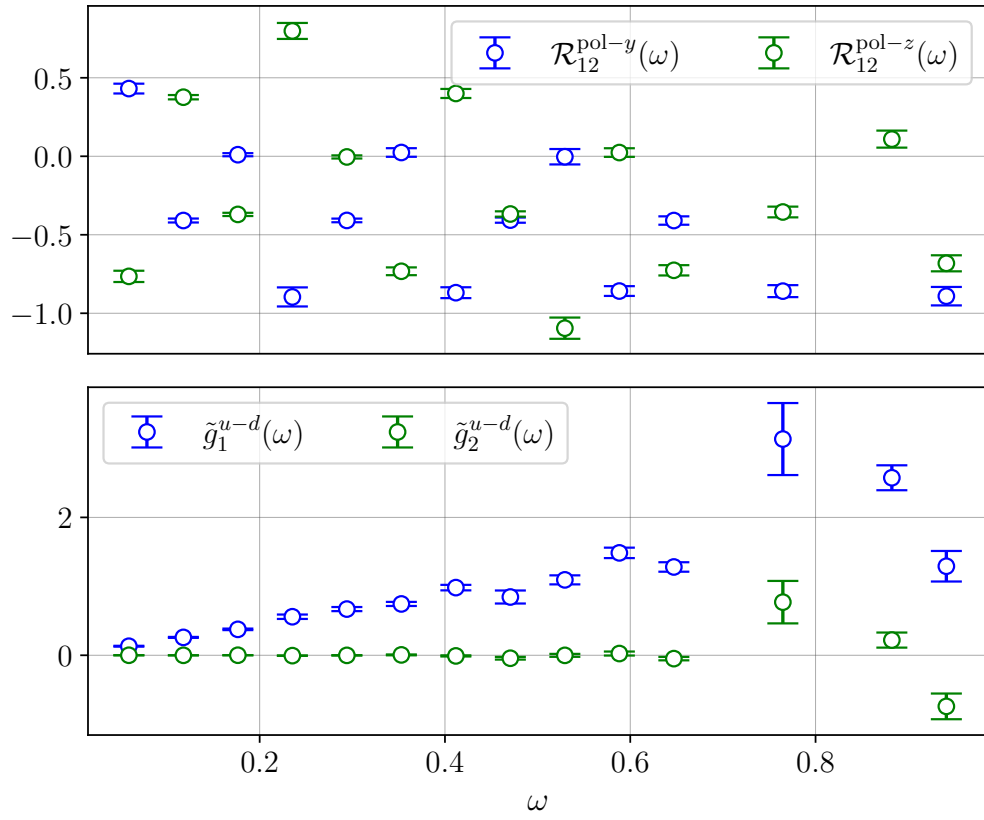


Figure 7.4: Top: the ω dependence of \mathcal{R} as defined in Eq. (7.1), for the two chosen polarisation directions and the isovector, $u - d$, combination. Bottom: the polarised structure functions, $\tilde{g}_{1,2}$, extracted from the \mathcal{R} , using Eq. (7.3).

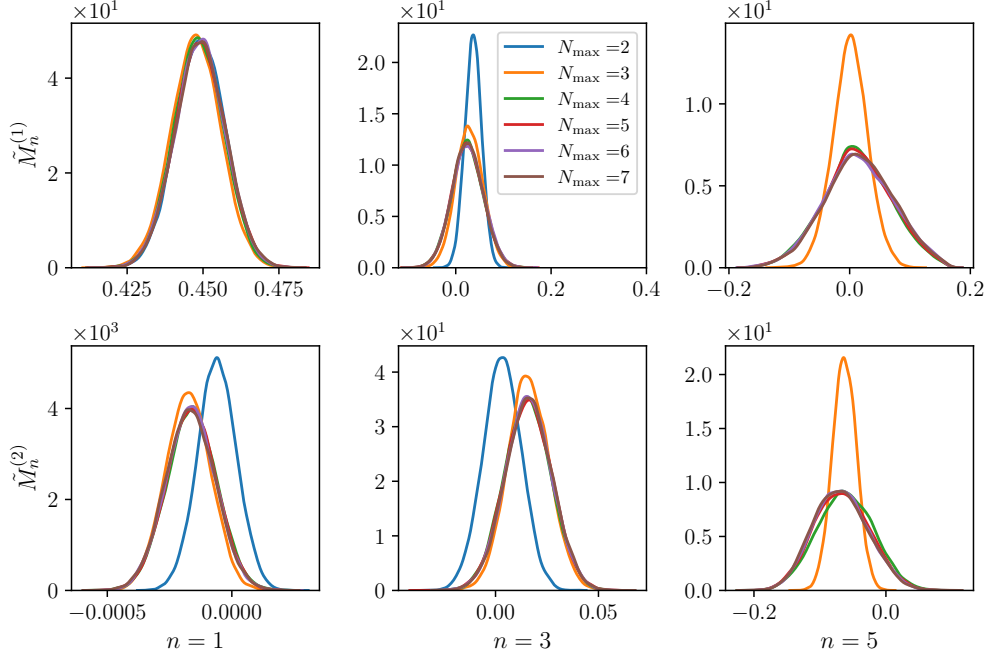


Figure 7.5: Density distributions for the n^{th} moment of the g_1 structure function (top), and the g_2 structure function (bottom)—up quark contributions only.

Moment fits

As in Chapters 5 and 6, we fit to the ω dependence using Bayesian Markov chain Monte Carlo [220, 221]. Since we explicitly construct a signal that is odd in \mathbf{q} and moreover this is how we expect the physical structure functions to behave, we fit to the function

$$f_{N_{\max}}(\omega, Q^2) = 4 \sum_{n=1}^{N_{\max}} \omega^{2n-1} \tilde{M}_{2n-1}(Q^2). \quad (7.17)$$

As in previous chapters, we vary N_{\max} to test the effect of this truncation on the leading moments.

The prior distributions we sample for the moments of g_1 are given in Eqs. (7.8) and (7.9). For g_2 , we use the prior distributions given in Eqs. (7.13) and (7.14). These prior distributions provide somewhat looser bounds on the moments of g_2 compared to those of g_1 .

In Fig. 7.5 we plot the posterior distributions for the moments of g_1 and g_2 ; only the up quark moments are shown. For g_1 , we observe that the leading moment is very stable with N_{\max} , reflecting the fact that this moment is well-constrained by the low to mid ω values. By contrast, the higher moments are more variable with N_{\max} ; however, they appear to stabilise for $N_{\max} \geq 4$. It is unclear how much we can trust these higher moments, since they should be largely constrained by higher ω values, the largest three of which appear to be affected by lattice artefacts.

Similarly, for all the g_2 moments, there appears to be convergence for $N_{\max} \geq 4$. The comparatively large size of the $n = 5$ moment is fairly untrustworthy, since this moment

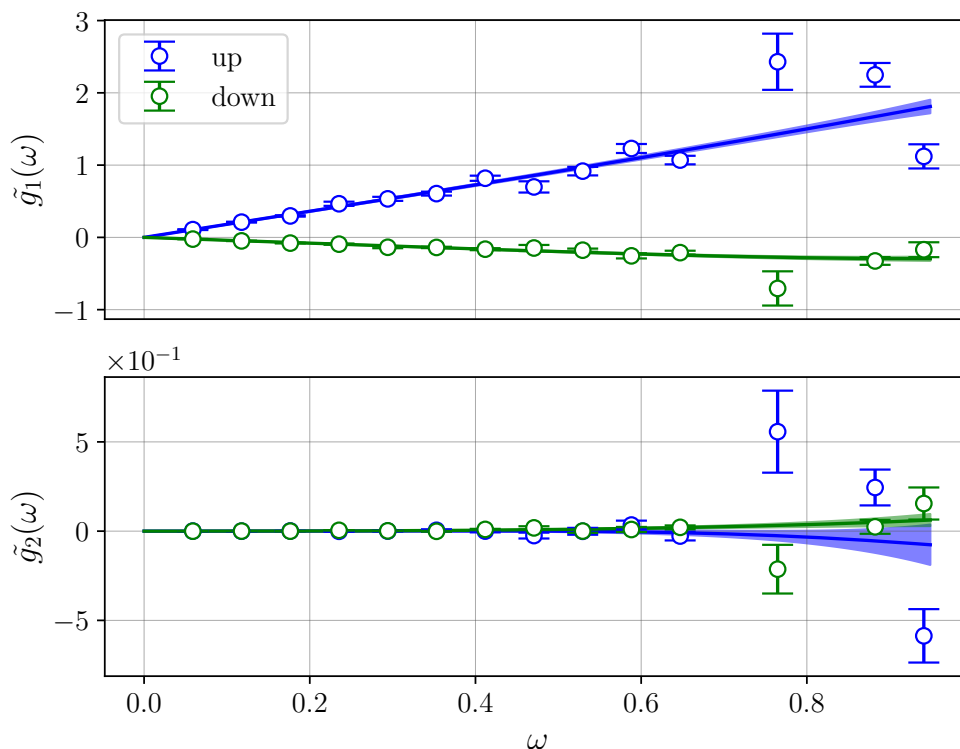


Figure 7.6: Comparison of fit to Eq. (7.17) for $\tilde{g}_{1,2}$ and discrete ω data values.

is most constrained by the three largest ω values. However, the well-defined distribution for $n = 1, 3$ moments, despite their loose bounds, is encouraging. We choose $N_{\max} = 7$ due to the large number of ω values and the stability of the moments beyond $N_{\max} \geq 4$.

In Fig. 7.6 we plot the fit in ω space compared to the discrete values. Encouragingly, the \tilde{g}_1 fit does not appear to be over-fit to the largest three ω values, and maintains linear-in- ω -dominated behaviour. The extent of over-fitting is harder to discern in the \tilde{g}_2 structure function due to its small size.

Results

As outlined in the Section 7.1, there are many phenomenologically interesting quantities we can determine from the moments of $g_{1,2}$. We focus on

- The first moment of g_1 , $\tilde{M}_1^{(1)}$, which gives the axial coupling, g_A , Eq. (2.65).
- The first moment of g_2 , $\tilde{M}_1^{(2)}$, through which we can test the Burkardt-Cottingham sum rule, Eq. (2.67).
- The d_2 term, Eq. (2.71), which is a linear combination of $\tilde{M}_3^{(1)}$ and $\tilde{M}_3^{(2)}$.

The results are collected in Table 7.2.

Table 7.2: Summary of key physical quantities from the moments.

	u	d	$u - d$	proton
g_A	1.069(20)	-0.2413(70)	1.310(21)	0.4483(88)
$M_1^{g_2}$	-0.000166(99)	-0.000079(42)	-0.00009(10)	-0.000083(45)
d_2	0.20(15)	0.146(54)	0.05(16)	0.103(65)

Axial charge

Recall the Ellis-Jaffe sum rule, Eq. (2.65), which relates the axial coupling, g_A , to the first moment of g_1 :

$$2\tilde{M}_1^{(1)} = c_1(\alpha_S(Q^2))g_A,$$

where $c_1(\alpha_S(Q^2))$ is the Wilson coefficient. This relation is different to the other factorisation relations in this thesis, as there are no other operators that contribute to the OPE for this moment [57]. As a result, we can factor out the Wilson coefficient to determine g_A from our moment directly.

Therefore, we use a perturbative calculation to determine this Wilson coefficient up to α_S^4 [271]:

$$\begin{aligned} c_1(\alpha_S(Q^2)) &= 1 - \frac{\alpha_S(Q^2)}{\pi} + (-4.583 + 0.3333N_f) \left(\frac{\alpha_S(Q^2)}{\pi}\right)^2 \\ &\quad + (-41.44 + 7.607N_f - 0.1775N_f^2) \left(\frac{\alpha_S(Q^2)}{\pi}\right)^3 \\ &\quad + (-479.4 + 123.4N_f - 7.697N_f^2 + 0.1037N_f^3) \left(\frac{\alpha_S(Q^2)}{\pi}\right)^4, \end{aligned} \quad (7.18)$$

where N_f is the number of quark flavours and $\alpha_S(Q^2)$ is the strong coupling; $N_f = 3$ for our calculation. For $\alpha_S(Q^2)$, we use Refs. [272, 273].

Using this Wilson coefficient, our result for the $u - d$ axial charge is $g_A^{u-d} = 1.310(21)$; see Table 7.2 for other flavour combinations. Experimentally, this axial charge can be determined from neutron beta decay. From the Particle Data Group's meta-analysis [48], we have the averaged experimental value of $g_A^{u-d} = 1.2724(23)$. This is not quite consistent with our determination, but they are obviously close.

The discrepancy between our results and experiment is likely due to a number of systematics. Unlike experiment, our calculation uses $N_f = 2 + 1$ flavours with isospin symmetry, whereas experiment has all six flavours of quark at different masses. Moreover, our quark masses are unphysically large with no attempt at a chiral extrapolation. Finally, we have not attempted to account for discretisation artefacts in our calculation or the electromagnetic interactions among quarks. Addressing such systematics is a goal of future work.

Similarly, we can compare our result to the Flavour Lattice Averaging Group's (FLAG's) meta-determination of the same quantity using lattice three-point functions and first-order Feynman-Hellmann. For $N_f = 2 + 1$ flavour results, FLAG report the value $g_A^{u-d} = 1.248(23)$ [104]. Again, our result is close to this value, but not quite consistent within one sigma.

There are a number of possible sources for these discrepancies. Firstly, our determination uses heavier-than-physical quark masses. Therefore, calculating with lighter quark masses and performing a chiral extrapolation could reduce the disagreement between ours and other lattice results, which are mostly at lighter masses and/or have a chiral extrapolation[‡]. Another possible contributing factor to the discrepancy is our Wilson coefficient, Eq. (7.18), and it may be necessary to include higher-order in α_S terms or compute a discretised Wilson coefficient to account for lattice artefacts. Finally, since all other g_A determinations use either direct three-point evaluations or first-order Feynman-Hellmann, there will be different excited state corrections and discretisation artefacts compared with ours, which could also contribute to this discrepancy.

Burkardt-Cottingham sum rule

Recall that the Burkardt-Cottingham sum rule (Eq. (2.67)) predicts that the first moment of g_2 vanishes for all Q^2 :

$$\tilde{M}_1^{(2)}(Q^2) = 0.$$

However, this sum rule is model-dependent and hence it may be violated in QCD.

While we find extremely small values for $\tilde{M}_1^{(2)}$ ($\lesssim 10^{-4}$), the u , d and proton results are not consistent within one standard deviation with zero—see Table 7.2. It is possible that this could be caused by highly suppressed corrections that violate the Burkardt-Cottingham sum rule. Similarly, results from experimental studies of the Burkardt-Cottingham sum rule suggest small violations of this sum rule [255].

However, we need to be cautious in interpreting these results. Since the moments are $\tilde{M}_1^{(2)} \sim 10^{-6}$, and our Feynman-Hellmann couplings at $\lambda^2 \sim 10^{-4}$, the whole signal is $\sim 10^{-10}$. Therefore, our results may be affected by the machine precision of the gauge links (single precision) and the propagators (double precision). Moreover, such a small contribution could easily be the result of some other lattice systematics, such as discretisation artefacts. As such, further investigation is needed into the first moment of g_2 .

d_2 term

Finally, we determine the d_2 term from a linear combination of the $n = 3$ moments of g_1 and g_2 :

$$d_2 = 4\tilde{M}_3^{(1)} + 6\tilde{M}_3^{(2)}.$$

For the proton, we find $d_2^p = 0.103(65)$; see Table 7.2 for other flavour combinations. Experimental values of d_2 for the proton range from as low as $d_2^p = -0.00828(656)$ to as high as $d_2^p = 0.0296(214)$ [262–268]. Therefore, our results are close to some of these determinations, and even consistent with a few due to the large relative errors of both our calculation and the experimental values. From lattice three-point calculations d_2 has been determined as $d_2^p = 0.004(5)$ [119] and $d_2^p = 0.0105(19)(65)$ [120]. While not consistent with our results, we note that this type of three-point study is still exploratory, and their determinations of d_2 appear sensitive to variations in pion mass and lattice spacing.

[‡]Note that the three-point results for g_A are usually *smaller* for larger pion masses. By contrast, our large pion mass results are larger than expected. However, since our determination and those from three-point studies use completely different operators, the pion mass dependence of each is likely different.

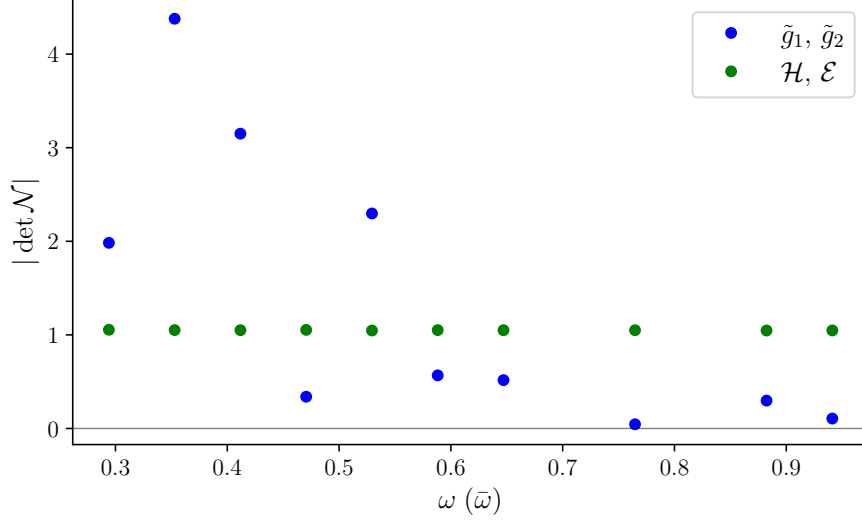


Figure 7.7: Comparison of $|\det \mathcal{N}|$ for the calculation of $\tilde{g}_{1,2}$ and the off-forward amplitudes, \mathcal{H} and \mathcal{E} . Values for smaller ω are not included since these are all very large, $|\det \mathcal{N}| \sim \mathcal{O}(10)$ and greater, for the $\tilde{g}_{1,2}$ matrix.

Moreover, discrepancies could arise between our calculation and three-point studies due to higher-twist and power-suppressed corrections that are present in our results.

Finally, we note that, as can be seen in Figs. 7.3 and 7.6, the behaviour of $\tilde{g}_{1,2}$ at large ω appears somewhat anomalous. Any anomalous behaviour at large ω is likely to impact the higher moments more than the leading moment, as discussed in Chapter 6. Therefore, it is unclear to what extent we can trust our results for higher moments given this behaviour. We discuss a possible source of this anomalous behaviour in the next section.

7.2.3 Systematic errors

Here, as in Chapter 6, we discuss some difficulties with our large ω results. These points require sink momentum to be large and to project out the largest values of q_μ . Hence both the $\mathcal{O}(ap_\mu)$ and $\mathcal{O}(aq_\mu)$ discretisation effects are maximised for such points. Moreover, since we also have a dependence on the q_μ and P_μ directions—see the N factors, Eq. (7.4)—this induces additional discretisation artefacts, as the continuum Ward identities are violated on the lattice [236, 237]

However, the relative size of these discretisation artefacts can be exacerbated or suppressed by the linear system of equations we use to solve for the structure functions. Recall from Eq. (7.3) that to access the $\tilde{g}_{1,2}$ we need to invert the matrix of N factors:

$$\mathcal{N} \equiv \begin{pmatrix} N_y^{(1)} & N_y^{(2)} \\ N_z^{(1)} & N_z^{(2)} \end{pmatrix}. \quad (7.19)$$

If this matrix is close to singular—i.e. $\det \mathcal{N}$ is very small but not zero—it can enhance lattice artefacts with respect to the structure functions. Moreover, even without lattice

artefacts, a small $\det \mathcal{N}$ means that only one structure function can be well-determined, which blows up the statistical error on the other structure function.

To see how a small $\det \mathcal{N}$ can enhance lattice artefacts, we write out the vector of \mathcal{R} s with the inclusion of discretisation artefacts, $\delta a^{y,z}$, which are different for the y and z polarisations:

$$\begin{pmatrix} \mathcal{R}_{12}^{\text{pol}-y} \\ \mathcal{R}_{12}^{\text{pol}-z} \end{pmatrix} = \begin{pmatrix} N_y^{(1)} \tilde{g}_1 + N_y^{(2)} \tilde{g}_2 + \delta a^y \\ N_z^{(1)} \tilde{g}_1 + N_z^{(2)} \tilde{g}_2 + \delta a^z \end{pmatrix}.$$

After applying \mathcal{N}^{-1} to this vector, we have

$$\mathcal{N}^{-1} \begin{pmatrix} \mathcal{R}_{12}^{\text{pol}-y} \\ \mathcal{R}_{12}^{\text{pol}-z} \end{pmatrix} = \begin{pmatrix} \tilde{g}_1 + (N_z^{(2)} \delta a^y - N_y^{(2)} \delta a^z) / \det \mathcal{N} \\ \tilde{g}_2 - (N_z^{(1)} \delta a^y - N_y^{(1)} \delta a^z) / \det \mathcal{N} \end{pmatrix}.$$

Since there is no reason for $N_z^{(1,2)} \delta a^y - N_y^{(1,2)} \delta a^z$ to be $\mathcal{O}(\det \mathcal{N})$, these contributions pick up an extra factor of $1/\det \mathcal{N}$ with respect to the structure functions. As such, a near-singular \mathcal{N} matrix ($\det \mathcal{N} \approx 0$) will enhance the discretisation artefacts by $1/\det \mathcal{N}$. Hence even with relatively small values of δa in the \mathcal{R} , it is possible to have a sizeable discretisation error in the Compton structure functions.

In Fig. 7.7 we plot $|\det \mathcal{N}|$, which is a measure of the orthogonality of the matrix's rows, against ω . We do not plot the smallest four values of ω , since these are all $|\det \mathcal{N}| \sim \mathcal{O}(10)$ or greater, and hence not a concern. We see that the three largest ω values have the smallest three values of $|\det \mathcal{N}|$. In particular, $\omega = 0.76$ has by far the worst orthogonality with $|\det \mathcal{N}| \sim \mathcal{O}(10^{-2})$. Comparing this to the results for the structure functions, Fig. 7.4, there appears to be a relationship between small values of $|\det \mathcal{N}|$ and ‘jittery’-looking points in the structure functions. In particular, $\omega = 0.76$, which has the smallest $|\det \mathcal{N}|$, appears to be the most anomalous value of the structure functions

As a point of comparison, we also plot in Fig. 7.7 the determinant of the \mathcal{N} matrix for the the \mathcal{H} and \mathcal{E} amplitudes from the previous chapter, Eq. (6.27). One can see that this $\det \mathcal{N}$ is reasonably orthogonal for all values of $\bar{\omega}$. Hence we do not expect the same problem for the \mathcal{H}_1 and \mathcal{E}_1 amplitudes.

Therefore, the anomalous behaviour of the larger ω values for $\tilde{g}_{1,2}$ is likely due to small lattice artefacts being enhanced with respect to the Compton structure functions by a system of equations that is barely linearly independent. This orthogonality issue is straightforward to remedy: by taking equivalent values of the momentum transfer, such as $q_\mu = \frac{2\pi}{L}(0, 3, 5)$, and/or different Lorentz indices, one has a different \mathcal{N} matrix.

A complementary method of improving the extraction of $g_{1,2}$ would be to use the lattice perturbation theory (LPT) calculation carried out in Ref. [254] to account for some of the $\mathcal{O}(a|\mathbf{p}|)$ and $\mathcal{O}(a|\mathbf{q}|)$ artefacts. In such an analysis the \mathcal{N} matrix would be altered to include such corrections, which in principle would improve the extraction of the Compton structure functions. In practice, it is likely that a combination of choosing a more orthogonal \mathcal{N} matrix and insights from the aforementioned LPT calculation will lead to an accurate isolation of $g_{1,2}$ —this is a goal of future work.

7.3 Conclusion and Outlook

In this chapter we have presented an exploratory calculation of the polarised forward Compton amplitude. Such a calculation is a natural and straightforward application of techniques we developed to analyse the off-forward Compton amplitude in Chapters 5 and 6. Moreover, the spin-dependent Compton amplitude is particularly well-suited to our method, as there is a great amount of phenomenological interest in the moments of structure functions and their non-leading-twist contributions.

Our initial results show a great deal of promise: the signal for this amplitude is of good quality and FH excited states seem to be under control. In terms of the moments, the extracted g_A is physically reasonable—it is likely that with corrections for systematics it will be possible to match state-of-the-art three-point determinations. Interestingly, the first moment of g_2 , which the Burkardt-Cottingham sum rule predicts to be zero, is found to be very small but non-zero, in agreement with experimental determinations. Finally, the d_2 form factor is roughly in the same area as most lattice and experimental results, which themselves show a great deal of variance. Although, greater precision on this result is necessary.

As in Chapter 6, there are discretisation artefacts for large ω values that affect the quality of these results. As large ω is necessary for constraining higher moments, such artefacts need to be controlled to improve determinations of d_2 and other higher moments. However, unlike in the case of Chapter 6, we showed the matrix \mathcal{N} , which we need to invert to isolate the structure functions, can enhance existing lattice artefacts. As such, a judicious choice of q_μ and current direction could allow us to tame these lattice artefacts; this is a goal of future work.

Once such artefacts can be controlled, a major area of interest is the Q^2 dependence of the amplitude. For the leading moment of g_1 , this would improve our determination of g_A . Moreover, from the same moment we could determine α_{g_1} , the effective strong coupling, defined in Eq. (2.66). This effective strong coupling allows for a determination of the running of the coupling below the perturbative threshold, $Q < \Lambda_{\text{QCD}}$, which provides highly interesting information about quark confinement and the transition from the confining to asymptotically free regions [72].

Moreover, the Q^2 dependence of the first moment of g_2 would tell us more about the breaking of the Burkardt-Cottingham sum rule. And finally, the Q^2 dependence of the second moments of $g_{1,2}$ would help in phenomenological determinations of the d_2 observable, which so far has been difficult to constrain experimentally.

The Compton Amplitude Subtraction Function

In this chapter, we use our Feynman-Hellmann method to calculate the Compton amplitude subtraction function. In the preceding chapters, we presented results for a number of physical quantities that are generally in agreement with other determinations, with some deviations at large ω values. However, our results for the subtraction function exhibit behaviour that is drastically at odds with many other determinations of the same quantity. In particular, our calculation appears to violate predictions from the operator product expansion (OPE).

Naturally, this anomalous behaviour makes it necessary to investigate lattice artefacts. Since the OPE is a short-distance relation, we focus on investigating short-distance lattice artefacts, and present a different implementation of lattice Feynman-Hellmann that allows us to test for the presence of these artefacts.

In Chapter 2 we defined the forward Compton amplitude subtraction function, Eq. (2.28), as

$$\mathcal{F}_1(\omega = 0, Q^2) = S_1(Q^2).$$

We also briefly discussed the off-forward generalisation of this quantity in Chapters 5 and 6; see Eq. (5.18) for a definition. Here, we limit ourselves to the forward subtraction function.

Recall that we first showed the subtraction function in a dispersion relation, Eq. (2.26):

$$\overline{\mathcal{F}}_1(\omega, Q^2) = \mathcal{F}_1(\omega, Q^2) - S_1(Q^2) = 2\omega^2 \int_0^1 dx \frac{2xF_1(x, Q^2)}{1 - x^2\omega^2 - i\epsilon}.$$

Since F_1 is the physically measurable quantity, it is not possible to obtain $S_1(Q^2)$ from deep-inelastic scattering*. By contrast, it is straightforward to calculate $S_1(Q^2)$ using the Feynman-Hellmann method outlined in the preceding chapters. Hence in principle our method gives us the ability to access this subtraction function, which is otherwise difficult to constrain from experimental measurements.

The Compton amplitude subtraction function is a necessary input for two important physical quantities. First, it is required for theoretical predictions of the mass difference between the proton and neutron. Part of this mass difference is generated by the differ-

*It is possible to measure the subtraction function from a Compton scattering process, such as DVCS. However, these processes will often have off-forward kinematics, and hence it is necessary to extrapolate to the forward limit to access $S_1(Q^2)$.

ent charges of the constituent quarks [61, 62]. This electromagnetic contribution can be evaluated from the Cottingham sum rule [274],

$$\delta m^{\text{EM}} = -\frac{i}{2m_p} \frac{\alpha}{(2\pi)^3} \int d^4q \frac{T_{\mu\nu} g^{\mu\nu}}{Q^2 - i\epsilon}, \quad (8.1)$$

where $T_{\mu\nu}$ is the forward, spin-averaged Compton amplitude for a proton. The Compton structure functions $\overline{\mathcal{F}}_1$ and \mathcal{F}_2 can be measured using DIS structure functions—see Eqs. (2.26) and (2.27). On the other hand, the subtraction function cannot be determined from scattering data, which leads to conflicting evaluations of this contribution based on the model that is used [275, 276].

Similarly, this subtraction function is an input for the hadronic background of the proton charge radius. In particular, recent determinations of the charge radius from the muonic-hydrogen Lamb shift disagree with previous results from electron–proton scattering [277] by seven standard deviations [278]—a tension commonly called the ‘proton radius puzzle’ [59].

As the hadronic backgrounds for the muon and electron experiments are different, a more precise determination of this background could help resolve this puzzle [279, 280]. The ‘two-photon exchange’ hadronic corrections to the Lamb shift are dependent on the Compton amplitude:

$$\mathcal{M}_{\text{TPE}} = -ie^4 \int \frac{d^4q}{(2\pi)^4} \frac{T_{\mu\nu} L^{\mu\nu}}{Q^4 - i\epsilon}, \quad (8.2)$$

where $L_{\mu\nu}$ is the leptonic contribution, which can be calculated from QED, and $T_{\mu\nu}$ is the proton Compton amplitude. Since the Compton subtraction function is not well constrained, it contributes the dominant uncertainty to the hadronic background [281–283]. As such, a more precise determination of the subtraction function could help resolve the proton radius puzzle.

Finally, as discussed in Chapter 6, the subtraction function for the off-forward Compton amplitude, $S_1(\vartheta, t, \overline{Q}^2)$, is an input for the determination of the proton’s pressure distribution through deeply virtual Compton scattering [88, 89]. While this is potentially an area where our FH method could prove useful, in this chapter we limit ourselves to the discussion of the forward Compton subtraction function.

Though it is difficult to measure this forward subtraction function experimentally, it has been determined from effective theory schemes [276, 281, 283–288], and a non-relativistic calculation [282]. These effective theory and non-relativistic calculations are typically only applicable for small values of the hard scale: $Q^2 \ll m_N^2, \Lambda_{\text{QCD}}^2$. Moreover, these calculations have sizeable errors and are not always consistent with one another [289].

At large Q^2 , the subtraction function can be evaluated using the operator product expansion (OPE) [290, 291], and the following asymptotic behaviour is predicted:

$$S_1(Q^2) \sim \frac{m_N^2}{Q^2}, \quad \text{for } Q^2 \gg m_N^2. \quad (8.3)$$

However, as can be seen in Eqs. (8.1) and (8.2), a determination for the whole domain of $S_1(Q^2)$ is necessary for inputs into the aforementioned physical quantities.

At intermediate Q^2 , a lattice calculation of the Compton subtraction function is ideal. One such calculation has been performed using a direct four-point function [107]. However,

Table 8.1: Details of the gauge ensembles used in previous calculations of the Compton subtraction function [218, 239].

Set	N_f	$N_L^3 \times N_T$	L [fm]	a [fm]	m_π [MeV]
#1	2 + 1	$32^3 \times 64$	2.4	0.074	470
#2	2 + 1	$48^3 \times 96$	3.3	0.068	410
#3	2 + 1	$48^3 \times 96$	2.8	0.058	430

this calculation isolated the nucleon in the intermediate state, making it only sensitive to the low-energy nucleon pole contribution.

Here, we apply the Feynman-Hellmann method to calculate the Compton amplitude subtraction function. Our calculation is ideally suited for $Q^2 \in [2, 12]$ GeV²; that is, in the intermediate range where the $S_1(Q^2)$ is difficult to determine. However, previous calculations of the Compton subtraction function using Feynman-Hellmann [36–38, 40] have found behaviour highly at odds with the OPE prediction, Eq. (8.3): instead of asymptoting to zero at large Q^2 , our results asymptote to a *large non-zero value*.

In this chapter, we argue that this anomalous high-energy behaviour can be largely attributed to short-distance artefacts, where the separation between the two currents is on the order of the lattice spacing: $|z| \sim a$. Therefore, we design an alternative implementation of FH, temporal interlacing, that is less sensitive to these effects. We apply this temporal interlacing to structureless fermions, where the exact continuum solution is known, and to nucleons. These results show that the anomalous behaviour of the subtraction function is largely due to a lattice artefact.

The outline of this chapter is as follows: In Section 8.1, we outline the existing results and discuss other comparable lattice calculations. Then, in Section 8.2, we investigate the short-distance artefacts in the Compton amplitude. We start by examining the structureless fermion results, which are computationally inexpensive and for which the continuum result can be calculated analytically. We then introduce the interlacing procedure, applying it to both the nucleon and structureless fermions. Finally, we discuss possible methods to parameterise these short-distance artefacts analytically, allowing us to better isolate the physical contributions.

8.1 Background and Existing Results

Recall that in Chapter 4 we derived the Feynman-Hellmann relations relating the perturbed two-point functions and the spin-dependent and off-forward Compton amplitude. It is completely straightforward to take our perturbed two-point function for either case, Eq. (4.45) or (4.61), and set either $\lambda_{1,2} = 0$, to derive the FH relation for the spin-averaged forward Compton amplitude:

$$\left. \frac{\partial^2}{\partial \lambda^2} \frac{\mathcal{G}_\lambda(\tau)}{\mathcal{G}_0(\tau)} \right|_{\lambda=0} \stackrel{\tau \gg a}{\simeq} B_{\text{int}} + \frac{\tau}{E_N(\mathbf{p})} T_{33}(\mathbf{p}, \mathbf{q}). \quad (8.4)$$

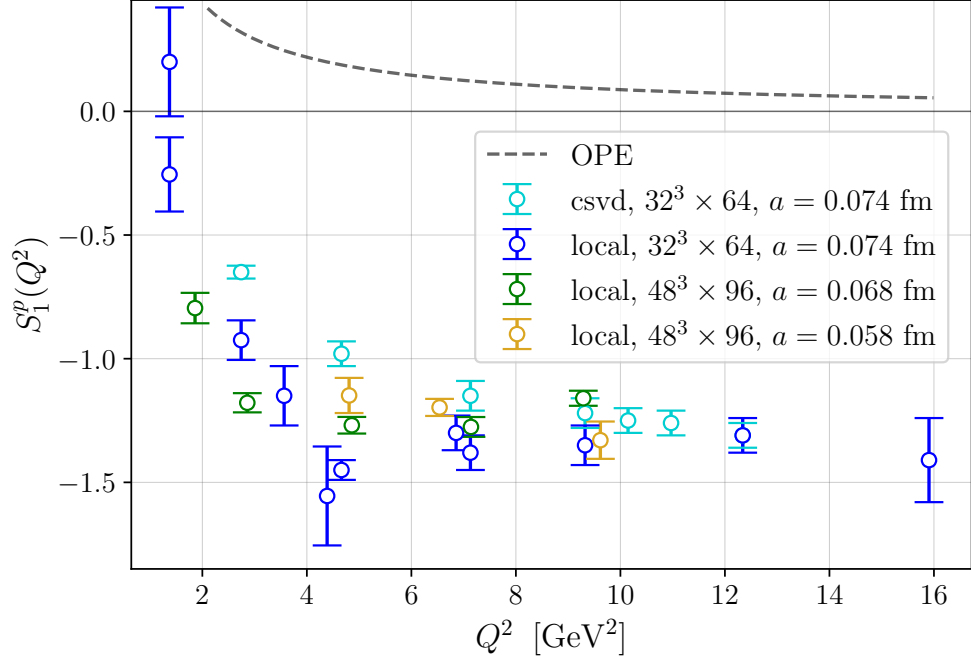


Figure 8.1: Existing results for the forward subtraction function calculated with Feynman-Hellmann using both the local and conserved currents [40, 178]. The OPE line is from a the parameterisation in Ref. [291] using scalar charges [174] and moments [37] for the $32^3 \times 64$ lattice.

Or, through the energy shift,

$$\left. \frac{\partial^2 E_\lambda}{\partial \lambda^2} \right|_{\lambda=0} = -\frac{T_{33}(\mathbf{p}, \mathbf{q})}{E_N(\mathbf{p})}, \quad (8.5)$$

where we have chosen $\mu = \nu = 3$ to eliminate the spin-dependent terms. This type of calculation has been performed and presented in Refs. [36–38, 40].

By simply taking $\mathbf{p} = 0$, Eq. (8.4) becomes

$$\left. \frac{\partial^2 \mathcal{G}_\lambda(\tau)}{\partial \lambda^2} \frac{\mathcal{G}_0(\tau)}{\mathcal{G}_0(\tau)} \right|_{\lambda=0} \stackrel{\tau \gg a}{\simeq} B_{\text{int}} + \frac{\tau}{m_N} S_1(Q^2), \quad (8.6)$$

and hence we can use it to easily calculate the Compton amplitude subtraction function.

8.1.1 Existing results

We start by presenting the existing results for the forward spin-averaged Compton subtraction function using the Feynman-Hellmann method [36–38, 40]. These were calculated on the configurations given in Table 8.1, and include results for the local current, Eq. (3.40), as well as the conserved current[†], Eq. (3.41).

All of these results are presented in Fig. 8.1. We have indicated the OPE prediction from Ref. [291] with a dashed line. This OPE prediction only includes the leading m_N^2/Q^2

[†]For the Feynman-Hellmann implementation of the conserved current, see Refs. [40, 178].

term, which may not be sufficient for intermediate values of Q^2 . For inputs into the physical OPE, we use inputs for the lattice ensemble labelled #1 in Table 8.1; further details on our evaluation of the OPE result are supplied in Appendix I. One can observe the remarkable disagreement between the OPE prediction and the lattice results.

On the other hand, the FH results in Fig. 8.1 indicate a relatively good agreement among themselves: the different lattice spacings, volumes and the conserved and local current results appear fairly consistent with one another. While there are some discrepancies among the FH results, especially at intermediate Q^2 , they are much more consistent with each other than with the OPE prediction. Moreover, there is no clear trend in lattice spacing or volume[‡] towards the continuum OPE value.

Similarly, the off-forward subtraction function, as discussed in Chapters 5 and 6, appears to suffer from this anomalous high-energy behaviour—Figs. 5.8 and 6.6. However, in the off-forward case it is desirable to sample a greater \bar{Q}^2 range to confirm that the predicted asymptotic behaviour, Eq. (8.3), is violated.

From the discrepancy between the lattice results and the OPE, we cannot immediately conclude that our results suffer from a lattice artefact. While the validity of the OPE is widely-accepted, it is still not completely independent of assumptions, as discussed in Appendix C. Several studies using Regge analysis have considered the potential for OPE-breaking effects to emerge from a spin-zero intermediate state (a ‘ $J = 0$ fixed pole’) [217, 293], which could account for the discrepancy seen in Fig. 8.1. However, this fixed pole hypothesis remains a contentious issue[§] with arguments for and against [216, 294–297].

8.1.2 Short-distance artefacts

The general form of the operator product expansion is given by Eq. (2.38):

$$A(z)B(0) \xrightarrow{z \rightarrow 0} \sum_i c_i(z) \mathcal{O}_i(0).$$

Since this relation only describes the short-distance, $|z| \approx 0$, behaviour, it is natural to expect that OPE-breaking lattice artefacts will similarly arise from the short-distance behaviour on the lattice.

To examine the coordinate space behaviour of the Compton amplitude calculated with Feynman-Hellmann, consider the perturbed propagators we calculate:

$$S_\lambda = [M - \lambda \mathcal{O}_q]^{-1}. \quad (8.7)$$

To get the four-point function, one can take a second-derivative of this with respect to λ :

$$\left. \frac{\partial^2}{\partial \lambda^2} S_\lambda(\tau, \mathbf{z}; 0, \mathbf{0}) \right|_{\lambda=0} = \sum_{\substack{\mathbf{z}', \mathbf{z}'' \\ \tau', \tau''}} S(\tau, \mathbf{z}; \tau', \mathbf{z}') \mathcal{O}_q(\mathbf{z}') S(\tau', \mathbf{z}'; \tau'', \mathbf{z}'') \mathcal{O}_q(\mathbf{z}'') S(\tau'', \mathbf{z}''; 0, \mathbf{0}), \quad (8.8)$$

where $S = M^{-1}$ is the unperturbed propagator.

[‡]An effective field theory calculation of finite volume effects showed the Compton amplitude is not particularly sensitive to changes in volume [292].

[§]Moreover, it would complicate the Cottingham sum rule, Eq. (8.1), and hadronic contributions to the Lambshift, Eq. (8.2): a non-zero Q^2 independent term would make the integrals over q diverge.

The above equation shows that our calculation has a sum over *all spacetime points for the intermediate propagator*, including $|z' - z''| = 0, a, 2a$. Therefore, writing this out in terms of a discretisation of the Compton amplitude,

$$T_{\mu\nu} = \sum_z e^{iqz} \langle P | \mathcal{T} \{ j_\mu(z) j_\nu(0) \} | P \rangle,$$

this corresponds to having the current separation, z , as small as $|z| = 0, a, 2a$.

Such extremely short-distance contributions are a concern, as it has been shown that at $|z| \sim a$ the coordinate space current product has lattice artefacts [298, 299]:

$$\mathcal{T} \{ j_\mu(z) j_\nu(0) \} \stackrel{|z| \approx 0}{\simeq} \mathcal{T} \{ j_\mu(z) j_\nu(0) \}_{\text{continuum}} + \mathcal{O} \left(\frac{a}{|z|} \right).$$

Note that in Euclidean spacetime $|z| = \sqrt{\tau^2 + |\mathbf{z}|^2}$.

These artefacts are due to the well-known operator mixing problem arising from broken Lorentz symmetry [300, 301], which we discussed in Section 3.2. Since our lattice calculation includes contributions from this very short-distance region, $|z| \sim a$, it is possible these artefacts are responsible for the OPE-breaking behaviour seen in Fig. 8.1.

For this reason, Refs. [298, 299] suggest keeping the spatial separation in the window

$$a \ll |z| \ll \Lambda_{\text{QCD}}^{-1}, \quad (8.9)$$

so that the spatial separation will be sufficiently large to suppress lattice artifacts, but sufficiently small so that physical short-distance contributions are not removed.

We emphasise that our discretisation of the Compton amplitude is not incorrect—it should recover the physical Compton amplitude in the continuum limit. It is more a question of convergence: if the discretisation converges to the continuum poorly, our results may be unphysical even at relatively fine lattice spacings.

Other lattice calculations

Short-distance lattice artefacts in matrix elements of a two-current operator have been studied in other numerical lattice calculations, some of which we mentioned in Section 3.2.

For instance, there are calculations of matrix elements that are Fourier transformed in space but not time:

$$\mathcal{T}(\Delta t) = \int d^3 e^{-i\mathbf{q}\cdot\mathbf{z}} \langle \text{out} | \mathcal{J}^{(1)}(\Delta t, \mathbf{z}) \mathcal{J}^{(2)}(0) | \text{in} \rangle. \quad (8.10)$$

Such calculations include: the hadronic vacuum polarisation (HVP), where the ‘in’/‘out’ states are both the vacuum [302]; the heavy-quark OPE method, where the ‘out’ state is the vacuum and the ‘in’ is a pion [95]; and the hadronic tensor, where the ‘in’/‘out’ states are both hadrons [94].

Lattice QCD calculations of the HVP are related to the famous $g_\mu - 2$ puzzle, and as such their lattice artefacts have been investigated thoroughly. It has been found that short Euclidean time intervals, $\Delta t \sim a$, contribute significant lattice artefacts to the HVP [302].

In particular, it has been shown [303,304] that for the currents between vacuum states the lattice correlation function has short Euclidean time artefacts in the form

$$\mathcal{T}(\Delta t) = \mathcal{T}^{\text{continuum}}(\Delta t) \left[1 + \sum_{n=1} b_n \frac{a^{2n}}{(\Delta t)^{2n}} \right]. \quad (8.11)$$

Hence by a mixture of fitting to such parameterisations through varying Δt , taking the continuum limit, and using different lattice spacings, it is possible to control these artefacts [302].

Similarly, for the heavy-quark OPE it was found that at $\Delta t \leq 2a$ results using this method exhibit anomalous behaviour, which these studies attributed to short-distance lattice artefacts [159,305]. However, as yet no calculations of the hadronic tensor have examined these effects.

Another related class of calculation are those that are of purely coordinate space matrix elements:

$$\langle \text{out} | j_1(\tau, \mathbf{z}) j_2(0) | \text{in} \rangle. \quad (8.12)$$

For an early lattice calculation using a non-linear sigma model, it was found that the lattice results exhibited OPE-breaking for $|z| \lesssim 2a$ [306]. When similar short-distance artefacts were examined in the pseudo-distribution method, it was found that large artefacts appeared for the smallest current separations considered, $|z| = a, 2a$ [307–310].

Therefore, there are good reasons, from both analytic and numerical studies, to suspect that the OPE-breaking observed in Fig. 8.1 is at least partially due to short-distance lattice artefacts.

8.2 Investigating Short-Distance Artefacts

In this section, we investigate short-distance artefacts in our calculation of the Compton amplitude. We focus on the subtraction function, but naturally such artefacts may also affect the ω dependent part of the Compton amplitude. As such, they could be responsible for some of the anomalous results presented in Chapters 6 and 7.

We investigate these short-distance artefacts in three ways: (1) we calculate the structureless fermion Compton amplitude, which are computationally inexpensive to calculate and for which the continuum result can be determined analytically; (2) we use a different implementation of Feynman-Hellmann that allows us to control the separation in Euclidean time and thereby vary the effects of short-distance artefacts; and (3) we finish by applying the results of a lattice perturbation theory (LPT) parameterisation for the $\mathcal{O}(a)$ artefacts of the Compton amplitude.

8.2.1 Structureless fermion calculation

As previously discussed, we cannot conclusively say that there are no physical OPE-breaking mechanisms for a hadron. For a structureless fermion, however, we can calculate the Compton amplitude exactly with simple QED—see the Feynman diagrams in Fig. 8.2.

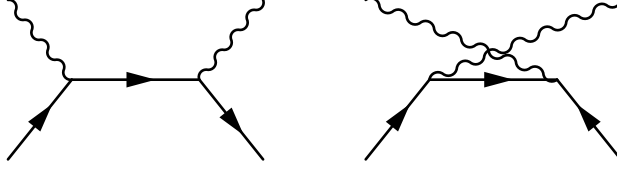


Figure 8.2: Feynman diagrams for Compton scattering with a structureless fermion.

We obtain

$$T_{\mu\nu}(\omega, Q^2) = \frac{2\omega^2}{1-\omega^2} \left[\frac{p_\mu q_\nu + p_\nu q_\mu}{p \cdot q} + \frac{Q^2}{(p \cdot q)^2} p_\mu p_\nu - g_{\mu\nu} \right] + \frac{2\omega}{1-\omega^2} \frac{i}{p \cdot q} \epsilon_{\mu\nu\rho\sigma} q^\rho s^\sigma. \quad (8.13)$$

Therefore, if we choose $\mu = \nu = 3$ and $p_3 = q_3 = 0$, we have

$$T_{33}(\omega) = \frac{2\omega^2}{1-\omega^2}.$$

And hence at $\omega = 0$,

$$T_{33}(\omega = 0, Q^2) = 0. \quad (8.14)$$

As such, we can calculate this structureless fermion Compton amplitude using our lattice FH method and compare it to the known continuum result. A significant deviation from Eq. (8.14) would indicate the presence of lattice artefacts. Consequently, this structureless fermion case is an ideal testing ground for lattice artefacts.

We define the structureless fermion analogue of a subtraction function as simply the $\omega = 0$ contribution to the $g_{\mu\nu}$ coefficient in Eq. (8.13):

$$\hat{S}(Q^2) = T_{33}^{\text{latt}}(\omega = 0, Q^2), \quad (8.15)$$

where we choose $p_3 = q_3 = 0$.

Lattice setup

To calculate this on the lattice, we set the strong coupling to zero by choosing unit gauge links $U_\mu = 1$ for the gauge link defined in Eq. (3.11). Then, instead of taking multiple Wick contractions to construct a hadron as outlined in Chapter 3, we simply use the single Wilson fermion propagator. The implementation of Feynman-Hellmann is then identical to the hadron case; we use the FH relation Eq. (8.4) with the local current and set $Z_V = 1$.

We work with dimensionless quantities: the reduced momentum,

$$\hat{q}_\mu = \frac{L}{2\pi} \mathbf{q}_\mu, \quad (8.16)$$

and the hopping parameter, Eq. (3.19):

$$\kappa = \frac{1}{2am_0 + 8r}. \quad (8.17)$$

Note we always use $r = 1$, and hence $m_0 = 0$ corresponds to $\kappa = 1/8$.

Table 8.2: Details of the structureless fermion calculation.

κ	am	$L^3 \times T$	λ	\hat{q}^2
0.0956–0.1248	0.064–0.802	$32^3 \times 64$	0.00625, 0.0125	4–34

We also define m , the pole mass of a structureless fermion. This is the positive energy pole of the Wilson propagator at zero momentum. Even for a free theory we have $m \neq m_0$, although this is not the result of the fermion being dressed by an interaction; it is simply due to the small discretisation effects. Typically $m \approx m_0$, and hence κ and am are approximately inversely proportional.

Results

The details of the structureless fermion calculation are given in Table 8.2. We choose the range of κ between 0.0956 and 0.1248. At $\kappa = 0.1248$ (i.e. just less than $1/8$), we have a pole mass of $am = 0.064$, and hence the $\mathcal{O}(am)$ discretisation effects are minimal, and our results should look very close to the continuum, up to potential finite volume effects. On the other hand, our largest κ is 0.0956 with a mass $am = 0.802$, which is extremely coarse but allows us to observe the extremity of lattice artefacts. In total there are 10 κ values in this range.

Recall in Chapter 4 when we discussed FH excited terms, we noted that $Q^2 \ll m_N^2$ kinematics induce FH excited terms. For the structureless fermion case, where we have $\mathbf{p} = 0$, these excited states behave like

$$\exp \left\{ -m \left(\sqrt{1 + \mathbf{q}^2/m^2} - 1 \right) \tau \right\}. \quad (8.18)$$

Hence for $a|\mathbf{q}| \ll am$, these terms will not be suppressed. As such, to suppress the effects of these FH excited terms, we calculate results that have $\hat{q}^2 \geq 4$. Although, for the largest am and smallest \hat{q}^2 such excited states may still contribute significantly.

As the structureless fermion results only have one configuration ($U_\mu = 1$) and are very regular, we perform a simple Euclidean time fit to the function $f(\tau) = a\tau + b$, and extract the slope, which is proportional to the Compton amplitude. We perform these calculations for two different λ values: $\lambda = 0.00625, 0.0125$, and perform λ fits as in the previous sections.

Although these fitting procedures come with error bars, we do not report these since the errors are typically very small, they do not reflect physical uncertainties like gauge noise, and the purpose here is mostly to get a qualitative understanding of the structureless fermion's behaviour.

We use a similar ratio to previous calculations,

$$R_\lambda \equiv \frac{\mathcal{G}_\lambda + \mathcal{G}_{-\lambda} - 2\mathcal{G}_0}{\mathcal{G}_0},$$

to approximate the second-order derivative.

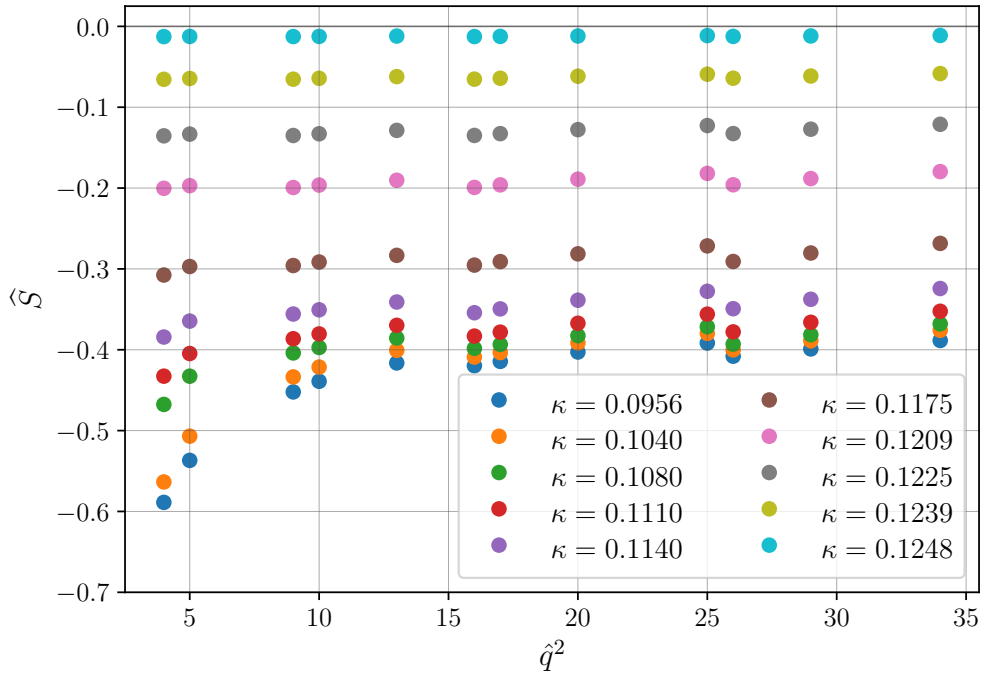


Figure 8.3: Subtraction function analogue for structureless fermion, Eq. (8.15), for a range of κ and \hat{q}^2 . Note it appears to vanish as $\kappa \rightarrow 1/8$.

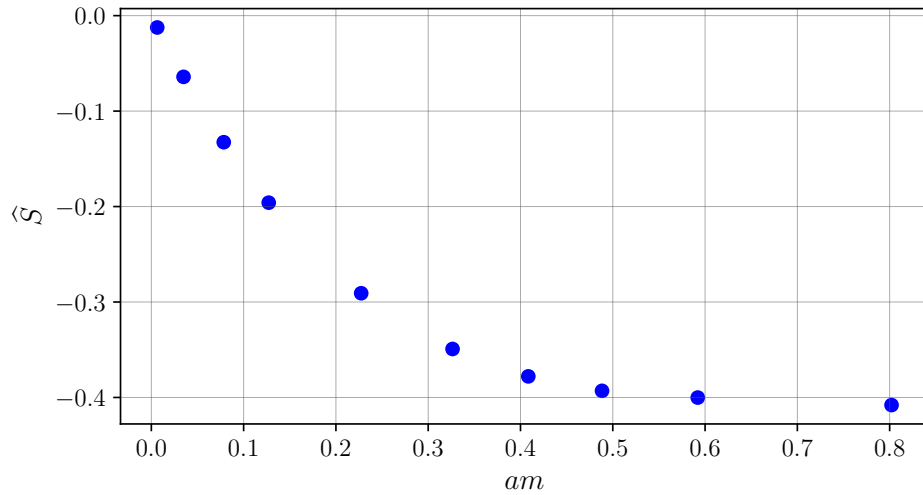


Figure 8.4: Subtraction function for $\hat{q}^2 = 26$ as a function of am . While it appears to converge to the continuum limit as $am \rightarrow 0$, even at relatively fine discretisations, the lattice artefacts are quite large.

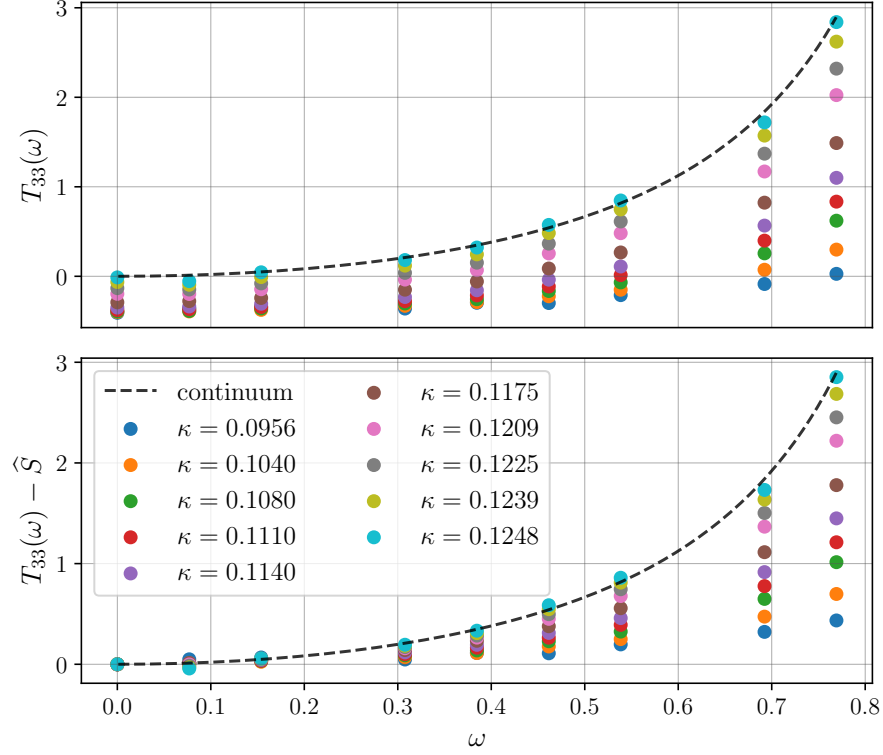


Figure 8.5: ω dependence of structureless fermion results for $\hat{q}^2 = 26$.

Discussion

In Fig. 8.3, we see that the results for \widehat{S} , the structureless fermion ‘subtraction function’, appear to have significant \hat{q}^2 dependence for low \hat{q}^2 and small κ (equivalently large am). As per Eq. (8.18) and the accompanying discussion, we expect low \hat{q}^2 and large am results to be most affected by poorly suppressed Feynman-Hellmann excited states. However, for sufficiently small am and large \hat{q}^2 , \widehat{S} is mostly flat, with some small jitters. Hence we interpret these results with small am and large \hat{q}^2 as the structureless fermion subtraction function.

As we can see in both Figs. 8.3 and 8.4, even where the FH excited states appear suppressed, the structureless fermion subtraction function is noticeably distinct from the continuum value of zero. However, as $\kappa \rightarrow 1/8$ or equivalently $am \rightarrow 0$, we have $\widehat{S} \rightarrow 0$, the continuum prediction. While this is encouraging, the deviation from the continuum is still evident even at moderately fine discretisations.

In Fig. 8.5 we plot the ω dependence of the structureless fermion Compton amplitude. Similarly, at $\kappa = 0.1248$ we see good agreement between the continuum and lattice results. However, at coarser discretisations, even after subtracting \widehat{S} , there is a significant discrepancy between lattice and continuum results. This indicates the presence of lattice artefacts in the ω dependence as well. However, whether this occurs as the result of poorly suppressed FH excited states occurring as $\omega \rightarrow \pm 1$, or as a genuine artefact to the lattice Compton amplitude needs to be examined in future work.

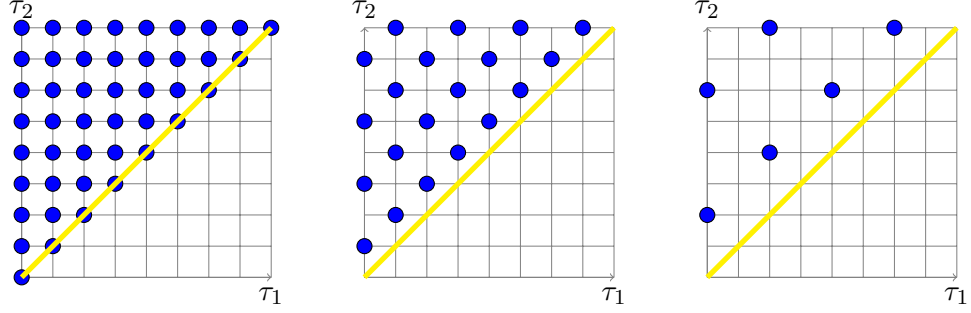


Figure 8.6: Integration regions for different temporal interlacings, with the time-ordering $\tau_2 \geq \tau_1$. The blue dots represent pairs of time-slices with current insertions, while the yellow line is the $\tau_1 = \tau_2$ line. Left: no interlacing, i.e. $\tau_{\min} = 0$. Center: $\tau_{\min} = 1$ interlacing. Right: $\tau_{\min} = 2$ interlacing.

8.2.2 Temporal interlacing: formulation

In the case of the structureless fermion we are able to vary κ down to extremely fine discretisations to test for the presence of short-distance lattice artefacts. In the nucleon case, an equivalent calculation would be prohibitively expensive: not only would such fine lattice spacings require expensive new gauge configurations, but because nucleons are extended objects, we would need to greatly increase the number of lattice sites. Instead, in this section we formulate a different implementation of FH that allows us to vary the Euclidean time separation, and hence vary the contribution for the $|z| \sim a$ region. In doing so, we test for the presence of short-distance lattice artefacts without needing to vary the lattice spacing. We apply this new implementation to the structureless fermion first and then the nucleon.

As discussed in Chapter 4, a major advantage of the FH method is that we get all time-slices with one inversion. However, this comes with a disadvantage: we cannot easily control which time-slices the two currents are inserted on. As a solution, we can use two perturbing currents, each on different, non-overlapping sets of time-slices. This enforces a minimum temporal separation, τ_{\min} . Hence we have $|z| = \sqrt{\mathbf{z}^2 + \tau^2} \geq \tau_{\min}$, and thereby introduce a non-zero minimum current separation.

The general form of the perturbing matrices is

$$[\mathcal{O}_{1,2}]_{n,m} = \Gamma_{\tau_n, \tau_m}^{(1),(2)} \delta_{\mathbf{z}_n, \mathbf{z}_m} (e^{i\mathbf{z}_n \cdot \mathbf{q}} + e^{-i\mathbf{z}_n \cdot \mathbf{q}}) \gamma_3, \quad (8.19)$$

where $\Gamma^{(1),(2)}$ are matrices in Euclidean time space.

For the simplest case, where one of the currents is on every even time-slice and the other on every odd, we have

$$\Gamma_{\tau, \tau'}^{(1)} \equiv \begin{cases} 1 & \text{if } \tau = \tau' \text{ and } \tau, \tau' \text{ both even,} \\ 0 & \text{otherwise.} \end{cases}$$

Similarly, $\Gamma_{\tau, \tau'}^{(2)}$ is 1 if $\tau = \tau'$ are odd, and zero for all other combinations. This leads to one of the currents being inserted on all the odd time-slices and the other on all the even.

Hence there is a minimum temporal separation of $\tau_{\min} = 1$ (using the $a = 1$ convention for simplicity). See Fig. 8.6 center.

The perturbed propagator is

$$S_\lambda(z_n, z_m) = \left[[M - \lambda_1 \mathcal{O}_1 - \lambda_2 \mathcal{O}_2]^{-1} \right]_{n,m}. \quad (8.20)$$

Therefore, the mixed second-order derivative of the perturbed propagator is

$$\frac{\partial^2}{\partial \lambda_1 \partial \lambda_2} S_\lambda(\tau, \mathbf{z}; 0, \mathbf{0}) \Big|_{\lambda=0} = \sum_{\substack{\mathbf{z}', \mathbf{z}'' \\ \tau', \tau''}} S(\tau, \mathbf{z}; \tau', \mathbf{z}') \mathcal{O}_{\mathbf{q}}(\mathbf{z}') \mathbb{S}(\tau', \mathbf{z}'; \tau'', \mathbf{z}'') \mathcal{O}_{\mathbf{q}}(\mathbf{z}'') S(\tau'', \mathbf{z}''; 0, \mathbf{0}), \quad (8.21)$$

where we have defined

$$\mathbb{S}(\tau, \mathbf{z}; \tau', \mathbf{z}') \equiv \begin{cases} 0 & \text{if } \tau, \tau' \text{ are both even or both odd,} \\ S(\tau, \mathbf{z}; \tau', \mathbf{z}') & \text{otherwise.} \end{cases}$$

Therefore, the Feynman-Hellmann relation for $\tau_{\min} = 1$ interlacing is

$$E_N \frac{\partial^2 \mathcal{G}_\lambda}{\partial \lambda_1 \partial \lambda_2} \Big|_{\lambda=0} \simeq \tau \sum_{\tau_1=0,2,4,6\dots} \sum_{\tau_2=1,3,5,\dots} \sum_{\mathbf{z}} e^{-i\mathbf{q}\cdot\mathbf{z}} \langle P | \mathcal{T} \{ j_3(\mathbf{z}, \tau_1) j_3(0, \tau_2) \} | P \rangle. \quad (8.22)$$

With a judicious choice of kinematics, the RHS of Eq. (8.22) is proportional to a discretisation of $S_1(Q^2)$. The interlacing in Eq. (8.22) changes the measure of the two sums over time-slices from $a \rightarrow 2a$, which must be accounted for by a factor of four:

$$E_N \frac{\partial^2 \mathcal{G}_\lambda}{\partial \lambda_1 \partial \lambda_2} \Big|_{\lambda=0} \simeq \frac{1}{4} \tau T_{33}.$$

However, once this normalisation is accounted for, in the continuum limit Eq. (8.22) approaches the same object as our previous discretisations of the Compton amplitude.

In the case of $\tau_{\min} = 2$ interlacing, $\Gamma^{(1)}$ is zero except when $\tau = \tau' = 4n$ for $n \in \mathbb{Z}$, while $\Gamma^{(2)}$ is zero except when $\tau = \tau' = 4n + 2$.

This gives us

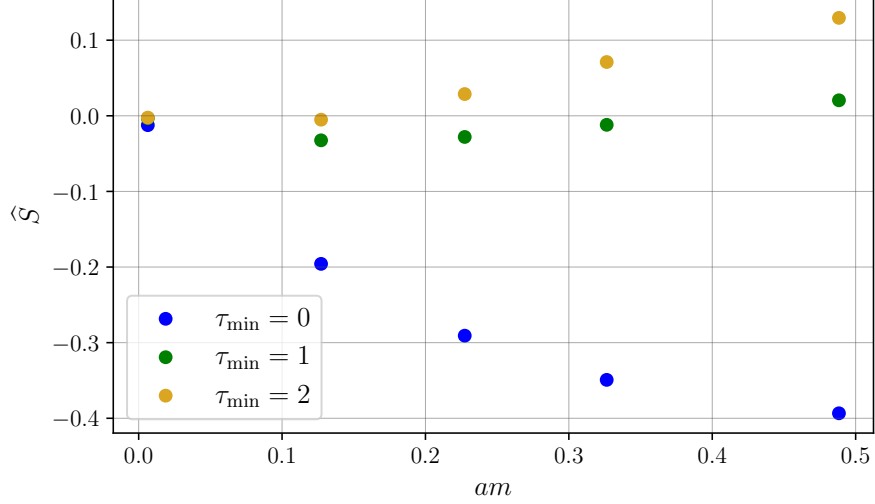
$$E_N \frac{\partial^2 \mathcal{G}_\lambda}{\partial \lambda_1 \partial \lambda_2} \Big|_{\lambda=0} \simeq \tau \sum_{\tau_1=0,4,8,12\dots} \sum_{\tau_2=2,6,10,\dots} \sum_{\mathbf{z}} e^{-i\mathbf{q}\cdot\mathbf{z}} \langle P | \mathcal{T} \{ j_3(\mathbf{z}, \tau_1) j_3(0, \tau_2) \} | P \rangle. \quad (8.23)$$

Again, the measure of the sum goes $a \rightarrow 4a$, and hence we must account for this with an overall factor of 16. See right-hand diagram in Fig. 8.6 for an illustration.

Therefore, the temporal interlacing for $\tau_{\min} = 1$ removes contributions with $|z| = 0$, while the $\tau_{\min} = 2$ interlacing removes contributions with $|z| = 0, a$; see Fig. 8.6. However, the larger τ_{\min} is, the more coarsely the integration region is sampled, which removes points even where $|z| \gg a$. As such, to avoid different lattice artefacts induced by an overly coarse sampling of the Euclidean time interval, the largest τ_{\min} we implement is $\tau_{\min} = 2$.

Table 8.3: Details of the structureless fermion calculation with interlacing.

κ	am	$N_L^3 \times N_T$	λ	\hat{q}^2	τ_{\min}
0.1080—0.1248	0.064—0.488	$32^3 \times 64$	0.00625, 0.0125	26	0,1,2

**Figure 8.7:** The structureless fermion subtraction function analogue at $\hat{q}^2 = 26$ for both interlaced results, $\tau_{\min} = 1, 2$, and the regular results, $\tau_{\min} = 0$.

8.2.3 Temporal interlacing: structureless fermion

We now apply the alternative FH implementation, temporal interlacing, to the structureless fermion case. The relevant FH relations are Eqs. 8.22 and 8.23. We calculate two sets of interlaced results with $\tau_{\min} = 1, 2$, and compare these to the regular (uninterlaced) implementation, which we denote as $\tau_{\min} = 0$.

We choose a more limited range of κ and \hat{q} than the uninterlaced results. In particular, we calculate only $\hat{q}^2 = 26$. The details of the calculation are given in Table 8.3. We use the same λ values as the uninterlaced results. However, because we now have two currents (one for each set of time-slices) we use the familiar ratio, Eq. (4.53), to approximate the mixed second-order derivative:

$$R_\lambda \equiv \frac{\mathcal{G}_{(\lambda,\lambda)} + \mathcal{G}_{(-\lambda,-\lambda)} - \mathcal{G}_{(\lambda,-\lambda)} - \mathcal{G}_{(-\lambda,\lambda)}}{\mathcal{G}_{(0,0)}}.$$

Discussion

We can see in Fig. 8.7 that $\hat{S} \rightarrow 0$ with $am \rightarrow 0$ for all the results, $\tau_{\min} = 0, 1, 2$. While the interlacing results appear closer to the continuum result, for $am \approx 0.2$ and above, $\tau_{\min} = 1$ outperforms $\tau_{\min} = 2$ in terms of agreement with the continuum. For $am \approx 0.1$ and below, the $\tau_{\min} = 2$ results outperform the $\tau_{\min} = 1$ results.

Similarly, we plot the ω dependence in Fig. 8.8. We can see that the subtracted $\tau_{\min} = 0$ results and the $\tau_{\min} = 1$ results appear very close. Also, note that the $\tau_{\min} = 2$

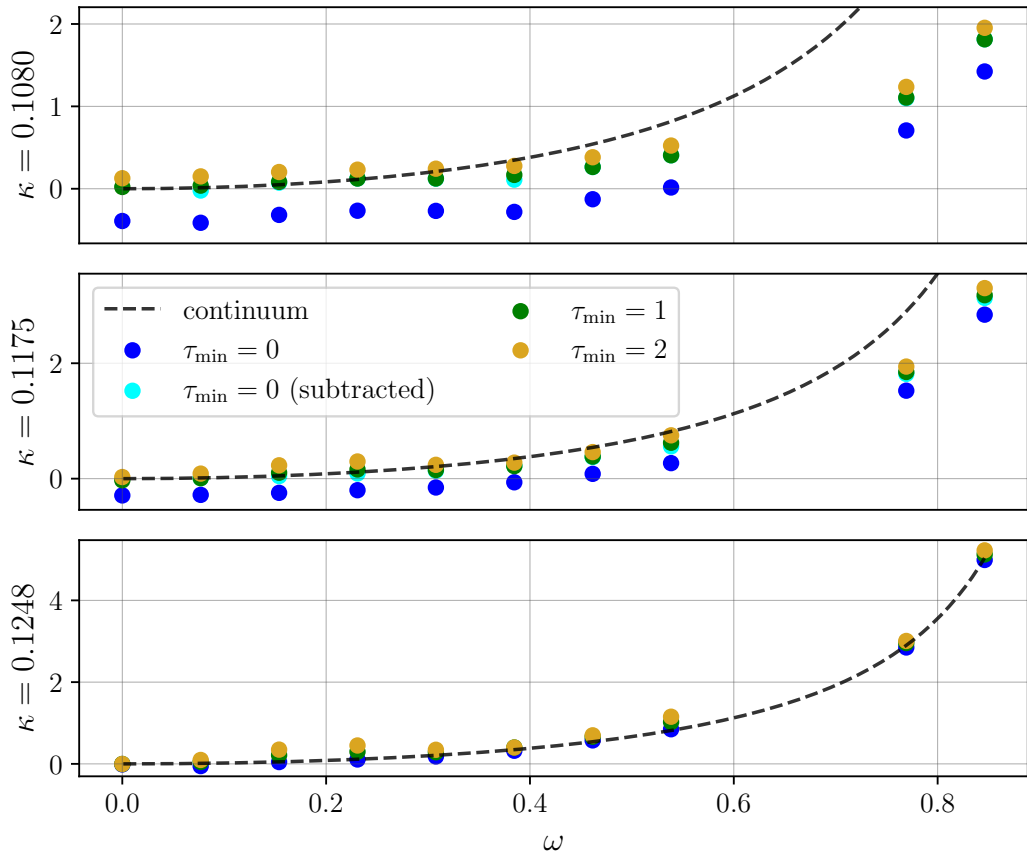


Figure 8.8: ω dependence of T_{33} for $\hat{q}^2 = 26$ and $\kappa = 0.1080$ (top), $\kappa = 0.1175$ (middle), and $\kappa = 0.1248$ (bottom). Note that $\tau_{\min} = 0$ results are uninterlaced (regular), and the ‘subtracted’ results are $T_{33}(\omega) - \hat{S}$.

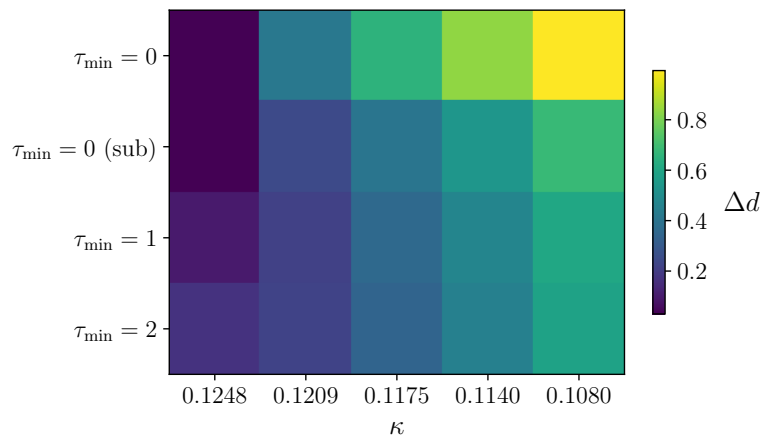


Figure 8.9: A heatmap of Δd , defined in Eq. (8.24), for different interlacings and κ values. Smaller Δd indicates better agreement with the continuum. Again, ‘ $\tau_{\min} = 0$ (sub)’ are the $T_{33}(\omega) - \hat{S}$ uninterlaced results.

results appear more jittery; that is, they deviate from the expected ω polynomial with positive coefficients.

However, since it is difficult to judge by eye the agreement between the lattice results and the continuum, we define a simple metric:

$$\Delta d \equiv \sum_{i=1}^N \frac{|T_{33}^{\text{cont}}(\omega_i) - T_{33}^{\text{latt}}(\omega_i)|}{N}, \quad (8.24)$$

where $T_{33}^{\text{cont(latt)}}(\omega_i)$ is the Compton amplitude for the continuum (lattice). As such, Δd quantifies how close the results are across all ω values for different κ and τ_{\min} ; large Δd corresponds to poor agreement with the continuum.

The results are presented in the heat map in Fig. 8.9. We can see that the interlacing is a significant improvement on the uninterlaced results for all κ values except $\kappa = 0.1248$, which has the finest discretisation. Moreover, it appears that, in contrast to the \widehat{S} results, the $\tau_{\min} = 2$ results are best for the coarser (larger am) results.

Conclusion

From all of these structureless fermion results, we can make a number of conclusions about the lattice Compton amplitude for a structureless fermion:

- This Compton amplitude contains a significant degree of contamination from lattice artefacts.
- As $\kappa \rightarrow 1/8$ or equivalently $am \rightarrow 0$, we recover the continuum Compton amplitude. However, significant artefacts remain even at relatively fine discretisations.
- At all κ values but the finest, the interlacing significantly improves agreement with the continuum.
- At the finest discretisation ($\kappa = 0.1248$), the interlacing increases the disagreement with the continuum.

These last two points indicate the trade-offs of the interlacing procedure: while it does suppress the lattice artefacts from short-distance effects, $|z| \sim a$, it also more coarsely samples the integration region which likely introduces its own artefacts. The artefacts from a coarser sampling would be removed in the $N_T \rightarrow \infty$ limit. Therefore, at all but the finest lattice spacing, the price of the interlacing procedure is worth paying, but for sufficiently fine lattice spacings it appears to impair the results.

We must be careful about applying interpretations of structureless fermion results to the nucleon case (for instance, the nucleon is an extended object, while a structureless fermion is point-like). Nonetheless, this test motivates a similar application of the interlacing procedure to the nucleon.

8.2.4 Temporal interlacing: nucleon

Now we apply this temporal interlacing procedure to the nucleon results, and again observe the change in the subtraction function, $S_1(Q^2)$, as well as the ω dependence.

Simulation details

For the hadron interlacing results, we use the gauge ensemble labelled #1 in Table 8.1. These gauge configurations were used in Chapter 5 and more details are given in Table 5.1. To summarise, they are $N_L^3 \times N_T = 32^3 \times 64$, at a pion mass of $m_\pi \approx 470$ MeV, and a lattice spacing of $a = 0.074$ fm.

We apply the interlacing procedure for $\tau_{\min} = 1, 2$, and note that $\tau_{\min} = 0$ corresponds to the regular (existing) FH results for this lattice. The $\tau_{\min} = 1, 2$ results have low statistics, $N_{\text{meas}} = 200$. To test the Q^2 dependence, we calculate the interlaced results for four values of the hard scale: $Q^2 = 2.7, 4.7, 7.1, 12.3$ GeV².

The Feynman-Hellmann perturbations to the fermion matrices are identical to those in the structureless fermion case, Eq. (8.19), except with the QCD fermion matrix and with the quark propagators inserted into a nucleon two-point function. The FH relations are given in Eqs. (8.22) and (8.23).

Again, we approximate the mixed second-order derivative with the ratio given in Eq. (4.53). Hence, as in the preceding chapters, we calculate four pairs of (λ_1, λ_2) : $(\pm\lambda, \pm\lambda)$ and $(\pm\lambda, \mp\lambda)$. For the interlaced results the diagonal terms, $(\pm\lambda, \pm\lambda)$, are simply the *uninterlaced* propagators, and hence we need not calculate them.

τ and λ fits

We fit the combination of correlators, R_λ , to the usual linear fit function, $f(\tau) = a\tau + b$, and interpret the slope as proportional to the Compton amplitude. Unlike Chapters 6 and 7, we do not apply our more involved weighted average fitting method. Instead, we choose a uniform fit window of $\tau \in [6, 11]$. This is simply because our interlacing results are low statistics, and we are more interested in general, qualitative behaviour.

Then, as in previous chapters, after isolating the slope in Euclidean time, we fit the λ dependence of the result to the function $f(\lambda) = c\lambda^2$ in order to determine c . Note that the λ values for $\tau_{\min} = 0, 1$ results are $\lambda = 0.0125, 0.025$, while for $\tau_{\min} = 2$ they are $\lambda = 0.00625, 0.0125$. We resolve a good signal for both. We show these fits in Fig. 8.10, where they exhibit good agreement with the quadratic-only fit function.

Also in Fig. 8.10, we plot the analogue of the effective mass, $\Delta_\tau R_\lambda(\tau)$,

$$\Delta_\tau R_\lambda(\tau) = \frac{R_\lambda(\tau + \delta\tau) - R_\lambda(\tau)}{\delta\tau},$$

with the fits for the slope in τ . Since the interlacing results have time-dependent background fields, we might expect some unusual behaviour in the Euclidean time fits. However, in Fig. 8.10, we see a good signal for $\tau_{\min} = 1, 2$ even at 200 measurements.

Results and discussion

In Fig. 8.11, we present our results for the subtraction function for all τ_{\min} and Q^2 values. In this plot, all results have $N_{\text{meas}} = 200$. As before, the OPE prediction is from Ref. [291] with scalar charge [174] and structure function moments [37] determined on the same gauge configurations as our Feynman-Hellmann results.

We observe a dramatically improved agreement between the lattice results and the continuum OPE as τ_{\min} increases. As with the structureless fermion, Fig. 8.4, the hadron results appear to be very sensitive to changes in τ_{\min} . This confirms the existence of large

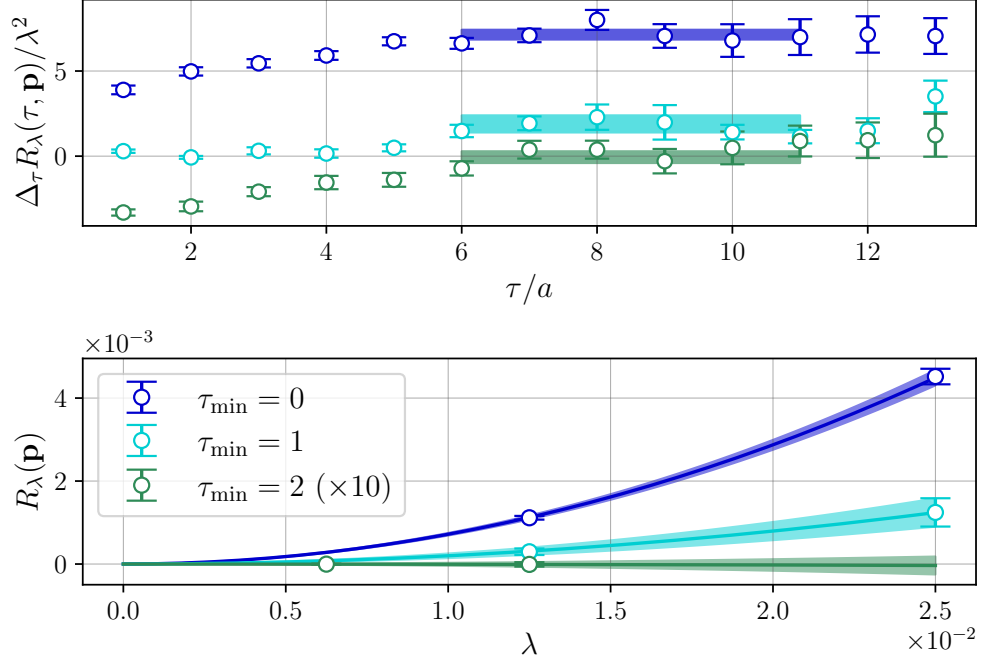


Figure 8.10: $\mathbf{p} = (0, 0, 0)$, for up quarks and the smallest λ values. Note that the $\tau_{\min} = 2$ results have different λ values. Moreover, we multiply the $\tau_{\min} = 2$ results by a factor of 10, so that the signal quality can be better shown despite their small size.

lattice artefacts in our original calculation of $S_1(Q^2)$. Hence the anomalous behaviour we presented at the start of the chapter, Fig. 8.1, can be attributed to short-distance lattice artefacts.

However, this comes with a caveat: even at $\tau_{\min} = 2$, the results do not appear to asymptote to zero as $Q^2 \rightarrow \infty$. This result is frustratingly ambiguous; it could be due to unsuppressed lattice artefacts or physical OPE-breaking. We do not calculate results for $\tau_{\min} = 3$, as this is likely too coarse a sampling of the integration region in Euclidean time.

Moreover, there is no strong convergence in the $\tau_{\min} = 1, 2$ results that would allow us to isolate the physical subtraction function. As such, while we have confirmed the presence of large lattice artefacts, we can neither determine the continuum $S_1(Q^2)$ nor rule out OPE-breaking.

In addition to the subtraction function, we are interested in the effect of the interlacing on the ω dependence. Hence we also determine the subtracted Compton structure function,

$$\bar{\mathcal{F}}_1(\omega, Q^2) = \mathcal{F}_1(\omega, Q^2) - S_1(Q^2),$$

for all values of τ_{\min} . This is plotted in Fig. 8.12.

In contrast to the results for $S_1(Q^2)$, the results for $\bar{\mathcal{F}}_1(\omega, Q^2)$ show relatively good agreement among the three values of τ_{\min} . This is reassuring: it tells us that our determinations of the subtracted Compton amplitude, from which we determine the moments, is not heavily affected by these short-distance artefacts.

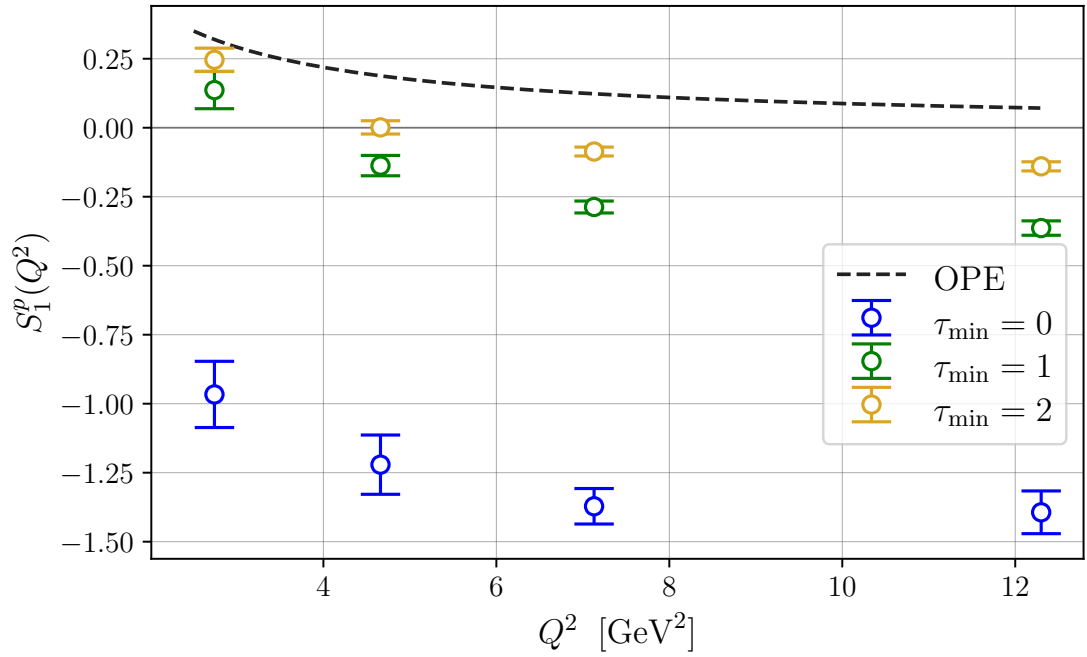


Figure 8.11: The Compton amplitude subtraction function for multiple values of τ_{\min} , compared to the OPE prediction from Ref. [291]. All results have $N_{\text{meas}} = 200$.

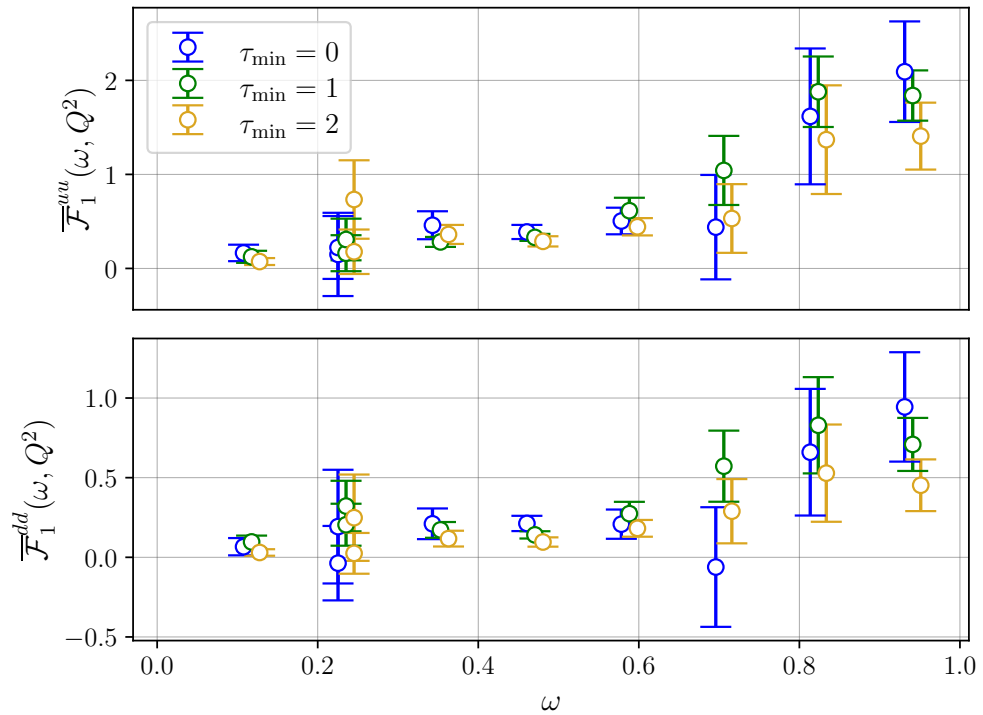


Figure 8.12: The subtracted Compton structure function $\bar{\mathcal{F}}_1$ at a fixed value of $Q^2 = 4.6 \text{ GeV}^2$. Note that the uninterlaced, $\tau_{\min} = 0$, results have $N_{\text{meas}} = 1000$, while $N_{\text{meas}} = 200$ for the interlaced results, $\tau_{\min} = 1, 2$.

However, we note that for the results in Fig. 8.12, the regular $\tau_{\min} = 0$ results have $N_{\text{meas}} = 1000$, while the interlacing results have $N_{\text{meas}} = 200$. This is because it is harder to get a reasonable signal from the $\tau_{\min} = 0$ results for high momentum at low statistics. As such, this reflects well on the interlaced results.

8.2.5 Towards a parameterisation of discretisation artefacts

While the interlacing results confirm the presence of large lattice artefacts in the Compton amplitude subtraction function, it is difficult to isolate $S_1(Q^2)$ using these results alone: the number of τ_{\min} values is limited and it is difficult to establish convergence with our limited range of τ_{\min} values.

Therefore, in this section we use the results of a lattice perturbation theory (LPT) calculation [254] to parameterise the $\mathcal{O}(a)$ artefacts of the lattice Compton amplitude. We then compare these results to our structureless fermion and nucleon Compton amplitudes.

A lattice perturbation theory expansion was performed for the lattice Compton amplitude with Wilson fermions up to $\mathcal{O}(a^2)$ in Ref. [254]. However, the discretisation of the Compton amplitude considered in this work differs from ours in two ways: (1) it has an additional ‘seagull’ operator, which is independent of q_μ ; and (2) it uses the conserved current, Eq. (3.41), whereas our numerical results largely use the local current, Eq. (3.40), with only limited calculations using the conserved [40].

To address the first difference, we simply drop terms in the expansion that originate from the seagull operator. To address the second, we note that the conserved current can be expressed in terms of the local current without its renormalisation factor, plus higher dimension operators involving derivatives:

$$j_\mu^{\text{con}}(z) = \bar{\psi}(z)\gamma_\mu\psi(z) + \frac{a}{2}\bar{\psi}(z)\gamma_\mu\left(\vec{D}_\mu + \vec{D}_\mu\right)\psi(z) + \frac{ar}{2}\bar{\psi}(z)\left(\vec{D}_\mu - \vec{D}_\mu\right)\psi(z), \quad (8.25)$$

where

$$\vec{D}_\mu f(z) = \frac{U_\mu(z)f(z+a\hat{\mu}) - f(z)}{a}, \quad f(z)\vec{D}_\mu = \frac{f(z+a\hat{\mu})U_\mu^\dagger(z) - f(z)}{a}. \quad (8.26)$$

The key point is that the derivative operators in Eq. (8.25) are of dimension four and hence only appear in the LPT expansion at $\mathcal{O}(a^2)$ and higher [311]. Therefore, the $\mathcal{O}(a)$ contributions are the same for the Compton amplitude with conserved current and the local current (not including the Z_V renormalisation factor).

Therefore, if we define the lattice Compton amplitude as

$$T_{\mu\nu}^{\text{latt}} = T_{\mu\nu}^{\text{cont}} + \underbrace{T_{\mu\nu}^{(1)}}_{\mathcal{O}(a)} + \underbrace{T_{\mu\nu}^{(2)}}_{\mathcal{O}(a^2)} + \dots \quad (8.27)$$

then the relevant $\mathcal{O}(a)$ correction for a quark of flavour f , $\mu = \nu = 3$ and $q_3 = 0$, using the LPT expansion in Ref. [254], is**

$$T_{33}^{(1),f}(a, q) = \frac{2a}{\widehat{Q}^2} \sum_{\sigma} (\cos(aq_\sigma) - 1) \langle P | \bar{\psi}_f \psi_f | P \rangle, \quad (8.28)$$

** Calling this contribution $\mathcal{O}(a)$ is slightly confusing since it has the form $a(1 + \mathcal{O}(a^2|q|^2))$. However, since $|q| \propto 1/a$, the whole expression is $\mathcal{O}(a)$. These $a|q|$ terms are suppressed by $1/N_L$.

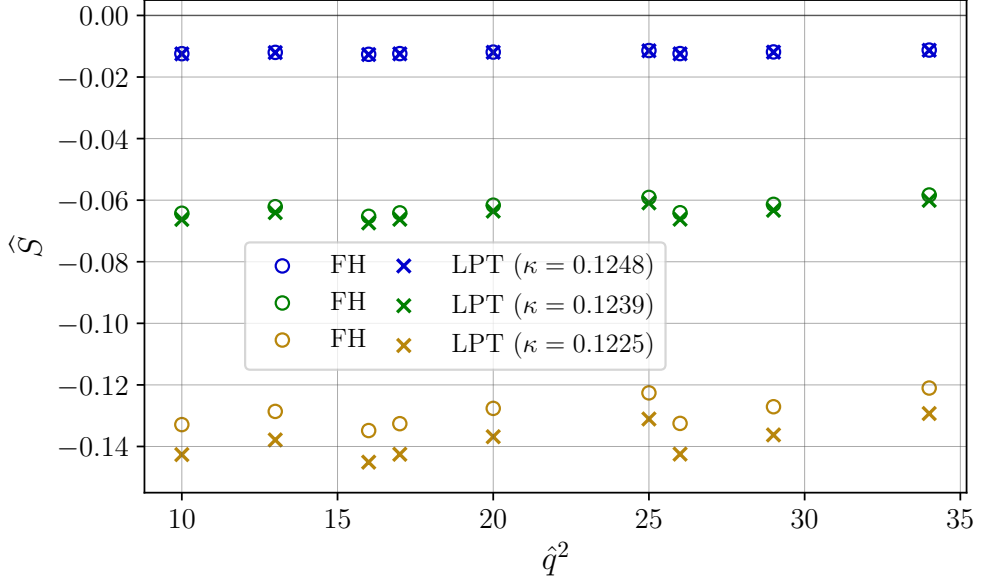


Figure 8.13: The $\omega = 0$ contribution to the structureless fermion Compton amplitude on the lattice, using numerical Feynman-Hellmann results for the local current (circles) and the analytic $\mathcal{O}(a)$ corrections in Eq. (8.28) (crosses).

where

$$\hat{Q}^2 = \sum_{\sigma} \sin(aq_{\sigma})^2 + \left(\sum_{\sigma} (\cos(aq_{\sigma}) - 1) \right)^2. \quad (8.29)$$

Note that the scalar charge here is for the bare (unrenormalised) operator. For the full expression see Ref. [254], Eq. (3.3).

In Eq. (8.28), we also have the matrix element $\langle p | \bar{\psi}_f \psi_f | p \rangle = 2E_p a_S$, where a_S is the scalar charge. For the structureless fermion $a_S = 1 + \mathcal{O}(a)$. It is straightforward to calculate a_S for structureless Wilson fermions—see Appendix I. For the nucleon, we use $\langle P | \bar{\psi}_f \psi_f | P \rangle = 2E_N a_S^f$, where a_S is the scalar charge. We use a_S calculated for the $32^3 \times 64$ lattice [174].

Comparison to numerical results

We start with the structureless fermion. Since the continuum result for $\omega = 0$ vanishes for the structureless fermion, Eq. (8.14), all non-zero contributions must be lattice artefacts. As such, we compare the three finest discretisations $\kappa = 0.1248, 0.1239, 0.1225$ to the $\mathcal{O}(a)$ LPT expansion given in Eq. (8.28).

In Figs. 8.13 and 8.14, we observe very good agreement between the LPT expansion and the numerical Feynman-Hellmann for the finest discretisations, $\kappa = 0.1248, 0.1239, 0.1225$. Moreover, for all results the analytic expansion appears to match the ‘jitters’ of the numerical results with remarkable accuracy.

However, in Fig. 8.14, we can see that for coarser discretisations, $am \gtrsim 0.2$, there is a notable divergence between the LPT and our numerical results. This suggests significant $\mathcal{O}(a^2)$ contributions, which are not included in the LPT results to the order we choose.

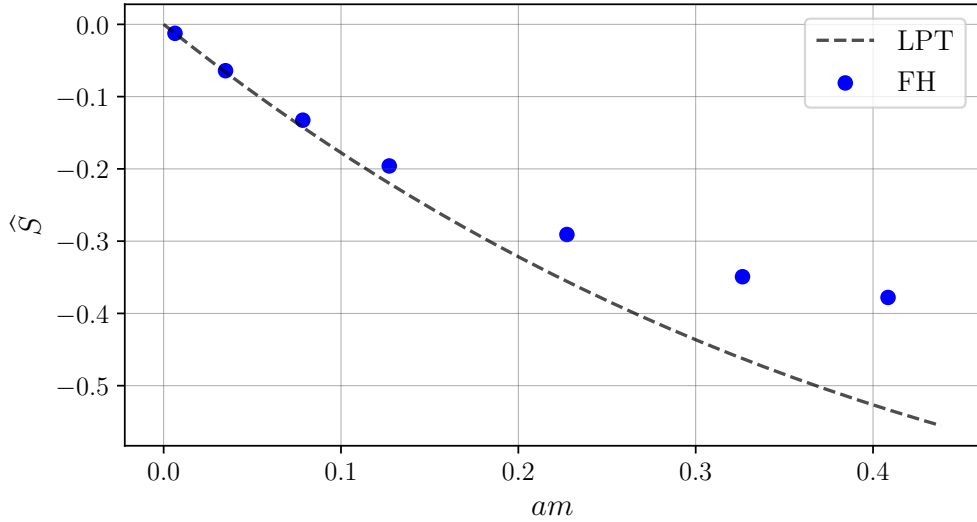


Figure 8.14: Structureless fermion subtraction function for $\hat{q}^2 = 26$ as a function of am (the pole mass), compared to the $\mathcal{O}(a)$ LPT correction. Note that this LPT correction is not simply linear in am , since we include corrections from the scalar charge—see Appendix I.

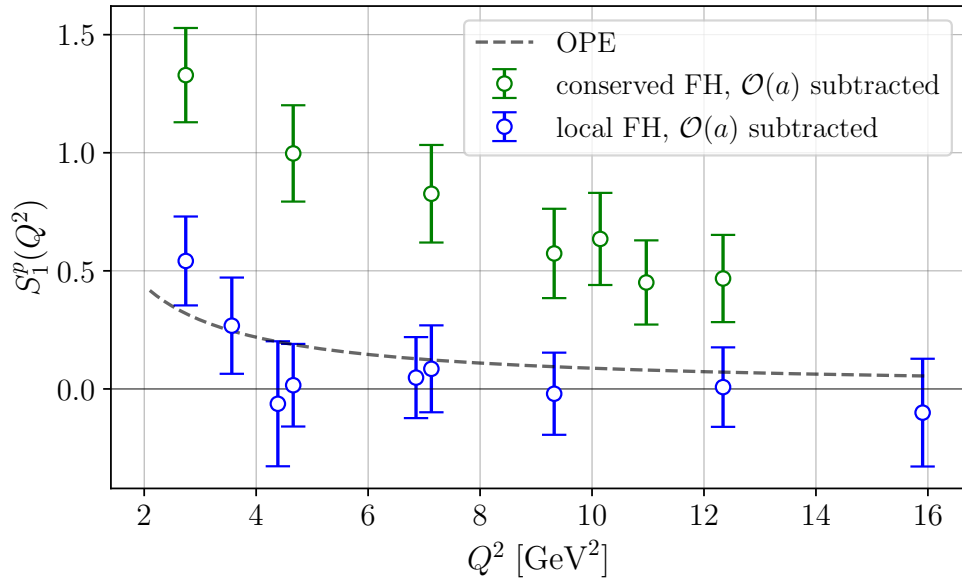


Figure 8.15: The Compton amplitude subtraction function for local and conserved currents calculated on the $32^3 \times 64$ lattice [37,40,178]. The $\mathcal{O}(a)$ LPT term is subtracted from our Feynman-Hellmann result as in Eq. (8.30). See Appendix I.1 for details of OPE prediction, the dashed line.

We need to be wary in extrapolating these results to the nucleon case. Nonetheless it seems that for structureless fermions, even at relatively coarse discretisations, the $\mathcal{O}(a)$ correction from the LPT result account for most of the lattice artefact.

For the numerical results of the nucleon, we perform an $\mathcal{O}(a)$ improvement on the conserved and local Compton amplitudes. The definition for this improvement, in terms of the quantities in Eqs. (8.28) and (8.27), are

$$T_{\mu\nu}^{\text{csv-imp}} = T_{\mu\nu}^{\text{csv}} - T_{\mu\nu}^{(1)}, \quad T_{\mu\nu}^{\text{loc-imp}} = T_{\mu\nu}^{\text{loc}} - Z_V^2 T_{\mu\nu}^{(1)}, \quad (8.30)$$

where we drop the seagull contribution from the LPT term for the conserved as well. Recall that we have to multiply the LPT corrections by Z_V^2 for the local current.

We plot this comparison in Fig. 8.15. Again, we compare this to the OPE prediction from Ref. [291]; see Appendix I for more details on the calculation of the OPE prediction. We observe that the local current results match the predicted OPE very well, while the conserved results are still not consistent with the OPE.

Lattice perturbation theory for interlacing results

Finally, we can estimate the $\mathcal{O}(a)$ corrections as performed above for the interlacing results. To do so requires altering the LPT result in Eq. (8.28) in a straightforward way.

We start by rewriting Eq. (8.28) as

$$T_{33}^{(1),f}(a, q) = \mathcal{C}(q) \langle P | \bar{\psi}_f \psi_f | P \rangle, \quad (8.31)$$

where \mathcal{C} is the coefficient given by

$$\mathcal{C}(q) = \frac{2a}{\widehat{Q}^2} \sum_{\sigma} (\cos(aq_{\sigma}) - 1). \quad (8.32)$$

To adapt this to the interlacing results then we only need to alter $\mathcal{C}(q)$, since this is the only part that depends on q , while the operator is local and hence unaffected by interlacing.

To alter this $\mathcal{C}(q)$, we first Fourier transform to a mixed time-momentum space:

$$\tilde{\mathcal{C}}(\mathbf{q}, \Delta t) = \sum_{q_4} e^{-iq_4 \Delta t} \mathcal{C}(\mathbf{q}, q_4). \quad (8.33)$$

See Appendix A for definitions of discrete Fourier transforms.

We can then find the $\mathcal{C}(q)$ coefficient for the interlaced results by taking the inverse Fourier transform except with Δt starting from $a\tau_{\min}$ instead of zero:

$$\mathcal{C}^{(\tau_{\min})}(\mathbf{q}, q_4) = \sum_{\Delta t=a\tau_{\min}}^{T-a} e^{iq_4 \Delta t} \tilde{\mathcal{C}}(\mathbf{q}, \Delta t). \quad (8.34)$$

Then, we can perform the subtraction of the $\mathcal{O}(a)$ corrections:

$$T_{33}^{\text{imp}}(q, \tau_{\min}) = T_{33}(q, \tau_{\min}) - Z_V^2 \mathcal{C}^{(\tau_{\min})}(q) \langle P | \bar{\psi}_f \psi_f | P \rangle. \quad (8.35)$$

The results for $\tau_{\min} = 0, 1, 2$ are plotted in Fig. 8.16. We note that compared to the initial interlacing results, Fig. 8.11, the three interlacings agree quite well with each other

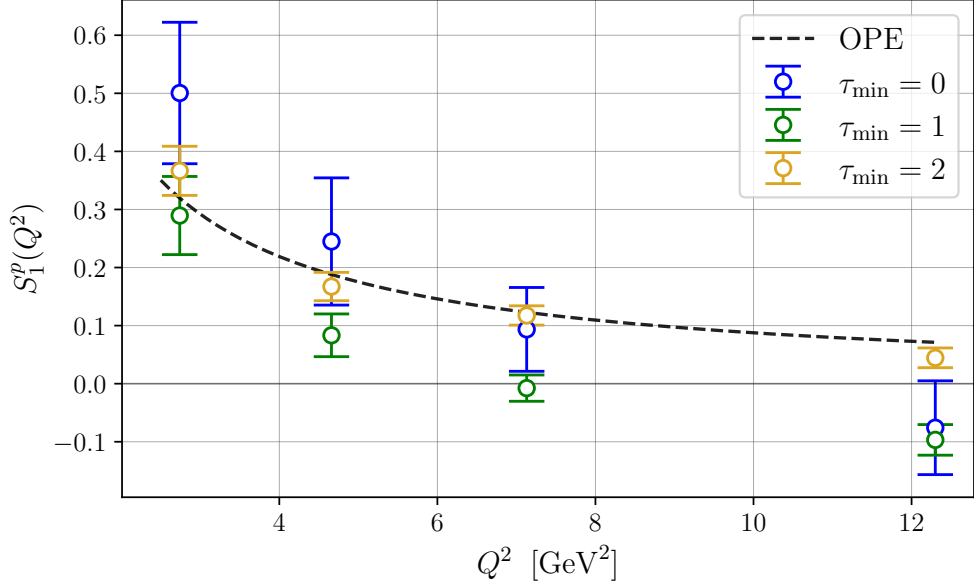


Figure 8.16: Comparison of proton subtraction function for all three interlacings, which have the $\mathcal{O}(a)$ corrections subtracted off according to Eq. (8.35). The dashed grey line is the OPE prediction from the calculation in Appendix I. Note that all the results in this figure, including the $\tau_{\min} = 0$, are for 200 configurations only and hence different to those in Fig. 8.15.

and with the OPE expectation. In particular, the $\tau_{\min} = 2$ results show strong agreement with the OPE prediction. This suggests that the discretisation artefacts are largely under control with a combination of the interlacing results and the LPT improvement. Finally, we note that it is somewhat strange that there is no obvious trend in the results of Fig. 8.16 as τ_{\min} increases. This could possibly be due to opposing signs in the $\mathcal{O}(a^2)$ and $\mathcal{O}(a^3)$ terms, which become the dominant lattice artefacts once the $\mathcal{O}(a)$ is removed. Moreover, as our results are only for 200 configurations, a more high statistics calculation with multiple gauge ensembles would be necessary before further comment on such a trend is made.

Nonetheless the results presented in Fig. 8.16 are very encouraging, with further work needed to ensure that discretisation artefacts are fully controlled: extending the LPT expansion to $\mathcal{O}(a^2)$, and calculations on different gauge configurations would both improve our degree of certainty in these results.

Finally, we note that, given the success of applying LPT in the case of the subtraction function, we could also use the LPT result to account for $\mathcal{O}(a|\mathbf{p}|)$ and $\mathcal{O}(a|\mathbf{q}|)$ kinematic artefacts. Such artefacts are likely responsible for the anomalous large ω and $\bar{\omega}$ behaviour as seen in Chapters 6 and 7. As such, applying LPT to these artefacts could significantly improve our extractions of the forward and off-forward amplitudes, and in turn the parton distributions themselves.

8.3 Conclusion and Outlook

In this chapter we have investigated the Compton amplitude subtraction function, focusing on its anomalous high-energy behaviour, which violates predictions from the operator product expansion. Using the structureless fermion as a playground, we showed that there are significant lattice artefacts to this Compton amplitude that could account for this OPE-breaking behaviour.

Although these artefacts vanish in the continuum limit, such a limit is very expensive for the nucleon case. Therefore, we designed an alternative implementation of Feynman-Hellmann, temporal interlacing, that allowed us to test for these artefacts without taking extremely fine lattice spacings. The temporal interlacing results confirmed the existence of large lattice artefacts for $S_1(Q^2)$, and moreover showed that almost all the OPE-breaking could be attributed to short-distance lattice artefacts. On the other hand, the temporal interlacing had only minimal effect on the ω dependent part of the Compton structure functions.

Finally, we compared the results of an $\mathcal{O}(a)$ lattice perturbation theory calculation [254] to our results. For the structureless fermion results at finer discretisations, these $\mathcal{O}(a)$ corrections were a very good description, but for coarser results they diverged. We performed an $\mathcal{O}(a)$ improvement to the local and conserved Compton subtraction functions. To bring both the interlacing and the LPT together, we performed the $\mathcal{O}(a)$ improvement on the interlacing results, which showed strong agreement among the interlacings and with the OPE prediction. While this indicates that discretisation artefacts are largely under control, further work—extending the LPT to $\mathcal{O}(a^2)$ and calculations on different gauge ensembles—would improve our certainty in this result.

Another approach not explored in this chapter to control such short-distance artefacts is to perform the calculation with gradient flowed gauge links. It has been shown analytically that this method can control short-distance artefacts in quasi-parton distributions [312,313] and for coordinate space current products [117]. Test calculations with gradient flow for hadronic observables have been performed by the CSSM/QCDSF collaboration [314], with an extension to the Compton amplitude an aim of future work.

A first principles calculation of the Compton amplitude subtraction function would be of great physical interest for a number of reasons:

1. Our calculation is best suited for $Q^2 \in [2, 12]$ GeV², a range that is inaccessible for effective theory and non-relativistic calculations, but also a range in which we cannot necessarily assume only perturbative contributions are significant. As such, results from lattice Feynman-Hellmann are well positioned to fill in the gaps of our understanding of $S_1(Q^2)$.
2. Since both the Cottingham sum rule and the two-photon exchange term (Eqs. (8.1) and (8.2), respectively) require an integral over q , this intermediate range of Q^2 is necessary for evaluations of the proton–neutron mass difference and the hadronic backgrounds to the proton charge radius. Hence our results could improve determinations of the proton–neutron mass difference and help clarify the proton charge radius puzzle.
3. Finally, we could extend our control of systematics to the off-forward subtraction function. The off-forward case is of great interest as it is an input for experimental

measurements of the D -term, which gives access to the proton pressure distribution among other quantities. As such, a determination of the off-forward subtraction function could help make experimental determinations of the D -term more model-independent and accurate.

Moreover, it is possible that the path to control discretisation artefacts discussed here could help control the anomalous large ω behaviour presented in Chapters 6 and 7, and thereby improve our determinations of parton distributions and their moments.

As such, the work in this chapter represents the first steps towards a lattice QCD determination of the Compton amplitude subtraction function, as well as the first steps in controlling short-distance discretisation artefacts that may affect our determination of parton distributions.

Conclusion and Outlook

In this thesis, we have shown that the Feynman-Hellmann method is a versatile and powerful framework, capable of determining the Compton amplitude in lattice QCD for both off-forward and forward kinematics, as well as polarised and unpolarised contributions. The calculation of the Compton amplitude from first principles has enormous potential, allowing us to determine parton distributions, which complement existing efforts in quasi- and pseudo-distribution frameworks. In addition, a determination of the Compton amplitude allows us to access information, such as the scaling, which has direct relevance to experiment. While the work presented here demonstrates the potential of the Feynman-Hellmann Compton amplitude approach, we have also exposed major sources of systematic error, and discussed various methods to control them. As such, this work breaks new ground for our method, allowing for the calculation of new quantities and developing techniques to control systematics.

In Chapters 5 and 6 we investigated the unpolarised off-forward Compton amplitude (OFCA), performing the first calculation of this amplitude in lattice QCD. Since there was previously no suitable parameterisation of the OFCA in the literature, our first step was to derive such a parameterisation. We then applied this to a proof-of-concept calculation, which was published in Ref. [39]. This initial calculation, however, was fairly limited as we could not separate the helicity-conserving or -flipping amplitudes, \mathcal{H} and \mathcal{E} , respectively. In Chapter 6, we significantly improved upon this calculation, and showed how to separate \mathcal{H}_1 and \mathcal{E}_1 . We calculated these amplitudes for zero-skewness kinematics and $t \approx -0.3, -0.6 - 1.1 \text{ GeV}^2$. We determined their leading moments, which agreed well with three-point calculations at a similar pion mass and volume. While this is encouraging, we also saw the limits of the present method: both the higher moments and a model-dependent reconstruction of the GPD yielded results at odds with experimental determinations. We argued that lattice artefacts affecting the large $\bar{\omega}$ results are to blame for our inability to go beyond the leading moments.

Similarly, in Chapter 7 we performed the first lattice QCD calculation of the polarised forward Compton amplitude. Using analogous methods to the off-forward calculation, we separated the $\tilde{g}_{1,2}$ amplitudes, and determined their moments. As with the off-forward case, our leading Mellin moments showed reasonable agreement with phenomenology, but the higher moments and large ω values appeared to be affected by artefacts. Unlike the off-forward case, however, we showed that these artefacts are enhanced by a system of equations with poor orthogonality in the separation of $\tilde{g}_{1,2}$. Therefore, we outlined a path for future work to improve this orthogonality, and thereby significantly improve our control of these artefacts.

Finally, in Chapter 8 we investigated lattice artefacts affecting the Compton amplitude subtraction function. To study and control these artefacts, we employed a range of tools: structureless fermion calculations, varying the discretisation of the Compton amplitude, and an analytic lattice perturbation theory (LPT) expansion. We showed that short-distance lattice artefacts are the *dominant contribution* to the subtraction function. However, we also showed that the ω dependent part of our amplitude is not as affected by these short-distance artefacts, and hence our previous results for the moments are not completely invalidated. Nonetheless, due to the dominance of these short-distance artefacts in our signal, controlling such artefacts is a priority in future calculations.

Even before major efforts are undertaken to control these artefacts, there are still quantities to explore with the Feynman-Hellmann Compton amplitude method:

- As we argued that the leading moments are largely unaffected by the short-distance artefacts, we could determine the \bar{Q}^2 dependence of the leading off-forward moments, as has been done in the forward case [38]. This would probe non-leading-twist contributions to the OFCA, which are not well-studied theoretically or experimentally.
- Since the polarised amplitudes appear less affected by short-distance artefacts, we can also pursue meaningful work here. By improving the separation of $\tilde{g}_{1,2}$ and determining these amplitudes over a range of Q^2 values, we can study a range of properties discussed in Chapter 7.
- Similarly, our methods could be extended to the polarised off-forward amplitudes, $\tilde{\mathcal{H}}$ and $\tilde{\mathcal{E}}$. This would give access to the polarised GPDs as well as an off-forward analogue of the d_2 structure [315].

To address Feynman-Hellmann specific systematics, there are a few major areas of interest:

- Controlling the short-distance lattice artefacts discussed in Chapter 8, using alternative implementations of Feynman-Hellmann such as temporal interlacing and Wilson flow [314], or analytic parameterisation that account for these artefacts.
- In terms of Euclidean time fitting, methods such as distillation and momentum smearing would allow us to access better signal for higher momenta [144, 252, 253], giving us a greater spread of ω values. Similarly, one could include Feynman-Hellmann excited states in these fits, as was done in Ref. [173].
- Finally, there is the inclusion of disconnected diagrams, which has previously been achieved in first-order Feynman-Hellmann [180]. Although these contributions are expected to be small, sea quark contributions to the Compton amplitude are of significant interest [316].

In addition, there are systematics that are not specific to Feynman-Hellmann, such as pion mass, lattice spacing and volume dependence, for which we have barely scratched the surface, and must be investigated before strong comparisons with experiment are made.

If the systematics can be sufficiently controlled, our method would realise its full potential: an accurate and completely first principles determination of the Compton amplitude and the wealth of physical information that would entail. The work in this thesis takes us closer to that goal, showing both our method's great promise and starting the project of addressing key systematics.

Definitions and Conventions

Here, we collect a few useful definitions and conventions used throughout this thesis.

Symmetrisation of Lorentz tensors

For symmetrisation and anti-symmetrisation of a rank-2 tensor, we use the convention

$$T^{\{\mu\nu\}} = \frac{1}{2}[T^{\mu\nu} + T^{\nu\mu}], \quad T^{[\mu\nu]} = \frac{1}{2}[T^{\mu\nu} - T^{\nu\mu}], \quad (\text{A.1})$$

while the general expression for a fully symmetrised rank- n tensor is

$$T^{\{\mu_1 \dots \mu_n\}} = \frac{1}{n!} \sum_{\sigma \in S_n} T^{\nu_{\sigma(1)} \dots \nu_{\sigma(n)}}, \quad (\text{A.2})$$

where S_n is the group of permutations of the numbers $1, 2, \dots, n$, and σ is an element of S_n . Here, we denote the i^{th} component of some group element, $\sigma \in S_n$, as $\sigma(i)$.

Continuum normalisations

In the continuum, we define the identity in the space of hadron states as

$$\mathbb{I} = \sum_{X,s} \int \frac{d^3p}{(2\pi)^3} \frac{1}{2E_X(\mathbf{p})} |X(\mathbf{p}, s)\rangle \langle X(\mathbf{p}, s)|, \quad (\text{A.3})$$

with the normalisation

$$\langle X(\mathbf{p}_1) | Y(\mathbf{p}_2) \rangle = (2\pi)^3 2E_X \delta^{(3)}(\mathbf{p}_1 - \mathbf{p}_2) \delta_{X,Y}. \quad (\text{A.4})$$

For the unique case of the vacuum, we have $\langle \Omega | \Omega \rangle = 1$.

For Fourier transforms, we use the convention

$$\tilde{f}(p) = \int d^4x e^{ip \cdot x} f(x), \quad f(x) = \int \frac{d^4p}{(2\pi)^4} e^{-ip \cdot x} \tilde{f}(p), \quad (\text{A.5})$$

for four-vectors p and x .

Hence the Dirac deltas are

$$\int d^4x e^{ip \cdot x} = (2\pi)^4 \delta^{(4)}(p), \quad \int d^4p e^{-ip \cdot x} = (2\pi)^4 \delta^{(4)}(x). \quad (\text{A.6})$$

Lattice normalisations

We define a coordinate space four-vector on the lattice

$$x_\mu = an_\mu \quad \text{for the elements of } n_\mu \text{ in } \{0, 1, \dots, N-1\},$$

where N is the number of lattice sites in a given dimension. Similarly, we define a momentum space four-vector

$$k_4 = \frac{2\pi}{L}m_4, \quad \mathbf{k}_i = \frac{2\pi}{aN}\mathbf{m}_i \quad \text{for the elements of } m_\mu \text{ in } \left\{-\frac{N}{2}+1, -\frac{N}{2}+2, \dots, \frac{N}{2}\right\}.$$

For the lattice results in this thesis we have $N_T = 2N_L$, where $N_{T,L}$ are the number of lattice sites for the temporal and spatial dimensions of the lattice.

Given these definitions, the Fourier transform for coordinate space is

$$\tilde{f}(p) = \sum_{x_\mu} e^{ip \cdot x} f(x) = a^4 \sum_{n_0=0}^{N_T-1} \sum_{\mathbf{n}_i=0}^{N_L-1} e^{i\frac{2\pi}{N_T}m_4n_4} e^{-i\frac{2\pi}{N_L}\mathbf{m} \cdot \mathbf{n}} F(n), \quad (\text{A.7})$$

since the measure of the sum for each spatial dimension is a .

Similarly, the momentum space Fourier transform is

$$\begin{aligned} f(x) &= \frac{1}{(2\pi)^4} \sum_{p_\mu} e^{-ip \cdot x} \tilde{f}(p) \\ &= \frac{1}{TL^3} \sum_{m_0=-N_T/2+1}^{N_T/2} \sum_{\mathbf{m}_i=-N_L/2+1}^{N_L/2} e^{-i\frac{2\pi}{N_T}m_4n_4} e^{i\frac{2\pi}{N_L}\mathbf{m} \cdot \mathbf{n}} \tilde{F}(m), \end{aligned} \quad (\text{A.8})$$

since the measure of the sum is $2\pi/L$ for the spatial sum, and $2\pi/T$ for the temporal. Note that the F functions above are simply the f functions, with their arguments transformed to be dimensionless integers.

Using a geometric series, it can be shown that the Kronecker delta is

$$\delta_{n,m} = \frac{1}{N} \sum_{k=0}^{N-1} e^{i\frac{2\pi k}{N}(n-m)} = \frac{1}{N} \sum_{k=-N/2+1}^{N/2} e^{i\frac{2\pi k}{N}(n-m)}, \quad (\text{A.9})$$

so long as $|n-m| < N$.

Hence, comparing to Eq. (A.6), the discrete equivalents of the Dirac deltas are

$$\delta^{(4)}(p) = \frac{1}{(2\pi)^4} \sum_{x_\mu} e^{ip \cdot x} = \frac{TL^3}{(2\pi)^4} \delta_{m,0}^{(4)}, \quad \delta^{(4)}(x) = \frac{1}{(2\pi)^4} \sum_{p_\mu} e^{-ip \cdot x} = \frac{1}{a^4} \delta_{n,0}^{(4)}, \quad (\text{A.10})$$

where $\delta_{m,0}^{(4)} = \delta_{m_1,0}\delta_{m_2,0}\delta_{m_3,0}\delta_{m_4,0}$, the four-dimensional Kronecker delta.

This keeps the normalisation in the space of states

$$\langle X(\mathbf{p}_1) | Y(\mathbf{p}_2) \rangle = 2E_X L^3 \delta_{\mathbf{m}_1, \mathbf{m}_2}^{(3)} \delta_{X,Y}. \quad (\text{A.11})$$

Analyticity of the Compton Amplitude

In this appendix we show how to derive dispersion relations for the scalar amplitudes of the Compton amplitude. For lattice calculations of the Compton amplitude these relations are particularly important, as they connect the $|\bar{\omega}| \lesssim 1$ region, which is accessible in Euclidean spacetime, to the physical $|\bar{\omega}| \gtrsim 1$ region. Here, we focus on off-forward kinematics, as it is straightforward to take $t = 0$ and recover the forward dispersion relations.

Analytic Region

To begin, we expand the time-ordering of the OFCA, defined in Eq. (2.72):

$$T^{\mu\nu} = i \int d^4z e^{i\bar{q}\cdot z} \left[\langle P' | j^\mu(z/2) j^\nu(-z/2) | P \rangle \Theta(z^0) + \langle P' | j^\nu(-z/2) j^\mu(z/2) | P \rangle \Theta(-z^0) \right], \quad (\text{B.1})$$

where Θ is the Heaviside step function. Inserting a complete set of states, and using the translation operator,

$$T^{\mu\nu} = \sum_X i \int \frac{d^3P_X}{(2\pi)^3} \frac{1}{2P_X^0} \int d^4z \left[e^{i(\bar{q} + \bar{P} - P_X)\cdot z} \langle P' | j^\mu(0) | X \rangle \langle X | j^\nu(0) | P \rangle \Theta(z^0) + e^{i(\bar{q} + P_X - \bar{P})\cdot z} \langle P' | j^\nu(0) | X \rangle \langle X | j^\mu(0) | P \rangle \Theta(-z^0) \right], \quad (\text{B.2})$$

where P_X is the four momentum of state $|X\rangle$. Now apply the definition of the Dirac delta:

$$T^{\mu\nu} = \sum_X (2\pi)^3 i \int \frac{d^3P_X}{(2\pi)^3} \frac{1}{2P_X^0} \int dz^0 \times \left[\delta^{(3)}(\bar{\mathbf{q}} + \bar{\mathbf{P}} - \mathbf{P}_X) e^{iz^0(\bar{q}^0 + \bar{P}^0 - P_X^0)} \langle P' | j^\mu(0) | X \rangle \langle X | j^\nu(0) | P \rangle \Theta(z^0) + \delta^{(3)}(\bar{\mathbf{q}} + \mathbf{P}_X - \bar{\mathbf{P}}) e^{iz^0(\bar{q}^0 + P_X^0 - \bar{P}^0)} \langle P' | j^\nu(0) | X \rangle \langle X | j^\mu(0) | P \rangle \Theta(-z^0) \right]. \quad (\text{B.3})$$

The integral representation of the step function is

$$\Theta(z^0) = \frac{1}{2\pi i} \lim_{\epsilon \rightarrow 0^+} \int_{-\infty}^{\infty} ds \frac{e^{isz^0}}{s - i\epsilon}, \quad (\text{B.4})$$

where we evaluate Eq. (B.4) with a semi-circle contour in the upper half of the complex plane, whose radius goes to infinity. Then,

$$\Theta(z^0) = \lim_{\epsilon \rightarrow 0^+} \begin{cases} e^{-\epsilon z^0} & \text{if } z^0 > 0 \\ 0 & \text{if } z^0 < 0, \end{cases} \quad (\text{B.5})$$

$$\Theta(-z^0) = \lim_{\epsilon \rightarrow 0^+} \begin{cases} 0 & \text{if } z^0 > 0 \\ e^{\epsilon z^0} & \text{if } z^0 < 0. \end{cases} \quad (\text{B.6})$$

Now we can evaluate Eq. (B.3):

$$\int_{-\infty}^{\infty} dz^0 e^{iz^0(\bar{q}^0 + \bar{P}^0 - P_X^0)} \Theta(z^0) = \frac{-i}{P_X^0 - \bar{q}^0 - \bar{P}^0 - i\epsilon}, \quad (\text{B.7})$$

$$\int_{-\infty}^{\infty} dz^0 e^{iz^0(\bar{q}^0 - \bar{P}^0 + P_X^0)} \Theta(-z^0) = \frac{-i}{P_X^0 + \bar{q}^0 - \bar{P}^0 - i\epsilon}, \quad (\text{B.8})$$

where from now on we suppress the limit $\epsilon \rightarrow 0^+$. Putting Eqs. (B.7) and (B.8) into Eq. (B.3), we get

$$\begin{aligned} T^{\mu\nu}(P, q; P', q') = \sum_X & \left[\frac{\langle P' | j^\mu(0) | X(\mathbf{P} + \mathbf{q}) \rangle \langle X(\mathbf{P} + \mathbf{q}) | j^\nu(0) | P \rangle}{2P_X^0(P_X^0 - (P^0 + q^0) - i\epsilon)} \right. \\ & \left. + \frac{\langle P' | j^\nu(0) | X(\mathbf{P} - \mathbf{q}') \rangle \langle X(\mathbf{P} - \mathbf{q}') | j^\mu(0) | P \rangle}{2P_X^0(P_X^0 - (P^0 - q'^0) - i\epsilon)} \right]. \end{aligned} \quad (\text{B.9})$$

Therefore, we have discontinuities in our amplitude where the intermediate state goes on-shell: at $P_X^0 = P^0 + q^0$ or $P_X^0 = P^0 - q'^0$.

In the incoming nucleon's rest frame, this becomes

$$(P_X^0)^2 = (P^0 + q^0)^2 \quad \Rightarrow \quad m_X^2 + \mathbf{q}^2 = m_N^2 + 2q^0 m_N + (q^0)^2 \quad \Rightarrow \quad m_X^2 = (P + q)^2.$$

Similarly,

$$(P_X^0)^2 = (P^0 - q'^0)^2 \quad \Rightarrow \quad m_X^2 + \mathbf{q}'^2 = m_N^2 - 2q'^0 m_N + (q'^0)^2 \quad \Rightarrow \quad m_X^2 = (P - q')^2.$$

Hence the discontinuities are where the invariant mass of the intermediate state is $m_X^2 = (P + q)^2$ or $m_X^2 = (P - q')^2$. We can use this to determine the kinematic discontinuities of each the amplitudes, \mathcal{A} , in Eq. (5.11). We assume that the momentum transfers, t and \bar{Q}^2 , are fixed, and investigate the cuts in the variables $\bar{\omega}$ and ϑ ; see Eq. (2.74) for definitions of the kinematic scalars.

Since the nucleon is the ground state, we have that $m_X^2 \geq m_N^2$. Therefore, $m_X^2 = (P + q)^2$ implies

$$m_X^2 = (P + q)^2 = (\bar{P} + \bar{q})^2 = \bar{P}^2 + 2\bar{P} \cdot \bar{q} - \bar{Q}^2 = -\bar{Q}^2 \left(1 + \frac{t}{4\bar{Q}^2} - \bar{\omega}\right) + m_N^2 \geq m_N^2, \quad (\text{B.10})$$

and $m_X^2 = (P - q')^2$ implies

$$m_X^2 = (P - q')^2 = (\bar{P} - \bar{q}')^2 = \bar{P}^2 - 2\bar{P} \cdot \bar{q}' - \bar{Q}^2 = -\bar{Q}^2 \left(1 + \frac{t}{4\bar{Q}^2} + \bar{\omega}\right) + m_N^2 \geq m_N^2, \quad (\text{B.11})$$

where we have used $\bar{P}^2 = m_N^2 - t/4$. Therefore, we have the relation

$$-\bar{Q}^2\left(1 + \frac{t}{4\bar{Q}^2} \pm \bar{\omega}\right) \geq 0 \quad (\text{B.12})$$

If we assume that \bar{Q}^2 is fixed, then Eq. (B.12) implies that there are discontinuities in the $\bar{\omega}$ plane for

$$|\bar{\omega}| \geq 1 + t/(4\bar{Q}^2). \quad (\text{B.13})$$

Similarly, we can hold $\bar{\omega}$ fixed in Eq. (B.12) to derive cuts in ϑ . If we have $\bar{\omega} > 1 + t/(4\bar{Q}^2)$ and $-\bar{Q}^2(1 + \frac{t}{4\bar{Q}^2} - \bar{\omega}) \leq 0$, this implies that $\bar{Q}^2 \geq 0$, which implies that

$$-\frac{1}{4}(q^2 + 2q \cdot q' + q'^2) \geq 0 \quad \Rightarrow \quad q^2 + q'^2 \leq \frac{t}{2} < 0. \quad (\text{B.14})$$

Hence we must have $q^2 < 0$ and/or $q'^2 < 0$. These imply that

$$0 > q^2 = (\bar{q} + \Delta/2)^2 = t/4 + \Delta \cdot \bar{q} - \bar{Q}^2 \quad \Rightarrow \quad \vartheta < -1 + \frac{t}{4\bar{Q}^2}. \quad (\text{B.15})$$

$$0 < q'^2 = (\bar{q} - \Delta/2)^2 = t/4 - \Delta \cdot \bar{q} - \bar{Q}^2 \quad \Rightarrow \quad \vartheta > 1 - \frac{t}{4\bar{Q}^2}. \quad (\text{B.16})$$

However, since our lattice calculations in Chapters 5 and 6 focus on the $\vartheta = 0$ with $\bar{\omega} \neq 0$ case, we will also focus on the dispersion relation in $\bar{\omega}$.

Regge Behaviour

Recall in Chapter 5 that we quoted some results from Regge theory [213–215] that give us the behaviour of the scalar amplitudes of the Compton amplitude as a function of

$$\nu = \frac{\bar{P} \cdot \bar{q}}{m_N}. \quad (\text{B.17})$$

To repeat these results: at fixed t and \bar{Q}^2 , we have that

$$\mathcal{H}_1, \mathcal{E}_1, \mathcal{K}_6 \sim \nu^{\alpha_M(t)}, \quad \text{all other amplitudes} \sim \nu^{\alpha_M(t)-1}, \nu^{\alpha_M(t)-2}, \text{ or } \nu^{\alpha_M(t)-3}, \quad (\text{B.18})$$

where $\alpha_M(t) \lesssim 0.5$. Since $\bar{\omega} = m_N \nu / \bar{Q}^2$, at fixed \bar{Q}^2 the amplitudes have the behaviour

$$\lim_{\bar{\omega} \rightarrow \infty} \mathcal{H}_1, \mathcal{E}_1, \mathcal{K}_6 \longrightarrow \infty, \quad \text{while} \quad \lim_{\bar{\omega} \rightarrow \infty} \mathcal{A} \longrightarrow 0, \quad (\text{B.19})$$

for all other amplitudes.

Unsubtracted Dispersion Relation

The amplitudes defined in Ref. [215] are all even functions of $\bar{\omega}$. However, for the amplitudes that go like $\nu^{\alpha_M(t)-2}$ or $\nu^{\alpha_M(t)-3}$, we can factor out $1/\bar{P} \cdot \bar{q}$, and get that these amplitudes still behave like $\nu^{\alpha_M(t)-1}$ or $\nu^{\alpha_M(t)-2}$. Hence even with this factor taken out, they still vanish as $\bar{\omega} \rightarrow 0$. Moreover, by taking out a factor of $1/\bar{P} \cdot \bar{q}$, they become odd functions of $\bar{\omega}$, which is important for their dispersion relations.

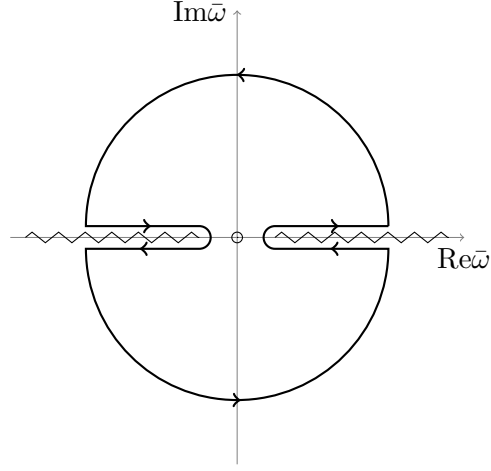


Figure B.1: Contour the dispersion relations in $\bar{\omega}$. The cuts on the real axis start at $\bar{\omega} \approx 1$. The radius of the contour is taken to infinity.

Here, we derive a dispersion relation for the amplitudes that have a $1/\bar{P} \cdot \bar{q}$ factored out—see Eq. (5.11). These are $\tilde{\mathcal{H}}_{1,2}$, $\tilde{\mathcal{E}}_{1,2}$, and $\mathcal{H}_{2,3}$, \mathcal{E}_2 . We note that, in the forward limit,

$$\mathcal{H}_2 + \mathcal{H}_3 \xrightarrow{t \rightarrow 0} \mathcal{F}_2, \quad \tilde{\mathcal{H}}_{1,2} \xrightarrow{t \rightarrow 0} \tilde{g}_{1,2}, \quad (\text{B.20})$$

where we studied the latter two in Chapter 7.

To derive a dispersion relation for these amplitudes, recall from Eq. (B.13) that these amplitudes have cuts for $|\bar{\omega}| \geq 1 + t/(4\bar{Q}^2)$. Here, we will drop the $t/(4\bar{Q}^2)$ corrections as these are highly suppressed for our kinematics.

We consider an amplitude $\mathcal{A}(\bar{\omega}_0, t, \bar{Q}^2)$ at some fixed values of the momentum transfer variables t, \bar{Q}^2 , which is odd under $\bar{\omega} \rightarrow -\bar{\omega}$ and which vanishes as $\bar{\omega} \rightarrow \infty$. We can take $\bar{\omega}$ as a complex variable by analytic continuation. Then, for $\bar{\omega}_0$ real and $|\bar{\omega}_0| \leq 1$, we apply Cauchy's theorem for a contour \mathcal{C} , with a radius less than one, centered at the origin:

$$\mathcal{A}(\bar{\omega}_0, t, \bar{Q}^2) = \frac{1}{2\pi i} \oint_{\mathcal{C}} d\bar{\omega} \frac{\mathcal{A}(\bar{\omega}, t, \bar{Q}^2)}{\bar{\omega} - \bar{\omega}_0}. \quad (\text{B.21})$$

To evaluate this integral we transform \mathcal{C} into the contour given in figure B.1. Letting the contour along the cuts be a distance $\epsilon > 0$ above or below the real axis, we can write Eq. (B.21) as

$$\begin{aligned} \mathcal{A}(\bar{\omega}_0, t, \bar{Q}^2) = & \frac{1}{2\pi i} \left[\int_1^\infty d\bar{\omega} \frac{\mathcal{A}(\bar{\omega} + i\epsilon, t, \bar{Q}^2) - \mathcal{A}(\bar{\omega} - i\epsilon, t, \bar{Q}^2)}{\bar{\omega} - \bar{\omega}_0} \right. \\ & \left. + \int_{-\infty}^{-1} d\bar{\omega} \frac{\mathcal{A}(\bar{\omega} + i\epsilon, t, \bar{Q}^2) - \mathcal{A}(\bar{\omega} - i\epsilon, t, \bar{Q}^2)}{\bar{\omega} - \bar{\omega}_0} \right] + \text{arc contributions}. \end{aligned} \quad (\text{B.22})$$

Now we let $\bar{\omega} \rightarrow -\bar{\omega}$ in the second integral. For simplicity we suppress the t, \bar{Q}^2 arguments:

$$\begin{aligned} \mathcal{A}(\bar{\omega}_0) = & \frac{1}{2\pi i} \left[\int_1^\infty d\bar{\omega} \frac{\mathcal{A}(\bar{\omega} + i\epsilon) - \mathcal{A}(\bar{\omega} - i\epsilon)}{\bar{\omega} - \bar{\omega}_0} \right. \\ & \left. + \int_\infty^1 d\bar{\omega} \frac{-\mathcal{A}(-\bar{\omega} + i\epsilon) + \mathcal{A}(-\bar{\omega} - i\epsilon)}{-\bar{\omega} - \bar{\omega}_0} \right] + \text{arcs}, \end{aligned} \quad (\text{B.23})$$

where we have used the fact that these amplitudes are odd under $\bar{\omega} \rightarrow -\bar{\omega}$. Hence $\mathcal{A}(\bar{\omega}_0, t, \bar{Q}^2) = -\mathcal{A}(-\bar{\omega}_0, t, \bar{Q}^2)$. Moreover, since \mathcal{A} vanishes for $\bar{\omega} \rightarrow \infty$, the arc contributions must vanish. Therefore, Eq. (B.23) becomes

$$\mathcal{A}(\bar{\omega}_0) = \frac{1}{2\pi i} \int_1^\infty d\bar{\omega} [\mathcal{A}(\bar{\omega} + i\epsilon) - \mathcal{A}(\bar{\omega} - i\epsilon)] \left(\frac{1}{\bar{\omega} - \bar{\omega}_0} - \frac{1}{\bar{\omega}_0 + \bar{\omega}} \right). \quad (\text{B.24})$$

The Schwarz reflection principle states that a function with real number boundary value on the real axis has the property $f^*(z) = f(z^*)$ [317]. Therefore, by the Schwarz reflection principle $\mathcal{A}(\bar{\omega}_0 + i\epsilon) - \mathcal{A}(\bar{\omega}_0 - i\epsilon) = 2i\text{Im}[\mathcal{A}(\bar{\omega}_0 + i\epsilon)]$, and hence we will define a spectral function: $2\pi\rho(\bar{\omega} + i\epsilon) = \text{Im}[\mathcal{A}(\bar{\omega} + i\epsilon)]$.

Therefore,

$$\mathcal{A}(\bar{\omega}_0) = 2 \int_1^\infty d\bar{\omega} \rho(\bar{\omega}) \left(\frac{1}{\bar{\omega} - \bar{\omega}_0} - \frac{1}{\bar{\omega}_0 + \bar{\omega}} \right) = 2 \int_1^\infty d\bar{\omega} \rho(\bar{\omega}) \frac{2\bar{\omega}_0}{\bar{\omega}^2 - \bar{\omega}_0^2}. \quad (\text{B.25})$$

Using the substitution $x = 1/\bar{\omega}$, we get

$$\mathcal{A}(\bar{\omega}_0) = 4\bar{\omega}_0 \int_0^1 dx \frac{\tilde{\rho}(x)}{1 - x^2\bar{\omega}_0^2}. \quad (\text{B.26})$$

In the case of forward kinematics, we can use the optical theorem, $2\pi g_{1,2} = \text{Im}\tilde{g}_{1,2}$ the spectral function $\tilde{\rho}$ can be identified with one of the deep-inelastic scattering structure functions: F_2 or $g_{1,2}$. Hence we derive Eqs. (2.27) and (2.54).

However, in the off-forward case we cannot use the optical theorem. Therefore, for instance, the dispersion relation for \mathcal{H}_2 is just

$$\mathcal{H}_2(\bar{\omega}_0, t, \bar{Q}^2) = \frac{2}{\pi} \bar{\omega}_0 \int_0^1 dx \frac{\text{Im}\mathcal{H}_2(1/x, t, \bar{Q}^2)}{1 - x^2\bar{\omega}_0^2}. \quad (\text{B.27})$$

This is still a useful relation, as it allows us to relate the amplitude in the unphysical region that is accessible in Euclidean spacetime, to the physical region.

Subtracted Dispersion Relation

For the subtracted dispersion relation, we are considering amplitudes such as \mathcal{H}_1 and \mathcal{E}_1 , which are even functions under $\bar{\omega} \rightarrow -\bar{\omega}$, and which do not vanish as $\bar{\omega} \rightarrow \infty$.

We repeat all the steps that got us to Eq. (B.22) in the unsubtracted case:

$$\begin{aligned} \mathcal{A}(\bar{\omega}_0, t, \bar{Q}^2) = & \frac{1}{2\pi i} \left[\int_1^\infty d\bar{\omega} \frac{\mathcal{A}(\bar{\omega} + i\epsilon, t, \bar{Q}^2) - \mathcal{A}(\bar{\omega} - i\epsilon, t, \bar{Q}^2)}{\bar{\omega} - \bar{\omega}_0} \right. \\ & \left. + \int_{-\infty}^{-1} d\bar{\omega} \frac{\mathcal{A}(\bar{\omega} + i\epsilon, t, \bar{Q}^2) - \mathcal{A}(\bar{\omega} - i\epsilon, t, \bar{Q}^2)}{\bar{\omega} - \bar{\omega}_0} \right] + \text{arc contributions}. \end{aligned} \quad (\text{B.28})$$

Now we let $\bar{\omega} \rightarrow -\bar{\omega}$ in the second integral, and use the Schwarz reflection principle to get

$$\mathcal{A}(\bar{\omega}_0) = 2 \int_1^\infty d\bar{\omega} \rho(\bar{\omega}) \left(\frac{1}{\bar{\omega} - \bar{\omega}_0} + \frac{1}{\bar{\omega}_0 + \bar{\omega}} \right) + \text{arcs}, \quad (\text{B.29})$$

where we have again defined $2\pi\rho(\bar{\omega} + i\epsilon) = \text{Im}[\mathcal{A}(\bar{\omega} + i\epsilon)]$.

Unlike the case of the unsubtracted dispersion relation, the arc contributions do not disappear on their own. Therefore, we wish to remove these contributions so that we will have a relationship between the amplitude in the unphysical region and the amplitude in the physical, without the appearance of the unknown arc contributions. As such, we note that the $\bar{\omega} = 0$ contribution is

$$\mathcal{A}(0) = 2 \int_1^\infty d\bar{\omega} \frac{2\rho(\bar{\omega})}{\bar{\omega}} + \text{arcs}. \quad (\text{B.30})$$

Therefore, we can remove the arc contributions:

$$\begin{aligned} \mathcal{A}(\bar{\omega}_0) - \mathcal{A}(0) &= 2 \int_1^\infty d\bar{\omega} \rho(\bar{\omega}) \left(\frac{1}{\bar{\omega} - \bar{\omega}_0} + \frac{1}{\bar{\omega}_0 + \bar{\omega}} - \frac{2}{\bar{\omega}} \right) \\ &= 4\bar{\omega}_0^2 \int_1^\infty d\bar{\omega} \frac{\rho(\bar{\omega})}{\bar{\omega}(\bar{\omega}^2 - \bar{\omega}_0^2)}. \end{aligned} \quad (\text{B.31})$$

Substituting the variable $x = 1/\bar{\omega}$, we get

$$\mathcal{A}(\bar{\omega}_0) - \mathcal{A}(0) = 4\bar{\omega}_0^2 \int_0^1 dx x \frac{\tilde{\rho}(x)}{1 - (\bar{\omega}_0 x)^2}, \quad (\text{B.32})$$

which is the form of the subtracted dispersion relations such as Eqs. (2.26) and (5.18).

Again, in the case of \mathcal{F}_1 , the forward Compton structure function, $\tilde{\rho} = F_1$, the deep-inelastic structure function. However, for the off-forward case, we do not have this relationship.

Operator Product Expansion

In Chapter 2 we discussed the operator product expansion (OPE) in QCD and its application to deep-inelastic scattering. Then, in Chapter 5 we performed a leading-order OPE on the nucleon off-forward Compton amplitude. In this chapter, we discuss in greater detail the OPE relation, its justification, and the more formal method of applying it. Our discussion uses Refs. [47, 51, 318] as guides.

We start by assuming that the OPE relation,

$$A(z)B(0) \xrightarrow{z \rightarrow 0} \sum_i c_i(z) \mathcal{O}_i(0),$$

applies to the product of currents. Note that the OPE has been proven to all orders in perturbation theory [319]. However, for a matrix element where not all contributions are perturbative (such as QCD), the OPE is only a conjecture [320, 321]. Although there is no formal proof, the OPE has been extremely successful from a phenomenological perspective, and there are many good theoretical reasons to believe that the OPE relation holds in cases such as the Compton amplitude [322].

To apply the OPE to the time-ordered product of currents in the Compton amplitude we use a slightly different but equivalent form:

$$\mathcal{T}\{j(z)j(0)\} \xrightarrow{z \rightarrow 0} \sum_{n,i} C_n^{(i)}(z^2) z_{\mu_1} \dots z_{\mu_n} \mathcal{O}_i^{\mu_1 \dots \mu_n}(0). \quad (\text{C.1})$$

Note that $C_n^{(i)}(z^2)$ are the reduced Wilson coefficients

Now there is something slightly confusing: the OPE is an expansion about $z_\mu \approx 0$, whereas the dominant contribution to the current product in deep-inelastic scattering comes from the $z^2 \approx 0$ region [64]. Therefore, we are only interested in the singularity of the Wilson coefficient in powers of $(z^2)^{-1}$, which are most dominant for $z^2 \approx 0$. Such singularities are not affected by the $z_{\mu_1} \dots z_{\mu_n}$ terms.

Power Counting: Canonical Dimension

Since the operators that are most dominant in deep-inelastic scattering will be those attached to the most singular reduced Wilson coefficients, $C_n^{(i)}(z^2)$, we start by examining the degree of singularity in these functions.

The simplest way to do this is to examine the dimension of the operator, $\mathcal{O}_i^{\mu_1 \dots \mu_n}(0)$. Since $\mathcal{T}\{j(z)j(0)\}$ has a fixed dimension of six*, the RHS of Eq. (C.1) must also match this dimension. The spacetime coordinate has dimension $[z] = -1$. Comparing the dimension of the two sides of Eq. (C.1), we have that the dimension of $C_n^{(i)}(z^2)$ is

$$d_{C_{i,n}} = 2d_j - (d_{\mathcal{O}_{i,n}} - n), \quad (\text{C.2})$$

where $d_{\mathcal{O}_{i,n}}$ is the dimension of the operator $\mathcal{O}_i^{\mu_1 \dots \mu_n}$, we get a dimension of $-n$ from $z_{\mu_1} \dots z_{\mu_n}$, and d_j is the dimension of a current. Then, since the only dimensionful parameter that $C_n^{(i)}(z^2)$ can depend on is z^2 , we have that in the limit $z^2 \rightarrow 0$,

$$\lim_{z^2 \rightarrow 0} C_n^{(i)}(z^2) \sim \frac{1}{(z^2)^{(2d_j - (d_{\mathcal{O}_{i,n}} - n))/2}} = \frac{1}{(z^2)^{(2d_j - \tau)/2}}, \quad (\text{C.3})$$

where we have defined the ‘twist’ of an operator as $\tau = d_{\mathcal{O}_{i,n}} - n$. Since d_j is fixed, it is clear from Eq. (C.3) that the most divergent $C_n^{(i)}(z^2)$ will be attached to the operator with the lowest twist. Therefore, the operators that contribute most to deep-inelastic scattering will be those with the lowest twist.

Leading Twist Operators

More generally, the twist of an operator is defined as $\tau \equiv \text{dimension} - \text{spin}$ [54]. For example, a quark field has spin 1/2 and dimension $[\psi] = 3/2$ (as per the QCD Lagrangian, Eq. (2.10)), resulting in a twist of 1. Similarly, the twist of the gluon field strength tensor is also 1. Therefore, the lowest twist terms one can have are twist-two, since our operators must be bilinears in our particle fields. On the other hand, the covariant derivative has canonical dimension $[D_\mu] = 1$ and spin 1, making its overall twist 0. As a result, we can add as many covariant derivatives as we like without changing the twist of the operator, and so the light-cone OPE has an infinite number of leading-order terms, in contrast to the short distance OPE.

In addition, to have definite spin, an operator must belong to an irreducible representation of the Lorentz group. This means it must be symmetrised in its Lorentz indices, and any terms proportional to $g^{\mu_i \mu_j}$ (traces) must be subtracted (the justifications for this are quite involved; see Ref. [323]).

Therefore, the basis of twist-two operators is

$$\mathcal{O}_f^{(n)\mu_1 \dots \mu_n}(X) = \bar{\psi}_f(X) \gamma^{\{\mu_1} i \overleftrightarrow{D}^{\mu_2} \dots i \overleftrightarrow{D}^{\mu_n\}} \psi_f(X) - \text{traces}, \quad (\text{C.4})$$

$$\tilde{\mathcal{O}}_f^{(n)\mu_1 \dots \mu_n}(X) = \bar{\psi}_f(X) \gamma^{\{\mu_1} \gamma^5 i \overleftrightarrow{D}^{\mu_2} \dots i \overleftrightarrow{D}^{\mu_n\}} \psi_f(X) - \text{traces}. \quad (\text{C.5})$$

These are the same operators used in Chapter 2. As discussed in Section 5.1, we technically also need to include operators with total derivatives. However, for the standard presentation of the OPE, we leave these out.

*We count dimension in terms of mass, so $[m] = 1$. Here, we only consider the canonical dimension; considering additional quantum mechanical effects, this is altered by the anomalous dimension.

For gluons, the twist two operators are

$$\mathcal{O}_g^{(n)\mu_1\dots\mu_n}(X) = F_\alpha^{\{\mu_1}(X) iD^{\leftrightarrow\mu_2} \dots iD^{\leftrightarrow\mu_n\}} F^{\alpha\mu_n\}(X) - \text{traces.} \quad (\text{C.6})$$

The leading-order Wilson coefficients for any operators with gluon fields will be zero, since adding gluon lines to the leading-order handbag diagrams introduces terms of order α_S^2 . Therefore, we do not give these operators in our final result.

Form of Current Product

Obtaining the basis of operators is the most challenging part of the expansion process. However, once we have identified these operators, we can determine the operator product expansion (OPE) by leveraging various general properties of the current product. These include Lorentz covariance, crossing symmetry (which eliminates q -odd terms in the symmetric Compton tensor), and current conservation ($\partial_z j(z) = 0$).

Then, the OPE of the time-ordered current product is

$$\begin{aligned} \mathcal{T}\{j^\mu(z)j^\nu(0)\} &\xrightarrow{z\rightarrow 0} (\partial_\mu\partial_\nu - g_{\mu\nu}\partial^2) \sum_{n=0,2,4}^{\infty} C_n^{(1)}(z^2) z_{\mu_1}\dots z_{\mu_n} \mathcal{O}_n^{\mu_1\dots\mu_n}(0) \\ &+ (g_{\mu\kappa}\partial_\rho\partial_\nu + g_{\rho\nu}\partial_\mu\partial_\kappa - g_{\mu\kappa}g_{\nu\rho}\partial^2 - g_{\mu\nu}\partial_\rho\partial_\kappa) \sum_{n=0,2,4}^{\infty} C_n^{(2)}(z^2) z_{\mu_1}\dots z_{\mu_n} \mathcal{O}_{n+2}^{\mu\nu\mu_1\dots\mu_n}(0) \quad (\text{C.7}) \end{aligned}$$

+ anti-symmetric in $\mu \leftrightarrow \nu$ terms.

Free field approximation

To derive the form of the current product used in Eqs. (2.44) and (2.56), we use a slightly different method that is equivalent to the above expansion, so long as we take the Wilson coefficients of the above expansion to leading-order. The key idea behind this alternative expansion is to take the current of products as operators for non-interacting quarks. This then gives us the ‘handbag’ contribution that is identical to the leading-twist OPE with leading-order Wilson coefficients.

For the non-interacting or free quark fields in the current product, we can apply Wick’s theorem to get

$$\begin{aligned} \mathcal{T}\{\bar{\psi}_f(z)\gamma^\mu\psi_f(z)\bar{\psi}_f(y)\gamma^\nu\psi_f(y)\} &= -\text{trace}[\overbrace{\gamma^\mu\psi_f(z)\bar{\psi}_f(y)} \overbrace{\gamma^\nu\psi_f(y)\bar{\psi}_f(z)}] \\ &+ : \bar{\psi}_f(z)\gamma^\mu \overbrace{\psi_f(z)\bar{\psi}_f(y)} \overbrace{\gamma^\nu\psi_f(y)} : + : \overbrace{\bar{\psi}_f(z)\gamma^\mu\psi_f(z)} \overbrace{\bar{\psi}_f(y)\gamma^\nu\psi_f(y)} : \\ &+ : \bar{\psi}_f(z)\gamma^\mu\psi_f(z)\bar{\psi}_f(y)\gamma^\nu\psi_f(y) :, \end{aligned} \quad (\text{C.8})$$

where the contractions yield free quark propagators, $S_F(z-y)$, which are singular both in the limit that $z \rightarrow y$ and $(z-y)^2 \rightarrow 0$ [47].

Therefore, in the short-distance limit $z \rightarrow y$, the trace term will be the most singular of Eq. C.8, the second two terms less singular. The last term corresponds to a power-suppressed cat’s ears diagram (See Figure C.1). We are only interested in the most singular terms. Therefore, we can ignore the cat’s ears term. Further, the trace term (vacuum

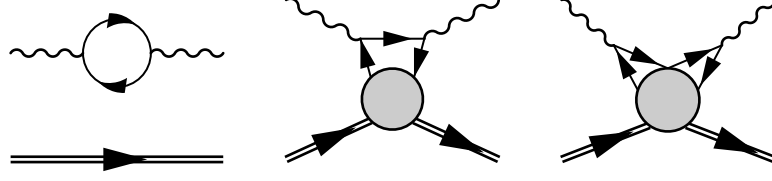


Figure C.1: Feynman diagrams corresponding to terms in Eq. C.8: the trace term (left), the two terms with a single contraction (center), the term with no contraction (right).

polarisation) doesn't contribute to the scattering process, so we ignore this term too. This leaves us with the two terms that have only one propagator each: the 'handbag' terms.

Hence we keep only the terms in Eq. (C.8) with one contraction. These contractions yield free quark propagators. Therefore, after using γ -matrix identities, we get

$$\begin{aligned} \mathcal{T}\{j_\mu(z/2)j_\nu(-z/2)\} &= S^\rho(z) \left(\mathcal{S}_{\mu\rho\nu\kappa} [\bar{\psi}_f(z/2)\gamma^\kappa\psi_f(-z/2) - \bar{\psi}_f(-z/2)\gamma^\kappa\psi_f(z/2)] \right. \\ &\quad \left. - i\epsilon_{\mu\nu\rho\kappa} [\bar{\psi}_f(z/2)\gamma^\kappa\gamma^5\psi_f(-z/2) + \bar{\psi}_f(-z/2)\gamma^\kappa\gamma^5\psi_f(z/2)] \right), \end{aligned} \quad (\text{C.9})$$

where we have introduced the reduced leading-order quark propagator:

$$S^\mu(z) \equiv \frac{i}{2\pi^2} \frac{z^\mu}{(z^2 - i\epsilon)^2} \quad \Rightarrow \quad \gamma_\mu S^\mu(z) = S_F(z),$$

and $\mathcal{S}_{\mu\rho\nu\kappa} = g_{\mu\rho}g_{\nu\kappa} + g_{\mu\kappa}g_{\nu\rho} - g_{\mu\nu}g_{\rho\kappa}$. This is the component of the quark propagator that contributes in the short-distance limit [324].

We can Taylor expand the operators about $z_\mu = 0$, and isolate their twist-two component:

$$[\bar{\psi}_f(z/2)\gamma^\kappa\psi_f(-z/2)]_{\text{twist-two}} = \sum_{n=0}^{\infty} \frac{(-i)^n}{n!} z_{\mu_1} \dots z_{\mu_n} \mathcal{O}_f^{(n+1)\kappa\mu_1 \dots \mu_n}(0), \quad (\text{C.10})$$

where $\mathcal{O}_f^{(n+1)\kappa\mu_1 \dots \mu_n}(X)$ are the standard twist-two local operators, given in Eq. (2.40).

We can apply the same procedure to the polarised operators

$$[\bar{\psi}_f(z/2)\gamma^\kappa\gamma^5\psi_f(-z/2)]_{\text{twist-two}} = \sum_{n=0}^{\infty} \frac{(-i)^n}{n!} z_{\mu_1} \dots z_{\mu_n} \tilde{\mathcal{O}}_f^{(n+1)\kappa\mu_1 \dots \mu_n}(0), \quad (\text{C.11})$$

where $\tilde{\mathcal{O}}_f^{(n+1)\kappa\mu_1 \dots \mu_n}(0)$ are the polarised twist-two local operators from Eq. (2.41).

Therefore, the twist-two symmetric under $\mu \leftrightarrow \nu$ component of the current product in the short-distance limit ($z^\mu \rightarrow 0$) is

$$\begin{aligned} \mathcal{T}\{j_{\{\mu}(z/2)j_{\nu\}}(-z/2)\} &= -2 \frac{i}{2\pi^2} \frac{z^\rho}{(z^2 - i\epsilon)^2} \left(g_{\mu\rho}g_{\nu\kappa} + g_{\mu\kappa}g_{\nu\rho} - g_{\mu\nu}g_{\rho\kappa} \right) \\ &\quad \times \sum_{n=1,3,5}^{\infty} \frac{(-i)^n}{n!} z_{\mu_1} \dots z_{\mu_n} \mathcal{O}_f^{(n+1)\kappa\mu_1 \dots \mu_n}, \end{aligned} \quad (\text{C.12})$$

which is Eq. (2.44). The anti-symmetric component is

$$\begin{aligned} \mathcal{T}\{j_{[\mu}(z/2)j_{\nu]}(-z/2)\} &= -2\frac{i}{2\pi^2}\frac{z^\rho}{(z^2-i\epsilon)^2}i\varepsilon_{\mu\nu\rho\kappa} \\ &\times \sum_{n=0,2,4}^{\infty} \frac{(-i)^n}{n!} z_{\mu_1}\dots z_{\mu_n} \tilde{\mathcal{O}}_f^{(n+1)\kappa\mu_1\dots\mu_n}(0), \end{aligned} \quad (\text{C.13})$$

which is Eq. (2.56).

More Fun with GPDs

In this appendix we discuss in further detail the properties of generalised parton distributions (GPDs), expanding on the discussion in Chapters 2 and 5.

Kinematic relations

Some standard relations between the momentum vectors we defined for off-forward scattering (Eq. (2.73)) are

$$\bar{P} \cdot \Delta = \frac{1}{2}(P^2 - P'^2) = 0, \quad \bar{P}^2 = m_N^2 - \frac{t}{4}. \quad (\text{D.1})$$

Sudakov decomposition

As discussed in Chapters 2 and 5, light-cone operators and expansions of the off-forward Compton amplitude often employ a pair of collinear lightlike vectors:

$$n^\mu = \Lambda(1, 0, 0, 1), \quad \bar{n}^\mu = \frac{1}{2\Lambda}(1, 0, 0, -1), \quad (\text{D.2})$$

where Λ is a normalisation chosen such that $n \cdot \bar{P} = 1$.

Given these two vectors, we can decompose any vector into

$$k^\mu = (\bar{n} \cdot k)n^\mu + (n \cdot k)\bar{n}^\mu + k_\perp^\mu, \quad (\text{D.3})$$

where $k_\perp \cdot n = 0 = k_\perp \cdot \bar{n}$. Hence k_\perp has two degrees of freedom, which accounts for all four degrees of freedom of any four-vector. Equation (D.3) is sometimes called the ‘Sudakov decomposition’.

Applying this to the case of off-forward scattering, we get

$$\bar{P}^\mu = \frac{m_N^2 - t/4}{2}n^\mu + \bar{n}^\mu, \quad (\text{D.4a})$$

$$\Delta^\mu = (m_N^2 - t/4)\xi n^\mu - 2\xi\bar{n}^\mu + \Delta_\perp^\mu, \quad (\text{D.4b})$$

$$\bar{q}^\mu = -\frac{1}{\bar{\omega}}\bar{n}^\mu + \frac{\bar{Q}^2\bar{\omega}}{2}n^\mu, \quad (\text{D.4c})$$

where we have defined $\xi = -n \cdot \Delta/2$ and assumed that the transverse components of \bar{P} and \bar{q} are small. Moreover, we only recover the usual Lorentz scalars from the above light-cone decomposition up to terms of order M^2/\bar{Q}^2 and t/\bar{Q}^2 , which are suppressed.

Finally, for some vector k it is common to see the notation $k^+ = k \cdot n$ and $k^- = k \cdot \bar{n}$.

Polarised generalised parton distributions

Here, we define polarised GPDs and give some of their basic properties. Although not a focus of our investigations, these GPDs are interesting to us for two reasons: (1) we include them in our parameterisation of the off-forward Compton amplitude in Chapter 5, and (2) they are the generalisation of the polarised moments we calculate in Chapter 7. Moreover, it would be straightforward to extend the methods in this thesis to calculate the moments of polarised GPDs using Feynman-Hellmann.

In terms of light-cone operators, we defined in Eq. (2.52), the polarised GPDs are defined as

$$\int \frac{d\lambda}{2\pi} e^{i\lambda x} \langle P' | \bar{\psi}_f(-\lambda n/2) \not{n} \gamma_5 \psi_f(\lambda n/2) | P \rangle = \tilde{H}^f(x, \vartheta/\bar{\omega}, t) \bar{u}(P') \gamma^\mu \gamma_5 n_\mu u(P) + \tilde{E}^f(x, \vartheta/\bar{\omega}, t) \frac{\Delta \cdot n}{2m_N} \bar{u}(P') \gamma_5 u(P), \quad (\text{D.5})$$

where \tilde{H}^f and \tilde{E}^f are the polarised twist-two GPDs for a quark of flavour f .

Now we will define the polarised generalised form factors. We start with the matrix elements of the twist-two local operators, Eq. (2.41). Note that these are the same local operators we used to parameterise the forward polarised Compton amplitude.

In terms of the polarised GFFs, $\tilde{A}_{n,j}(t)$ and $\tilde{B}_{n,j}(t)$, the matrix element of the polarised twist-two operators are

$$\begin{aligned} & \langle P' | \tilde{\mathcal{O}}_f^{(n+1)\kappa\mu_1\dots\mu_n}(0) | P \rangle \\ &= \bar{u}(P', s') \gamma^{\{\kappa} \gamma_5 u(P, s) \sum_{j=0,2,4}^n \tilde{A}_{n+1,j}^f(t) \Delta^{\mu_1} \dots \Delta^{\mu_j} \bar{P}^{\mu_{j+1}} \dots \bar{P}^{\mu_n} \} \\ &+ \frac{\Delta^{\{\kappa}}{2m_N} \bar{u}(P', s') \gamma_5 u(P, s) \sum_{j=0,2,4}^n \tilde{B}_{n+1,j}^f(t) \Delta^{\mu_1} \dots \Delta^{\mu_j} \bar{P}^{\mu_{j+1}} \dots \bar{P}^{\mu_n} \}. \end{aligned} \quad (\text{D.6})$$

Then, applying Eq. (2.53), we get that the Mellin moments of the GPDs are

$$\begin{aligned} \int_{-1}^1 dx x^n \tilde{H}^f(x, \vartheta/\bar{\omega}, t) &= \sum_{i=0,2,4}^n (2\vartheta/\bar{\omega})^i \tilde{A}_{n+1,i}^f(t), \\ \int_{-1}^1 dx x^n \tilde{E}^f(x, \vartheta/\bar{\omega}, t) &= \sum_{i=0,2,4}^n (2\vartheta/\bar{\omega})^i \tilde{B}_{n+1,i}^f(t). \end{aligned} \quad (\text{D.7})$$

Note also that $\tilde{A}_{n,0}(t=0) = 2\tilde{a}_n$, for the polarised forward matrix element defined in Eq. (2.58).

Off-Forward OPE and Tensor Decomposition (Ch. 5)

In this appendix we provide further details for the derivations of the operator product expansion (OPE) and tensor decomposition presented in Chapter 5.

E.1 Operator Product Expansion

As in Chapter 5, we start with the OPE of the current product that was discussed in Chapter 2 and derived in Appendix C:

$$\begin{aligned} \mathcal{T}\{j_\mu(z/2)j_\nu(-z/2)\} = & -2\frac{i}{2\pi^2}\frac{z^\mu}{(z^2-i\epsilon)^2}\left[\mathcal{S}_{\mu\rho\nu\kappa}\sum_{n=1,3,5}^{\infty}\frac{(-i)^n}{n!}z_{\mu_1\dots\mu_n}\mathcal{O}_f^{(n+1)\kappa\mu_1\dots\mu_n}(0)\right. \\ & \left.+i\varepsilon_{\mu\nu\rho\kappa}\sum_{n=0,2,4}^{\infty}\frac{(-i)^n}{n!}z_{\mu_1\dots\mu_n}\tilde{\mathcal{O}}_f^{(n+1)\kappa\mu_1\dots\mu_n}(0)\right]. \end{aligned}$$

Similarly, recall the Dirac bilinears defined in Eq. (5.4):

$$\begin{aligned} h^\mu &= \bar{u}(P')\gamma^\mu u(P), & e^\mu &= \bar{u}(P')\frac{i\sigma^{\mu\alpha}\Delta_\alpha}{2m_N}u(P), \\ \tilde{h}^\mu &= \bar{u}(P')\gamma^\mu\gamma_5 u(P), & \tilde{e}^\mu &= \frac{\Delta^\mu}{2m_N}\bar{u}(P')\gamma_5 u(P). \end{aligned}$$

To take the off-forward matrix element of the leading-order current product, we simply insert the off-forward matrix elements from Eqs. (2.78) and (D.6) into this expression. The $\mu \leftrightarrow \nu$ symmetric term was given in Eq. (5.5), while the anti-symmetric term is

$$\begin{aligned} \langle P'|\mathcal{T}\{j_{[\mu}(z/2)j_{\nu]}(-z/2)\}|P\rangle = & -2S^p(z)i\varepsilon_{\mu\nu\rho\kappa}\sum_{n=0,2,4}^{\infty}\frac{(-i)^n}{n!} \\ & \times\sum_{j=0,2,4}^n\left\{\frac{1}{n+1}(\Delta\cdot z)^j(\bar{P}\cdot z)^{n-j}[\tilde{h}^\kappa\tilde{A}_{n+1,j}^f(t)+\tilde{e}^\kappa\tilde{B}_{n+1,j}^f(t)]\right. \\ & +\frac{n-j}{n+1}(\Delta\cdot z)^j(\bar{P}\cdot z)^{n-j-1}\bar{P}^\kappa[\tilde{A}_{n+1,j}^f(t)\tilde{h}\cdot z+\tilde{B}_{n+1,j}^f(t)\tilde{e}\cdot z] \\ & \left.+\frac{j}{n+1}(\Delta\cdot z)^{j-1}(\bar{P}\cdot z)^{n-j}\Delta^\kappa[\tilde{A}_{n+1,j}^f(t)\tilde{h}\cdot z+\tilde{B}_{n+1,j}^f(t)\tilde{e}\cdot z]\right\}. \end{aligned} \quad (\text{E.1})$$

Fourier transform

Since we are interested in calculating the leading-order part of the off-forward Compton amplitude,

$$T^{\mu\nu} = i \int d^4z e^{i\bar{q}\cdot z} \langle P' | T [j^\mu(z/2) j^\nu(-z/2)] | P \rangle,$$

we now need to Fourier transform this matrix element.

Recall that the general recipe given in Chapter 5 is:

1. Introduce Fourier conjugates,

$$\begin{aligned} (\bar{P} \cdot z)^n &= i^n \int_{-\infty}^{\infty} d\chi e^{i\chi \bar{P} \cdot z} \frac{\partial^n}{\partial \chi^n} \delta(\chi), \\ (\Delta \cdot z)^n &= i^n \int_{-\infty}^{\infty} d\eta e^{i\eta \Delta \cdot z} \frac{\partial^n}{\partial \eta^n} \delta(\eta), \\ h \cdot z &= i \int_{-\infty}^{\infty} d\tilde{\chi}_1 e^{i\tilde{\chi}_1 h \cdot z} \frac{\partial}{\partial \tilde{\chi}_1} \delta(\tilde{\chi}_1), \\ e \cdot z &= i \int_{-\infty}^{\infty} d\tilde{\chi}_2 e^{i\tilde{\chi}_2 e \cdot z} \frac{\partial}{\partial \tilde{\chi}_2} \delta(\tilde{\chi}_2). \end{aligned}$$

For the $\mu \leftrightarrow \nu$, we need $h(e) \rightarrow \tilde{h}(\tilde{e})$.

2. Use the identity

$$\int d^4z S^\mu(z) = \int d^4z e^{il \cdot z} \frac{z^\mu}{2\pi^2(z^2 - i\epsilon)^2} = \frac{l^\mu}{l^2 + i\epsilon}$$

to integrate out the z -dependence.

3. Use the identity

$$\int_a^b dx f(x) \frac{\partial^n}{\partial x^n} \delta(x - y) = (-1)^n \frac{\partial^n}{\partial x^n} f(x) \Big|_{x=y},$$

to evaluate the integrals over the Fourier conjugates.

After applying this recipe, we have that the symmetric component of the twist-two nucleon OFCA is

$$\begin{aligned}
T^{\{\mu\nu\}} = & \sum_{n=2,4,6}^{\infty} \sum_{j=0,2,4}^{n-1} \left\{ \frac{4}{Q^2} \frac{1}{n} \bar{\omega}^{n-2} (-2\xi)^{j-1} [h^{\{\mu} A_{n,j}^f(t) + e^{\{\mu} B_{n,j}^f(t)] \right. \\
& \times \left[\bar{\omega}(-2\xi) \bar{q}^{\nu\}} + \frac{2(n-j-1)}{n-1} (-2\xi) \bar{P}^{\nu\}} + \frac{2j}{n-1} \Delta^{\nu\}} \right] \\
& + \frac{8}{Q^4} \frac{1}{n} \bar{\omega}^{n-3} (-2\xi)^{j-2} [A_{n,j}^f(th \cdot \bar{q} + B_{n,j}^f(t)e \cdot \bar{q}) \left[(n-j-1) \bar{\omega}(-2\xi)^2 \bar{P}^{\{\mu} \bar{q}^{\nu\}} \right. \\
& + \frac{2(n-j-1)j}{n-1} (-2\xi) \bar{P}^{\{\mu} \Delta^{\nu\}} + j \bar{\omega}(-2\xi) \Delta^{\{\mu} \bar{q}^{\nu\}} \\
& + \frac{j(j-1)}{n-1} \Delta^{\mu} \Delta^{\nu} + \frac{(n-j-1)(n-j-2)}{n-1} \bar{\omega}(-2\xi)^2 \bar{P}^{\mu} \bar{P}^{\nu} \left. \right] \\
& + \frac{8}{Q^4} \delta_{j,0} \bar{\omega}^{n-3} (-2\xi)^{n-2} C_n^f(t) (h \cdot \bar{q} - e \cdot \bar{q}) \left[(-2\xi) \bar{\omega} \Delta^{\{\mu} \bar{q}^{\nu\}} + \Delta^{\mu} \Delta^{\nu} \right] \\
& \left. - g^{\mu\nu} \bar{\omega}^n \left[(-2\xi)^j [A_{n,j}^f(t) h \cdot \bar{q} + B_{n,j}^f(t) e \cdot \bar{q}] + \delta_{j,0} (-2\xi)^n C_n^f(t) (h \cdot \bar{q} - e \cdot \bar{q}) \right] \right\}, \tag{E.2}
\end{aligned}$$

where we have used $\xi = \vartheta/\bar{\omega}$.

Similarly, for the anti-symmetric component we get

$$\begin{aligned}
T^{[\mu\nu]} = & \frac{2}{Q^2} i \varepsilon^{\mu\nu\rho\kappa} \sum_{n=0,2,4}^{\infty} \sum_{j=0,2,4}^n \tilde{A}_{n+1,j}^f(t) (-2\xi)^{j-1} \\
& \times \left\{ \frac{1}{n+1} \tilde{h}_{\kappa} \bar{\omega}^{n-1} \left[\bar{\omega}(-2\xi) \bar{q}_{\rho} + \frac{n-j}{n} (-2\xi) \bar{P}_{\rho} + \frac{j}{n} \Delta_{\rho} \right] + \frac{n-j}{n+1} \bar{\omega}^{n-2} \bar{P}_{\kappa} \right. \\
& \times \left[\bar{\omega}(-2\xi) \frac{2\tilde{h} \cdot \bar{q}}{Q^2} \bar{q}_{\rho} + \frac{n-j-1}{n} (-2\xi) \frac{2\tilde{h} \cdot \bar{q}}{Q^2} \bar{P}_{\rho} + \frac{j}{n} \frac{2\tilde{h} \cdot \bar{q}}{Q^2} \Delta_{\rho} + \frac{1}{n} \bar{\omega}(-2\xi) \tilde{h}_{\rho} \right] \\
& + \frac{j}{n+1} \bar{\omega}^{n-2} (-2\xi)^{-1} \Delta_{\kappa} \left[\bar{\omega}(-2\xi) \frac{2\tilde{h} \cdot \bar{q}}{Q^2} \bar{q}_{\rho} + \frac{n-j}{n} (-2\xi) \frac{2\tilde{h} \cdot \bar{q}}{Q^2} \bar{P}_{\rho} \right. \\
& \left. \left. + \frac{j-1}{n} \frac{2\tilde{h} \cdot \bar{q}}{Q^2} \Delta_{\rho} + \frac{1}{n} \bar{\omega}(-2\xi) \tilde{h}_{\rho} \right] \right\} + (\tilde{A} \rightarrow \tilde{B} \text{ and } \tilde{h} \rightarrow \tilde{e}), \tag{E.3}
\end{aligned}$$

where the term in brackets indicates that there is an additional contribution to the anti-symmetric component identical to that shown but with the given substitutions.

Equations E.2 and E.3 are extremely unwieldy. Therefore, to produce a cleaner result, we first define* $\Delta_{\perp}^{\mu} \equiv \Delta^{\mu} + 2\xi \bar{P}^{\mu}$. Since $\Delta_{\perp} \cdot \bar{q} = 0$, we have that $\Delta_{\perp} \cdot q^{(t)} \sim t$, which will give us suppressed t/Q^2 terms. Therefore, we discard tensor structures with Δ_{\perp} and reintroduce them when we come to talk about gauge invariance[†].

*We note that other studies use the definition $\Delta_{\perp}^{\mu} \equiv \Delta^{\mu} + \frac{2}{\bar{\omega}} \bar{P}^{\mu}$. These definitions are equivalent for DVCS kinematics, where $\xi \simeq \bar{\omega}^{-1}$.

[†]Recall from Chapter 5 we discussed the fact that leading-twist expansions of the OFCA do not satisfy their Ward identities unless additional operators are included in the OPE basis. Therefore, it seems possible that this may all be due to the dropping of the Δ_{\perp} terms. However, as can be confirmed by considering these expressions prior to throwing out Δ_{\perp} , Eqs. E.2 and E.3, this is not the case.

Therefore, we substitute $\Delta^\mu = \Delta_\perp^\mu - 2\xi\bar{P}^\mu$ into Eq. E.2 and throw out all Δ_\perp terms to get

$$\begin{aligned}
T^{\{\mu\nu\}}(\bar{\omega}, \vartheta, t) &= \frac{2}{Q^2} \sum_{n=2,4,6}^{\infty} \sum_{j=0,2,4}^{n-1} \left\{ \frac{2}{n} \bar{\omega}^{n-2} (-2\xi)^j [h^{\{\mu} A_{n,j}^f(t) + e^{\{\mu} B_{n,j}^f(t)] (\bar{\omega} \bar{q}^{\nu\}} + 2\bar{P}^{\nu\})} \right. \\
&+ \frac{4}{Q^2} \frac{1}{n} \bar{\omega}^{n-3} (-2\xi)^j [A_{n,j}^f(t) h \cdot \bar{q} + B_{n,j}^f(t) e \cdot \bar{q}] \left((n-1) \bar{\omega} \bar{P}^{\{\mu} \bar{q}^{\nu\}} + (n-2) \bar{P}^\mu \bar{P}^\nu \right) \\
&+ \frac{4}{Q^2} \delta_{j,0} \bar{\omega}^{n-3} (-2\xi)^n C_n^f(t) (h \cdot \bar{q} - e \cdot \bar{q}) \left(\bar{\omega} \bar{P}^{\{\mu} \bar{q}^{\nu\}} + \bar{P}^\mu \bar{P}^\nu \right) \\
&\left. - g^{\mu\nu} \bar{\omega}^{n-1} \left((-2\xi)^j [A_{n,j}^f(t) h \cdot \bar{q} + B_{n,j}^f(t) e \cdot \bar{q}] + \delta_{j,0} (-2\xi)^n C_n^f(t) (h \cdot \bar{q} - e \cdot \bar{q}) \right) \right\},
\end{aligned}$$

which was our final expression for the symmetric component, Eq. (5.6).

The procedure for the anti-symmetric component is slightly more complicated. We start by substituting for $\Delta = \Delta_\perp - 2\xi\bar{P}^\mu$ and throwing out Δ_\perp terms again:

$$\begin{aligned}
T^{[\mu\nu]} &= \frac{2}{Q^2} i\varepsilon^{\mu\nu\rho\kappa} \sum_{n=0,2,4}^{\infty} \sum_{j=0,2,4}^n \left\{ \frac{1}{n+1} \tilde{h}_\kappa \tilde{A}_{n+1,j}^f(t) \bar{\omega}^{n-1} (-2\xi)^j (\bar{\omega} \bar{q}_\rho + \bar{P}_\rho) \right. \\
&+ \frac{n}{n+1} \bar{\omega}^{n-2} (-2\xi)^j \bar{P}_\kappa \tilde{A}_{n+1,j}^f(t) \left(\bar{\omega} \frac{2\tilde{h} \cdot \bar{q}}{Q^2} \bar{q}_\rho + \frac{n-1}{n} \frac{2\tilde{h} \cdot \bar{q}}{Q^2} \bar{P}_\rho + \frac{1}{n} \bar{\omega} \tilde{h}_\rho \right) \left. \right\} \\
&+ (\tilde{A} \rightarrow \tilde{B} \text{ and } \tilde{h} \rightarrow \tilde{e}).
\end{aligned} \tag{E.4}$$

Moving the $n \rightarrow n-1$ and dropping terms that cancel by the $\bar{P}_\rho \bar{P}_\kappa$ terms which vanish when contracted with the Levi-Civita, we get

$$\begin{aligned}
T^{[\mu\nu]} &= \frac{2}{Q^2} i\varepsilon_{\mu\nu\rho\kappa} \sum_{n=1,3,5}^{\infty} \sum_{j=0,2,4}^{n-1} \bar{\omega}^{n-2} (-2\xi)^j \left\{ \frac{1}{n} \tilde{h}_\kappa \tilde{A}_{n,j}^f(t) (\bar{\omega} \bar{q}_\rho + \bar{P}_\rho) \right. \\
&+ \frac{n-1}{n} \bar{P}_\kappa \bar{q}_\rho \tilde{A}_{n,j}^f(t) \frac{2\bar{q} \cdot \tilde{h}}{Q^2} + \frac{1}{n} \bar{P}_\kappa \tilde{A}_{n,j}^f(t) \tilde{h}_\rho \left. \right\} + (\tilde{A} \rightarrow \tilde{B} \text{ and } \tilde{h} \rightarrow \tilde{e}).
\end{aligned} \tag{E.5}$$

Then, since the $\tilde{h}_\kappa \bar{P}_\rho$ and $\tilde{e}_\kappa \bar{P}_\rho$ terms are symmetrised in their Lorentz indices, they also vanish when contracted with the Levi-Civita. This gives us

$$\begin{aligned}
T^{[\mu\nu]}(\bar{\omega}, \vartheta, t) &= \frac{2}{Q^2} i\varepsilon^{\mu\nu\rho\kappa} \sum_{n=1,3,5}^{\infty} \sum_{j=0,2,4}^{n-1} \bar{\omega}^{n-2} (-2\xi)^j \left\{ \frac{1}{n} [\tilde{h}_\kappa \tilde{A}_{n,j}^f(t) + \tilde{e}_\kappa \tilde{B}_{n+1,j}^f(t)] \bar{\omega} \bar{q}_\rho \right. \\
&+ \frac{2}{Q^2} \frac{n-1}{n} \bar{P}_\kappa \bar{q}_\rho [\tilde{A}_{n,j}^f(t) \tilde{h} \cdot \bar{q} + \tilde{B}_{n+1,j}^f(t) \tilde{e} \cdot \bar{q}] \left. \right\},
\end{aligned}$$

which was our final expression for the anti-symmetric component, Eq. (5.7).

E.2 Tensor Decomposition

As discussed in Chapter 5, a general tensor decomposition of the OFCA was performed by Tarrach [197]. Here, we do not take this decomposition for reasons given in Chapter 5, but instead use it to derive our own that matches the OPE results, Eqs. (5.6) and (5.7).

We start with the 34 generators given by Tarrach (Eq. 8 of that work)—that is, the 34 tensor structures that satisfy the necessary discrete symmetries. Then, we perform the following manipulations:

- Remove from Tarrach’s 34 generators the 14 structures with q'^μ or q'^ν terms, which by the Ward identities must be linearly dependent with other tensor structures.
- Remove generators 13 and 28 (according to Tarrach’s Eq. 8) due to the linear dependence of these terms with other generators, as explained in Tarrach. This leaves 18 gauge independent, linearly independent tensor structures.
- Reorganise these structures with the Gordon identity and related identities, so that they can be matched to leading twist GPD structures.
- Identify which scalar amplitudes must vanish at zero skewness ($q^2 = q'^2$), using crossing symmetry and time reversal.
- Gauge project these 18 tensor structures.

The result is a zero-skewness tensor decomposition, with structure functions that can be matched to the leading-twist OPE results.

Tarrach’s generators are[‡]

$$\begin{aligned}
 f_1^{\mu\nu} &= g_{\mu\nu} \bar{u}' u, & f_{10}^{\mu\nu} &= \bar{P}^\mu \bar{u}' \gamma^\mu u^\nu + \bar{P}^\nu \bar{u}' \gamma^\nu u^\mu, & (E.6) \\
 f_2^{\mu\nu} &= \bar{P}^\mu \bar{P}^\nu \bar{u}' u, & f_{11}^{\mu\nu} &= \bar{P}^\mu \bar{u}' \gamma^\mu u^\nu - \bar{P}^\nu \bar{u}' \gamma^\nu u^\mu, \\
 f_3^{\mu\nu} &= (\bar{P}^\mu q'^\nu + \bar{P}^\nu q'^\mu) \bar{u}' u, & f_{12}^{\mu\nu} &= q'^\mu \bar{u}' \gamma^\mu u^\nu + q'^\nu \bar{u}' \gamma^\nu u^\mu, \\
 f_4^{\mu\nu} &= (\bar{P}^\mu q'^\nu - \bar{P}^\nu q'^\mu) \bar{u}' u, & f_{13}^{\mu\nu} &= q'^\mu \bar{u}' \gamma^\mu u^\nu - q'^\nu \bar{u}' \gamma^\nu u^\mu, \\
 f_5^{\mu\nu} &= g^{\mu\nu} \bar{u}' \not{q}' u, & f_{14}^{\mu\nu} &= 2(\bar{P}^\mu \bar{q}'_\alpha \bar{u}' i \sigma^{\alpha\nu} u + \bar{P}^\nu \bar{q}'_\alpha \bar{u}' i \sigma^{\alpha\mu} u), \\
 f_6^{\mu\nu} &= \bar{P}^\mu \bar{P}^\nu \bar{u}' \not{q}' u, & f_{15}^{\mu\nu} &= 2(q'^\mu \bar{q}'_\alpha \bar{u}' i \sigma^{\alpha\nu} u + q'^\nu \bar{q}'_\alpha \bar{u}' i \sigma^{\alpha\mu} u), \\
 f_7^{\mu\nu} &= (\bar{P}^\mu q'^\nu + \bar{P}^\nu q'^\mu) \bar{u}' \not{q}' u, & f_{16}^{\mu\nu} &= 2(q'^\mu \bar{q}'_\alpha \bar{u}' i \sigma^{\alpha\nu} u - q'^\nu \bar{q}'_\alpha \bar{u}' i \sigma^{\alpha\mu} u), \\
 f_8^{\mu\nu} &= (\bar{P}^\mu q'^\nu - \bar{P}^\nu q'^\mu) \bar{u}' \not{q}' u, & f_{17}^{\mu\nu} &= -2i \bar{u}' \sigma^{\mu\nu} u, \\
 f_9^{\mu\nu} &= q'^\mu q'^\nu \bar{u}' u, & f_{18}^{\mu\nu} &= 4i \varepsilon^{\mu\nu\rho\kappa} \bar{q}'_\rho \bar{u}' \gamma_\kappa \gamma_5 u.
 \end{aligned}$$

In principle, this basis is sufficient for the tensor decomposition. However, we would like to be able to compare our decomposition to the leading-twist GPD structures. Therefore, we will use the Gordon identity and related identities (see Ref. [203] for a comprehensive

[‡]Note that our amplitude, following conventions of more recent papers, has Tarrach’s Lorentz indices swapped: $\mu \leftrightarrow \nu$. Moreover, also in contrast to Tarrach, our generators are sandwiched between the spinors.

list of on-shell identities that can be derived from the Dirac equation) to make the basis in Eq. E.6 more suitable to compare to leading-twist expressions.

We can use the Gordon identity to derive

$$\bar{P}^\mu \bar{u}' u = m_N (h^\mu - e^\mu) \quad \Rightarrow \quad \bar{P} \cdot \bar{q} \bar{u}' u = m_N (h \cdot \bar{q} - e \cdot \bar{q}). \quad (\text{E.7})$$

This allows us to re-define generators 1-4 of Eq. E.6, by making the substitution $\bar{u}' u \rightarrow e \cdot \bar{q}$.

Furthermore, we can rearrange $f_{17}^{\mu\nu}$ using the relation

$$i\varepsilon^{\mu\nu\rho\kappa} \bar{q}_\rho \tilde{e}_\kappa = i\varepsilon^{\mu\nu\rho\kappa} \bar{q}_\rho \tilde{h}_\kappa - \frac{1}{m_N} \left(\bar{P}^\mu \bar{u}' i\sigma^{\alpha\nu} u \bar{q}_\alpha - \bar{P}^\nu \bar{u}' i\sigma^{\alpha\mu} u \bar{q}_\alpha + \bar{P} \cdot \bar{q} \bar{u}' i\sigma^{\mu\nu} u \right).$$

The first term on the RHS is proportional to tensor structure 18, while the last term is proportional to 17. The middle two terms are actually proportional to Tarrach's generator 28, which is non-trivially linearly dependent with the other generators. Therefore, we can make the replacement:

$$f_{17}^{\mu\nu} = i\varepsilon^{\mu\nu\rho\kappa} \bar{q}_\rho \tilde{e}_\kappa.$$

By a similar argument, we can use the relation

$$\bar{P}^\mu \bar{u}' \gamma_5 u = \frac{1}{2} \bar{u}' i\sigma^{\alpha\mu} \gamma_5 u \Delta_\alpha, \quad (\text{E.8})$$

to replace

$$\begin{aligned} i\varepsilon^{\mu\nu\rho\kappa} \bar{q}_\rho \bar{P}_\kappa \tilde{e} \cdot \bar{q} &= \Delta \cdot \bar{q} i\varepsilon^{\mu\nu\rho\kappa} \bar{q}_\rho \Delta^\alpha \bar{u}' i\sigma_{\alpha\kappa} u \\ &= \frac{\Delta \cdot \bar{q}}{m_N} \left(\Delta^\mu \bar{u}' i\sigma^{\alpha\nu} u \bar{q}_\alpha - \Delta^\nu \bar{u}' i\sigma^{\alpha\mu} u \bar{q}_\alpha + \Delta \cdot \bar{q} \bar{u}' i\sigma^{\mu\nu} u \right). \end{aligned} \quad (\text{E.9})$$

The last term of the RHS is proportional to generator 17 of Eq. E.6, while the first two terms are (up to gauge terms) proportional to generator 15.

Therefore, we can make the replacement

$$f_{15}^{\mu\nu} = i\varepsilon^{\mu\nu\rho\kappa} \bar{q}_\rho \bar{P}_\kappa \tilde{e} \cdot \bar{q}. \quad (\text{E.10})$$

Then,

$$i\varepsilon^{\mu\nu\rho\kappa} \bar{q}_\rho \bar{P}_\kappa \tilde{h} \cdot \bar{q} = f_{15}^{\mu\nu} + \frac{1}{2m_N} i\varepsilon^{\mu\nu\rho\kappa} \varepsilon^{\alpha\beta\delta\lambda} \bar{q}_\rho \bar{P}_\kappa \bar{q}_\alpha \bar{P}_\beta \bar{u}' i\sigma^{\delta\lambda} u. \quad (\text{E.11})$$

The second term on the RHS creates terms that are proportional to structures 3, 4, and 9 of Eq. E.6, and a term proportional to

$$\bar{P} \cdot \bar{q} \left(\bar{P}^\mu \bar{u}' i\sigma^{\alpha\nu} u \bar{q}_\alpha - \bar{P}^\nu \bar{u}' i\sigma^{\alpha\mu} u \bar{q}_\alpha \right) - \bar{P}^2 \left(\bar{q}^\mu \bar{u}' i\sigma^{\alpha\nu} u \bar{q}_\alpha - \bar{q}^\nu \bar{u}' i\sigma^{\alpha\mu} u \bar{q}_\alpha \right). \quad (\text{E.12})$$

The first term in the above expression, as we already mentioned, is linearly dependent with the rest of the basis. The second term is linearly dependent with generator 16 up to gauge terms.

Therefore, we can make the replacement

$$f_{16}^{\mu\nu} = i\varepsilon^{\mu\nu\rho\kappa} \bar{q}_\rho \bar{P}_\kappa \tilde{h} \cdot \bar{q}. \quad (\text{E.13})$$

Our basis can then be written in a form that matches easily to leading-twist structures:

$$\begin{aligned}
f_1^{\mu\nu} &= g_{\mu\nu} h \cdot \bar{q}, & f_{10}^{\mu\nu} &= \bar{P}^\mu h^\nu + \bar{P}^\nu h^\mu, & (E.14) \\
f_2^{\mu\nu} &= \bar{P}^\mu \bar{P}^\nu h \cdot \bar{q}, & f_{11}^{\mu\nu} &= \bar{P}^\mu h^\nu - \bar{P}^\nu h^\mu, \\
f_3^{\mu\nu} &= (\bar{P}^\mu q'^\nu + \bar{P}^\nu q'^\mu) h \cdot \bar{q}, & f_{12}^{\mu\nu} &= h^\mu q'^\nu + h^\nu q'^\mu, \\
f_4^{\mu\nu} &= (\bar{P}^\mu q'^\nu - \bar{P}^\nu q'^\mu) h \cdot \bar{q}, & f_{13}^{\mu\nu} &= h^\mu q'^\nu - h^\nu q'^\mu, \\
f_5^{\mu\nu} &= g^{\mu\nu} e \cdot \bar{q}, & f_{14}^{\mu\nu} &= 2(\bar{P}^\mu \bar{q}_\alpha \bar{u}' i\sigma^{\alpha\nu} u + \bar{P}^\nu \bar{q}_\alpha \bar{u}' i\sigma^{\alpha\mu} u), \\
f_6^{\mu\nu} &= \bar{P}^\mu \bar{P}^\nu e \cdot \bar{q}, & f_{15}^{\mu\nu} &= i\varepsilon^{\mu\nu\rho\kappa} \bar{q}_\rho \bar{P}_\kappa \tilde{e} \cdot \bar{q}, \\
f_7^{\mu\nu} &= (\bar{P}^\mu q'^\nu + \bar{P}^\nu q'^\mu) e \cdot \bar{q}, & f_{16}^{\mu\nu} &= i\varepsilon^{\mu\nu\rho\kappa} \bar{q}_\rho \bar{P}_\kappa \tilde{h} \cdot \bar{q}, \\
f_8^{\mu\nu} &= (\bar{P}^\mu q'^\nu - \bar{P}^\nu q'^\mu) e \cdot \bar{q}, & f_{17}^{\mu\nu} &= i\varepsilon^{\mu\nu\rho\kappa} \bar{q}_\rho \tilde{e}_\kappa, \\
f_9^{\mu\nu} &= q'^\mu q'^\nu (h \cdot \bar{q} - e \cdot \bar{q}), & f_{18}^{\mu\nu} &= i\varepsilon^{\mu\nu\rho\kappa} \bar{q}_\rho \tilde{h}_\kappa.
\end{aligned}$$

This is the basis that gives us the final tensor decomposition, Eq. (5.11), after taking out factors of $1/\bar{P} \cdot \bar{q}$ to match conventions in the forward limit.

Due to the zero skewness condition, we can eliminate amplitudes that are odd under $\xi \rightarrow -\xi$. This eliminates the amplitudes for $i = 4, 8, 11, 13, 14, 15$. Therefore, the generators become

$$\begin{aligned}
f_1^{\mu\nu} &= g_{\mu\nu} h \cdot \bar{q}, & f_9^{\mu\nu} &= q'^\mu q'^\nu (h \cdot \bar{q} - e \cdot \bar{q}), & (E.15) \\
f_2^{\mu\nu} &= \bar{P}^\mu \bar{P}^\nu h \cdot \bar{q}, & f_{10}^{\mu\nu} &= \bar{P}^\mu h^\nu + \bar{P}^\nu h^\mu, \\
f_3^{\mu\nu} &= (\bar{P}^\mu q'^\nu + \bar{P}^\nu q'^\mu) h \cdot \bar{q}, & f_{12}^{\mu\nu} &= h^\mu q'^\nu + h^\nu q'^\mu, \\
f_5^{\mu\nu} &= g^{\mu\nu} e \cdot \bar{q}, & f_{16}^{\mu\nu} &= i\varepsilon^{\mu\nu\rho\kappa} \bar{q}_\rho \bar{P}_\kappa \tilde{h} \cdot \bar{q}, \\
f_6^{\mu\nu} &= \bar{P}^\mu \bar{P}^\nu e \cdot \bar{q}, & f_{17}^{\mu\nu} &= i\varepsilon^{\mu\nu\rho\kappa} \bar{q}_\rho \tilde{e}_\kappa, \\
f_7^{\mu\nu} &= (\bar{P}^\mu q'^\nu + \bar{P}^\nu q'^\mu) e \cdot \bar{q}, & f_{18}^{\mu\nu} &= i\varepsilon^{\mu\nu\rho\kappa} \bar{q}_\rho \tilde{h}_\kappa.
\end{aligned}$$

E.2.1 Gauge Projection

Since our Ward identities in the continuum are $q_\mu T^{\mu\nu} = 0 = T^{\mu\nu} q'_\mu$, our gauge projector is

$$\mathcal{P}^{\mu\nu} = g^{\mu\nu} - \frac{q'^\mu q'^\nu}{q \cdot q'}.$$

And hence our final tensor decomposition for the zero-skewness case is

$$T^{\mu\nu}(q, q'; P) = \sum_i A_i(\bar{\omega}, t, \bar{Q}^2) f_{\mu'\nu'}^i \mathcal{P}^{\mu\mu'} \mathcal{P}^{\nu'\nu}. \quad (E.16)$$

It is convenient to keep the gauge projectors implicit, particularly in the case of a lattice calculation, where the Ward identities will be broken by $\mathcal{O}(aq'^\mu)$ and $\mathcal{O}(aq'^\nu)$ terms. For

a conserved current on the lattice, the Ward identities are

$$\frac{2}{a} \sin(aq_\mu/2) T^{\mu\nu} = 0 = T^{\mu\nu} \frac{2}{a} \sin(aq'_\nu/2),$$

and hence the discretisation corrections are well-behaved, and our lattice projector can be changed accordingly:

$$\mathcal{P}_{\text{latt}}^{\mu\nu} = g^{\mu\nu} - \frac{\sin(aq'^\mu/2) \sin(aq^\nu/2)}{\sin(aq'^\alpha/2) \sin(aq_\alpha/2)}.$$

E.2.2 Comparison to OPE

Comparing to the OPE, the leading-twist contributions to the scalar amplitudes in Eq. (5.11) are

$$\begin{aligned} \mathcal{H}_1(\bar{\omega}, \vartheta, t) &= 2 \sum_{n=1}^{\infty} \bar{\omega}^{2n} \int_{-1}^1 dx x^{2n-1} H(x, \vartheta/\bar{\omega}, t), \\ \mathcal{H}_2(\bar{\omega}, \vartheta, t) &= \frac{2\bar{Q}^2}{\bar{P} \cdot \bar{q}} \sum_{n=1}^{\infty} \bar{\omega}^{2n} \int_{-1}^1 dx x^{2n-1} \left[H(x, \vartheta/\bar{\omega}, t) - \frac{1}{n} [H(x, \vartheta/\bar{\omega}, t) + E(x, \vartheta/\bar{\omega}, t)] \right], \\ \mathcal{H}_3(\bar{\omega}, \vartheta, t) &= \frac{2\bar{Q}^2}{\bar{P} \cdot \bar{q}} \sum_{n=1}^{\infty} \bar{\omega}^{2n} \frac{1}{n} \int_{-1}^1 dx x^{2n-1} [H(x, \vartheta/\bar{\omega}, t) + E(x, \vartheta/\bar{\omega}, t)], \\ \mathcal{E}_1(\bar{\omega}, \vartheta, t) &= 2 \sum_{n=1}^{\infty} \bar{\omega}^{2n} \int_{-1}^1 dx x^{2n-1} E(x, \vartheta/\bar{\omega}, t), \\ \mathcal{E}_2(\bar{\omega}, \vartheta, t) &= \frac{2\bar{Q}^2}{\bar{P} \cdot \bar{q}} \sum_{n=1}^{\infty} \bar{\omega}^{2n} \int_{-1}^1 dx x^{2n-1} E(x, \vartheta/\bar{\omega}, t), \\ \tilde{\mathcal{H}}_1(\bar{\omega}, \vartheta, t) &= 2 \sum_{n=1}^{\infty} \bar{\omega}^{2n-1} \int_{-1}^1 dx x^{2n-2} \tilde{H}(x, \vartheta/\bar{\omega}, t), \\ \tilde{\mathcal{E}}_1(\bar{\omega}, \vartheta, t) &= 2 \sum_{n=1}^{\infty} \bar{\omega}^{2n-1} \int_{-1}^1 dx x^{2n-2} \tilde{E}(x, \vartheta/\bar{\omega}, t), \\ \tilde{\mathcal{H}}_2(\bar{\omega}, \vartheta, t) &= 4 \sum_{n=1}^{\infty} \frac{n-1}{1-2n} \bar{\omega}^{2n-1} \int_{-1}^1 dx x^{2n-2} \tilde{H}(x, \vartheta/\bar{\omega}, t), \\ \tilde{\mathcal{E}}_2(\bar{\omega}, \vartheta, t) &= 4 \sum_{n=1}^{\infty} \frac{n-1}{1-2n} \bar{\omega}^{2n-1} \int_{-1}^1 dx x^{2n-2} \tilde{E}(x, \vartheta/\bar{\omega}, t), \\ \mathcal{K}_i(\bar{\omega}, \vartheta, t) &= 0, \quad \text{for all } i. \end{aligned} \tag{E.17}$$

Dirac Traces (Chs. 5-7)

For our Dirac traces, we consider the Dirac bilinears in Eq. (5.4):

$$\begin{aligned} h^\mu &= \bar{u}(P', s') \gamma^\mu u(P, s), & e^\mu &= \bar{u}(P', s') \frac{i\sigma^{\mu\alpha} \Delta_\alpha}{2m_N} u(P, s), \\ \tilde{h}^\mu &= \bar{u}(P', s') \gamma^\mu \gamma_5 u(P, s). \end{aligned}$$

Instead of \tilde{e}^μ as defined in Eq. (5.4), we will use the more general $\bar{u}(P', s') \gamma_5 u(P, s)$, which survives the $t \rightarrow 0$ limit.

For each of these bilinears, we are interested in the Dirac trace, which we denote by the function $\mathcal{F}(\Gamma, b)$:

$$\mathcal{F}(\Gamma, b) \equiv \frac{\sum_{s, s'} \text{tr}[\Gamma u(P', s') b \bar{u}(P, s)]}{\sum_s \text{tr}[\Gamma_{\text{unpol}} u(P', s') \bar{u}(P', s')]},$$

for some bilinear b , where Γ is a spin-parity projector. In this thesis, we only consider

$$\Gamma_{\text{unpol}} = \frac{1}{2}(\mathbb{I} + \gamma_0), \quad \Gamma_{\text{pol}} = \frac{1}{2}(\mathbb{I} + \gamma_0) \boldsymbol{\gamma} \cdot \hat{\mathbf{e}}_{\text{pol}} \gamma^5,$$

where $\hat{\mathbf{e}}_{\text{pol}}$ is the direction of the polarisation vector. For more general results, see Refs. [179, 203].

Note the following

- We are in the equal energy frame: $P^0 = P'^0 = \bar{P}^0 = E_N$.
- We use the notation $\varepsilon^{\mu\nu\rho V} = \varepsilon^{\mu\nu\rho\sigma} V_\sigma$ for the Levi-Civita.

Therefore, for the unpolarised spin-parity projector, we have

$$\begin{aligned} \mathcal{F}(\Gamma_{\text{unpol}}, h_\mu) &= 2\bar{P}_\mu + \frac{g_{0\mu} \Delta^2 - \Delta_0 \Delta_\mu}{2(E_N + m_N)}, \\ \mathcal{F}(\Gamma_{\text{unpol}}, e_\mu) &= \frac{\Delta^2 \bar{P}_\mu + m_N (g_{0\mu} \Delta^2 - \Delta_0 \Delta_\mu)}{2m_N (E_N + m_N)}, \\ \mathcal{F}(\Gamma_{\text{unpol}}, \tilde{h}_\mu) &= \frac{i\epsilon^{\mu 0 \Delta \bar{P}}}{E_N + m_N}, \\ \mathcal{F}(\Gamma_{\text{unpol}}, \bar{u}' \gamma_5 u) &= 0. \end{aligned} \tag{F.1}$$

For the polarised spin-parity projector, where we choose $\hat{\mathbf{e}}_{\text{pol}} = \hat{\mathbf{k}}$ for simplicity of notation, we get

$$\begin{aligned}
\mathcal{F}(\Gamma_{\text{pol}}, h_\mu) &= \frac{i(\epsilon_{k\mu\bar{P}\Delta} - m\epsilon_{k\mu\Delta 0})}{E_N + m_N}, \\
\mathcal{F}(\Gamma_{\text{pol}}, e_\mu) &= \left\{ (4m_N^2 + \Delta^2)\epsilon_{k\mu\Delta 0} - 2(\Delta_0 + 4m_N + 2E_N)\epsilon_{k\mu\bar{P}\Delta} - 2(2\bar{P}_k + \Delta_k)\epsilon_{\mu\bar{P}\Delta 0} \right. \\
&\quad \left. - 2(2\bar{P}_\mu - \Delta_\mu)\epsilon_{k\bar{P}\Delta 0} + 2\Delta^2\epsilon_{k\mu\bar{P}0} \right\} \left(8im_N(E_N + m_N) \right)^{-1}, \\
\mathcal{F}(\Gamma_{\text{pol}}, \tilde{h}_\mu) &= \frac{-4(m_N(E_N + m_N) - t/4)g^{k\mu} + 4\bar{P}^k(m_N g^{0\mu} + \bar{P}^\mu) + \Delta^\mu(2m_N g^{0k} - \Delta^k)}{2(E_N + m_N)}, \\
\mathcal{F}(\Gamma_{\text{pol}}, \bar{u}'\gamma_5 u) &= \frac{1}{4} \left(t g^{0k} - 2(E_N + m_N)\Delta^k + 2\Delta^0\bar{P}^k \right).
\end{aligned} \tag{F.2}$$

Forward kinematics

Setting $\bar{P} = P$ and $\Delta = 0$ gives us the forward limit. From Eq. (5.4), we note that $e_\mu = 0$ in the forward limit. Moreover, we denote the forward bilinears as

$$v_\mu = \bar{u}(P)\gamma_\mu u(P) = h_\mu \Big|_{P=P'}, \quad a_\mu = \bar{u}(P)\gamma_\mu\gamma_5 u(P) = \tilde{h}_\mu \Big|_{P=P'}, \tag{F.3}$$

which decouples them from their GPD associations.

Therefore, for the unpolarised projector, we have

$$\begin{aligned}
\mathcal{F}(\Gamma_{\text{unpol}}, v_\mu) &= 2P_\mu, \\
\mathcal{F}(\Gamma_{\text{unpol}}, a_\mu) &= 0, \\
\mathcal{F}(\Gamma_{\text{unpol}}, \bar{u}\gamma_5 u) &= 0.
\end{aligned} \tag{F.4}$$

Similarly, for the polarised spin-parity projector, we get

$$\begin{aligned}
\mathcal{F}(\Gamma_{\text{pol}}, v_\mu) &= 0, \\
\mathcal{F}(\Gamma_{\text{pol}}, a_\mu) &= \frac{-2(E_N + m_N)g^{k\mu} + 2P^k(m_N g^{0\mu} + P^\mu)}{E_N + m_N}, \\
\mathcal{F}(\Gamma_{\text{pol}}, \bar{u}\gamma_5 u) &= 0.
\end{aligned} \tag{F.5}$$

Off-forward N factors

Recall our final tensor decomposition in Chapter 6, Eq. (6.6):

$$T_{kk} = \frac{1}{2\bar{P} \cdot \bar{q}} \left(h \cdot \bar{q} \mathcal{H}_1 + e \cdot \bar{q} \mathcal{E}_1 \right),$$

and the spin-parity traced Compton amplitude, Eq. (4.55):

$$\mathcal{R}_{\mu\nu}^\Gamma \equiv \frac{\sum_{s,s'} \text{tr} [\Gamma u(P', s') T_{\mu\nu} \bar{u}(P, s)]}{\sum_s \text{tr} [\Gamma_{\text{unpol}} u(P', s) \bar{u}(P', s)]}.$$

Therefore, our N factors are simply

$$N_{\Gamma}^{\mathcal{H}} = \frac{\mathcal{F}(\Gamma, h \cdot \bar{q})}{2\bar{\mathbf{P}} \cdot \bar{q}}, \quad N_{\Gamma}^{\mathcal{E}} = \frac{\mathcal{F}(\Gamma, e \cdot \bar{q})}{2\bar{\mathbf{P}} \cdot \bar{q}}. \quad (\text{F.6})$$

Unpolarised

For the unpolarised projector, note that our choice of the current direction and $\mathbf{q}_{1,2}$ in chapters 5 and 6, means that $g_{0\mu}\Delta^2 - \Delta_0\Delta_{\mu}$ vanishes. Hence we arrive at the very simple linear combination

$$N_{\text{unpol}}^{\mathcal{H}} = 1, \quad N_{\text{unpol}}^{\mathcal{E}} = \frac{t}{4m_N(E_N + m_N)}. \quad (\text{F.7})$$

Polarised

For the polarised projector, the results are not as simple. First,

$$N_{\text{pol}}^{\mathcal{H}} = \frac{\mathcal{F}(\Gamma_{\text{pol}}, h \cdot \bar{q})}{2\bar{\mathbf{P}} \cdot \bar{q}} = \frac{1}{2\bar{\mathbf{P}} \cdot \bar{q}} \frac{i(\epsilon_{k\bar{q}\bar{\mathbf{P}}\Delta} - m\epsilon_{k\bar{q}\Delta 0})}{E_N + m_N}. \quad (\text{F.8})$$

Then, since in our choice of kinematics, \bar{q} , Δ and $\hat{\mathbf{k}}$ are all three vectors with no $\mu = 0$ component, we must have

$$\epsilon_{k\bar{q}\bar{\mathbf{P}}\Delta} = \bar{P}^0 \epsilon_{k\bar{q}0\Delta} = E_N \epsilon_{k\bar{q}0\Delta}, \quad (\text{F.9})$$

since the Levi-Civita vanishes if any one of the contracted vectors is linearly dependent with the others.

Then, with some rearranging, we have

$$N_{\text{pol}}^{\mathcal{H}} = \mathcal{F}(\Gamma_{\text{pol}}, h \cdot \bar{q}) = \frac{i(E_N + m)}{E_N + m_N} \epsilon_{k\bar{q}0\Delta} = i\epsilon_{0\bar{q}\Delta k} = \frac{i(\Delta \times \hat{\mathbf{k}}) \cdot \bar{\mathbf{q}}}{2\bar{\mathbf{P}} \cdot \bar{q}}. \quad (\text{F.10})$$

For the \mathcal{E} Compton form factor, we use

$$N_{\text{pol}}^{\mathcal{E}} = \frac{\mathcal{F}(\Gamma_{\text{pol}}, e \cdot \bar{q})}{2\bar{\mathbf{P}} \cdot \bar{q}}. \quad (\text{F.11})$$

To evaluate $\mathcal{F}(\Gamma_{\text{pol}}, e \cdot \bar{q})$, we note that

$$\begin{aligned} \epsilon_{k\bar{q}\Delta 0} &= -(\Delta \times \hat{\mathbf{k}}) \cdot \bar{\mathbf{q}}, & \epsilon_{k\bar{q}\bar{\mathbf{P}}\Delta} &= E_N(\Delta \times \hat{\mathbf{k}}) \cdot \bar{\mathbf{q}}, \\ \epsilon_{\bar{q}\bar{\mathbf{P}}\Delta 0} &= (\Delta \times \hat{\mathbf{P}}) \cdot \bar{\mathbf{q}}, & \epsilon_{k\bar{\mathbf{P}}\Delta 0} &= -(\Delta \times \hat{\mathbf{k}}) \cdot \bar{\mathbf{P}}, \\ \epsilon_{k\bar{q}\bar{\mathbf{P}}0} &= -(\bar{\mathbf{P}} \times \hat{\mathbf{k}}) \cdot \bar{\mathbf{q}}. \end{aligned} \quad (\text{F.12})$$

Substituting these into Eq. (F.2) and the choices we make in our lattice calculation, $\Delta^0 = 0$ and $\Delta \cdot \bar{q} = 0$, we get

$$\begin{aligned}
\mathcal{F}(\Gamma_{\text{pol}}, e \cdot \bar{q}) &= \left\{ (4m_N^2 + \Delta^2) \epsilon_{k\mu\Delta 0} - 2(\Delta_0 + 4m_N + 2E_N) \epsilon_{k\mu\bar{P}\Delta} \right. \\
&\quad \left. - 2(2\bar{P}_k + \Delta_k) \epsilon_{\mu\bar{P}\Delta 0} - 2(2\bar{P}_\mu - \Delta_\mu) \epsilon_{k\bar{P}\Delta 0} + 2\Delta^2 \epsilon_{k\mu\bar{P}0} \right\} \left(8im_N (E_N + m_N) \right)^{-1} \\
&= - \left\{ (4(E_N + m_N)^2 + \Delta^2) (\Delta \times \hat{\mathbf{k}}) \cdot \bar{\mathbf{q}} - 2(2\bar{P}_k + \Delta_k) (\Delta \times \hat{\mathbf{P}}) \cdot \bar{\mathbf{q}} \right. \\
&\quad \left. + 4\bar{P} \cdot \bar{q} (\Delta \times \hat{\mathbf{k}}) \cdot \bar{\mathbf{P}} - 2\Delta^2 (\bar{\mathbf{P}} \times \hat{\mathbf{k}}) \cdot \bar{\mathbf{q}} \right\} \left(8im_N (E_N + m_N) \right)^{-1} \\
&= i \left\{ ((E_N + m_N)^2 + t/4) (\Delta \times \hat{\mathbf{k}}) \cdot \bar{\mathbf{q}} - (\bar{P}_k + \Delta_k/2) (\Delta \times \hat{\mathbf{P}}) \cdot \bar{\mathbf{q}} \right. \\
&\quad \left. + \bar{P} \cdot \bar{q} (\Delta \times \hat{\mathbf{k}}) \cdot \bar{\mathbf{P}} - t/2 (\bar{\mathbf{P}} \times \hat{\mathbf{k}}) \cdot \bar{\mathbf{q}} \right\} \left(2m_N (E_N + m_N) \right)^{-1}
\end{aligned} \tag{F.13}$$

For simplicity, we normalise by $\mathcal{F}(\Gamma_{\text{pol}}, h \cdot \bar{q})$:

$$N_{\text{pol}}^{\mathcal{H}} = 1, \quad N_{\text{pol}}^{\mathcal{E}} = \frac{\mathcal{F}(\Gamma_{\text{pol}}, e \cdot \bar{q})}{\mathcal{F}(\Gamma_{\text{pol}}, h \cdot \bar{q})}, \tag{F.14}$$

which keeps the coefficient of \mathcal{H}_1 unity, as in the unpolarised case.

Polarised forward N factors

$$T_{12} = -\frac{i}{P \cdot q} q_3 \left(\tilde{g}_1 s^0 + \left(s^0 - \frac{s \cdot q}{P \cdot q} E_N \right) \tilde{g}_2 \right). \tag{F.15}$$

First, recall that the spin vector is defined as $s_\mu = a_\mu/2$ in Eq. (2.21).

Hence, since we must have $k \neq 0$, then

$$\mathcal{F}(\Gamma_{\text{pol}}, s_0) = \frac{1}{2} \mathcal{F}(\Gamma_{\text{pol}}, a_0) = \frac{P^k (E_N + m_N)}{E_N + m_N}. \tag{F.16}$$

And

$$\mathcal{F}(\Gamma_{\text{pol}}, s \cdot q) = \frac{1}{2} \mathcal{F}(\Gamma_{\text{pol}}, a \cdot q) = \frac{(E_N + m_N) q_k + P \cdot q P^k}{E_N + m_N}. \tag{F.17}$$

Hence, if we take $\hat{\mathbf{k}} = \hat{\mathbf{e}}_{\text{pol}}$, then we have

$$N_{e_{\text{pol}}}^{(1)} = -i \frac{\mathcal{F}(\Gamma_{e_{\text{pol}}}, s_0)}{P \cdot q} q_3, \quad N_{e_{\text{pol}}}^{(2)} = \frac{iq_3}{P \cdot q} \left[\frac{\mathcal{F}(\Gamma_{e_{\text{pol}}}, s \cdot q)}{P \cdot q} E_N - \mathcal{F}(\Gamma_{e_{\text{pol}}}, s_0) \right], \tag{F.18}$$

which gives us

$$N_{e_{\text{pol}}}^{(1)} = \frac{i \mathbf{p} \cdot \hat{\mathbf{e}}_{\text{pol}}}{\mathbf{p} \cdot \mathbf{q}} q_3, \quad N_{e_{\text{pol}}}^{(2)} = \frac{im_N q_3}{\mathbf{p} \cdot \mathbf{q}} \left[\frac{\mathbf{p} \cdot \hat{\mathbf{e}}_{\text{pol}}}{E_N + m_N} - \frac{E_N \mathbf{q} \cdot \hat{\mathbf{e}}_{\text{pol}}}{\mathbf{p} \cdot \mathbf{q}} \right]. \tag{F.19}$$

Feynman-Hellmann Parameter Fits (Chs. 5-8)

In this appendix we discuss our fits to the Feynman-Hellmann parameter, λ , as carried out in Chapters 5–8. We use data from Chapter 5. Using the χ^2 metric, these λ fits appear very poor with $\chi^2/\text{dof} \sim \mathcal{O}(10)$ and larger. On the other hand, judging by eye, the fits pass through the error bars of the data points (for instance, see Fig. 5.4), suggesting that the fits are reasonable. Here, we show that the large χ^2 values can be traced to the fact that the statistical fluctuations in the data are highly correlated for the two values of the Feynman-Hellmann parameter, λ . Highly correlated data and its effect on the χ^2 has been studied in the context of lattice QCD before, and alternative goodness-of-fit measures have been proposed [325–327]. However, we limit ourselves to describing the nature of the problem, and do not discuss alternative metrics.

The χ^2 metric

In the following discussion, our data is the ratio R_λ , defined in Eq. (4.53), where the Euclidean time fits have already been performed. Therefore, for a given sink momentum, \mathbf{p}' , and a given λ , our data R_λ has N samples*. Moreover, we only consider the case where there are two λ values.

We start by defining the elements of the sample covariance matrix, C :

$$C_{ij} = \frac{1}{N-1} \sum_{n=1}^N (R_{\lambda_i}^{(n)} - \bar{R}_{\lambda_i})(R_{\lambda_j}^{(n)} - \bar{R}_{\lambda_j}), \quad (\text{G.1})$$

where $R_{\lambda_i}^{(n)}$ is the n^{th} sample of the ratio for λ_i , and \bar{R}_{λ_i} is the average of the samples for the same λ .

In terms of the sample covariance matrix, the χ^2 is

$$\chi^2 = \sum_{i,j=1}^2 (R_{\lambda_i}^{\text{fit}} - \bar{R}_{\lambda_i}) [C^{-1}]_{ij} (R_{\lambda_j}^{\text{fit}} - \bar{R}_{\lambda_j}). \quad (\text{G.2})$$

It is useful to define the vector in the space of samples:

$$\mathbf{r}_{\lambda_i}^{(n)} = R_{\lambda_i}^{(n)} - \bar{R}_{\lambda_i}. \quad (\text{G.3})$$

*In the way we perform statistical analysis, N is the number of bootstraps [99].

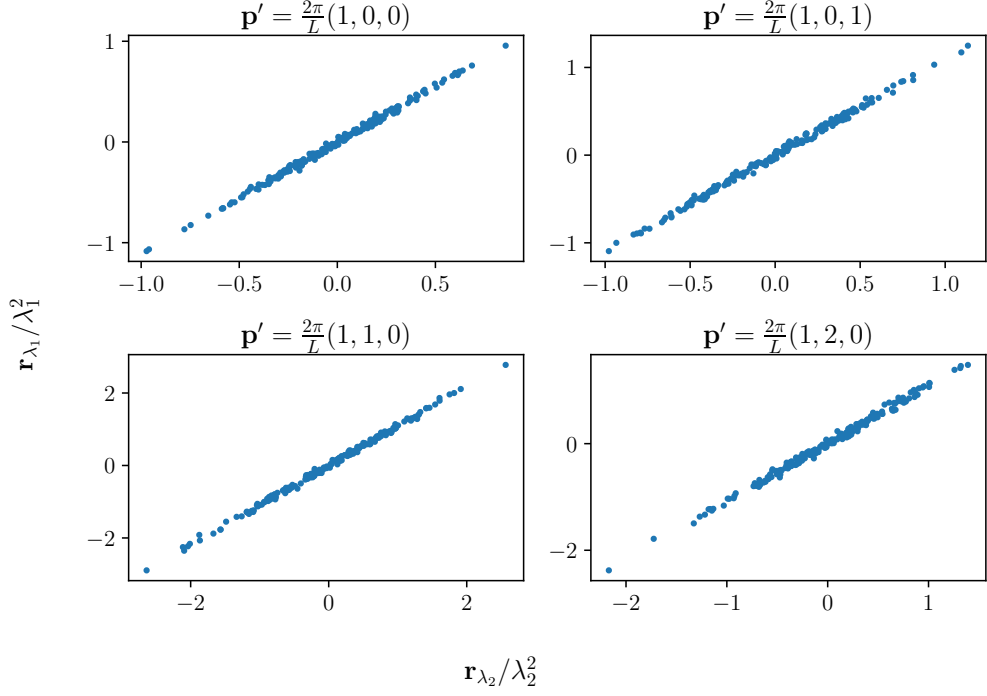


Figure G.1: Plots of $\mathbf{r}_{\lambda_1}/\lambda_1^2$ against $\mathbf{r}_{\lambda_2}/\lambda_2^2$ for the $t = -1.10 \text{ GeV}^2$ data from Chapter 5, with \mathbf{r}_{λ_i} defined in Eq. (G.3). Each data point is the n^{th} sample. Clearly, statistical fluctuations are highly correlated for the two λ values.

Using this vector, we write the covariance matrix as

$$C_{ij} = \frac{1}{N-1} \mathbf{r}_{\lambda_i} \cdot \mathbf{r}_{\lambda_j}. \quad (\text{G.4})$$

Hence the inverse is

$$C^{-1} = \frac{1}{\det C} \frac{1}{N-1} \begin{pmatrix} \mathbf{r}_{\lambda_2} \cdot \mathbf{r}_{\lambda_2} & -\mathbf{r}_{\lambda_2} \cdot \mathbf{r}_{\lambda_1} \\ -\mathbf{r}_{\lambda_1} \cdot \mathbf{r}_{\lambda_2} & \mathbf{r}_{\lambda_1} \cdot \mathbf{r}_{\lambda_1} \end{pmatrix}, \quad (\text{G.5})$$

with

$$\det C = \frac{1}{N-1} \left(|\mathbf{r}_{\lambda_1}|^2 |\mathbf{r}_{\lambda_2}|^2 - (\mathbf{r}_{\lambda_1} \cdot \mathbf{r}_{\lambda_2})^2 \right). \quad (\text{G.6})$$

Therefore, if \mathbf{r}_{λ_1} and \mathbf{r}_{λ_2} are approximately parallel (i.e. statistical fluctuations in the two data sets are highly correlated), then $\det C \approx 0$ and hence $1/\det C$ blows up. Since $\chi^2 \sim (\det C)^{-1}$, this can cause a very large χ^2 , even for good agreement between the data and the fit (i.e. small $R_{\lambda_i}^{\text{fit}} - \bar{R}_{\lambda_i}$).

We can see in Fig. G.1 that the statistical fluctuations in \mathbf{r}_{λ} are highly correlated for the two λ values: the two distributions are almost identical. Similarly, comparing the values of $\det C$ in Table G.1, we can see that all momentum projections have extremely small values of $\det C$, with the largest χ^2 corresponding to the smallest $\det C$. This strongly suggests that the large χ^2 values are caused by highly correlated statistical fluctuations in the two λ values.

Table G.1: Relevant quantities for the up quark data, $t = -1.10 \text{ GeV}^2$ in Chapter 5.

\mathbf{n}'	χ^2/dof	$\det C$
(1,0,0)	216	2×10^{-19}
(1,0,1)	91.0	3×10^{-19}
(1,0,2)	0.18	7×10^{-18}
(1,1,-1)	9.53	1×10^{-19}
(1,1,0)	89.8	4×10^{-19}
(1,1,1)	16.9	8×10^{-19}
(1,2,0)	1.81	2×10^{-17}

The strong correlation between the data at two different λ values is unsurprising, since we generate our perturbed quark propagators by

$$S_\lambda = [M - \lambda\mathcal{O}]^{-1}, \quad (\text{G.7})$$

where the majority of the statistical noise comes from the gauge fields in M , the unperturbed fermion matrix, Eq. (3.18). As such, we expect the statistical fluctuations for two different λ values to be almost exactly correlated—this is what we see in Fig. G.1.

Again, we refer the reader to the existing literature [325–327] for a discussion of alternative goodness-of-fit metrics.

Additional Lattice Results (Ch. 6)

In this appendix, we present some additional results from the calculation presented in Chapter 6. In particular, for the Euclidean time dependence of the polarised, $t = -0.57 \text{ GeV}^2$ results, and for the unpolarised $t = -0.29, -1.14 \text{ GeV}^2$ results. We also plot the $\bar{\omega}$ dependence of the $t = -0.29, -1.14 \text{ GeV}^2$ data sets.

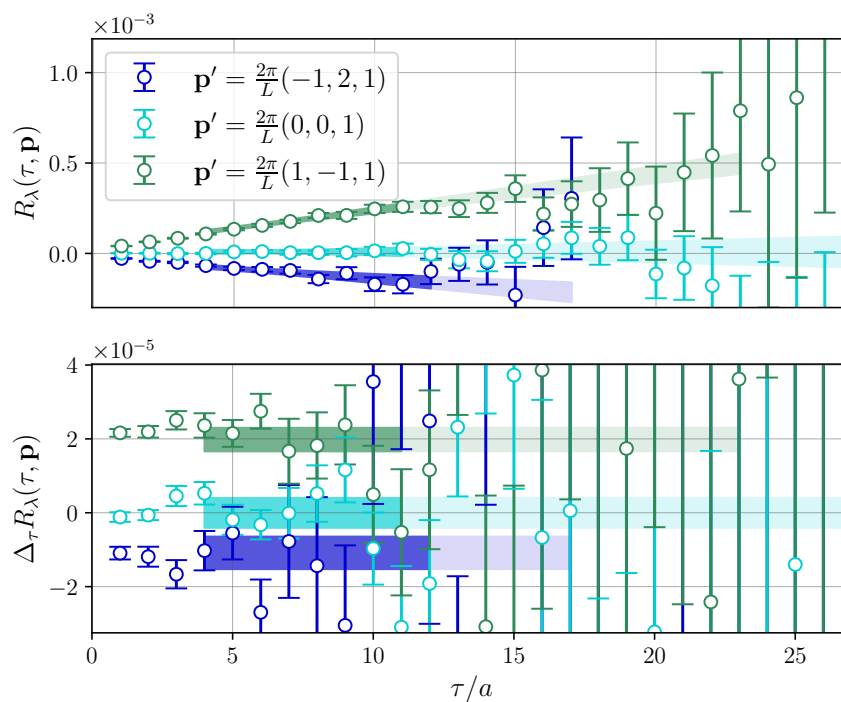


Figure H.1: Plot of τ fits for R_λ , as defined in Eq. (4.53) and the ‘effective mass’, $\Delta_\tau R_\lambda$, defined in Eq. (6.24), for the up quarks, *polarised*, and $\lambda = 0.0125$, $t = -0.57 \text{ GeV}^2$. The shaded bands are fits to the function $f(\tau) = a\tau + b$ using weighted averages; the lighter shade is the whole range considered, and the darker shade is the fit window with the highest weight.

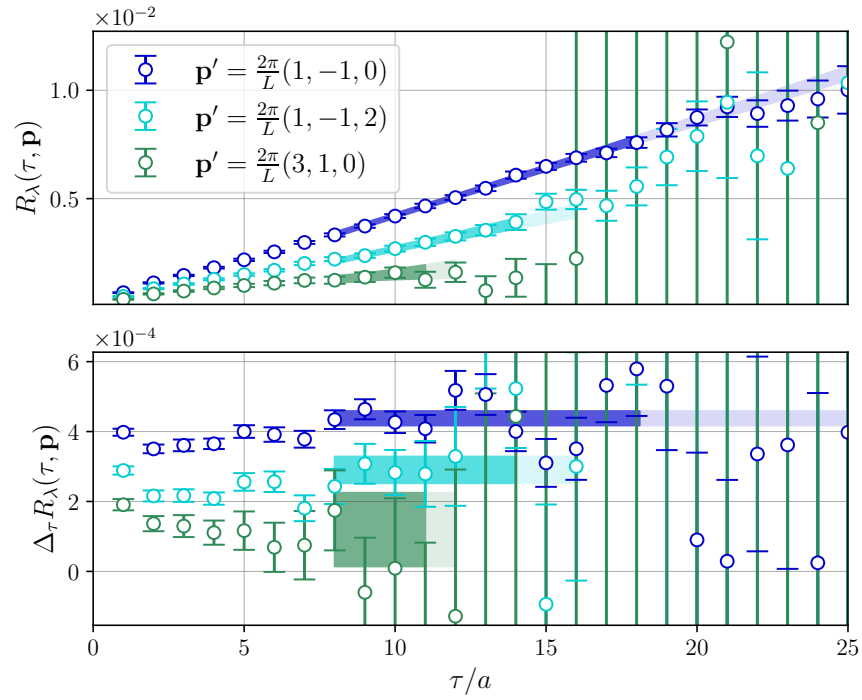


Figure H.2: The same plot as Fig. H.1 but for the unpolarised projector and $t = -0.29 \text{ GeV}^2$.

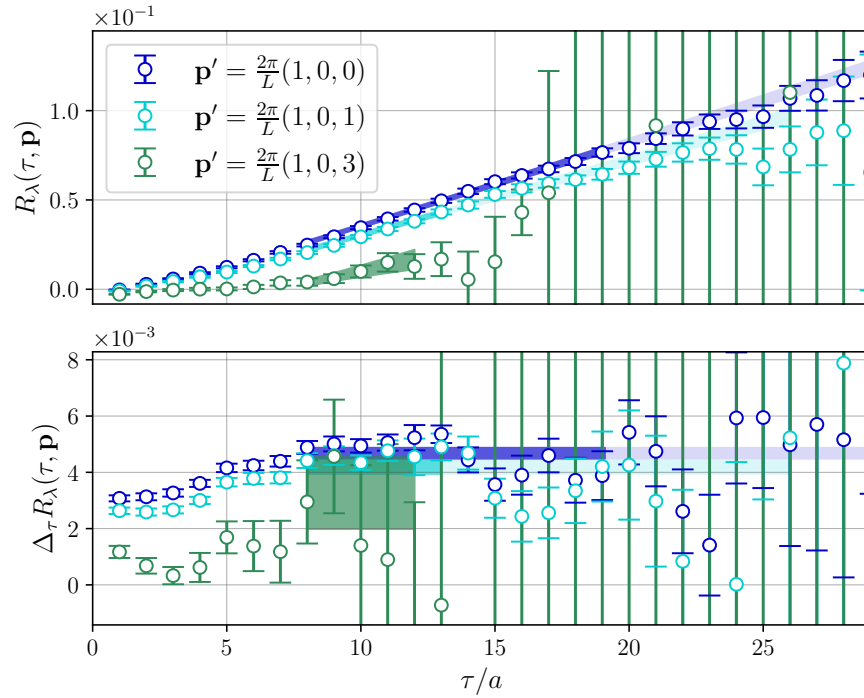


Figure H.3: The same plot as Fig. H.2 but for the $t = -1.14 \text{ GeV}^2$ data.

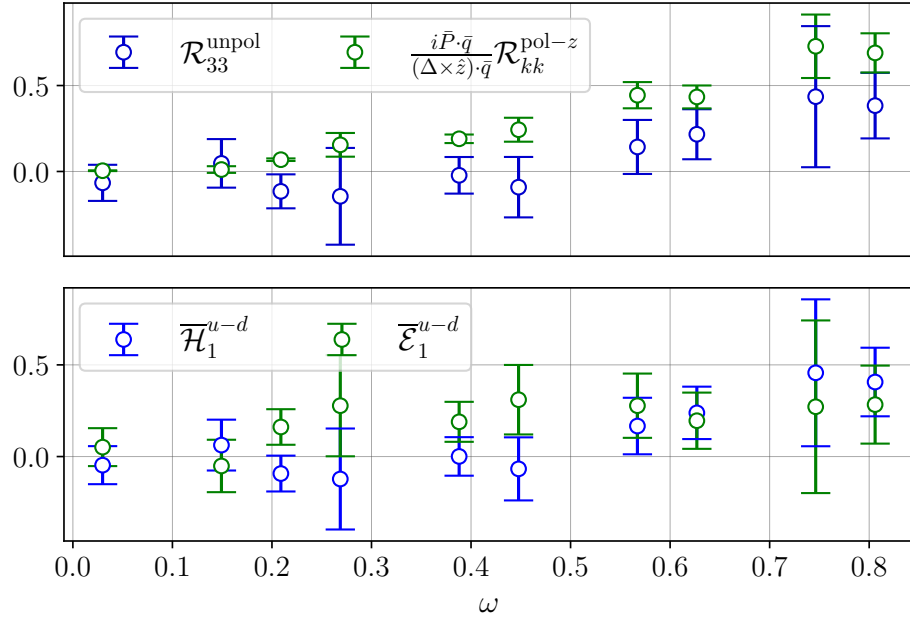


Figure H.4: Top: the quantity \mathcal{R}_{kk}^Γ , as defined in Eq. (4.55), for $t = -0.29 \text{ GeV}^2$, $u - d$ quarks; note the polarised is normalised to keep the pre-factor of \mathcal{H}_1 unity. Bottom: the extracted Compton form factors.

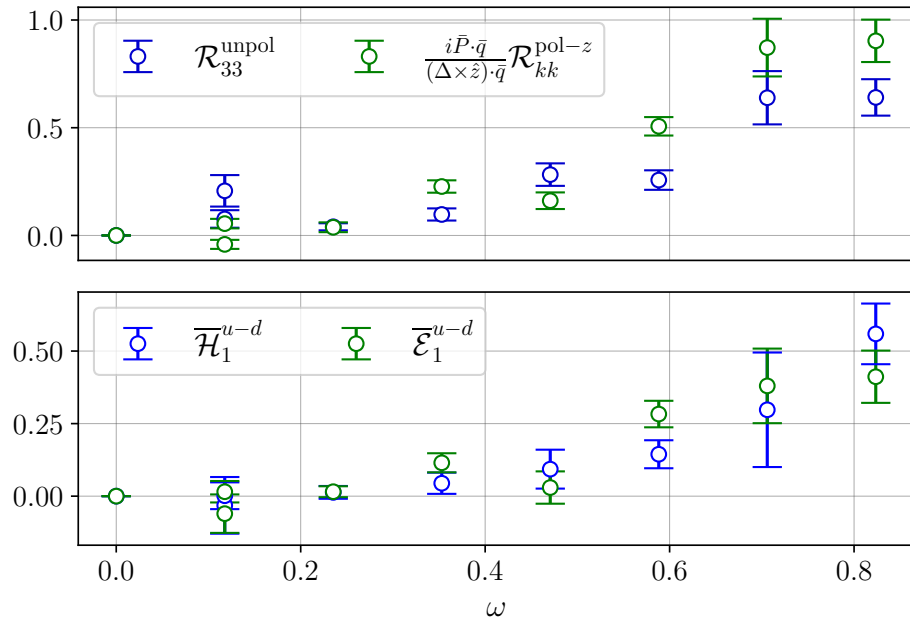


Figure H.5: The same plot as Fig. H.4 but for $t = -1.14 \text{ GeV}^2$.

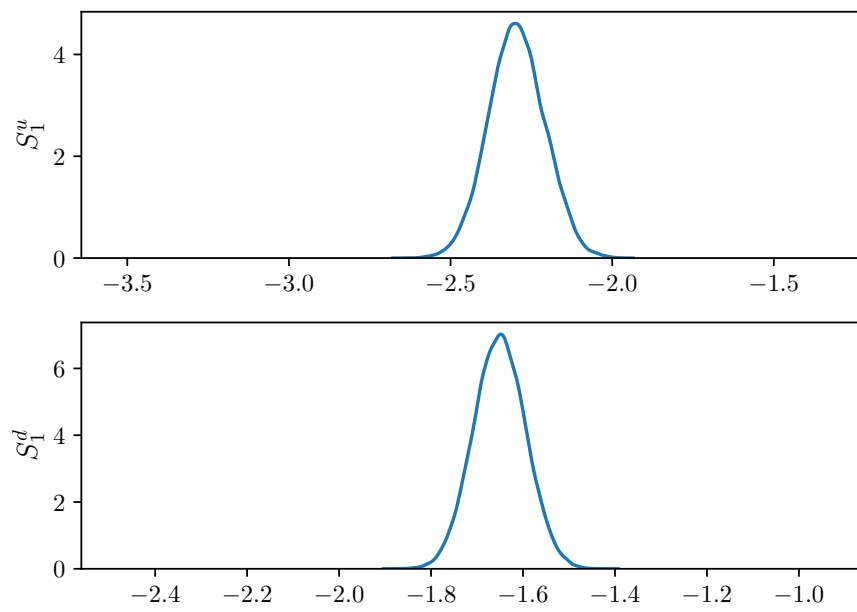


Figure H.6: Posterior distribution for the fit to the subtraction function, Eq. (6.31), for the data set with $t = -0.29 \text{ GeV}^2$. The limits of the x -axis are the limits of the prior distribution, given in Eq. (6.33).

Supplementary Calculations

(Ch. 8)

In this appendix, we present some supplementary calculations to Chapter 8. First, in Section I.1 we present our the OPE prediction of the subtraction function from Ref. [291], using inputs calculated on one of our gauge ensembles. Then, in Section I.2 we present our calculation of the scalar charge for a structureless Wilson fermion.

I.1 OPE of the Subtraction Function

We compare our Feynman-Hellmann subtraction function results to the prediction from the OPE given in Ref. [291]. We use inputs from lattice ensemble in Table 5.1: the mass, the scalar charges [174], and the structure function (parton distribution function) moments [37].

From Ref. [291], the spin-0 and spin-2 contributions to the nucleon subtraction function for a quark of flavour f are

$$S_1^f(Q^2) = \frac{2}{Q^2}(2m_N^2 a_2^f - \sigma_f), \quad (\text{I.1})$$

where a_2 is the second PDF moment and

$$\sigma_f = m_f \langle P | \bar{\psi}_f \psi_f | P \rangle = 2m_N m_f a_s^f, \quad (\text{I.2})$$

with a_s^f the scalar charge. Note that we ignore the ‘gluon contributions’ from Ref. [291], since these correspond to disconnected diagrams, which are not calculated in our Feynman-Hellmann implementation.

Finally,

$$S_1(Q^2) = \sum_f e_f^2 S_1^f(Q^2). \quad (\text{I.3})$$

The result is plotted against our Feynman-Hellmann results in Figs. 8.1 and 8.15.

I.2 Structureless Fermion Scalar Charge

In Chapter 8, in order to compare the lattice perturbation theory to our Feynman-Hellmann results for a structureless fermion, we needed to determine the matrix element

$\langle p|\bar{\psi}\psi|p\rangle = 2E_{\mathbf{p}}a_s$, where $|p\rangle$ is a structureless fermion state and a_s is the scalar charge. In the continuum, $a_s = 1$, while on the lattice it is $a_s = 1 + \mathcal{O}(a)$. In this section, we present two methods to calculate the scalar charge, and show that they are equivalent.

Three-Point Function

The three-point function we start with is

$$\langle \psi(x)\bar{\psi}(y)\gamma_4\psi(y)\bar{\psi}(0)\rangle_T. \quad (\text{I.4})$$

We wish to calculate the partial Fourier transform of this quantity:

$$\mathcal{G}_{3\text{-pt}}(\mathbf{k}, t, \tau) = \sum_{\mathbf{x}, \mathbf{y}} e^{-i\mathbf{k}\cdot\mathbf{x}} \langle \psi(x)\bar{\psi}(y)\gamma_4\psi(y)\bar{\psi}(0)\rangle_T, \quad (\text{I.5})$$

where $x_4 = \tau$, $y_4 = \tau'$.

It is simple to show that the above equation can be expressed as

$$\mathcal{G}_{3\text{-pt}}(\mathbf{k}, \tau, \tau') = \frac{1}{\mathcal{Z}_T} \frac{\langle 0|\psi(0)|k\rangle\langle k|\bar{\psi}(0)|0\rangle}{2E_{\mathbf{k}}} e^{-E_{\mathbf{k}}(\tau-\tau')} \gamma_4 \frac{\langle 0|\psi(0)|k\rangle\langle k|\bar{\psi}(0)|0\rangle}{2E_{\mathbf{k}}} e^{-E_{\mathbf{k}}\tau'}, \quad (\text{I.6})$$

ignoring the negative parity state.

Or equivalently,

$$\begin{aligned} \mathcal{G}_{3\text{-pt}}(\mathbf{k}, \tau, \tau') &= \frac{1}{\mathcal{Z}_T} \frac{\langle 0|\psi(0)|k\rangle\langle k|\bar{\psi}(0)|0\rangle}{(2E_{\mathbf{k}})^2} \langle k|\bar{\psi}(0)\psi(0)|k\rangle e^{-E_{\mathbf{k}}\tau} \\ &= \frac{1}{\mathcal{Z}_T} \frac{u(\mathbf{k})\bar{u}(\mathbf{k})}{2E_{\mathbf{k}}} a_s e^{-E_{\mathbf{k}}\tau}, \end{aligned} \quad (\text{I.7})$$

where a_s is the scalar charge and $u(\mathbf{k})$ is a spinor for a positive parity fermion.

In contrast to our derivations of the nucleon n -point functions in Chapter 3, we retain the partition function $\mathcal{Z}_T = 1 + e^{-E_{\mathbf{k}}T}$. Unlike all other matrix elements we have so far discussed, for the structureless fermions we take am close to zero, and hence $e^{-E_{\mathbf{k}}T}$ is not approximately zero. Therefore, $\mathcal{Z}_T \approx 1$ is not a good approximation for our finest discretisations.

The free Wilson fermion propagator has the exact solution:

$$S(k) = \sum_{k_\mu} e^{ik\cdot(x-y)} \langle \psi(x)\bar{\psi}(y)\rangle_T = a \frac{\mathcal{M}(k) - i\gamma_\mu \sin(ak_\mu)}{\mathcal{M}(k)^2 + \sum_\mu \sin^2(ak_\mu)}, \quad (\text{I.8})$$

where

$$\mathcal{M}(k) = am_0 + \sum_\mu \left(1 - \cos(ak_\mu)\right) \quad (\text{I.9})$$

Therefore, a partial Fourier transform gives us the time-momentum propagator:

$$S(\mathbf{k}, \tau) = \sum_{k_4} e^{ik_4\tau} a \frac{\mathcal{M}(k) - i\gamma_\mu \sin(ak_\mu)}{\mathcal{M}(k)^2 + \sum_\mu \sin^2(ak_\mu)}. \quad (\text{I.10})$$

In terms of operators, this is

$$\begin{aligned} S(\mathbf{k}, \tau) &= \frac{1}{\mathcal{Z}_T} \langle 0 | \psi(0) | k \rangle \langle k | \bar{\psi}(0) | 0 \rangle e^{-E_{\mathbf{k}} \tau} \\ &= \frac{1}{\mathcal{Z}_T} \frac{u(\mathbf{k}) \bar{u}(\mathbf{k})}{2E_{\mathbf{k}}} e^{-E_{\mathbf{k}} \tau}, \end{aligned} \quad (\text{I.11})$$

where we again ignore the negative parity state.

Therefore, Eq. (I.6) can be expressed as

$$\mathcal{G}_{3\text{-pt}}(\mathbf{k}, t, \tau) = \mathcal{Z}_T S(\mathbf{k}, t - \tau) \gamma_4 S(\mathbf{k}, \tau). \quad (\text{I.12})$$

Note that since each Wilson propagator carries a factor of $1/\mathcal{Z}_T$, whereas our three-point function needs only one such term, we multiply by \mathcal{Z}_T to fix this normalisation. Although this makes little difference where $N_T \gg (am)^{-1}$, since we take $am \rightarrow 0$ with N_T fixed, we need to keep the partition function explicit.

More explicitly, we calculate the ratio

$$R_s(\mathbf{k}, t) = \frac{\text{tr} \left\{ \Gamma_{\text{unpol}} \mathcal{G}_{3\text{-pt}}(\mathbf{k}, t, \tau) \right\}}{\text{tr} \left\{ \Gamma_{\text{unpol}} S(\mathbf{k}, t) \right\}} = \frac{\text{tr} \left\{ \Gamma_{\text{unpol}} \mathcal{Z}_T S(\mathbf{k}, t - \tau) \gamma_4 S(\mathbf{k}, \tau) \right\}}{\text{tr} \left\{ \Gamma_{\text{unpol}} S(\mathbf{k}, t) \right\}} = a_s, \quad (\text{I.13})$$

the scalar charge. It is best to set $\mathbf{k} = \mathbf{0}$.

Feynman-Hellmann

While Eq. (I.13) is fairly straightforward to compute, especially compared to nucleon three-point functions, we can derive a simpler and totally analytic expression for a_s for Wilson fermions.

Using the Feynman-Hellmann theorem for sigma terms [165], we have

$$a_s = \frac{\partial m_{\text{pole}}}{\partial m_0}, \quad (\text{I.14})$$

where m_{pole} is the pole mass from the Wilson fermion propagator.

The pole mass can be found by solving the following equation for $m_{\text{pole}} = -ik_4$:

$$\left(am_0 + 2 \sin \left(\frac{iam_{\text{pole}}}{2} \right) \right)^2 + \sin(iam_{\text{pole}})^2 = 0. \quad (\text{I.15})$$

From this we find a range of solutions:

$$am_{\text{pole}} = \pm \log(1 + am_0) + 4i\pi n, \quad \text{for } n \in \mathbb{Z}. \quad (\text{I.16})$$

Since the Taylor series of $\log(1 + x)$ is

$$\log(1 + x) = x - \frac{x^2}{2} + \frac{x^3}{3} - \frac{x^4}{4} + \dots \quad (\text{I.17})$$

this means that the positive pole mass is $am_{\text{pole}} = \log(1 + am_0)$.

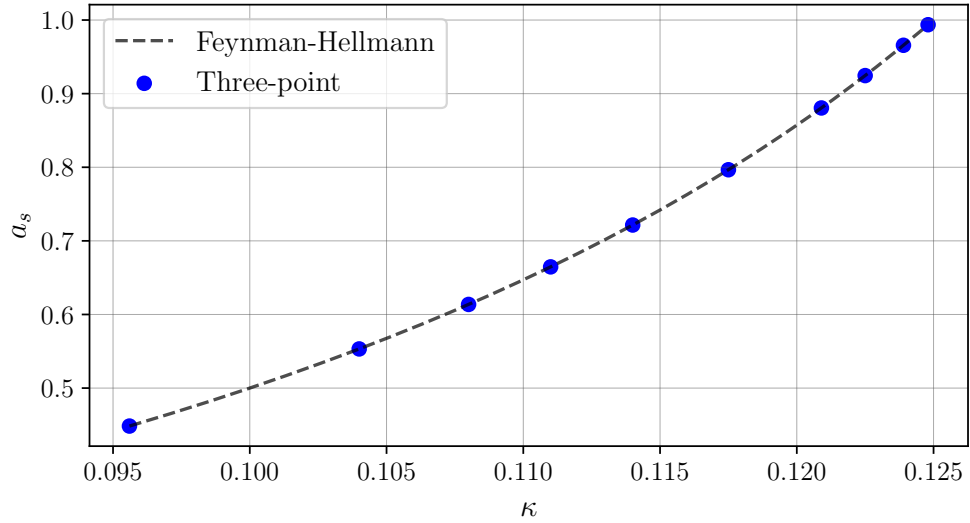


Figure I.1: Comparison of the structureless fermion scalar charge calculated using Eq. (I.13) (three-point), to the same quantity calculated with Eq. (I.18) (Feynman-Hellmann).

Therefore,

$$a_s = \frac{\log(1 + am_0)}{\partial m_0} = \frac{1}{1 + am_0}. \quad (\text{I.18})$$

Although much simpler, this expression for the scalar charge is less fundamental than the three-point expression in Eq. (I.13). However, comparing the values from the two different methods for a range of $\kappa = 0.1080 - 0.1248$ and $N_T = 64$, they match remarkably well, as shown in Fig. I.1. Note that for $\kappa = 0.095$ the discrepancy between the Feynman-Hellmann and three-point results is $\sim 10^{-9}$, while for $\kappa = 0.1248$ the discrepancy is $\sim 10^{-15}$, both of which are negligible given that $a_s \sim 1$. Therefore, we use Eq. (I.18) for our structureless fermion scalar charges in Chapter 8.

Bibliography

- [1] E. Rutherford, “The scattering of alpha and beta particles by matter and the structure of the atom,” *Phil. Mag. Ser.6*, vol. 21, pp. 669–688, 1911.
- [2] J. Chadwick, “The Existence of a Neutron,” *Proc. Roy. Soc. Lond. A*, vol. 136, no. 830, pp. 692–708, 1932.
- [3] H. Yukawa, “On the Interaction of Elementary Particles I,” *Proc. Phys. Math. Soc. Jap.*, vol. 17, pp. 48–57, 1935.
- [4] M. Gell-Mann, “A Schematic Model of Baryons and Mesons,” *Phys. Lett.*, vol. 8, pp. 214–215, 1964.
- [5] J. D. Bjorken, “Asymptotic sum rules at infinite momentum,” *Phys. Rev.*, vol. 179, pp. 1547–1553, Mar 1969.
- [6] T. Y. Cao, *From current algebra to quantum chromodynamics: A case for structural realism*. Cambridge, UK: Cambridge Univ. Pr., 2010.
- [7] E. D. Bloom, D. H. Coward, H. DeStaebler, J. Drees, G. Miller, L. W. Mo, R. E. Taylor, M. Breidenbach, J. I. Friedman, G. C. Hartmann, and H. W. Kendall, “High-energy inelastic e-p scattering at 6 degrees and 10 degrees,” *Phys. Rev. Lett.*, vol. 23, pp. 930–934, Oct 1969.
- [8] R. P. Feynman, “Very high-energy collisions of hadrons,” *Phys. Rev. Lett.*, vol. 23, pp. 1415–1417, 1969.
- [9] C. G. Callan, Jr. and D. J. Gross, “High-energy electroproduction and the constitution of the electric current,” *Phys. Rev. Lett.*, vol. 22, pp. 156–159, 1969.
- [10] H. Fritzsch and M. Gell-Mann, “Current algebra: Quarks and what else?,” *eConf*, vol. C720906V2, pp. 135–165, 1972.
- [11] D. J. Gross and F. Wilczek, “Ultraviolet behavior of non-abelian gauge theories,” *Phys. Rev. Lett.*, vol. 30, pp. 1343–1346, Jun 1973.
- [12] H. D. Politzer, “Reliable perturbative results for strong interactions?,” *Phys. Rev. Lett.*, vol. 30, pp. 1346–1349, Jun 1973.
- [13] K. G. Wilson, “Confinement of Quarks,” *Phys. Rev.*, vol. D10, pp. 2445–2459, 1974.
- [14] J. C. Collins, D. E. Soper, and G. Sterman, “Factorization of hard processes in qcd,” 2004.
- [15] J. Collins, “Foundations of perturbative QCD,” *Camb. Monogr. Part. Phys. Nucl. Phys. Cosmol.*, vol. 32, pp. 1–624, 2011.

-
- [16] J. Ashman *et al.*, “A measurement of the spin asymmetry and determination of the structure function g_1 in deep inelastic muon-proton scattering,” *Physics Letters B*, vol. 206, no. 2, pp. 364 – 370, 1988.
- [17] E. S. Ageev *et al.*, “Measurement of the spin structure of the deuteron in the DIS region,” *Phys. Lett. B*, vol. 612, pp. 154–164, 2005.
- [18] V. Y. Alexakhin *et al.*, “The Deuteron Spin-dependent Structure Function $g_1(d)$ and its First Moment,” *Phys. Lett. B*, vol. 647, pp. 8–17, 2007.
- [19] A. Airapetian *et al.*, “Precise determination of the spin structure function $g(1)$ of the proton, deuteron and neutron,” *Phys. Rev. D*, vol. 75, p. 012007, 2007.
- [20] A. Belitsky and D. Müller, “Twist-three effects in two-photon processes,” *Nuclear Physics B*, vol. 589, p. 611–630, Nov 2000.
- [21] A. V. Radyushkin, “Nonforward parton distributions,” *Physical Review D*, vol. 56, p. 5524–5557, Nov 1997.
- [22] X. Ji, “Gauge-invariant decomposition of nucleon spin,” *Physical Review Letters*, vol. 78, p. 610–613, Jan 1997.
- [23] M. Burkardt, “Impact parameter dependent parton distributions and off-forward parton distributions for $\zeta \rightarrow 0$,” *Phys. Rev. D*, vol. 62, p. 071503, Sep 2000.
- [24] M. Polyakov, “Generalized parton distributions and strong forces inside nucleons and nuclei,” *Physics Letters B*, vol. 555, p. 57–62, Feb 2003.
- [25] A. Accardi *et al.*, “Electron Ion Collider: The Next QCD Frontier: Understanding the glue that binds us all,” *Eur. Phys. J. A*, vol. 52, no. 9, p. 268, 2016.
- [26] M. Creutz, L. Jacobs, and C. Rebbi, “Experiments with a Gauge Invariant Ising System,” *Phys. Rev. Lett.*, vol. 42, p. 1390, 1979.
- [27] K. Symanzik, “Continuum Limit and Improved Action in Lattice Theories. 1. Principles and ϕ^4 Theory,” *Nucl. Phys. B*, vol. 226, pp. 187–204, 1983.
- [28] C. Best, M. Gockeler, R. Horsley, E.-M. Ilgenfritz, H. Perlt, P. E. L. Rakow, A. Schafer, G. Schierholz, A. Schiller, and S. Schramm, “Pion and rho structure functions from lattice QCD,” *Phys. Rev. D*, vol. 56, pp. 2743–2754, 1997.
- [29] G. Martinelli and C. T. Sachrajda, “A Lattice Calculation of the Pion’s Form-Factor and Structure Function,” *Nucl. Phys. B*, vol. 306, pp. 865–889, 1988.
- [30] G. Martinelli and C. Sachrajda, “On the difficulty of computing higher-twist corrections,” *Nuclear Physics B*, vol. 478, p. 660–684, Nov 1996.
- [31] Y. Aoki, “Non-perturbative renormalization in lattice QCD,” *PoS*, vol. LAT2009, p. 012, 2009.
- [32] X. Ji, “Parton physics on a euclidean lattice,” *Physical Review Letters*, vol. 110, Jun 2013.

-
- [33] A. Radyushkin, “Quasi-parton distribution functions, momentum distributions, and pseudo-parton distribution functions,” *Physical Review D*, vol. 96, Aug 2017.
- [34] Y.-Q. Ma and J.-W. Qiu, “Exploring partonic structure of hadrons using ab initio lattice qcd calculations,” *Phys. Rev. Lett.*, vol. 120, p. 022003, Jan 2018.
- [35] R. S. Sufian, J. Karpie, C. Egerer, K. Orginos, J.-W. Qiu, and D. G. Richards, “Pion Valence Quark Distribution from Matrix Element Calculated in Lattice QCD,” *Phys. Rev. D*, vol. 99, no. 7, p. 074507, 2019.
- [36] A. Chambers, R. Horsley, Y. Nakamura, H. Perlt, P. Rakow, G. Schierholz, A. Schiller, K. Somfleth, R. Young, and J. Zanotti, “Nucleon structure functions from operator product expansion on the lattice,” *Physical Review Letters*, vol. 118, Jun 2017.
- [37] K. Can, A. Hannaford-Gunn, R. Horsley, Y. Nakamura, H. Perlt, P. Rakow, G. Schierholz, K. Somfleth, H. Stüben, R. Young, and J. M. Zanotti, “Lattice qcd evaluation of the compton amplitude employing the feynman-hellmann theorem,” *Physical Review D*, vol. 102, Dec 2020.
- [38] M. Batelaan, K. Can, A. Hannaford-Gunn, R. Horsley, Y. Nakamura, H. Perlt, P. Rakow, G. Schierholz, H. Stüben, R. Young, and J. Zanotti, “Moments and power corrections of longitudinal and transverse proton structure functions from lattice QCD,” *Phys. Rev. D*, vol. 107, no. 5, p. 054503, 2023.
- [39] A. Hannaford-Gunn, K. U. Can, R. Horsley, Y. Nakamura, H. Perlt, P. E. L. Rakow, H. Stüben, G. Schierholz, R. D. Young, and J. M. Zanotti, “Generalized parton distributions from the off-forward Compton amplitude in lattice QCD,” *Phys. Rev. D*, vol. 105, no. 1, p. 014502, 2022.
- [40] A. Hannaford-Gunn, E. Sankey, K. U. Can, R. Horsley, H. Perlt, P. E. L. Rakow, G. Schierholz, K. Somfleth, H. Stüben, R. D. Young, and J. M. Zanotti, “Investigating the Compton amplitude subtraction function in lattice QCD,” *PoS*, vol. LAT-TICE2021, p. 028, 2022.
- [41] J. D. Bjorken and E. A. Paschos, “Inelastic Electron Proton and gamma Proton Scattering, and the Structure of the Nucleon,” *Phys. Rev.*, vol. 185, pp. 1975–1982, 1969.
- [42] D. Müller, D. Robaschik, B. Geyer, F.-M. Dittes, and J. Hořejši, “Wave functions, evolution equations and evolution kernels from light-ray operators of qcd,” *Fortschritte der Physik/Progress of Physics*, vol. 42, no. 2, p. 101–141, 1994.
- [43] A. Radyushkin, “Scaling limit of deeply virtual compton scattering,” *Physics Letters B*, vol. 380, p. 417–425, Jul 1996.
- [44] W. Melnitchouk, R. Ent, and C. Keppel, “Quark-hadron duality in electron scattering,” *Phys. Rept.*, vol. 406, pp. 127–301, 2005.
- [45] H.-Y. Cheng, “The Strong CP Problem Revisited,” *Phys. Rept.*, vol. 158, p. 1, 1988.

-
- [46] C. A. Baker, D. D. Doyle, P. Geltenbort, K. Green, M. G. D. van der Grinten, P. G. Harris, P. Iaydjiev, S. N. Ivanov, D. J. R. May, J. M. Pendlebury, J. D. Richardson, D. Shiers, and K. F. Smith, “Improved experimental limit on the electric dipole moment of the neutron,” *Phys. Rev. Lett.*, vol. 97, p. 131801, Sep 2006.
- [47] T. Muta, *Foundations of Quantum Chromodynamics: An Introduction to Perturbative Methods in Gauge Theories, (3rd ed.)*, vol. 78 of *World scientific Lecture Notes in Physics*. Hackensack, N.J.: World Scientific, 2010.
- [48] P. A. Zylar *et al.*, “Review of Particle Physics,” *Progress of Theoretical and Experimental Physics*, vol. 2020, 08 2020. 083C01.
- [49] A. M. Jaffe and E. Witten, “Quantum Yang-Mills theory,” 2000.
- [50] J. C. Collins, D. E. Soper, and G. F. Sterman, “Factorization of Hard Processes in QCD,” *Adv. Ser. Direct. High Energy Phys.*, vol. 5, pp. 1–91, 1989.
- [51] J. C. Collins, *Renormalization*, vol. 26 of *Cambridge Monographs on Mathematical Physics*. Cambridge University Press, 1986.
- [52] O. Nachtmann, “Positivity constraints for anomalous dimensions,” *Nucl. Phys. B*, vol. 63, pp. 237–247, 1973.
- [53] R. L. Jaffe and X.-D. Ji, “Chiral odd parton distributions and Drell-Yan processes,” *Nucl. Phys. B*, vol. 375, pp. 527–560, 1992.
- [54] D. J. Gross and S. B. Treiman, “Light-cone structure of current commutators in the gluon-quark model,” *Phys. Rev. D*, vol. 4, pp. 1059–1072, Aug 1971.
- [55] M. D. Schwartz, *Quantum Field Theory and the Standard Model*. Cambridge University Press, 2014.
- [56] A. Hannaford-Gunn, “Generalised Parton Distributions from Lattice Feynman-Hellmann Techniques,” Master’s thesis, Adelaide U., 2020.
- [57] A. V. Manohar, “An Introduction to spin dependent deep inelastic scattering,” in *Lake Louise Winter Institute: Symmetry and Spin in the Standard Model*, 3 1992.
- [58] D. Drechsel, B. Pasquini, and M. Vanderhaeghen, “Dispersion relations in real and virtual Compton scattering,” *Phys. Rept.*, vol. 378, pp. 99–205, 2003.
- [59] R. Pohl, R. Gilman, G. A. Miller, and K. Pachucki, “Muonic hydrogen and the proton radius puzzle,” *Ann. Rev. Nucl. Part. Sci.*, vol. 63, pp. 175–204, 2013.
- [60] A. Antognini, F. Hagelstein, and V. Pascalutsa, “The proton structure in and out of muonic hydrogen,” *Ann. Rev. Nucl. Part. Sci.*, vol. 72, p. 389, 2022.
- [61] J. Gasser and H. Leutwyler, “Quark Masses,” *Phys. Rept.*, vol. 87, pp. 77–169, 1982.
- [62] G. A. Miller, B. M. K. Nefkens, and I. Slaus, “Charge symmetry, quarks and mesons,” *Phys. Rept.*, vol. 194, pp. 1–116, 1990.
- [63] F. Hausdorff, “Summationsmethoden und momentfolgen i.,” *Mathematische Zeitschrift*, vol. 9, pp. 74–109, 1921.

-
- [64] Y. Frishman, "Scale invariance and current commutators near the light cone," *Phys. Rev. Lett.*, vol. 25, pp. 966–969, Oct 1970.
- [65] J. M. Cornwall, "Spectral representations and their application to inclusive processes," *Phys. Rev. D*, vol. 5, pp. 2868–2877, Jun 1972.
- [66] K. G. Wilson, "Nonlagrangian models of current algebra," *Phys. Rev.*, vol. 179, pp. 1499–1512, 1969.
- [67] R. L. Jaffe, "Spin, twist and hadron structure in deep inelastic processes," in *Ettore Majorana International School of Nucleon Structure: 1st Course: The Spin Structure of the Nucleon*, pp. 42–129, 1 1996.
- [68] J. Blumlein and N. Kochelev, "On the twist -2 and twist - three contributions to the spin dependent electroweak structure functions," *Nucl. Phys. B*, vol. 498, pp. 285–309, 1997.
- [69] J. Blumlein and N. Kochelev, "On the twist -2 and twist - three contributions to the spin dependent electroweak structure functions," *Nucl. Phys. B*, vol. 498, pp. 285–309, 1997.
- [70] R. L. Jaffe, " g_2 -The Nucleon's Other Spin-Dependent Structure Function," *Comments Nucl. Part. Phys.*, vol. 19, no. 5, pp. 239–257, 1990.
- [71] J. Ellis and R. Jaffe, "Sum rule for deep-inelastic electroproduction from polarized protons," *Phys. Rev. D*, vol. 9, pp. 1444–1446, Mar 1974.
- [72] A. Deur, S. J. Brodsky, and G. F. de Teramond, "The QCD Running Coupling," *Nucl. Phys.*, vol. 90, p. 1, 2016.
- [73] H. Burkhardt and W. N. Cottingham, "Sum rules for forward virtual Compton scattering," *Annals Phys.*, vol. 56, pp. 453–463, 1970.
- [74] H. Burkhardt and W. N. Cottingham, "Sum rules for forward virtual Compton scattering," *Annals Phys.*, vol. 56, pp. 453–463, 1970.
- [75] S. Wandzura and F. Wilczek, "Sum Rules for Spin Dependent Electroproduction: Test of Relativistic Constituent Quarks," *Phys. Lett. B*, vol. 72, pp. 195–198, 1977.
- [76] J. L. Cortes, B. Pire, and J. P. Ralston, "Measuring the transverse polarization of quarks in the proton," *Z. Phys. C*, vol. 55, pp. 409–416, 1992.
- [77] M. Diehl, "Generalized parton distributions," *Physics Reports*, vol. 388, p. 41–277, Dec 2003.
- [78] X. Ji, "Deeply virtual compton scattering," *Physical Review D*, vol. 55, p. 7114–7125, Jun 1997.
- [79] X. Ji, "Off-forward parton distributions," *Journal of Physics G: Nuclear and Particle Physics*, vol. 24, p. 1181–1205, Jul 1998.
- [80] E. Leader and M. Anselmino, "A crisis in the parton model: Where, oh where is the proton's spin?," *Z. Phys.*, vol. C41, p. 239, 1988.

-
- [81] F. Myhrer and A. W. Thomas, “Understanding the proton’s spin structure,” *Journal of Physics G: Nuclear and Particle Physics*, vol. 37, p. 023101, Jan 2010.
- [82] M. V. Polyakov and P. Schweitzer, “Mechanical properties of particles,” 2018.
- [83] M. V. Polyakov and P. Schweitzer, “Forces inside hadrons: Pressure, surface tension, mechanical radius, and all that,” *International Journal of Modern Physics A*, vol. 33, p. 1830025, Sep 2018.
- [84] I. V. Anikin and O. V. Teryaev, “Dispersion relations and subtractions in hard exclusive processes,” *Physical Review D*, vol. 76, Sep 2007.
- [85] O. V. Teryaev, “Analytic properties of hard exclusive amplitudes,” in *11th International Conference on Elastic and Diffractive Scattering: Towards High Energy Frontiers: The 20th Anniversary of the Blois Workshops, 17th Rencontre de Blois*, 10 2005.
- [86] M. Diehl and D. Ivanov, “Dispersion representations for hard exclusive processes: beyond the born approximation,” *The European Physical Journal C*, vol. 52, p. 919–932, Oct 2007.
- [87] B. Pasquini, M. Polyakov, and M. Vanderhaeghen, “Dispersive evaluation of the d -term form factor in deeply virtual compton scattering,” *Physics Letters B*, vol. 739, p. 133–138, Dec 2014.
- [88] V. D. Burkert, L. Elouadrhiri, and F. X. Girod, “The pressure distribution inside the proton,” *Nature*, vol. 557, pp. 396–399, 2018.
- [89] K. Kumerički, “Measurability of pressure inside the proton,” *Nature*, vol. 570, no. 7759, pp. E1–E2, 2019.
- [90] M. Burkardt, “Impact parameter space interpretation for generalized parton distributions,” *International Journal of Modern Physics A*, vol. 18, p. 173–207, Jan 2003.
- [91] M. Troyer and U.-J. Wiese, “Computational complexity and fundamental limitations to fermionic quantum Monte Carlo simulations,” *Phys. Rev. Lett.*, vol. 94, p. 170201, 2005.
- [92] G. Pan and Z. Y. Meng, “Sign Problem in Quantum Monte Carlo Simulation,” 4 2022.
- [93] G. Aarts, “Complex Langevin dynamics and other approaches at finite chemical potential,” *PoS*, vol. LATTICE2012, p. 017, 2012.
- [94] K.-F. Liu and S.-J. Dong, “Origin of difference between u -bar and d -bar partons in the nucleon,” *Physical Review Letters*, vol. 72, p. 1790–1793, Mar 1994.
- [95] W. Detmold and C. J. D. Lin, “Deep-inelastic scattering and the operator product expansion in lattice QCD,” *Phys. Rev. D*, vol. 73, p. 014501, 2006.
- [96] I. Montvay and G. Münster, *Quantum Fields on a Lattice*. Cambridge Monographs on Mathematical Physics, Cambridge University Press, 1994.

-
- [97] J. Smit, *Introduction to quantum fields on a lattice: A robust mate*, vol. 15. Cambridge University Press, 1 2011.
- [98] R. Gupta, “Introduction to lattice qcd,” 1998.
- [99] C. Gattringer and C. B. Lang, “Quantum chromodynamics on the lattice,” *Lect. Notes Phys.*, vol. 788, pp. 1–343, 2010.
- [100] B. Sheikholeslami and R. Wohlert, “Improved Continuum Limit Lattice Action for QCD with Wilson Fermions,” *Nucl. Phys.*, vol. B259, p. 572, 1985.
- [101] S. Duane, A. D. Kennedy, B. J. Pendleton, and D. Roweth, “Hybrid Monte Carlo,” *Phys. Lett. B*, vol. 195, pp. 216–222, 1987.
- [102] P. E. Shanahan, A. Trewartha, and W. Detmold, “Machine learning action parameters in lattice quantum chromodynamics,” *Phys. Rev. D*, vol. 97, no. 9, p. 094506, 2018.
- [103] S. Collins *et al.*, “Dirac and Pauli form factors from lattice QCD,” *Phys. Rev. D*, vol. 84, p. 074507, 2011.
- [104] Y. Aoki *et al.*, “FLAG Review 2021,” *Eur. Phys. J. C*, vol. 82, no. 10, p. 869, 2022.
- [105] H.-W. Lin, E. R. Nocera, F. Olness, K. Orginos, J. Rojo, A. Accardi, C. Alexandrou, A. Bacchetta, G. Bozzi, J.-W. Chen, *et al.*, “Parton distributions and lattice qcd calculations: A community white paper,” *Progress in Particle and Nuclear Physics*, vol. 100, p. 107–160, May 2018.
- [106] K. Ottnad, “Excited states in nucleon structure calculations,” *Eur. Phys. J. A*, vol. 57, no. 2, p. 50, 2021.
- [107] Y. Fu, X. Feng, L.-C. Jin, and C.-F. Lu, “Lattice QCD Calculation of the Two-Photon Exchange Contribution to the Muonic-Hydrogen Lamb Shift,” *Phys. Rev. Lett.*, vol. 128, no. 17, p. 172002, 2022.
- [108] F. X. Lee, A. Alexandru, C. Culver, and W. Wilcox, “Charged pion electric polarizability from four-point functions in lattice QCD,” 1 2023.
- [109] J. Liang, T. Draper, K.-F. Liu, A. Rothkopf, and Y.-B. Yang, “Towards the nucleon hadronic tensor from lattice QCD,” *Phys. Rev. D*, vol. 101, no. 11, p. 114503, 2020.
- [110] K. Cichy and M. Constantinou, “A guide to light-cone PDFs from Lattice QCD: an overview of approaches, techniques and results,” *Adv. High Energy Phys.*, vol. 2019, p. 3036904, 2019.
- [111] K. Cichy, “Progress in x -dependent partonic distributions from lattice QCD,” *PoS*, vol. LATTICE2021, p. 017, 2022.
- [112] S. Capitani and G. Rossi, “Deep inelastic scattering in improved lattice qcd (i). the first moment of structure functions,” *Nuclear Physics B*, vol. 433, p. 351–389, Jan 1995.

-
- [113] G. Beccarini, M. Bianchi, S. Capitani, and G. Rossi, “Deep inelastic scattering in improved lattice qcd (ii). the second moment of structure functions,” *Nuclear Physics B*, vol. 456, p. 271–295, Dec 1995.
- [114] F. Ynduráin, “Reconstruction of the deep inelastic structure functions from their moments,” *Physics Letters B*, vol. 74, no. 1, pp. 68 – 72, 1978.
- [115] W. Detmold, W. Melnitchouk, and A. W. Thomas, “Extraction of parton distributions from lattice QCD,” *Mod. Phys. Lett. A*, vol. 18, pp. 2681–2698, 2003.
- [116] Z. Davoudi and M. J. Savage, “Restoration of Rotational Symmetry in the Continuum Limit of Lattice Field Theories,” *Phys. Rev. D*, vol. 86, p. 054505, 2012.
- [117] C. Monahan and K. Orginos, “Locally smeared operator product expansions in scalar field theory,” *Phys. Rev. D*, vol. 91, no. 7, p. 074513, 2015.
- [118] M. Gockeler, R. Horsley, W. Kurzinger, H. Oelrich, D. Pleiter, P. E. L. Rakow, A. Schafer, and G. Schierholz, “A Lattice calculation of the nucleon’s spin dependent structure function $g(2)$ revisited,” *Phys. Rev. D*, vol. 63, p. 074506, 2001.
- [119] M. Gockeler, R. Horsley, D. Pleiter, P. E. L. Rakow, A. Schafer, G. Schierholz, H. Stuben, and J. M. Zanotti, “Investigation of the second moment of the nucleon’s $g(1)$ and $g(2)$ structure functions in two-flavor lattice QCD,” *Phys. Rev. D*, vol. 72, p. 054507, 2005.
- [120] S. Bürger, T. Wurm, M. Löffler, M. Gockeler, G. Bali, S. Collins, A. Schäfer, and A. Sternbeck, “Lattice results for the longitudinal spin structure and color forces on quarks in a nucleon,” *Phys. Rev. D*, vol. 105, no. 5, p. 054504, 2022.
- [121] J. M. Bickerton, *Transverse Properties of Baryons using Lattice Quantum Chromodynamics*. PhD thesis, Adelaide U., 2020.
- [122] P. Hägler, J. W. Negele, D. B. Renner, W. Schroers, T. Lippert, and K. Schilling, “Moments of nucleon generalized parton distributions in lattice qcd,” *Physical Review D*, vol. 68, Aug 2003.
- [123] M. Gockeler, R. Horsley, D. Pleiter, P. E. L. Rakow, A. Schäfer, G. Schierholz, and W. Schroers, “Generalized parton distributions from lattice qcd,” *Physical Review Letters*, vol. 92, Jan 2004.
- [124] M. Gockeler, P. Hagler, R. Horsley, D. Pleiter, P. E. L. Rakow, A. Schafer, G. Schierholz, and J. M. Zanotti, “Quark helicity flip generalized parton distributions from two-flavor lattice QCD,” *Phys. Lett. B*, vol. 627, pp. 113–123, 2005.
- [125] M. Gockeler, P. Hägler, R. Horsley, Y. Nakamura, D. Pleiter, P. E. L. Rakow, A. Schäfer, G. Schierholz, H. Stüben, and J. M. Zanotti, “Transverse spin structure of the nucleon from lattice QCD simulations,” *Phys. Rev. Lett.*, vol. 98, p. 222001, 2007.
- [126] M. Ohtani, D. Brömmel, M. Gockeler, P. Hägler, R. Horsley, Y. Nakamura, D. Pleiter, P. E. L. Rakow, A. Schäfer, G. Schierholz, W. Schroers, H. Stuben,

-
- and J. M. Zanotti, “Moments of generalized parton distributions and quark angular momentum of the nucleon,” in *Proceedings, 25th International Symposium on Lattice field theory (Lattice 2007): Regensburg, Germany, July 30-August 4, 2007*, vol. LATTICE2007, p. 158, 2007.
- [127] P. Hägler, W. Schroers, J. Bratt, J. W. Negele, A. V. Pochinsky, R. G. Edwards, D. G. Richards, M. Engelhardt, G. T. Fleming, B. Musch, *et al.*, “Nucleon generalized parton distributions from full lattice qcd,” *Physical Review D*, vol. 77, May 2008.
- [128] D. Brömmel *et al.*, “The Spin structure of the pion,” *Phys. Rev. Lett.*, vol. 101, p. 122001, 2008.
- [129] J. D. Bratt, R. G. Edwards, M. Engelhardt, P. Hägler, H. W. Lin, M. F. Lin, H. B. Meyer, B. Musch, J. W. Negele, K. Orginos, *et al.*, “Nucleon structure from mixed action calculations using $2 + 1$ flavors of asqtad sea and domain wall valence fermions,” *Physical Review D*, vol. 82, Nov 2010.
- [130] C. Alexandrou, J. Carbonell, M. Constantinou, P. A. Harraud, P. Guichon, K. Jansen, C. Kallidonis, T. Korzec, and M. Papinutto, “Moments of nucleon generalized parton distributions from lattice qcd,” *Physical Review D*, vol. 83, Jun 2011.
- [131] A. Sternbeck and M. Göckeler and Ph. Hägler and R. Horsley and Y. Nakamura and A. Nobile and D. Pleiter and P. E. L. Rakow and A. Schäfer and G. Schierholz and J. Zanotti, “First moments of the nucleon generalized parton distributions from lattice QCD,” *PoS*, vol. LATTICE2011, p. 177, 2011.
- [132] P. Shanahan and W. Detmold, “Gluon gravitational form factors of the nucleon and the pion from lattice qcd,” *Physical Review D*, vol. 99, Jan 2019.
- [133] P. Shanahan and W. Detmold, “Pressure distribution and shear forces inside the proton,” *Physical Review Letters*, vol. 122, Feb 2019.
- [134] R. S. Sufian, C. Egerer, J. Karpie, R. G. Edwards, B. Joó, Y.-Q. Ma, K. Orginos, J.-W. Qiu, and D. G. Richards, “Pion Valence Quark Distribution from Current-Current Correlation in Lattice QCD,” *Phys. Rev. D*, vol. 102, no. 5, p. 054508, 2020.
- [135] R. A. Briceño, M. T. Hansen, and C. J. Monahan, “Role of the euclidean signature in lattice calculations of quasidistributions and other nonlocal matrix elements,” *Physical Review D*, vol. 96, Jul 2017.
- [136] X. Ji, “Parton physics from large-momentum effective field theory,” 2014.
- [137] T. Izubuchi, X. Ji, L. Jin, I. W. Stewart, and Y. Zhao, “Factorization Theorem Relating Euclidean and Light-Cone Parton Distributions,” *Phys. Rev. D*, vol. 98, no. 5, p. 056004, 2018.
- [138] V. M. Braun, A. Vladimirov, and J.-H. Zhang, “Power corrections and renormalons in parton quasidistributions,” *Physical Review D*, vol. 99, Jan 2019.

-
- [139] J. Karpie, K. Orginos, A. Rothkopf, and S. Zafeiropoulos, “Reconstructing parton distribution functions from Ioffe time data: from Bayesian methods to Neural Networks,” *JHEP*, vol. 04, p. 057, 2019.
- [140] X. Ji, “Large-Momentum Effective Theory vs. Short-Distance Operator Expansion: Contrast and Complementarity,” 9 2022.
- [141] C. Alexandrou, K. Cichy, M. Constantinou, K. Hadjiyiannakou, K. Jansen, A. Scapellato, and F. Steffens, “Systematic uncertainties in parton distribution functions from lattice QCD simulations at the physical point,” *Phys. Rev. D*, vol. 99, no. 11, p. 114504, 2019.
- [142] I. W. Stewart and Y. Zhao, “Matching the quasiparton distribution in a momentum subtraction scheme,” *Phys. Rev. D*, vol. 97, no. 5, p. 054512, 2018.
- [143] C. Alexandrou, G. Iannelli, K. Jansen, and F. Manigrasso, “Parton distribution functions from lattice QCD using Bayes-Gauss-Fourier transforms,” *Phys. Rev. D*, vol. 102, no. 9, p. 094508, 2020.
- [144] C. Egerer, R. G. Edwards, K. Orginos, and D. G. Richards, “Distillation at High-Momentum,” *Phys. Rev. D*, vol. 103, no. 3, p. 034502, 2021.
- [145] X. Gao, A. D. Hanlon, J. Holligan, N. Karthik, S. Mukherjee, P. Petreczky, S. Syritsyn, and Y. Zhao, “The Unpolarized Proton PDF at NNLO from Lattice QCD with Physical Quark Masses,” 12 2022.
- [146] J.-W. Chen, H.-W. Lin, and J.-H. Zhang, “Pion generalized parton distribution from lattice QCD,” *Nucl. Phys. B*, vol. 952, p. 114940, 2020.
- [147] H.-W. Lin, “Nucleon Tomography and Generalized Parton Distribution at Physical Pion Mass from Lattice QCD,” *Phys. Rev. Lett.*, vol. 127, no. 18, p. 182001, 2021.
- [148] C. Alexandrou, K. Cichy, M. Constantinou, K. Hadjiyiannakou, K. Jansen, A. Scapellato, and F. Steffens, “Unpolarized and helicity generalized parton distributions of the proton within lattice QCD,” *Phys. Rev. Lett.*, vol. 125, no. 26, p. 262001, 2020.
- [149] S. Bhattacharya, K. Cichy, M. Constantinou, J. Dodson, X. Gao, A. Metz, S. Mukherjee, A. Scapellato, F. Steffens, and Y. Zhao, “Generalized parton distributions from lattice QCD with asymmetric momentum transfer: Unpolarized quarks,” *Phys. Rev. D*, vol. 106, no. 11, p. 114512, 2022.
- [150] S. Bhattacharya, K. Cichy, M. Constantinou, X. Gao, A. Metz, J. Miller, S. Mukherjee, P. Petreczky, F. Steffens, and Y. Zhao, “Moments of proton GPDs from the OPE of nonlocal quark bilinears up to NNLO,” 5 2023.
- [151] J.-W. Chen, S. D. Cohen, X. Ji, H.-W. Lin, and J.-H. Zhang, “Nucleon Helicity and Transversity Parton Distributions from Lattice QCD,” *Nucl. Phys. B*, vol. 911, pp. 246–273, 2016.

-
- [152] H.-W. Lin, J.-W. Chen, X. Ji, L. Jin, R. Li, Y.-S. Liu, Y.-B. Yang, J.-H. Zhang, and Y. Zhao, “Proton isovector helicity distribution on the lattice at physical pion mass,” *Phys. Rev. Lett.*, vol. 121, p. 242003, Dec 2018.
- [153] C. Alexandrou, K. Cichy, M. Constantinou, K. Jansen, A. Scapellato, and F. Steffens, “Light-cone parton distribution functions from lattice qcd,” *Phys. Rev. Lett.*, vol. 121, p. 112001, Sep 2018.
- [154] R. G. Edwards *et al.*, “Non-singlet quark helicity PDFs of the nucleon from pseudo-distributions,” *JHEP*, vol. 03, p. 086, 2023.
- [155] U. Aglietti, M. Ciuchini, G. Corbò, E. Franco, G. Martinelli, and L. Silvestrini, “Model independent determination of the shape function for inclusive b decays and of the structure functions in dis,” *Physics Letters B*, vol. 432, p. 411–420, Jul 1998.
- [156] K.-F. Liu, “Parton distribution function from the hadronic tensor on the lattice,” 2016.
- [157] J. Liang, K.-F. Liu, and Y.-B. Yang, “Lattice calculation of hadronic tensor of the nucleon,” *EPJ Web of Conferences*, vol. 175, p. 14014, 2018.
- [158] W. Detmold, A. V. Grebe, I. Kanamori, C. J. D. Lin, R. J. Perry, and Y. Zhao, “Parton physics from a heavy-quark operator product expansion: Formalism and Wilson coefficients,” *Phys. Rev. D*, vol. 104, no. 7, p. 074511, 2021.
- [159] W. Detmold, A. V. Grebe, I. Kanamori, C. J. D. Lin, S. Mondal, R. J. Perry, and Y. Zhao, “Parton physics from a heavy-quark operator product expansion: Lattice QCD calculation of the second moment of the pion distribution amplitude,” *Phys. Rev. D*, vol. 105, no. 3, p. 034506, 2022.
- [160] W. Detmold, I. Kanamori, C. J. D. Lin, S. Mondal, and Y. Zhao, “Moments of pion distribution amplitude using operator product expansion on the lattice,” 2018.
- [161] R. Horsley, Y. Nakamura, H. Perlt, P. E. L. Rakow, G. Schierholz, K. Somfleth, R. D. Young, and J. M. Zanotti, “Structure functions from the Compton amplitude,” *PoS*, vol. LATTICE2019, p. 137, 2020.
- [162] L. Del Debbio, T. Giani, J. Karpie, K. Orginos, A. Radyushkin, and S. Zafeiropoulos, “Neural-network analysis of Parton Distribution Functions from Ioffe-time pseudodistributions,” *JHEP*, vol. 02, p. 138, 2021.
- [163] R. P. Feynman, “Forces in molecules,” *Phys. Rev.*, vol. 56, pp. 340–343, Aug 1939.
- [164] H. Hellmann, *Einführung in die Quantenchemie*. Leipzig: Franz Deuticke, 1937.
- [165] S. Dinter, V. Drach, R. Frezzotti, G. Herdoiza, K. Jansen, and G. Rossi, “Sigma terms and strangeness content of the nucleon with $n_f = 2 + 1 + 1$ twisted mass fermions,” *Journal of High Energy Physics*, vol. 2012, Aug 2012.
- [166] R. Horsley, Y. Nakamura, H. Perlt, D. Pleiter, P. E. L. Rakow, G. Schierholz, A. Schiller, H. Stüben, F. Winter, and J. M. Zanotti, “Hyperon sigma terms for $2 + 1$ quark flavors,” *Physical Review D*, vol. 85, Feb 2012.

-
- [167] S. Dürr, Z. Fodor, T. Hemmert, C. Hoelbling, J. Frison, S. D. Katz, S. Krieg, T. Kurth, L. Lellouch, T. Lippert, *et al.*, “Sigma term and strangeness content of octet baryons,” *Physical Review D*, vol. 85, Jan 2012.
- [168] P. E. Shanahan, A. W. Thomas, and R. D. Young, “Sigma terms from an $su(3)$ chiral extrapolation,” *Physical Review D*, vol. 87, Apr 2013.
- [169] A. Chambers, J. Dragos, R. Horsley, Y. Nakamura, H. Perlt, D. Pleiter, P. Rakow, G. Schierholz, A. Schiller, K. Somfleth, H. Stüben, R. Young, and J. Zanotti, “Electromagnetic form factors at large momenta from lattice qcd,” *Physical Review D*, vol. 96, Dec 2017.
- [170] A. Chambers, R. Horsley, Y. Nakamura, H. Perlt, D. Pleiter, P. Rakow, G. Schierholz, A. Schiller, H. Stüben, R. Young, and J. M. Zanotti, “Feynman-hellmann approach to the spin structure of hadrons,” *Physical Review D*, vol. 90, Jul 2014.
- [171] R. Horsley, Y. Nakamura, H. Perlt, D. Pleiter, P. E. L. Rakow, G. Schierholz, A. Schiller, H. Stüben, R. D. Young, and J. M. Zanotti, “The strange quark contribution to the spin of the nucleon,” 2019.
- [172] W. Detmold, “Flavor singlet physics in lattice qcd with background fields,” *Physical Review D*, vol. 71, Mar 2005.
- [173] C. Bouchard, C. C. Chang, T. Kurth, K. Orginos, and A. Walker-Loud, “On the feynman-hellmann theorem in quantum field theory and the calculation of matrix elements,” *Physical Review D*, vol. 96, Jul 2017.
- [174] R. E. Smail, M. Batelaan, R. Horsley, Y. Nakamura, H. Perlt, D. Pleiter, P. E. L. Rakow, G. Schierholz, H. Stüben, R. D. Young, and J. M. Zanotti, “Constraining beyond the Standard Model nucleon isovector charges,” 4 2023.
- [175] R. Horsley, T. Howson, W. Kamleh, Y. Nakamura, H. Perlt, P. E. L. Rakow, G. Schierholz, H. Stüben, R. D. Young, and J. M. Zanotti, “Determining the glue component of the nucleon,” *PoS*, vol. LATTICE2019, p. 220, 2020.
- [176] A. Hannaford-Gunn, R. Horsley, Y. Nakamura, H. Perlt, P. E. L. Rakow, G. Schierholz, K. Somfleth, H. Stüben, R. D. Young, and J. M. Zanotti, “Scaling and higher twist in the nucleon compton amplitude,” 2020.
- [177] A. Graham, *Matrix theory and applications for engineers and mathematicians*. Mathematics & its applications, Chichester [Eng: E. Horwood, 1979.
- [178] K. Somfleth, *Hadron Structure Using Feynman–Hellmann Theorem*. PhD thesis, The University of Adelaide, 2020.
- [179] A. J. Chambers, *Hadron structure and the Feynman-Hellmann theorem in lattice quantum chromodynamics*. PhD thesis, The University of Adelaide, 2017.
- [180] A. Chambers, R. Horsley, Y. Nakamura, H. Perlt, P. Rakow, G. Schierholz, A. Schiller, and J. Zanotti, “A novel approach to nonperturbative renormalization of singlet and nonsinglet lattice operators,” *Physics Letters B*, vol. 740, p. 30–35, Jan 2015.

-
- [181] A. Chambers, R. Horsley, Y. Nakamura, H. Perlt, D. Pleiter, P. Rakow, G. Schierholz, A. Schiller, H. Stüben, R. Young, and J. M. Zanotti, “Disconnected contributions to the spin of the nucleon,” *Physical Review D*, vol. 92, Dec 2015.
- [182] Z. Fodor and S. D. Katz, “A New method to study lattice QCD at finite temperature and chemical potential,” *Phys. Lett. B*, vol. 534, pp. 87–92, 2002.
- [183] C. Adloff, V. Andreev, B. Andrieu, T. Anthonis, V. Arkadov, A. Astvatsatourov, A. Babaev, J. Bähr, P. Baranov, E. Barrelet, *et al.*, “Measurement of deeply virtual compton scattering at hermes,” *Physics Letters B*, vol. 517, p. 47–58, Sep 2001.
- [184] S. Chekanov, M. Derrick, D. Krakauer, J. Loizides, S. Magill, B. Musgrave, J. Ropond, R. Yoshida, M. Mattingly, P. Antonioli, *et al.*, “Measurement of deeply virtual compton scattering at hermes,” *Physics Letters B*, vol. 573, p. 46–62, Oct 2003.
- [185] C. Adloff, V. Andreev, B. Andrieu, T. Anthonis, V. Arkadov, A. Astvatsatourov, A. Babaev, J. Bähr, P. Baranov, E. Barrelet, *et al.*, “Measurement of deeply virtual compton scattering at hermes,” *Physics Letters B*, vol. 517, p. 47–58, Sep 2001.
- [186] A. Airapetian, N. Akopov, Z. Akopov, E. Aschenauer, W. Augustyniak, R. Avakian, A. Avetissian, E. Avetisyan, S. Belostotski, N. Bianchi, *et al.*, “Measurement of double-spin asymmetries associated with deeply virtual compton scattering on a transversely polarized hydrogen target,” *Physics Letters B*, vol. 704, p. 15–23, Oct 2011.
- [187] A. Airapetian, N. Akopov, Z. Akopov, E. C. Aschenauer, W. Augustyniak, R. Avakian, A. Avetissian, E. Avetisyan, H. P. Blok, *et al.*, “Beam-helicity and beam-charge asymmetries associated with deeply virtual compton scattering on the unpolarised proton,” *Journal of High Energy Physics*, vol. 2012, Jul 2012.
- [188] P. J. Lin, “GPD measurements at COMPASS,” *Int. J. Mod. Phys. A*, pp. 586–591, 2020.
- [189] M. Defurne, M. Amaryan, K. A. Aniol, M. Beaumel, H. Benaoum, P. Bertin, M. Brossard, A. Camsonne, J.-P. Chen, E. Chudakov, *et al.*, “E00-110 experiment at jefferson lab hall a: Deeply virtual compton scattering off the proton at 6 gev,” *Physical Review C*, vol. 92, Nov 2015.
- [190] H. Jo, F. Girod, H. Avakian, V. Burkert, M. Garçon, M. Guidal, V. Kubarovsky, S. Niccolai, P. Stoler, K. Adhikari, *et al.*, “Cross sections for the exclusive photon electroproduction on the proton and generalized parton distributions,” *Physical Review Letters*, vol. 115, Nov 2015.
- [191] E. Seder, A. Biselli, S. Pisano, S. Niccolai, G. Smith, K. Joo, K. Adhikari, M. Amaryan, M. Anderson, S. Anefalos Pereira, *et al.*, “Longitudinal target-spin asymmetries for deeply virtual compton scattering,” *Physical Review Letters*, vol. 114, Jan 2015.
- [192] J. Dudek, R. Ent, R. Essig, K. S. Kumar, C. Meyer, R. D. McKeown, Z. E. Meziani, G. A. Miller, M. Pennington, D. Richards, *et al.*, “Physics opportunities with the 12 gev upgrade at jefferson lab,” *The European Physical Journal A*, vol. 48, Dec 2012.

-
- [193] K. Kumerički, S. Liuti, and H. Moutarde, “Gpd phenomenology and dvcs fitting,” *The European Physical Journal A*, vol. 52, Jun 2016.
- [194] M. Guidal, H. Moutarde, and M. Vanderhaeghen, “Generalized parton distributions in the valence region from deeply virtual compton scattering,” *Reports on Progress in Physics*, vol. 76, p. 066202, May 2013.
- [195] C. Egerer, *Forward and Off-Forward Parton Distributions from Lattice QCD*. PhD thesis, College of William and Mary, Williamsburg, VA (United States); Thomas Jefferson National Accelerator Facility (TJNAF), Newport News, VA (United States), William & Mary - Arts & Sciences, USA, Coll. William and Mary, 2021.
- [196] M. Perrottet, “Invariant amplitudes for Compton scattering of off-shell photons on polarized nucleons,” *Lett. Nuovo Cim.*, vol. 7S2, pp. 915–921, 1973.
- [197] R. Tarrach, “Invariant Amplitudes for Virtual Compton Scattering Off Polarized Nucleons Free from Kinematical Singularities, Zeros and Constraints,” *Nuovo Cim.*, vol. A28, p. 409, 1975.
- [198] D. Drechsel, G. Knochlein, A. Y. Korchin, A. Metz, and S. Scherer, “Structure analysis of the virtual Compton scattering amplitude at low-energies,” *Phys. Rev. C*, vol. 57, pp. 941–952, 1998.
- [199] G. Eichmann and C. S. Fischer, “Nucleon compton scattering in the dyson-schwinger approach,” *Physical Review D*, vol. 87, Feb 2013.
- [200] J. C. Collins, L. Frankfurt, and M. Strikman, “Factorization for hard exclusive electroproduction of mesons in qcd,” *Physical Review D*, vol. 56, p. 2982–3006, Sep 1997.
- [201] I. I. Balitsky and V. M. Braun, “Evolution Equations for QCD String Operators,” *Nucl. Phys.*, vol. B311, pp. 541–584, 1989.
- [202] X. Ji, “The Nucleon structure functions from deep inelastic scattering with electroweak currents,” *Nucl. Phys.*, vol. B402, pp. 217–250, 1993.
- [203] C. Lorcé, “New explicit expressions for dirac bilinears,” *Physical Review D*, vol. 97, Jan 2018.
- [204] K. Watanabe, “Elastic Scattering and Hadron Dynamics at Short Distances,” *Progress of Theoretical Physics*, vol. 66, pp. 1003–1024, 09 1981.
- [205] K. Watanabe, “Operator Product Expansion and Integral Representation for Two Photon Processes,” *Prog. Theor. Phys.*, vol. 67, p. 1834, 1982.
- [206] Z. Chen, “Non-forward and unequal mass virtual compton scattering,” *Nuclear Physics B*, vol. 525, p. 369–383, Aug 1998.
- [207] B. E. White, “Factorization in deeply virtual compton scattering: local ope formalism and structure functions,” *Journal of Physics G: Nuclear and Particle Physics*, vol. 28, p. 203–221, Jan 2002.

-
- [208] A. V. Radyushkin and C. Weiss, “Deeply virtual compton scattering amplitude at the tree level: Transversality, twist-3, and factorization,” *Physical Review D*, vol. 63, Apr 2001.
- [209] M. Diehl, T. Gousset, B. Pire, and J. P. Ralston, “Testing the handbag contribution to exclusive virtual Compton scattering,” *Phys. Lett.*, vol. B411, pp. 193–202, 1997.
- [210] A. Radyushkin and C. Weiss, “Dvcs amplitude with kinematical twist-3 terms,” *Physics Letters B*, vol. 493, p. 332–340, Nov 2000.
- [211] W. A. Bardeen and W.-K. Tung, “Invariant amplitudes for photon processes,” *Phys. Rev.*, vol. 173, pp. 1423–1433, Sep 1968.
- [212] A. V. Belitsky, D. Müller, and Y. Ji, “Compton scattering: from deeply virtual to quasi-real,” *Nucl. Phys. B*, vol. 878, pp. 214–268, 2014.
- [213] A. I. L’vov, V. A. Petrun’kin, and M. Schumacher, “Dispersion theory of proton compton scattering in the first and second resonance regions,” *Phys. Rev. C*, vol. 55, pp. 359–377, Jan 1997.
- [214] B. Pasquini, M. Gorchtein, D. Drechsel, A. Metz, and M. Vanderhaeghen, “Dispersion relation formalism for virtual compton scattering off the proton,” *The European Physical Journal A*, vol. 11, p. 185–208, Jul 2001.
- [215] D. Drechsel, B. Pasquini, and M. Vanderhaeghen, “Dispersion relations in real and virtual compton scattering,” *Physics Reports*, vol. 378, p. 99–205, May 2003.
- [216] D. Müller and K. M. Semenov-Tian-Shansky, “ $J = 0$ fixed pole and D -term form factor in deeply virtual Compton scattering,” *Phys. Rev. D*, vol. 92, no. 7, p. 074025, 2015.
- [217] S. J. Brodsky, F. J. Llanes-Estrada, and A. P. Szczepaniak, “Local Two-Photon Couplings and the $J=0$ Fixed Pole in Real and Virtual Compton Scattering,” *Phys. Rev. D*, vol. 79, p. 033012, 2009.
- [218] W. Bietenholz, V. Boryakov, M. Göckeler, R. Horsley, W. G. Lockhart, Y. Nakamura, H. Perlt, D. Pleiter, P. E. L. Rakow, G. Schierholz, A. Schiller, T. Streuer, H. Stüben, F. Winter, and J. M. Zanotti, “Flavor blindness and patterns of flavor symmetry breaking in lattice simulations of up, down, and strange quarks,” *Physical Review D*, vol. 84, Sep 2011.
- [219] M. Batelaan, K. U. Can, R. Horsley, Y. Nakamura, P. E. L. Rakow, G. Schierholz, H. Stüben, R. D. Young, and J. M. Zanotti, “Feynman–Hellmann approach to transition matrix elements and quasi-degenerate energy states,” 5 2023.
- [220] J. Salvatier, T. V. Wiecki, and C. Fonnesbeck, “Probabilistic programming in python using pymc3,” *PeerJ Computer Science*, vol. 2:e55, 2016.
- [221] M. D. Hoffman and A. Gelman, “The no-u-turn sampler: Adaptively setting path lengths in hamiltonian monte carlo,” *Journal of Machine Learning Research*, vol. 15, pp. 1593–1623, 2014.

-
- [222] L. Schoeffel, “Generalised parton distributions at HERA and prospects for COMPASS,” *Phys. Lett. B*, vol. 658, pp. 33–39, 2007.
- [223] M. Diehl and W. Kugler, “Some numerical studies of the evolution of generalized parton distributions,” *Physics Letters B*, vol. 660, p. 202–211, Feb 2008.
- [224] K. Kumerički and D. Müller, “Deeply virtual compton scattering at small x_b and the access to the gpd h ,” *Nuclear Physics B*, vol. 841, p. 1–58, Dec 2010.
- [225] P. Kroll, “Status of DVMP, DVCS and GPDs,” *EPJ Web Conf.*, vol. 85, p. 01005, 2015.
- [226] P. V. Pobylitsa, “Disentangling positivity constraints for generalized parton distributions,” *Physical Review D*, vol. 65, Jun 2002.
- [227] P. V. Pobylitsa, “Positivity bounds on generalized parton distributions in the impact parameter representation,” *Physical Review D*, vol. 66, Nov 2002.
- [228] P. V. Pobylitsa, “Virtual compton scattering in the generalized bjorken region and positivity bounds on generalized parton distributions,” *Physical Review D*, vol. 70, Aug 2004.
- [229] V. M. Braun, A. N. Manashov, and B. Pirnay, “Finite- t and target mass corrections to deeply virtual Compton scattering,” *Phys. Rev. Lett.*, vol. 109, p. 242001, 2012.
- [230] Y. Guo, X. Ji, and K. Shiells, “Higher-order kinematical effects in deeply virtual Compton scattering,” *JHEP*, vol. 12, p. 103, 2021.
- [231] C. M. n. Camacho *et al.*, “Scaling tests of the cross-section for deeply virtual compton scattering,” *Phys. Rev. Lett.*, vol. 97, p. 262002, 2006.
- [232] M. Defurne *et al.*, “E00-110 experiment at Jefferson Lab Hall A: Deeply virtual Compton scattering off the proton at 6 GeV,” *Phys. Rev. C*, vol. 92, no. 5, p. 055202, 2015.
- [233] M. Defurne *et al.*, “A glimpse of gluons through deeply virtual compton scattering on the proton,” *Nature Commun.*, vol. 8, no. 1, p. 1408, 2017.
- [234] F. Georges, *Deeply virtual Compton scattering at Jefferson Lab*. PhD thesis, Orsay, IPN, 2018.
- [235] V. Shastry, W. Broniowski, and E. Ruiz Arriola, “Generalized quasi-, Ioffe-time-, and pseudodistributions of the pion in the Nambu–Jona-Lasinio model,” *Phys. Rev. D*, vol. 106, no. 11, p. 114035, 2022.
- [236] L. H. Karsten and J. Smith, “Lattice fermions: Species doubling, chiral invariance and the triangle anomaly,” *Nuclear Physics B*, vol. 183, no. 1, pp. 103 – 140, 1981.
- [237] F. Guerin, “Ward identities on the lattice for wilson fermions,” *Nuclear Physics B*, vol. 282, pp. 495 – 508, 1987.

-
- [238] A. De Rújula, “AN INTRODUCTION TO THE POSITIVITY CONSTRAINTS ON ABSORPTIVE AMPLITUDES AND THEIR EXPERIMENTAL IMPLICATIONS,” in *7th Rencontres de Moriond: multiparticle phenomena and inclusive reactions*, p. 405, 1972.
- [239] V. G. Bornyakov, R. Horsley, R. Hudspith, Y. Nakamura, H. Perlt, D. Pleiter, P. E. L. Rakow, G. Schierholz, A. Schiller, H. Stüben, and J. M. Zanotti, “Wilson flow and scale setting from lattice QCD,” 8 2015.
- [240] S. R. Beane *et al.*, “Charged multihadron systems in lattice QCD+QED,” *Phys. Rev. D*, vol. 103, no. 5, p. 054504, 2021.
- [241] E. Rinaldi, S. Syritsyn, M. L. Wagman, M. I. Buchoff, C. Schroeder, and J. Wasem, “Lattice qcd determination of neutron-antineutron matrix elements with physical quark masses,” *Phys. Rev. D*, vol. 99, p. 074510, Apr 2019.
- [242] K. Goeke, J. Grabis, J. Ossmann, M. V. Polyakov, P. Schweitzer, A. Silva, and D. Urbano, “Nucleon form-factors of the energy momentum tensor in the chiral quark-soliton model,” *Phys. Rev. D*, vol. 75, p. 094021, 2007.
- [243] C. Lorcé, H. Moutarde, and A. P. Trawiński, “Revisiting the mechanical properties of the nucleon,” *Eur. Phys. J. C*, vol. 79, no. 1, p. 89, 2019.
- [244] R. J. Hill and G. Paz, “Model independent extraction of the proton charge radius from electron scattering,” *Phys. Rev. D*, vol. 82, p. 113005, 2010.
- [245] Y. Guo, X. Ji, and K. Shiells, “Generalized parton distributions through universal moment parameterization: zero skewness case,” *JHEP*, vol. 09, p. 215, 2022.
- [246] M. Burkardt, “Generalized parton distributions for large x,” *Phys. Lett. B*, vol. 595, pp. 245–249, 2004.
- [247] M. Guidal, M. V. Polyakov, A. V. Radyushkin, and M. Vanderhaeghen, “Nucleon form-factors from generalized parton distributions,” *Phys. Rev. D*, vol. 72, p. 054013, 2005.
- [248] K. Goeke, M. Polyakov, and M. Vanderhaeghen, “Hard exclusive reactions and the structure of hadrons,” *Progress in Particle and Nuclear Physics*, vol. 47, p. 401–515, Jan 2001.
- [249] V. Guzey and M. Polyakov, “Dual parameterization of generalized parton distributions and a description of dvcs data,” *The European Physical Journal C*, vol. 46, p. 151–156, Mar 2006.
- [250] D. Müller, T. Lautenschlager, K. Passek-Kumerički, and A. Schäfer, “Towards a fitting procedure to deeply virtual meson production — the next-to-leading order case,” *Nuclear Physics B*, vol. 884, p. 438u(P)2013546, Jul 2014.
- [251] D. Mueller, “Pomeron dominance in deeply virtual Compton scattering and the femto holographic image of the proton,” 5 2006.

-
- [252] G. S. Bali, B. Lang, B. U. Musch, and A. Schäfer, “Novel quark smearing for hadrons with high momenta in lattice QCD,” *Phys. Rev. D*, vol. 93, no. 9, p. 094515, 2016.
- [253] J. J. Wu, W. Kamleh, D. t. Leinweber, R. D. Young, and J. M. Zanotti, “Accessing high-momentum nucleons with dilute stochastic sources,” *J. Phys. G*, vol. 45, no. 12, p. 125102, 2018.
- [254] M. Gockeler, R. Horsley, H. Perlt, P. E. L. Rakow, G. Schierholz, and A. Schiller, “Operator product expansion on the lattice: Analytic Wilson coefficients,” *PoS*, vol. LAT2006, p. 119, 2006.
- [255] P. L. Anthony *et al.*, “Precision measurement of the proton and deuteron spin structure functions $g(2)$ and asymmetries $A(2)$,” *Phys. Lett. B*, vol. 553, pp. 18–24, 2003.
- [256] K. Abe *et al.*, “Precision measurement of the proton spin structure function $g_1(p)$,” *Phys. Rev. Lett.*, vol. 74, pp. 346–350, 1995.
- [257] G. Altarelli, B. Lampe, P. Nason, and G. Ridolfi, “The Burkhardt-Cottingham sum rule in perturbative QCD,” *Phys. Lett. B*, vol. 334, pp. 187–191, 1994.
- [258] M. Burkardt, “On the possible violation of sum rules for higher twist parton distributions,” *Phys. Rev. D*, vol. 52, pp. 3841–3852, 1995.
- [259] R. Kundu and A. Metz, “Higher twist and transverse momentum dependent parton distributions: A Light front Hamiltonian approach,” *Phys. Rev. D*, vol. 65, p. 014009, 2002.
- [260] M. Burkardt and Y. Koike, “Violation of sum rules for twist three parton distributions in QCD,” *Nucl. Phys. B*, vol. 632, pp. 311–329, 2002.
- [261] F. Aslan and M. Burkardt, “Singularities in Twist-3 Quark Distributions,” *Phys. Rev. D*, vol. 101, no. 1, p. 016010, 2020.
- [262] M. Osipenko, S. Simula, W. Melnitchouk, P. E. Bosted, V. Burkert, E. Christy, K. Griffioen, C. Keppel, S. E. Kuhn, and G. Ricco, “Global analysis of data on the proton structure function $g(1)$ and extraction of its moments,” *Phys. Rev. D*, vol. 71, p. 054007, 2005.
- [263] X. Zheng *et al.*, “Precision measurement of the neutron spin asymmetries and spin-dependent structure functions in the valence quark region,” *Phys. Rev. C*, vol. 70, p. 065207, 2004.
- [264] A. Airapetian *et al.*, “Measurement of the virtual-photon asymmetry A_2 and the spin-structure function g_2 of the proton,” *Eur. Phys. J. C*, vol. 72, p. 1921, 2012.
- [265] M. Posik *et al.*, “A Precision Measurement of the Neutron Twist-3 Matrix Element d_2^n : Probing Color Forces,” *Phys. Rev. Lett.*, vol. 113, no. 2, p. 022002, 2014.
- [266] W. Armstrong *et al.*, “Revealing Color Forces with Transverse Polarized Electron Scattering,” *Phys. Rev. Lett.*, vol. 122, no. 2, p. 022002, 2019.
- [267] K. Abe *et al.*, “Measurement of the neutron spin structure function $g_2(n)$ and asymmetry $A_2(n)$,” *Phys. Lett. B*, vol. 404, pp. 377–382, 1997.

-
- [268] K. Abe *et al.*, “Measurements of the proton and deuteron spin structure functions $g(1)$ and $g(2)$,” *Phys. Rev. D*, vol. 58, p. 112003, 1998.
- [269] M. M. Velasco, *A Study of the g_2 spin structure function and the A_2 nucleon - virtual photon through polarized deep inelastic muon - proton scattering*. PhD thesis, Northwestern University, 12 1995.
- [270] J. Soffer and O. V. Teryaev, “Improved positivity bound for deep inelastic scattering on transversely polarized nucleon,” in *Workshop on Polarized Protons at High Energies - Accelerator Challenges and Physics Opportunities*, pp. 419–421, 5 1999.
- [271] P. A. Baikov, K. G. Chetyrkin, and J. H. Kuhn, “Adler Function, Bjorken Sum Rule, and the Crewther Relation to Order α_s^4 in a General Gauge Theory,” *Phys. Rev. Lett.*, vol. 104, p. 132004, 2010.
- [272] K. G. Chetyrkin, J. H. Kuhn, and M. Steinhauser, “RunDec: A Mathematica package for running and decoupling of the strong coupling and quark masses,” *Comput. Phys. Commun.*, vol. 133, pp. 43–65, 2000.
- [273] P. A. Baikov, K. G. Chetyrkin, and J. H. Kuhn, “Order α_s^4 QCD Corrections to Z and tau Decays,” *Phys. Rev. Lett.*, vol. 101, p. 012002, 2008.
- [274] W. N. Cottingham, “The neutron proton mass difference and electron scattering experiments,” *Annals Phys.*, vol. 25, pp. 424–432, 1963.
- [275] J. Gasser, H. Leutwyler, and A. Rusetsky, “Sum rule for the Compton amplitude and implications for the proton–neutron mass difference,” *Eur. Phys. J. C*, vol. 80, no. 12, p. 1121, 2020.
- [276] A. W. Thomas, X. G. Wang, and R. D. Young, “Electromagnetic Contribution to the Proton-Neutron Mass Splitting,” *Phys. Rev. C*, vol. 91, no. 1, p. 015209, 2015.
- [277] J. C. Bernauer *et al.*, “High-precision determination of the electric and magnetic form factors of the proton,” *Physical Review Letters*, vol. 105, Dec 2010.
- [278] R. Pohl *et al.*, “The size of the proton,” *Nature*, vol. 466, pp. 213–216, 2010.
- [279] O. Tomalak and M. Vanderhaeghen, “Two-photon exchange correction in elastic unpolarized electron-proton scattering at small momentum transfer,” *Phys. Rev. D*, vol. 93, no. 1, p. 013023, 2016.
- [280] A. Afanasev, P. G. Blunden, D. Hasell, and B. A. Raue, “Two-photon exchange in elastic electron–proton scattering,” *Prog. Part. Nucl. Phys.*, vol. 95, pp. 245–278, 2017.
- [281] C. E. Carlson and M. Vanderhaeghen, “Higher order proton structure corrections to the Lamb shift in muonic hydrogen,” *Phys. Rev. A*, vol. 84, p. 020102, 2011.
- [282] R. J. Hill and G. Paz, “Model independent analysis of proton structure for hydrogenic bound states,” *Phys. Rev. Lett.*, vol. 107, p. 160402, Oct 2011.
- [283] G. A. Miller, “Proton Polarizability Contribution: Muonic Hydrogen Lamb Shift and Elastic Scattering,” *Phys. Lett. B*, vol. 718, pp. 1078–1082, 2013.

-
- [284] J. Gasser and H. Leutwyler, “Implications of Scaling for the Proton - Neutron Mass - Difference,” *Nucl. Phys. B*, vol. 94, pp. 269–310, 1975.
- [285] A. Walker-Loud, C. E. Carlson, and G. A. Miller, “The Electromagnetic Self-Energy Contribution to $M_p - M_n$ and the Isovector Nucleon Magnetic Polarizability,” *Phys. Rev. Lett.*, vol. 108, p. 232301, 2012.
- [286] F. B. Erben, P. E. Shanahan, A. W. Thomas, and R. D. Young, “Dispersive estimate of the electromagnetic charge symmetry violation in the octet baryon masses,” *Phys. Rev. C*, vol. 90, no. 6, p. 065205, 2014.
- [287] O. Tomalak, “Electromagnetic proton–neutron mass difference,” *Eur. Phys. J. Plus*, vol. 135, no. 6, p. 411, 2020.
- [288] A. Walker-Loud, “On the Cottingham formula and the electromagnetic contribution to the proton-neutron mass splitting,” *PoS*, vol. CD2018, p. 045, 2019.
- [289] J. Gasser, H. Leutwyler, and A. Rusetsky, “Sum rule for the Compton amplitude and implications for the proton–neutron mass difference,” *Eur. Phys. J. C*, vol. 80, no. 12, p. 1121, 2020.
- [290] J. C. Collins, “Renormalization of the Cottingham Formula,” *Nucl. Phys. B*, vol. 149, pp. 90–100, 1979. [Erratum: *Nucl.Phys.B* 153, 546 (1979), Erratum: *Nucl.Phys.B* 915, 392–393 (2017)].
- [291] R. J. Hill and G. Paz, “Nucleon spin-averaged forward virtual compton tensor at large q^2 ,” *Physical Review D*, vol. 95, May 2017.
- [292] J. Lozano, A. Agadjanov, J. Gegelia, U. G. Meißner, and A. Rusetsky, “Finite volume corrections to forward Compton scattering off the nucleon,” *Phys. Rev. D*, vol. 103, no. 3, p. 034507, 2021.
- [293] M. J. Creutz, S. D. Drell, and E. A. Paschos, “High-Energy Limit for the Real Part of Forward Compton Scattering,” *Phys. Rev.*, vol. 178, pp. 2300–2301, 1969.
- [294] M. Gorchtein, F. J. Llanes-Estrada, and A. P. Szczepaniak, “Muonic-hydrogen Lamb shift: Dispersing the nucleon-excitation uncertainty with a finite-energy sum rule,” *Phys. Rev. A*, vol. 87, no. 5, p. 052501, 2013.
- [295] H. Leutwyler, “Theoretical aspects of Chiral Dynamics,” *PoS*, vol. CD15, p. 022, 2015.
- [296] I. Caprini, “Constraints on the virtual Compton scattering on the nucleon in a new dispersive formalism,” *Phys. Rev. D*, vol. 93, no. 7, p. 076002, 2016.
- [297] I. Caprini, “Analyticity and Regge asymptotics in virtual Compton scattering on the nucleon,” *Eur. Phys. J. C*, vol. 81, no. 4, p. 309, 2021.
- [298] C. Dawson, G. Martinelli, G. Rossi, C. Sachrajda, S. Sharpe, M. Talevi, and M. Testa, “New lattice approaches to the rule,” *Nuclear Physics B*, vol. 514, p. 313–335, Mar 1998.

-
- [299] G. Martinelli, “Hadronic weak interactions of light quarks,” *Nucl. Phys. B Proc. Suppl.*, vol. 73, pp. 58–71, 1999.
- [300] S. Capitani and G. Rossi, “Deep inelastic scattering in improved lattice qcd (i). the first moment of structure functions,” *Nuclear Physics B*, vol. 433, p. 351–389, Jan 1995.
- [301] G. Beccarini, M. Bianchi, S. Capitani, and G. Rossi, “Deep inelastic scattering in improved lattice qcd (ii). the second moment of structure functions,” *Nuclear Physics B*, vol. 456, p. 271–295, Dec 1995.
- [302] C. Alexandrou *et al.*, “Lattice calculation of the short and intermediate time-distance hadronic vacuum polarization contributions to the muon magnetic moment using twisted-mass fermions,” *Phys. Rev. D*, vol. 107, no. 7, p. 074506, 2023.
- [303] M. Della Morte, R. Sommer, and S. Takeda, “On cutoff effects in lattice QCD from short to long distances,” *Phys. Lett. B*, vol. 672, pp. 407–412, 2009.
- [304] M. Cè, T. Harris, H. B. Meyer, A. Toniato, and C. Török, “Vacuum correlators at short distances from lattice QCD,” *JHEP*, vol. 12, p. 215, 2021.
- [305] W. Detmold, A. V. Grebe, I. Kanamori, C. J. D. Lin, R. J. Perry, and Y. Zhao, “Progress in calculation of the fourth Mellin moment of the pion light-cone distribution amplitude using the HOPE method,” *PoS*, vol. LATTICE2022, p. 119, 2023.
- [306] S. Caracciolo, A. Montanari, and A. Pelissetto, “Operator product expansion on the lattice: a numerical test in the two-dimensional non-linear sigma-model,” *Journal of High Energy Physics*, vol. 2000, p. 045–045, Sep 2000.
- [307] B. Joó, J. Karpie, K. Orginos, A. V. Radyushkin, D. G. Richards, R. S. Sufian, and S. Zafeiropoulos, “Pion valence structure from ioffe-time parton pseudodistribution functions,” *Physical Review D*, vol. 100, Dec 2019.
- [308] J. Karpie, K. Orginos, and S. Zafeiropoulos, “Moments of ioffe time parton distribution functions from non-local matrix elements,” *Journal of High Energy Physics*, vol. 2018, Nov 2018.
- [309] B. Joó, J. Karpie, K. Orginos, A. Radyushkin, D. Richards, and S. Zafeiropoulos, “Parton distribution functions from ioffe time pseudo-distributions,” *Journal of High Energy Physics*, vol. 2019, Dec 2019.
- [310] J. Karpie, K. Orginos, A. Radyushkin, and S. Zafeiropoulos, “The continuum and leading twist limits of parton distribution functions in lattice qcd,” 2021.
- [311] F. Burger, G. Hotzel, K. Jansen, and M. Petschlies, “The hadronic vacuum polarization and automatic $\mathcal{O}(a)$ improvement for twisted mass fermions,” *JHEP*, vol. 03, p. 073, 2015.
- [312] C. Monahan and K. Orginos, “Quasi parton distributions and the gradient flow,” *JHEP*, vol. 03, p. 116, 2017.

-
- [313] C. Monahan, “Smearred quasidistributions in perturbation theory,” *Phys. Rev. D*, vol. 97, no. 5, p. 054507, 2018.
- [314] J. Zanotti, K. U. Can, R. Horsley, Y. Nakamura, H. Perlt, P. E. L. Rakow, G. Schierholz, H. Stueben, and R. D. Young, “Advances in lattice hadron physics calculations using the gradient flow,” *PoS*, vol. LATTICE2021, p. 055, 2022.
- [315] F. P. Aslan, M. Burkardt, and M. Schlegel, “Transverse Force Tomography,” in *Probing Nucleons and Nuclei in High Energy Collisions: Dedicated to the Physics of the Electron Ion Collider*, pp. 186–189, 2020.
- [316] K.-F. Liu and S.-J. Dong, “Origin of difference between anti-d and anti-u partons in the nucleon,” *Phys. Rev. Lett.*, vol. 72, pp. 1790–1793, 1994.
- [317] R. Zwicky, “A brief introduction to dispersion relations and analyticity,” 2016.
- [318] C. Itzykson and J. B. Zuber, *Quantum Field Theory*. International Series In Pure and Applied Physics, New York: McGraw-Hill, 1980.
- [319] W. Zimmermann, “Composite operators in the perturbation theory of renormalizable interactions,” *Annals of Physics*, vol. 77, pp. 536–569, May 1973.
- [320] K. G. Wilson and W. Zimmermann, “Operator product expansions and composite field operators in the general framework of quantum field theory,” *Commun. Math. Phys.*, vol. 24, pp. 87–106, 1972.
- [321] P. Otterson and W. Zimmermann, “On the directional dependence of composite field operators,” *Comm. Math. Phys.*, vol. 24, no. 2, pp. 107–132, 1972.
- [322] V. A. Novikov, M. A. Shifman, A. I. Vainshtein, and V. I. Zakharov, “Wilson’s Operator Expansion: Can It Fail?,” *Nucl. Phys.*, vol. B249, pp. 445–471, 1985.
- [323] B. Geyer, M. Lazar, and D. Robaschik, “Decomposition of non-local light-cone operators into harmonic operators of definite twist,” *Nuclear Physics B*, vol. 559, p. 339–377, Oct 1999.
- [324] M. E. Peskin and D. V. Schroeder, *An Introduction to quantum field theory*. Reading, USA: Addison-Wesley, 1995.
- [325] C. Michael, “Fitting correlated data,” *Phys. Rev. D*, vol. 49, pp. 2616–2619, Mar 1994.
- [326] B. Yoon, Y.-C. Jang, C. Jung, and W. Lee, “Covariance fitting of highly correlated data in lattice QCD,” *J. Korean Phys. Soc.*, vol. 63, pp. 145–162, 2013.
- [327] M. Bruno and R. Sommer, “On fits to correlated and auto-correlated data,” *Comput. Phys. Commun.*, vol. 285, p. 108643, 2023.